University of Cyprus

DEPARTMENT OF MECHANICAL AND MANUFACTURING ENGINEERING

Ultrasound-mediated, image-guided approaches for drug delivery in a machine perfused pig liver

DOCTOR OF PHILOSOPHY DISSERTATION

CHRISTINA KERAVNOU

2015

University of Cyprus

DEPARTMENT OF MECHANICAL AND MANUFACTURING ENGINEERING

Ultrasound-mediated, image-guided approaches for drug delivery in a machine perfused pig liver

CHRISTINA KERAVNOU

A Dissertation Submitted to the University of Cyprus in Partial Fulfillment of the Requirements for the Degree of Doctor of Philosophy

AUGUST 2015

VALIDATION PAGE

Doctoral Candidate: Christina Keravnou

Doctoral Thesis Title: Ultrasound-mediated, image-guided approaches for drug delivery in a machine perfused pig liver

The present Doctoral Dissertation was submitted in partial fulfillment of the requirements for the Degree of Doctor of Philosophy at the ***Department of Mechanical and Manufacturing Engineering*** *and was approved on the 6th August 2015 by the members of the* ***Examination Committee.***

Examination Committee:

Research Supervisor:

Michalakis A. Averkiou, Associate Professor,
University of Cyprus, MME Department ----------

Committee Members:

Chrit Moonen, Professor,
University Medical Center Utrecht, The Netherlands ----------

Loucas Louca, Assistant Professor
University of Cyprus, MME Department ----------

Theodora Krasia-Christoforou, Assistant Professor
University of Cyprus, MME Department ----------

Constantinos Pitris, Associate Professor
University of Cyprus, ECE Department ----------

DECLARATION OF DOCTORAL CANDIDATE

The present doctoral dissertation was submitted in partial fulfillment of the requirements for the degree of Doctor of Philosophy of the University of Cyprus. It is a product of original work of my own, unless otherwise mentioned through references, notes, or any other statements.

Christina Keravnou

……

Περίληψη

Ο καρκίνος αποτελεί μια από τις κύριες αιτίες θανάτου στην Ευρώπη και τις Ηνωμένες Πολιτείες. Συνεπώς, κρίνεται επιτακτική η ανάγκη για βελτίωση της ιατροφαρμακευτικής περίθαλψης των ασθενών μέσω εξατομικευμένων θεραπειών που θα μειώσουν παράλληλα της ανεπιθύμητες παρενέργειες. Οι ιατρικοί υπέρηχοι σε συνδυασμό με τα σκιαγραφικά υπερήχων (μικροφυσαλλίδες) και τη χορήγηση φαρμάκων έχουν μεγάλες προοπτικές για την αντιμετώπιση σοβαρών παθήσεων, αφού υπόσχονται αυξημένη αποτελεσματικότητα των φαρμάκων και βελτίωση της ποιότητας ζωής των ασθενών. Η αλληλεπίδραση των υπερήχων και των μικροφυσαλίδων έχει τη δυνατότητα να ενισχύσει την εναπόθεση του φαρμάκου στην νοσούσα περιοχή διαφοροποιώντας τη διαπερατότητα της κυτταρικής μεμβράνης και επιτρέποντας την πρόσληψη ουσιών που υπό κανονικές συνθήκες δεν θα εισχωρούσαν στα καρκινικά κύτταρα.

Η πλειοψηφία των πειραμάτων σε προηγούμενες δημοσιευμένες εργασίες στον τομέα αυτό έγινε σε κυτταρικές καλλιέργειες ή σε μικρά ζώα. Έτσι, η παρούσα διατριβή έχει ως στόχο να προωθήσει την έρευνα στον τομέα την ενισχυμένης χορήγησης φαρμάκων με χρήση υπέρηχων και μικροφυσαλίδων αναπτύσσοντας καινούρια εργαλεία και μεθόδους σε ένα περιβάλλον με μεγάλη κλινική συσχέτιση. Συγκεκριμένα, σε αυτή τη διδακτορική διατριβή τα πειράματα πραγματοποιήθηκαν σε χοιρινό ήπαρ (συκώτι γουρουνιού) το οποίο διατηρείτο σε πλήρη λειτουργία μέσω μηχανικής αιμάτωσης και μοιάζει με το ανθρώπινο ήπαρ σε μέγεθος, ανατομία και φυσιολογία. Η συνεισφορά της παρούσας εργασίας στο πεδίο της ενισχυμένης χορήγησης φαρμάκων μέσω υπερήχων πραγματοποιήθηκε με: (α) την ανάπτυξη ενός κλινικά σχετιζόμενου περιβάλλοντος για την πραγματοποίηση των πειραμάτων (πλατφόρμα μηχανικής αιμάτωσης και διατήρησης του χοιρινού ύπατος), (β) τη μελέτη του ακουστικού πεδίου που εφαρμόζεται σε θεραπευτικές εφαρμογές υπερήχων, (γ) την ανάπτυξη μεθόδων απεικόνισης και ποσοτικοποίησης της ροής στη μικροκυκλοφορία για την παρακολούθηση της θεραπείας και των αποτελεσμάτων της και (δ) τη μελέτης της αλληλεπίδρασης των υπερήχων και των μικροφυσαλίδων στην μικρό-αγγείωση του χοιρινού ύπατος.

Τα χοιρινά ήπατα συλλέγονταν από τοπικά σφαγεία και διατηρούνταν στη πλατφόρμα μηχανικής αιμάτωσης. Κατά τη διάρκεια των πειραμάτων, η λειτουργικότητα τους αξιολογούταν με βιοχημικές μετρήσεις, ιστολογικά ευρήματα και απεικόνιση μέσω υπερήχων. Ο χαρακτηρισμός του ακουστικού πεδίου στο οποίο εκτίθεται ο ιστός κατά τη

διάρκεια θεραπευτικών εφαρμογών υπερήχων έγινε με βάση γραμμικών ακουστικών μετρήσεων στο νερό και μέτρηση του συντελεστή απόσβεσης στο χοιρινό ήπαρ.

Στη διατριβή αυτή έγιναν πειράματα ποσοτικοποίησης της ροής στο χοιρινό ήπαρ για να διερευνηθούν οι προοπτικές και οι αδυναμίες στη μέτρηση της ροής στην μικροκυκλοφορία σε ένα ελεγχόμενο περιβάλλον. Η ποσοτικοποίηση προτάθηκε ως ένα πολύτιμο εργαλείο για την παρακολούθηση των θεραπευτικών εφαρμογών που στοχεύουν το αγγειακό δίκτυο των όγκων. Επίσης, αναπτύχθηκε μια νέα μέθοδος για τον περιορισμό του κορεσμού του σήματος προκειμένου να βελτιωθεί η ποσοτικοποίηση της ροής στη μικροκυκλοφορία και να επιτραπεί η ακριβέστερη αξιολόγηση των αποτελεσμάτων της θεραπείας.

Όλες οι μέθοδοι και τα εργαλεία που αναπτύχθηκαν, χρησιμοποιήθηκαν για να μελετηθούν οι αλληλεπιδράσεις των υπερήχων και των μικροφυσαλίδων στην μικρό-αγγείωση του χοιρινού ύπατος. Οι ακουστικές παράμετροι που μπορούν να προκαλέσουν ανιχνεύσιμες αλλαγές της αιμάτωσης στην περιοχή η οποία εκτίθεται σε υπερήχους περιγράφονται στη παρούσα διατριβή.

Abstract

Cancer is considered to be one of the leading causes of death in Europe and the Unites States. Thus, the need for improved healthcare where the treatments will take into account individual patient needs emerges. The therapeutic prospective of ultrasound combined with microbubbles and drugs has gained increased attention in research and clinics as the advantages of such localized treatments are associated with increased medication efficacy and improved life quality of the patients. The physical interaction of ultrasound and microbubbles has the potential to enhance drug delivery by altering cell's membrane permeability, allowing for the uptake of normally impermeable macromolecules, a process often referred to as sonoporation. As the majority of previously published works in this field was performed *in-vitro* in cell cultures or in small animal models, this thesis aimed to contribute in the area of ultrasound-enhanced drug delivery by developing new tools and methods that will advance research to a full scale clinically relevant environment. The present thesis deals with the investigation of ultrasound-mediated drug delivery approaches in a machine perfused pig liver and specifically develops the following building blocks: (a) a clinically relevant machine perfused liver model, (b) methods for *in-situ* acoustic pressure calculation, (c) imaging and quantification approaches for closely monitoring therapy and its outcomes, and (d) study of ultrasound and microbubble mediated extravasation.

An *ex-vivo* machine perfusion system for pig liver preservation was used as the test platform for investigations associated with ultrasound therapeutic approaches. The proposed environment maintains high relevance to human livers with respect to physiology and anatomy. The functionality and viability of slaughterhouse pig livers sustained in machine perfusion was evaluated with hemodynamic and biochemical measurements and histological findings. In addition, dynamic contrast-enhanced ultrasound (DCEUS) was proposed in order to assess the condition of the organs during machine perfusion.

The characterization of the *in-situ* acoustic field when tissue is exposed to ultrasound is of great importance for cavitation-related phenomena. Thus, low amplitude acoustic measurements in water were collected and were combined with *ex-vivo* machine perfused liver tissue attenuation measurements, to enable the estimation of the acoustic pressure delivered *in-vivo* during ultrasound therapeutic applications.

DCEUS quantification based on indicator dilution theory was evaluated in the functioning *ex-vivo* pig liver model to find the range of accuracy and strength and weaknesses in measuring flow in the micro-circulation in a highly controlled environment which mimics *in-vivo* conditions. The established quantification methods were proposed as a valuable tool for real-time monitoring of therapeutic applications which target the vascular network of tumors. A method for limiting signal saturation was also developed, in order to improve DCEUS quantification approaches and allow for more accurate evaluation of the therapy results.

Finally, all developed methods and tools were combined to investigate the interactions of ultrasound-driven microbubbles with the microvasculature of a functioning machine-perfused pig liver under ultrasound imaging guidance. Ultrasound parameters that are capable of causing detectable perfusion changes and extravasation in the area exposed to ultrasound were derived in a test platform that highly resembles *in-vivo* conditions.

Acknowledgments

I would like to express my sincere gratitude to my advisor Prof. Mike Averkiou, for the continuous support of my PhD study, for his patience, motivation, and immense knowledge. His guidance helped me in all the time of research and writing of this thesis. Prof. Averkiou believed in my skills and capabilities from the time I was an undergraduate student in his numerical methods class. He was the one that introduced me to the field and made me love research. Working close to him the last 6 years and witnessing his passionate dedication to both research and teaching have been an endless source of inspiration.

My sincere thanks also goes to Dr. Maria-Louisa Izamis. She is such an amazing researcher, teacher and friend. Her guidance during the *ex-vivo* pig liver experiments was invaluable and it is greatly appreciated. I was very fortunate to collaborate with her. Maria-Louisa, know that I have learned a lot from you.

Dr. Damianos Christophides, my colleague and friend is also thanked for the help and support offered during our postgraduate studies. I always admired his programming skills, his devotion to research and his unique ability of coming up with new, amazing and genuine ideas. When I got to know him better, I was thrilled by his sense of humor. We shared a lot of happy memories and honestly the lab would not be the same without him.

I would also like to thank Dr. Christophoros Mannaris. He has been like a big brother to me in the lab from the time I was an undergraduate student. Performing experiments with him was always a fun and interesting learning experience. Most important he is acknowledged for believing in me and forcing me to continue even when I was disappointed and I thought I couldn't make it.

Mr. Kypros Stylianou, our laboratory technician who is so much more than that, is sincerely thanked for all his help in designing and building the experimental setups. He is also acknowledged for his help in pig liver procurement. Many experiments wouldn't have been accomplished without his exceptional skills. I would also like to acknowledge Mr. Chrysovalantis Papantonis, Ms. Elena Pieri, Ms. Charis Rousou, and Ms. Christiana Tapolou, all Masters Students at Biomedical Ultrasound Laboratory, for their help and contribution in liver experiments.

My two good friends and former lab colleagues Ms. Christina Kalli and Ms. Eleni Efthymiou are also thanked for their true friendship and support.

Special thanks goes to my parents and sister for always being there for me, supporting me for everything, and especially encouraging me throughout this experience. Their endless love accompanied me along the way.

Last, I would like to thank my husband and best friend George. He has been a gentle force all this years, standing by my side, listening and making me believe that I can succeed. He is my rock, and without his moral support I wouldn't have made it.

To my parents, sister and husband for their endless love and support

Contents

List of Figures

List of Tables

1 Introduction

1.1 Ultrasound imaging

Ultrasound is widely accepted as a non-invasive, non-ionizing and cost efficient diagnostic modality [1] which allows real-time imaging of anatomical features (Gray scale imaging) and blood flow (Doppler imaging) in the body. Although ultrasound imaging is best known for its use in prenatal care, it is also routinely used in cardiology (echocardiography), to provide information about cardiac muscles, valves and blood flow within the heart [2], [3], and in oncology for lesion detection and characterization [4], [5].

Ultrasound imaging utilizes high frequency pulses in the range of 1- 20 MHz and relies on the pulse-echo principle. These pulses travel through the human body and are partially reflected from structures (tissues and organs) with different acoustic impedances along the propagation path. Part of the echoes, return to the ultrasound system which process them into an image.

Blood flow measurements using the Doppler method are feasible since ultrasound echoes reflected from a moving target (e.g. red blood cells) face an apparent change in their transmitted frequency (Doppler shift). The change in frequency is proportional to the moving target velocity. However, red blood cells are weak reflectors, thus imaging flow in small vessels with this technique is still challenging. An approach to overcome the limitations of Doppler in imaging micro-vascular perfusion is to inject acoustic reflectors into the circulation, to increase backscattering from blood. The increased compressibility of a gas compared to the surrounding liquid and tissue enables gas-filled microbubbles to be such efficient scatterers, thus be used as ultrasound contrast agents.

A milestone in ultrasound imaging research was the development of nonlinear imaging in the early 1990s. Back then, nonlinear imaging was developed to establish a method for imaging echoes from ultrasound contrast agents (microbubbles) [6], as at that time it was assumed that there would not be any nonlinear echoes from tissue. Later works [7]–[9] showed that tissue produces also nonlinear echoes. While microbubbles are nonlinear scatterers, tissue nonlinearity arises from the distortion of the pulse due to nonlinear propagation of sound [10]. Various methods have been proposed for nonlinear imaging (tissue and contrast), like harmonic imaging [11], nonlinear pulsing schemes [12]–[14], sub-harmonic imaging [15], super-harmonic imaging [16], coded excitation and frequency modulation techniques [17]–[19] and dual frequency pulses methods [20]–[23], offering significant advantages in many clinical applications [24], [25].

Beyond the use of ultrasound as a diagnostic modality, today ultrasonic imaging is an integral part of therapeutic applications for guiding treatments [26]. The combination of diagnostic and therapeutic approaches – currently given the term "theranostics" [27] – has the potential of developing novel and personalized procedures to address specific patient needs.

1.2 Ultrasound contrast agents

Ultrasound contrast agents (UCAs) are microbubbles containing gas stabilized in an encapsulating shell made of a flexible, biocompatible material (lipid, polymer or protein). Microbubbles (MBs) are injected intravenously in the circulation and due to their size (1-10 μm) they have similar kinetics with red blood cells. As they are big enough not to leak into the interstitial space, they are a true blood-pool agent. Microbubbles no larger than roughly 5μm pass through the alveolar–capillary barrier of the lungs and they spread all over the cardiovascular system in any region that contains a blood-carrying vessel [28].

Microbubbles behave as resonant scatterers at the frequencies typically used in ultrasound imaging. Thus, when MBs encounter an ultrasound wave of low acoustic pressure, they undergo a series of stable oscillations (stable cavitation, Figure 1.1); expand at negative pressure (rarefaction) and compress at positive pressure (compression). However, MBs expansion and compression is not symmetrical, resulting in a nonlinear oscillation [Figure 1.2(b)]. The spectrum of backscattered MBs signals [Figure 1.2(c)] is filled with harmonics, and these nonlinear components can distinguish MBs from the surrounding tissue.

High acoustic pressures cause unstable MBs expansion and compression (inertial cavitation, Figure 1.1), resulting in fragmentation of the shell and microbubble destruction with diffusive loss of the gas core. The likelihood of bubble destruction is given by the mechanical index (MI) [29], defined with Eq. (1.1):

$$MI = \frac{p_-}{\sqrt{f}}, \qquad (1.1)$$

where p_- is the peak negative pressure and f is the frequency of the ultrasound pulse.

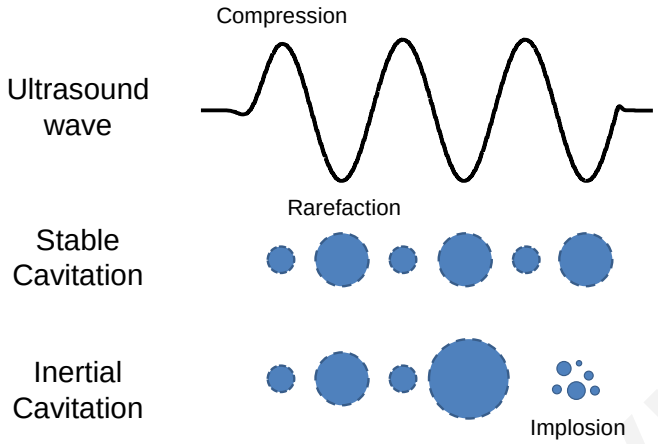

Figure 1.1: Schematic representation of stable and inertial cavitation of a microbubble driven by an ultrasound wave.

The use of UCAs combined with a variety of available nonlinear detection techniques [12]–[23], enables real-time visualization of the perfusion at macro- and micro-vascular level [28], [30], [31]. Dynamic contrast-enhanced ultrasound (DCEUS) imaging is clinically applied in many different fields including cardiology [2], [3] and oncology [4], [5] offering great diagnostic advantages.

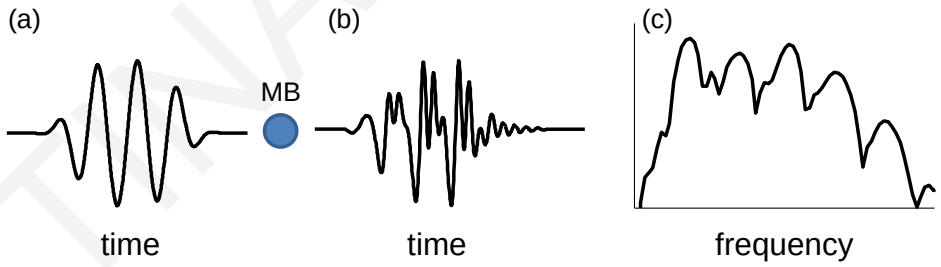

Figure 1.2: (a) A typical sinusoidal pulse used in US imaging. (b) The asymmetric, nonlinear signal scattered from microbubbles (MBs). (c) The frequency spectrum of microbubbles oscillations which is filled with harmonic components.

1.3 Quantification of dynamic contrast-enhanced ultrasound (DCEUS)

Beyond diagnosis in oncology, DCEUS has gained a foothold in clinics as a promising therapy monitoring tool by offering quantitative evaluation of macro- and micro- vascular perfusion. The underlying hypothesis is that local hemodynamic-related parameters extracted from DCEUS image loops reflect changes in blood flow such as those

caused by anti-angiogenic therapies [32], [33]. Anti-angiogenic therapies target the new vessels that are formed during tumor angiogenesis [34], thus tumor local blood supply is expected to change as therapy progresses.

There are two methods for flow quantification based on indicator dilution theory [35], which depend on the protocol of contrast agent administration; bolus injection (impulse input) or constant infusion (step input) [33], [36], [37]. In the present work, only the first method has been utilized and hence is further discussed here.

The bolus injection protocol involves a rapid injection of the contrast agent and low MI, real-time imaging. The contrast starts to enter the imaged area [Figure 1.3(b)] until it reaches a maximum concentration [Figure 1.3(c)]. After maximum is reached, concentration is reduced and asymptotically goes to zero [Figure 1.3(d, e)]. A region of interest (ROI) is drawn at a specific area of the image [Figure 1.3 (red circle)], and a time-intensity curve (TIC) is formed [Figure 1.3 (red dots)] that represents the mean pixel intensity of the ROI as a function of time.

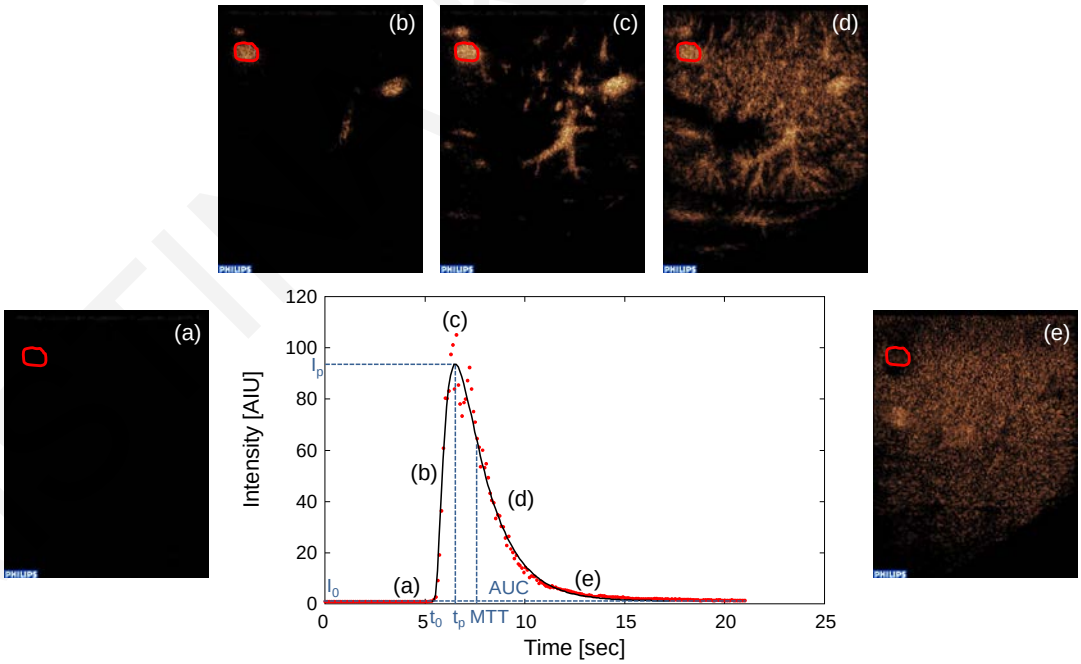

Figure 1.3: Formation of a time-intensity-curve (red dots) and curve fit of the data using a local density random walk (LDRW) model (solid line). Contrast images: (a) before contrast agent arrival, (b) after arrival of the contrast agent, (c) maximum concentration of contrast at the region of interest (ROI) and (d, e) asymptotic reduction to zero of the contrast agent. Quantification parameters extracted from LDRW model, such as peak intensity (I_p), time to peak (t_p), area under the curve (*AUC*) and mean transit time (*MTT*) are also noted at the figure.

Time-intensity curves are often noisy and affected by the recirculation of the microbubbles. Therefore, the data can be fitted to mathematical models (probability distribution functions) based on indicator dilution theory to limit the noise and isolate the primary pass of microbubbles [Figure 1.3 (solid line)] [38]. In addition, curve-fitting allows an analytical determination of important hemodynamic-related parameters such as the time to peak intensity (t_p), the mean transit time (MTT) and the area under the TIC curve (AUC). The most commonly used indicator dilution models are the lognormal function, the gamma-variate function, and the local density random walk (LDRW) model.

Bolus injection method is governed by the Stewart-Hamilton relationship [39], [40]. If the amount of indicator *m* in a bolus injection is known and the indicator concentration as a function of time is measured in a ROI, the volumetric blood flow (*Q*) and the blood volume (*V*) can be calculated in terms of AUC and MTT:

$$Q = m \cdot (AUC)^{-1} \qquad (1.2)$$

$$V = Q \cdot MTT\,. \qquad (1.3)$$

Microbubble concentration cannot be measured directly, thus the backscattered intensity $I(t)$ is measured instead. Since intensity is linearly proportional to the concentration [41], [42], one can use Eqs. (1.2), (1.3), to calculate *Q* and *V*.

A relatively simple way to investigate DCEUS quantification is with flow phantoms. In the past, several different studies focused on flow measurements using contrast agents quantification *in-vitro* [43]–[46]. In 2010, Lampaskis and Averkiou, [42] used a diagnostic ultrasound scanner and a flow phantom to investigate the relationship between image intensity and microbubbles concentration (SonoVue) at low MI. They confirmed a linear relationship between linearized image intensity and contrast agent concentration for low concentrations (up to 1‰) and a plateau for greater concentrations, attributed to signal saturation and acoustic shadowing. Signal saturation is often encountered in diagnostic ultrasound scanners especially when used to image microbubbles. Signal saturation can negatively influence the quantification of TICs, especially when the dynamic range of the backscattered signals varies dramatically depending on bubble concentration [42], [47]–[49].

Later the same authors, [50], presented measurements of relative blood flow rate using an *in-vitro* flow phantom setup, demonstrating the range of validity of indicator

dilution theory for DCEUS quantification. Gauthier et al. [51], used a dialysis cartridge as a flow phantom to evaluate the impact of ultrasound scanner settings and contrast bolus volume on TICs. This work is important to ensure the collection of accurate and reproducible data, and standardize DCEUS quantification technique in each specific organ of interest.

In-vitro experiments have however very little physiological relevance as they usually represent a single passage of contrast through a rubber tubing, ignoring the dispersion of microbubbles through branching vessels; their passage through fast-moving arteries, a slow micro-circulation and a low-pressure venous system and the different flow states (laminar or turbulence) along their propagation path. An additional difficulty in clinical investigations is the chaotic and uncontrolled vasculature that characterizes tumors. Reports from *ex-vivo* and preclinical *in-vivo* investigations confirming the validity of indicator dilution theory as a therapy monitoring metric are still missing from literature. The main question that remains unanswered is whether contrast enhanced ultrasound can become an accurate technique of micro-flow measurement. The need of deeper understanding of the dependency of quantification parameters with contrast concentration, flow variations and ultrasound scanner settings is therefore essential.

1.4 Machine perfusion for organ preservation

Machine perfusion (MP) is a method of sustaining an isolated organ alive outside the body (*ex-vivo*) by supplying it with oxygen and nutrients acting as natural perfusion. It originated as an experimental technique to study organ metabolism [52], however nowadays it has been suggested as a donor organ preservation modality that is superior to the gold standard of static cold storage currently used in transplantation [53]–[55]. Machine perfusion has also been proposed as an ideal environment for preclinical diagnostic, imaging and therapeutic investigations [56], [57] because it enables several hours of controlled and stable experimentation with the organ of interest, while maintains high physiological relevance lacking from *in-vitro* experiments.

Recently, Izamis et al. [56] developed and evaluated a sub-normothermic human-sized machine perfusion system suitable to preserve slaughterhouse pig livers. They showed using biochemical and hemodynamic measurements and dynamic contrast-enhanced ultrasound imaging that the developed model is a simple, cost-effective approach

for at least 3 hours of stable, *ex-vivo* whole organ preservation. The current thesis aims in advancing ultrasound-enhanced drug delivery research from cell cultures and small animal models to a full scale clinically relevant environment. Thus, the developed *ex-vivo* machine perfusion liver model [56] was used throughout this work as the test platform for preclinical investigations associated with ultrasound–enhanced drug delivery applications.

1.5 Ultrasound used in therapeutic applications

Through the years, ultrasound has seen development not only as a diagnostic device but also as a therapeutic modality which may cause either reversible or irreversible changes on the exposed tissue depending on the applied acoustic pressure levels and the goal of the treatment. Ultrasound therapies are broadly divided into two categories; “low intensity” and “high intensity”, while some therapies might also involve the combination of ultrasound with microbubbles and drugs [58].

Low intensity therapies are currently in widespread practice for physiotherapy, to treat conditions such as bursitis of the shoulder or tendonitis [59] and to enhance transdermal delivery – a process called sonophoresis [60], [61]. Today there is also great research activity and particular interest in thrombolysis [62], [63], drug delivery [26], [64], [65] and gene therapy [65] using low power ultrasound.

High intensity ultrasound is mainly used for permanent tissue changes and ablations. Some of the most common therapeutic applications of high intensity ultrasound include uterine fibroid ablation [66], [67], cardiac [68] and solid tumor ablation [69], treating essential tremor and Parkinson’s disease [70], and the breakup of renal stones (lithotripsy) [71]. This kind of interventions is usually extracorporeal and minimally invasive, especially beneficial for the treated patients. The resulting bioeffects of therapeutic ultrasound in previously mentioned applications can be attributed in two main mechanisms: thermal or non-thermal (mechanical) [72].

Thermal mechanisms involve heating and cause a rise in temperature of the insonified area as a result of the thermoviscous absorption of the ultrasonic energy during passage in biological tissue. The heating process is strongly related to the intensity and the duration of the propagated pulse. Depending on the application, the rise in temperature above normothermic levels may vary from a few degrees to tens of degrees Celsius and the

effects from the ultrasound exposure can include mild heating, coagulative necrosis, tissue vaporization or all three.

Mild, homogeneous heating (raising the temperature to 40 – 42 °C) in a large area can be achieved using unfocused ultrasound sources. In physiotherapy, mild heating is widely used to warm tendons, muscles and other tissues to improve blood flow and accelerate healing. Mild heating can also enhance localized drug delivery [73]; a topic that is further discussed in a following section.

Hyperthermia treatments were developed for the purpose of cancer therapy, aiming ultrasonic heating of relatively large volumes (tumors). During hyperthermia, tumor cells are exposed to temperatures 43 – 50 °C for periods up to 1 hour leading to reduction of tumor growth as cells are unable to divide under these conditions [58].

High intensity focused ultrasound (HIFU) treatments involves rapid increase of temperature above 56 °C in a very small and controlled area (few mm), using highly focused transducers. The resultant high temperature gradient leads to instantaneous cell death, thus HIFU is mainly used for ablations and permanent tissue changes [58].

The main non-thermal mechanism with potential therapeutic benefits is acoustic cavitation, defined by Apfel [74] as the “formation of a vapor cavity or bubble in response to an acoustic pressure field”. Acoustic cavitation depends on the rarefactional pressure amplitude of the transmitted ultrasound waves. In high enough levels (cavitation threshold), the rarefactional pressure may initiate cavitation activity in a tissue (if cavitation nuclei are present) or directly induce pulsation of pre-existing gas bodies. Cavitation threshold strongly depends on the amount and nature of nuclei and gas present in the exposed tissue [74]. Inertial cavitation characterized by violent expansion and rapid collapse of bubbles, can introduce bioeffects such as tissue injury, cell death and hemorrhage of blood vessels facilitating ablations and other ultrasound therapeutic applications.

Other non-thermal mechanisms responsible for ultrasound-induced bioeffects are the direct action of the compressional, tensile and shear stresses, the radiation pressure, and acoustic streaming [75]–[77].

One new research area of therapeutic ultrasound with induced bioeffects attributed to non-thermal mechanisms and specifically cavitation activity is histotripsy [78].

Histotripsy is a non-invasive tissue ablation method that depends on the initiation and maintenance of a cavitation cloud to fractionate soft tissue. This method utilizes high pressure (>10 MPa peak negative pressures) short pulses (<20 μs) at low duty cycles (<1%) to produce mechanical tissue fractionation [79]. It was shown that a single pulse with one high-amplitude negative cycle is enough to form the cavitation cloud, if the negative pressure amplitude directly exceeds a pressure threshold intrinsic to the medium [80]. Histotripsy lends itself to real time ultrasound imaging during treatment since the formed bubble cloud is clearly visible in B-mode image as a hyper echoic region while the fractionated tissue can also be identified as a dark region on the same image.

Another method which has been recently suggested for controlled tissue emulsification is boiling histotripsy [81]. In contrast to histotripsy, boiling histotripsy utilizes millisecond duration HIFU pulses and the induced bioeffects owe to boiling instead of cavitation. Specifically, the absorption of shock waves formed at the focus of the HIFU source results in temperatures over 100 °C, thus causes localized boiling in only several milliseconds. Recently published works, where the experiments performed in gels, in *ex-vivo* tissue samples and in an *in-vivo* porcine liver model, showed that millisecond boiling is an effective and reliable way to emulsify tissue and advance clinical applications related to tissue ablation [81], [82].

Other applications that owe to ultrasound mechanical aspect are blood brain barrier (BBB) opening [83], gene therapies and localized drug delivery [64], [65]. As this thesis focuses on the development of tools and methods which can advance ultrasound-mediated drug delivery applications, ultrasound-enhanced drug delivery is further discussed in the next section.

1.6 Image-guided ultrasound-enhanced drug delivery

Localized drug delivery can potentially increase the therapeutic index of many anticancer drugs by improving their efficacy, as higher doses manage to reach the diseased site. In addition, patients benefit from localized drug delivery because systemic toxicity and undesired site effects are reduced. The combination of ultrasound and microbubbles is currently of great clinical interest as it is promising in facilitating *in-situ* drug delivery and also enables real time monitoring of the process. Ultrasound can be used as external stimulus (via temperature or pressure increase) to locally release a novel generation of

drugs that are encapsulated into carriers. At the same time, ultrasound induced bioeffects can mediate drug and gene transfection into the cells.

1.6.1 Thermal action and activation

The encapsulation of drugs in carriers is currently one of the most common approaches used in targeted drug delivery applications. Liposomes have been explored as potential nano-vehicles since they are small enough to extravasate into the interstitial space and enter leaky tumor vasculature, increasing drug deposition in the diseased site while reducing toxic exposure to healthy tissue. However, even though drug accumulation in liposomal form is higher in tumors compared to non-encapsulated drugs, the slow passive release of the drug limits its effectiveness. A solution to this obstacle is the release of drugs from the carriers using an external stimulus.

Temperature-sensitive liposomes (TSLs) have been designed to release their payload once heated at the melting phase transition temperature of the lipid membrane. Ultrasound can induce hyperthermia in a non-invasive, localized and controlled manner, thus it has been proposed to be used as an external source of heating in temperature-triggered drug delivery applications [84]. The combination of ultrasound-triggered temperature-related drug delivery applications with other imaging modalities such as magnetic resonance (MR-HIFU) can provide temperature and spatial feedback during treatment and real-time evaluation of the process.

1.6.2 Mechanical action and activation

Microbubbles are considered to be an integral part of pressure-mediated drug delivery applications since they can both facilitate local release of therapeutics on the diseased site and increase local uptake. Microbubbles can act as the vehicles of a targeted delivery system by loading them with drugs and selectively fragmenting them in the desired location to release their payload. In this manner, drugs are protected while travelling in the blood stream and less toxicity is distributed in the rest of the body. Although there are various drug loading methods, it was shown that some types of MB drug carriers can retain their high echogenicity and act also as imaging agents [27], [85], enabling real time monitoring of the treatment.

Microbubbles cannot only act as drug carriers but they can also be co-administered with drugs during treatment to enhance local uptake. Several published studies have shown that the physical interaction of ultrasound and microbubbles has the potential to facilitate localized drug delivery by altering cell membrane permeability, allowing for the uptake of normally impermeable molecules into the cells [26], [64]. Stable cavitation, occurring at lower acoustic pressures and inertial cavitation observed at higher acoustic pressures are mainly responsible for the introduced bio-effects that lead to enhanced drug deposition *in-situ*.

Various aspects and patterns of stable and inertial cavitation (summarized in Figure 1.4) have been hypothesized as mechanisms that contribute towards cell membrane disruption. Specifically, during the expansion and compression phase of a stably cavitating microbubble, pushing and pulling of the cell membrane occurs [Figure 1.4(a)]. In addition, microbubbles are displaced towards the cells driven by the acoustic radiation force [Figure 1.4(b)]. Both interactions of microbubbles with cells can result in cell membrane disruption. Micro-streaming is also developed in the surrounding fluid by the stable oscillation of a microbubble [Figure 1.4(c)]. This effect exerts mechanical stress on the cell membrane and may cause pore formation. When microbubbles are exposed to high intensity ultrasound, inertial cavitation takes place leading to violent collapse of the oscillating bubble. Due to microbubbles asymmetrical oscillation and violent destruction, shock waves [Figure 1.4(d)] and high velocity liquid microjets are created [Figure 1.4(e)] causing pores formation on the cell membrane [64]. Consequently, two phenomena are mainly responsible for enhanced drug uptake; the direct pore formation on the cells, a process termed as sonoporation, and enhanced endocytosis [86] which may occur at the same time.

Sonoporation has been extensively studied both *in-vitro* (using multiple types of cell cultures) [87]–[89] and *in-vivo* (mainly in small animal models) [90], [91]. It was reported that small compounds (<1kDa) [92], macromolecules [93], genes [94], [95] and other therapeutic compounds have successfully been delivered into the cells. Recently a pilot clinical study on treating pancreatic cancer utilizing the combined effects of ultrasound, microbubbles and gemcitabine has also been published [96]. However there are differences among the studied environments and experimental setups, leading to a variety of published acoustical conditions under which enhanced uptake is observed. The reported parameters range in acoustic pressures from few kPa to few MPa, while pulse durations

vary between 10μs and 10ms. Therefore, the exact sonoporation mechanism has not yet been fully exploited.

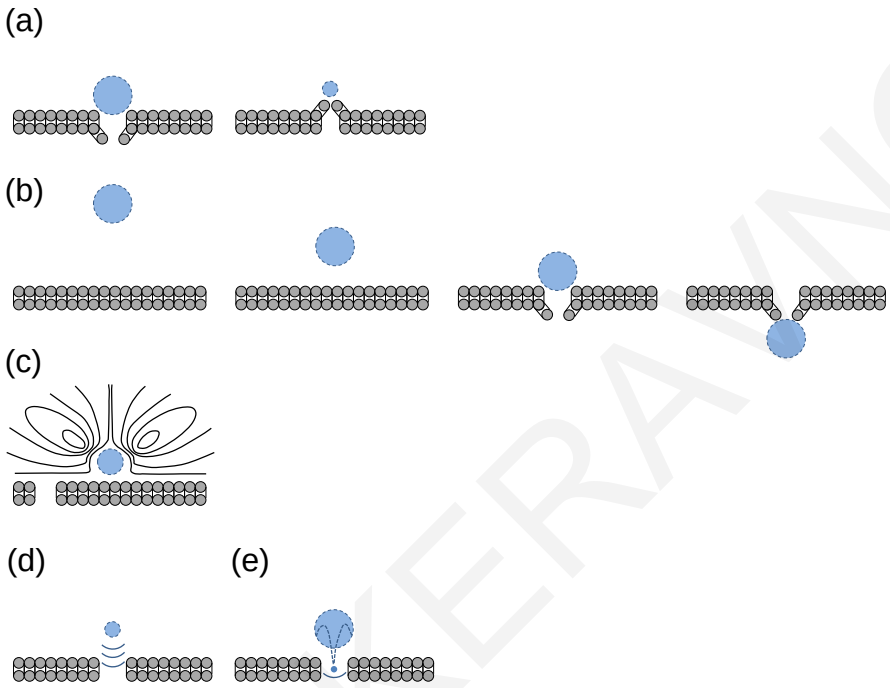

Figure 1.4: Biophysical effects of stably and inertial cavitating microbubbles.

The translation of the acoustic parameters of *in-vitro* experiments to the real clinical application is still a great challenge. This is because at *in-vitro* studies, tumor cells are directly exposed to the ultrasound field and microbubbles, thus the induced temporal or permanent openings increase cell membrane permeability allowing entrance to normally impermeable molecules. Depending on the applied acoustic pressure, the size of the pores varies [64]. If the pores are small they will stay open for some time (termed as temporal window) allowing the passage of therapeutics while if the pores are too large they cannot reseal leading to cell death. It has been reported in the literature that temporal pores close within seconds after ultrasound is turned off [97] while there are also reports that cellular uptake of small particles may last for hours [88], [98].

However, *in-vivo* applications of ultrasound-enhanced drug delivery are much more complicated. Since microbubbles and drugs circulate in the vasculature, the first step towards ultrasound-mediated drug delivery is to increase the permeability of endothelia cells of the vessel wall. If the endothelia permeability is altered, drugs that would

otherwise remain confined within the vasculature are allowed to extravasate into the interstitial space. It is after entering the interstitial space that drugs have to reach the diseased site (e.g. tumor cells). Extravasation is achieved as ultrasound and microbubble interactions (stable and inertial cavitation) can destabilize tight junctions and create openings between neighboring cells of the endothelial layer [99]. To obtain significant extravasation, the openings between the endothelia cells should remain open for an extended period of time. The magnitude of changes in both vascular and endothelia permeability are related to ultrasound frequency, acoustic pressure and microbubble parameters [27]. In addition, another factor that is significant at *in-vivo* applications, ignored at *in-vitro* experiments, is the immune system response after ultrasound exposure [100]. Vessel wall disruption can lead to activation of mechanisms of the human body responsible to confront inflammatory events, thus changing the local environment of drug delivery (e.g. inducing vasodilation of arterioles thus vascular flow changes, chemical reactions, etc.) [101].

1.7 Scope of the thesis

This thesis focuses on the development of tools and methods that can help the translation of ultrasound-mediated drug delivery applications to clinical studies. A novel experimental setup, an *ex-vivo* functioning human-sized liver, is developed allowing for the investigation of acoustic parameters utilized in drug delivery applications. The proposed experimental environment aims in advancing research from cell cultures and small animal models to a full scale clinically relevant *ex-vivo* model, which is significant in preclinical research. As the in-depth knowledge of the acoustic parameters is essential before proceeding to further investigations, in this thesis physical acoustics are employed to characterize the acoustic field applied in ultrasound therapeutic applications. Specifically, a simple, reliable, and reproducible method for estimating the acoustic pressure delivered in tissue exposed to ultrasound is presented and evaluated using both experiments and simulations. Bubble dynamics are also investigated here and a new technique for accurate characterization of contrast agents with an ultrasound scanner is developed. The proposed method can facilitate imaging during therapeutic procedures even in high MIs and advance DCEUS quantification as signal saturation can be removed from the collected data. One of the main questions posed in this work is whether DCEUS can

become an accurate technique of micro-flow measurements. Thus, dynamic contrast-enhanced ultrasound quantification is investigated in the functioning *ex-vivo* pig liver model, where the vasculature remains intact and microbubbles dispersion through branching vessels resembles reality. Following all above, DCEUS quantification is proposed as a metric for assessing therapy outcomes and evaluated whether can detect micro-vascular flow changes induced by ultrasound therapeutic approaches. The interaction of ultrasound-driven microbubbles with the capillaries under sonoporation conditions are also investigated in the developed *ex-vivo* pig liver model and the optimized ultrasound parameters that will lead to enhanced extravasation are derived under physiological conditions.

Chapter 2 presents the development of a sub-normothermic *ex-vivo* machine perfusion system suitable to preserve human-sized livers for at least 3 hours. The use of slaughterhouse animals as an alternative source of organs for diagnostic, imaging and therapeutic investigations is suggested and explored to minimize the regulatory requirements, operational costs and ethical burden associated with live animal surgery. Thus, healthy pig livers were procured from a local (food chain) slaughterhouse and sustained to the developed machine perfusion system. Porcine livers are preferred over livers from other species since they are more similar to human livers with respect to physiology and anatomy [102]. The developed model was chosen to serve as the test platform for the development and study of perfusion quantification methods and ultrasound-mediated drug delivery applications, as it provides an ideal environment for preclinical investigations with high physiological relevance not available in *in-vitro* experiments.

Chapter 3 focuses on the methods developed for characterization and *in-situ* estimation of the applied acoustic field during ultrasound therapeutic applications. A simple, reliable, and reproducible method for estimating the acoustic pressure delivered in tissue exposed to ultrasound is presented and evaluated. The proposed method is based (a) on low amplitude water measurements, that are easily collected and they do not suffer from nonlinear propagation effects, and (b) the attenuation coefficient of tissue of interest. *Ex-vivo* machine perfused pig liver tissue, harvested according to the methods described in Chapter 2, was used to validate the method for source pressures up to 3.5 MPa. The method can be used to estimate the delivered pressure *in-vivo* both in diagnostic and therapeutic applications of ultrasound.

Chapter 4 poses the question of microbubble response to increasing acoustic amplitude while at the same time develops methods to correct for signal saturation in diagnostic ultrasound scanners. The correction of signal saturation is very important for the perfusion quantification methods that are developed and described later in this thesis. A diagnostic ultrasound scanner is used to investigate microbubbles nonlinear response after being exposed to peak negative pressures between 0.06 MPa and 2.6 MPa. Various concentrations with clinical relevance are used in this study. The problem of signal saturation observed when ultrasound scanners are used to record backscattering from microbubbles is also addressed and a correction method is provided. In short, signal saturation with increasing pressure and bubble concentration was carefully avoided by continuously adjusting the scanner's 2D analog gain and accounting for it in the quantification software. Now with accurate recording of the backscattering from microbubbles, the intensity-concentration relationship was measured in detail for both low and high pressure amplitudes. Contrast-to-tissue ratio as a function of MI, without the effect of signal saturation, was calculated for a range of concentrations. The results of this study can be used to better guide drug delivery approaches and develop imaging techniques for therapeutic procedures.

Chapter 5 deals with the evaluation of therapeutic outcomes after ultrasound-mediated drug delivery applications. It is hypothesized that microvascular flow changes (often caused by a therapeutic procedure) can be detected using DCEUS quantification which is based on indicator dilution. Thus, DCEUS quantification methods are evaluated in the functioning *ex-vivo* pig liver model to find the range of accuracy and strength and weaknesses in measuring flow in the microcirculation in an environment where there is dispersion of microbubbles through branching vessels like *in-vivo* condition. The intensity-concentration relationship was first investigated by changing the amount of microbubble concentrations for fixed flow rates. Signal saturation was corrected using the method described in Chapter 4. Then, various flow changes with clinical/physiological relevance were dialed in the pig liver model and were measured with DCEUS quantification. Hemodynamic-related parameters (such as the rise time, mean transit time, area under the curve and peak intensity) extracted from curve fitting models based on indicator dilution theory were related to the induced flow changes in both macro- and micro- vascular level. The results here suggest that DCEUS quantification is capable of measuring flow changes

in the macro- and micro-circulation such as those induced by therapies targeting angiogenesis.

Finally, Chapter 6 focuses on the investigation of the interaction of ultrasound-driven microbubbles with the capillaries under sonoporation conditions. Specifically, the effect of acoustic pressure, number of cycles, and microbubble presence on vessel poration and extravasation are studied in the developed *ex-vivo* pig liver model. An experimental setup was developed that allows real time monitoring of the therapy procedure and imaging of the cavitation activity. Therapeutic outcomes were evaluated using gross morphology and lesion size examination, histology and detection of micro- vascular flow changes using DCEUS quantification based on indicator dilution theory. The optimized ultrasound parameters that lead to enhanced sonoporation and extravasation are derived.

The overall results from this thesis are further discussed and analyzed in Chapter 7 and conclusions are drawn together with suggestions for future direction for research in this area.

REFERENCES

[1] W. D. O. Jr, “Assessing the Risks for Modern Diagnostic Ultrasound Imaging,” *Jpn. J. Appl. Phys.*, vol. 37, no. 5S, p. 2781, 1998.

[2] K. Wei, A. R. Jayaweera, S. Firoozan, A. Linka, D. M. Skyba, and S. Kaul, “Quantification of myocardial blood flow with ultrasound-induced destruction of microbubbles administered as a constant venous infusion,” *Circulation*, vol. 97, no. 5, pp. 473–483, Feb. 1998.

[3] T. R. Porter and F. Xie, “Myocardial perfusion imaging with contrast ultrasound,” *JACC Cardiovasc. Imaging*, vol. 3, no. 2, pp. 176–187, Feb. 2010.

[4] P. Ricci, V. Cantisani, L. Ballesio, E. Pagliara, E. Sallusti, F. M. Drudi, F. Trippa, F. Calascibetta, S. M. Erturk, M. Modesti, and R. Passariello, “Benign and malignant breast lesions: efficacy of real time contrast-enhanced ultrasound vs. magnetic resonance imaging,” *Ultraschall Med. Stuttg. Ger. 1980*, vol. 28, no. 1, pp. 57–62, Feb. 2007.

[5] S. R. Wilson and P. N. Burns, “Liver mass evaluation with ultrasound: the impact of microbubble contrast agents and pulse inversion imaging,” *Semin. Liver Dis.*, vol. 21, no. 2, pp. 147–159, May 2001.

[6] Burns PN, “Harmonic imaging with ultrasound contrast agents.,” *Clin. Radiol.*, vol. 51, pp. 50–5, 1996.

[7] M. A. Averkiou, D. N. Roundhill, and J. E. Powers, “A New Imaging Technique Based on the Nonlinear Properties of Tissues,” *Proceedings /*, vol. 2, p. 1561, 1997.

[8] Christopher T, “Finite amplitude distortion-based inhomogeneous pulse echo ultrasonic imaging.,” *IEEE Trans. Ultrason. Ferroelectr. Freq. Control*, vol. 44, no. 1, pp. 125–39, 1997.

[9] Ward B, Baker AC, and Humphrey VF, “Nonlinear propagation applied to the improvement of resolution in diagnostic medical ultrasound.,” *J. Acoust. Soc. Am.*, vol. 101, no. 1, pp. 143–54, 1997.

[10] M. F. Hamilton and D. T. Blackstock, *Nonlinear acoustics*. San Diego, CA: Academic Press, 1998.

[11] M. A. Averkiou, “Tissue harmonic ultrasonic imaging,” *COMPTES RENDUS- Acad. Sci. PARIS Ser. 4 Phys. Astrophys.*, vol. 2, no. 8, pp. 1139–1151, 2001.

[12] M. A. Averkiou, C. Mannaris, M. Bruce, and J. Powers, “Nonlinear pulsing schemes for the detection of ultrasound contrast agents,” *J. Acoust. Soc. Am.*, vol. 123, no. 5, p. 3110, 2008.

[13] D. H. Simpson, C. T. Chin, and P. N. Burns, “Pulse inversion Doppler: a new method for detecting nonlinear echoes from microbubble contrast agents,” *IEEE Trans. Ultrason. Ferroelectr. Freq. Control*, vol. 46, no. 2, pp. 372–382, 1999.

[14] G. A. Brock-Fisher and D. M. Prater, “Acoustic border detection using power modulation,” *J. Acoust. Soc. Am.*, vol. 120, no. 2, p. 584, 2006.

[15] F. Forsberg, W. T. Shi, and B. B. Goldberg, “Subharmonic imaging of contrast agents,” *Ultrasonics*, vol. 38, no. 1–8, pp. 93–98, Mar. 2000.

[16] A. Bouakaz, S. Frigstad, F. J. Ten Cate, and N. de Jong, “Super harmonic imaging: a new imaging technique for improved contrast detection,” *Ultrasound Med. Biol.*, vol. 28, no. 1, pp. 59–68, Jan. 2002.

[17] R. Arshadi, A. C. H. Yu, and R. S. C. Cobbold, “Coded excitation methods for ultrasound harmonic imaging,” *Can. Acoust. - Acoust. Can.*, vol. 35, no. 2, pp. 35–46, 2007.

[18] J. M. G. Borsboom, C. T. Chin, A. Bouakaz, M. Versluis, and N. de Jong, “Harmonic chirp imaging method for ultrasound contrast agent,” *IEEE Trans. Ultrason. Ferroelectr. Freq. Control*, vol. 52, no. 2, pp. 241–249, Feb. 2005.

[19] J. Song, S. Kim, H. y. Sohn, T. k. Song, and Y. M. Yoo, “Coded excitation for ultrasound tissue harmonic imaging,” *Ultrasonics*, vol. 50, no. 6, pp. 613–619, 2010.

[20] B. A. J. Angelsen and R. Hansen, “7A-1 SURF Imaging - A New Method for Ultrasound Contrast Agent Imaging,” in *Ultrasonics Symposium, 2007. IEEE*, 2007, pp. 531–541.

[21] C. X. Deng, F. L. Lizzi, A. Kalisz, A. Rosado, R. H. Silverman, and D. J. Coleman, “Study of ultrasonic contrast agents using a dual-frequency band technique,” *Ultrasound Med. Biol.*, vol. 26, no. 5, pp. 819–831, Jun. 2000.

[22] C.-C. Shen, C.-H. Cheng, and C.-K. Yeh, “Phase-dependent dual-frequency contrast imaging at sub-harmonic frequency,” *IEEE Trans. Ultrason. Ferroelectr. Freq. Control*, vol. 58, no. 2, pp. 379–388, Feb. 2011.

[23] C. P. Keravnou and M. A. Averkiou, “Harmonic generation with a dual frequency pulse,” *J. Acoust. Soc. Am.*, vol. 135, no. 5, p. 2545, May 2014.

[24] H. Becher, K. Tiemann, T. Schlosser, C. Pohl, N. C. Nanda, M. A. Averkiou, J. Powers, and B. Luderitz, “Improvement in Endocardial Border Delineation Using Tissue Harmonic Imaging,” *Echocardiogr. Echocardiogr.*, vol. 15, no. 5, pp. 511–517, 1998.

[25] Tranquart F, Grenier N, Eder V, and Pourcelot L, “Clinical use of ultrasound tissue harmonic imaging.,” *Ultrasound Med. Biol.*, vol. 25, no. 6, pp. 889–94, 1999.

[26] M. R. Böhmer, A. L. Klibanov, K. Tiemann, C. S. Hall, H. Gruell, and O. C. Steinbach, “Ultrasound triggered image-guided drug delivery,” *Eur. J. Radiol.*, vol. 70, no. 2, pp. 242–253, May 2009.

[27] K. H. Martin and P. A. Dayton, “Current status and prospects for microbubbles in ultrasound theranostics,” *Wiley Interdiscip. Rev. Nanomed. Nanobiotechnol.*, vol. 5, no. 4, pp. 329–345, Aug. 2013.

[28] S. R. Wilson and P. N. Burns, “Microbubble-enhanced US in body imaging: what role?,” *Radiology*, vol. 257, no. 1, pp. 24–39, Oct. 2010.

[29] C. K. Holland and R. E. Apfel, “Thresholds for transient cavitation produced by pulsed ultrasound in a controlled nuclei environment,” *J. Acoust. Soc. Am.*, vol. 88, no. 5, pp. 2059–2069, Nov. 1990.

[30] D. Cosgrove and N. Lassau, “Imaging of perfusion using ultrasound,” *Eur. J. Nucl. Med. Mol. Imaging*, vol. 37 Suppl 1, pp. S65–85, Aug. 2010.

[31] V. Sboros and M.-X. Tang, "The assessment of microvascular flow and tissue perfusion using ultrasound imaging," *Proc. Inst. Mech. Eng. [H]*, vol. 224, no. 2, pp. 273–290, 2010.

[32] M. Averkiou, M. Lampaskis, K. Kyriakopoulou, D. Skarlos, G. Klouvas, C. Strouthos, and E. Leen, "Quantification of tumor microvascularity with respiratory gated contrast enhanced ultrasound for monitoring therapy," *Ultrasound Med. Biol.*, vol. 36, no. 1, pp. 68–77, Jan. 2010.

[33] E. Leen, M. Averkiou, M. Arditi, P. Burns, D. Bokor, T. Gauthier, Y. Kono, and O. Lucidarme, "Dynamic contrast enhanced ultrasound assessment of the vascular effects of novel therapeutics in early stage trials," *Eur. Radiol.*, vol. 22, no. 7, pp. 1442–1450, Jul. 2012.

[34] Y. Kubota, "Tumor angiogenesis and anti-angiogenic therapy," *Keio J. Med.*, vol. 61, no. 2, pp. 47–56, 2012.

[35] K. Zierler, "Indicator dilution methods for measuring blood flow, volume, and other properties of biological systems: a brief history and memoir," *Ann. Biomed. Eng.*, vol. 28, no. 8, pp. 836–848, Aug. 2000.

[36] C. F. Dietrich, M. A. Averkiou, J.-M. Correas, N. Lassau, E. Leen, and F. Piscaglia, "An EFSUMB introduction into Dynamic Contrast-Enhanced Ultrasound (DCE-US) for quantification of tumour perfusion," *Ultraschall Med. Stuttg. Ger. 1980*, vol. 33, no. 4, pp. 344–351, Aug. 2012.

[37] B. Kuersten, T. Nahar, and M. A. Vannan, "Methods of contrast administration for myocardial perfusion imaging: continuous infusion versus bolus injection," *Am. J. Cardiol.*, vol. 90, no. 10A, p. 35J–37J, Nov. 2002.

[38] C. Strouthos, M. Lampaskis, V. Sboros, A. McNeilly, and M. Averkiou, "Indicator dilution models for the quantification of microvascular blood flow with bolus administration of ultrasound contrast agents," *IEEE Trans. Ultrason. Ferroelectr. Freq. Control*, vol. 57, no. 6, pp. 1296–1310, Jun. 2010.

[39] W. F. Hamilton, J. W. Moore, J. M. Kinsman, and R. G. Spurling, "Simultaneous determination of the pulmonary and systemic circulation times in man and of a figure related to the cardiac output," *Am. J. Physiol. -- Leg. Content*, vol. 84, no. 2, pp. 338–344, Mar. 1928.

[40] G. N. Stewart, "Researches on the Circulation Time in Organs and on the Influences which affect it: Parts I.-III," *J. Physiol.*, vol. 15, no. 1–2, pp. 1–89, Jul. 1893.

[41] C. Keravnou, C. Mannaris, and M. Averkiou, "Accurate measurement of microbubble response to ultrasound with a diagnostic ultrasound scanner," *IEEE Trans. Ultrason. Ferroelectr. Freq. Control*, vol. 62, no. 1, pp. 176–184, Jan. 2015.

[42] M. Lampaskis and M. Averkiou, "Investigation of the relationship of nonlinear backscattered ultrasound intensity with microbubble concentration at low MI," *Ultrasound Med. Biol.*, vol. 36, no. 2, pp. 306–312, Feb. 2010.

[43] X. Chen, K. Q. Schwarz, D. Phillips, S. D. Steinmetz, and R. Schlief, "A mathematical model for the assessment of hemodynamic parameters using quantitative contrast echocardiography," *IEEE Trans. Biomed. Eng.*, vol. 45, no. 6, pp. 754–765, Jun. 1998.

[44] L. Claassen, G. Seidel, and C. Algermissen, “Quantification of flow rates using harmonic grey-scale imaging and an ultrasound contrast agent: an in vitro and in vivo study,” *Ultrasound Med. Biol.*, vol. 27, no. 1, pp. 83–88, Jan. 2001.

[45] P.-C. Li and M.-J. Yang, “Transfer function analysis of ultrasonic time-intensity measurements,” *Ultrasound Med. Biol.*, vol. 29, no. 10, pp. 1493–1500, Oct. 2003.

[46] P.-C. Li, C.-K. Yeh, and S.-W. Wang, “Time-intensity-based volumetric flow measurements: an in vitro study,” *Ultrasound Med. Biol.*, vol. 28, no. 3, pp. 349–358, Mar. 2002.

[47] T. Schlosser, C. Pohl, S. Kuntz-Hehner, H. Omran, H. Becher, and K. Tiemann, “Echoscintigraphy: a new imaging modality for the reduction of color blooming and acoustic shadowing in contrast sonography,” *Ultrasound Med. Biol.*, vol. 29, no. 7, pp. 985–991, Jul. 2003.

[48] S.-H. Hung, C.-K. Yeh, T.-H. Tsai, T. Chen, and R.-C. Chen, “A simple method for quantifying ultrasound-triggered microbubble destruction,” *Ultrasound Med. Biol.*, vol. 37, no. 6, pp. 949–957, Jun. 2011.

[49] T. P. Gauthier, M. A. Averkiou, and E. L. S. Leen, “Perfusion quantification using dynamic contrast-enhanced ultrasound: the impact of dynamic range and gain on time-intensity curves,” *Ultrasonics*, vol. 51, no. 1, pp. 102–106, Jan. 2011.

[50] M. Lampaskis and M. Averkiou, “In-vitro measurement of flow rate with bolus injection of contrast agent and DCE-US based on indicator dilution method,” presented at the The 16th European Symposium on Ultrasound contrast Imaging, Rotterdam, The Netherlands, 2011, pp. 103–106.

[51] T. P. Gauthier, M. Chebil, P. Peronneau, and N. Lassau, “In vitro evaluation of the impact of ultrasound scanner settings and contrast bolus volume on time-intensity curves,” *Ultrasonics*, vol. 52, no. 1, pp. 12–19, Jan. 2012.

[52] H. F. Woods and H. A. Krebs, “Lactate production in the perfused rat liver,” *Biochem. J.*, vol. 125, no. 1, pp. 129–139, Nov. 1971.

[53] C. Fondevila, A. J. Hessheimer, M.-H. J. Maathuis, J. Muñoz, P. Taurá, D. Calatayud, H. Leuvenink, A. Rimola, R. J. Ploeg, and J. C. García-Valdecasas, “Superior preservation of DCD livers with continuous normothermic perfusion,” *Ann. Surg.*, vol. 254, no. 6, pp. 1000–1007, Dec. 2011.

[54] H. Groen, C. Moers, J. M. Smits, J. Treckmann, D. Monbaliu, A. Rahmel, A. Paul, J. Pirenne, R. J. Ploeg, and E. Buskens, “Cost-effectiveness of hypothermic machine preservation versus static cold storage in renal transplantation,” *Am. J. Transplant. Off. J. Am. Soc. Transplant. Am. Soc. Transpl. Surg.*, vol. 12, no. 7, pp. 1824–1830, Jul. 2012.

[55] J. V. Guarrera, S. D. Henry, B. Samstein, R. Odeh-Ramadan, M. Kinkhabwala, M. J. Goldstein, L. E. Ratner, J. F. Renz, H. T. Lee, R. S. Brown, and J. C. Emond, “Hypothermic machine preservation in human liver transplantation: the first clinical series,” *Am. J. Transplant. Off. J. Am. Soc. Transplant. Am. Soc. Transpl. Surg.*, vol. 10, no. 2, pp. 372–381, Feb. 2010.

[56] M.-L. Izamis, A. Efstathiades, C. Keravnou, E. L. Leen, and M. A. Averkiou, “Dynamic contrast-enhanced ultrasound of slaughterhouse porcine livers in machine perfusion,” *Ultrasound Med. Biol.*, vol. 40, no. 9, pp. 2217–2230, Sep. 2014.

[57] R. Czymek, M. Gebhard, A. Lubienski, U. Roblick, H.-P. Bruch, and P. Hildebrand, "A comparison of the use of electrochemical treatment and radio frequency ablation in porcine liver," *Zentralblatt Für Chir.*, vol. 136, no. 4, pp. 379–385, Aug. 2011.

[58] G. ter Haar, "Therapeutic applications of ultrasound," *Prog. Biophys. Mol. Biol.*, vol. 93, no. 1–3, pp. 111–129, Apr. 2007.

[59] C. S. Enwemeka, O. Rodriguez, and S. Mendosa, "The biomechanical effects of low-intensity ultrasound on healing tendons," *Ultrasound Med. Biol.*, vol. 16, no. 8, pp. 801–807, 1990.

[60] B. E. Polat, D. Hart, R. Langer, and D. Blankschtein, "Ultrasound-Mediated Transdermal Drug Delivery: Mechanisms, Scope, and Emerging Trends," *J. Control. Release Off. J. Control. Release Soc.*, vol. 152, no. 3, pp. 330–348, Jun. 2011.

[61] D. Park, H. Park, J. Seo, and S. Lee, "Sonophoresis in transdermal drug deliverys," *Ultrasonics*, vol. 54, no. 1, pp. 56–65, Jan. 2014.

[62] B. Petit, Y. Bohren, E. Gaud, P. Bussat, M. Arditi, F. Yan, F. Tranquart, and E. Allémann, "Sonothrombolysis: the contribution of stable and inertial cavitation to clot lysis," *Ultrasound Med. Biol.*, vol. 41, no. 5, pp. 1402–1410, May 2015.

[63] S. Meairs, "Sonothrombolysis," *Front. Neurol. Neurosci.*, vol. 36, pp. 83–93, 2015.

[64] I. Lentacker, I. De Cock, R. Deckers, S. C. De Smedt, and C. T. W. Moonen, "Understanding ultrasound induced sonoporation: definitions and underlying mechanisms," *Adv. Drug Deliv. Rev.*, Nov. 2013.

[65] H.-D. Liang, J. Tang, and M. Halliwell, "Sonoporation, drug delivery, and gene therapy," *Proc. Inst. Mech. Eng. [H]*, vol. 224, no. 2, pp. 343–361, 2010.

[66] F. Orsi, L. Monfardini, G. Bonomo, M. Krokidis, P. Della Vigna, and D. Disalvatore, "Ultrasound guided high intensity focused ultrasound (USgHIFU) ablation for uterine fibroids: Do we need the microbubbles?," *Int. J. Hyperth. Off. J. Eur. Soc. Hyperthermic Oncol. North Am. Hyperth. Group*, pp. 1–7, Mar. 2015.

[67] C. M. C. Tempany, E. A. Stewart, N. McDannold, B. J. Quade, F. A. Jolesz, and K. Hynynen, "MR Imaging–guided Focused Ultrasound Surgery of Uterine Leiomyomas: A Feasibility Study," *Radiology*, vol. 226, no. 3, pp. 897–905, Mar. 2003.

[68] J. Ninet, X. Roques, R. Seitelberger, C. Deville, J. L. Pomar, J. Robin, O. Jegaden, F. Wellens, E. Wolner, C. Vedrinne, R. Gottardi, J. Orrit, M.-A. Billes, D. A. Hoffmann, J. L. Cox, and G. L. Champsaur, "Surgical ablation of atrial fibrillation with off-pump, epicardial, high-intensity focused ultrasound: results of a multicenter trial," *J. Thorac. Cardiovasc. Surg.*, vol. 130, no. 3, pp. 803–809, Sep. 2005.

[69] J. E. Kennedy, "High-intensity focused ultrasound in the treatment of solid tumours," *Nat Rev Cancer*, vol. 5, no. 4, pp. 321–327, Apr. 2005.

[70] P. P. Dobrakowski, A. K. Machowska-Majchrzak, B. Labuz-Roszak, K. G. Majchrzak, E. Kluczewska, and K. B. Pierzchała, "MR-guided focused ultrasound: a new generation treatment of Parkinson's disease, essential tremor and neuropathic pain," *Interv. Neuroradiol. J. Peritherapeutic Neuroradiol. Surg. Proced. Relat. Neurosci.*, vol. 20, no. 3, pp. 275–282, Jun. 2014.

[71] C. G. Chaussy and G. J. Fuchs, “Current state and future developments of noninvasive treatment of human urinary stones with extracorporeal shock wave lithotripsy,” *J. Urol.*, vol. 141, no. 3 Pt 2, pp. 782–789, Mar. 1989.

[72] K. G. Baker, V. J. Robertson, and F. A. Duck, “A review of therapeutic ultrasound: biophysical effects,” *Phys. Ther.*, vol. 81, no. 7, pp. 1351–1358, Jul. 2001.

[73] C. Mannaris, E. Efthymiou, M.-E. Meyre, and M. A. Averkiou, “In vitro localized release of thermosensitive liposomes with ultrasound-induced hyperthermia,” *Ultrasound Med. Biol.*, vol. 39, no. 11, pp. 2011–2020, Nov. 2013.

[74] R. E. Apfel, “Acoustic cavitation inception,” *Ultrasonics*, vol. 22, no. 4, pp. 167–173, Jul. 1984.

[75] M. R. Bailey, V. A. Khokhlova, O. A. Sapozhnikov, S. G. Kargl, and L. A. Crum, “Physical mechanisms of the therapeutic effect of ultrasound (a review),” *Acoust. Phys.*, vol. 49, no. 4, pp. 369–388, Jul. 2003.

[76] D. Miller, N. Smith, M. Bailey, G. Czarnota, K. Hynynen, I. Makin, and American Institute of Ultrasound in Medicine Bioeffects Committee, “Overview of Therapeutic Ultrasound Applications and Safety Considerations,” *J. Ultrasound Med. Off. J. Am. Inst. Ultrasound Med.*, vol. 31, no. 4, pp. 623–634, Apr. 2012.

[77] M. J. Shortencarier, P. A. Dayton, S. H. Bloch, P. A. Schumann, T. O. Matsunaga, and K. W. Ferrara, “A method for radiation-force localized drug delivery using gas-filled lipospheres,” *IEEE Trans. Ultrason. Ferroelectr. Freq. Control*, vol. 51, no. 7, pp. 822–831, Jul. 2004.

[78] W. W. Roberts, “Development and translation of histotripsy: current status and future directions,” *Curr. Opin. Urol.*, vol. 24, no. 1, pp. 104–110, Jan. 2014.

[79] E. Vlaisavljevich, A. Maxwell, M. Warnez, E. Johnsen, C. A. Cain, and Z. Xu, “Histotripsy-induced cavitation cloud initiation thresholds in tissues of different mechanical properties,” *IEEE Trans. Ultrason. Ferroelectr. Freq. Control*, vol. 61, no. 2, pp. 341–352, Feb. 2014.

[80] A. D. Maxwell, T.-Y. Wang, C. A. Cain, J. B. Fowlkes, O. A. Sapozhnikov, M. R. Bailey, and Z. Xu, “Cavitation clouds created by shock scattering from bubbles during histotripsy,” *J. Acoust. Soc. Am.*, vol. 130, no. 4, pp. 1888–1898, Oct. 2011.

[81] T. D. Khokhlova, M. S. Canney, V. A. Khokhlova, O. A. Sapozhnikov, L. A. Crum, and M. R. Bailey, “Controlled tissue emulsification produced by high intensity focused ultrasound shock waves and millisecond boiling,” *J. Acoust. Soc. Am.*, vol. 130, no. 5, pp. 3498–3510, Nov. 2011.

[82] T. D. Khokhlova, Y.-N. Wang, J. C. Simon, B. W. Cunitz, F. Starr, M. Paun, L. A. Crum, M. R. Bailey, and V. A. Khokhlova, “Ultrasound-guided tissue fractionation by high intensity focused ultrasound in an in vivo porcine liver model,” *Proc. Natl. Acad. Sci. U. S. A.*, vol. 111, no. 22, pp. 8161–8166, Jun. 2014.

[83] H. Chen and E. E. Konofagou, “The size of blood-brain barrier opening induced by focused ultrasound is dictated by the acoustic pressure,” *J. Cereb. Blood Flow Metab. Off. J. Int. Soc. Cereb. Blood Flow Metab.*, vol. 34, no. 7, pp. 1197–1204, Jul. 2014.

[84] H. Grüll and S. Langereis, “Hyperthermia-triggered drug delivery from temperature-sensitive liposomes using MRI-guided high intensity focused ultrasound,” *J. Control. Release Off. J. Control. Release Soc.*, vol. 161, no. 2, pp. 317–327, Jul. 2012.

[85] D. J. May, J. S. Allen, and K. W. Ferrara, "Dynamics and fragmentation of thick-shelled microbubbles," *IEEE Trans. Ultrason. Ferroelectr. Freq. Control*, vol. 49, no. 10, pp. 1400–1410, Oct. 2002.

[86] B. D. M. Meijering, L. J. M. Juffermans, A. van Wamel, R. H. Henning, I. S. Zuhorn, M. Emmer, A. M. G. Versteilen, W. J. Paulus, W. H. van Gilst, K. Kooiman, N. de Jong, R. J. P. Musters, L. E. Deelman, and O. Kamp, "Ultrasound and microbubble-targeted delivery of macromolecules is regulated by induction of endocytosis and pore formation," *Circ. Res.*, vol. 104, no. 5, pp. 679–687, Mar. 2009.

[87] M. M. Forbes, R. L. Steinberg, and W. D. O'Brien, "Examination of inertial cavitation of Optison in producing sonoporation of chinese hamster ovary cells," *Ultrasound Med. Biol.*, vol. 34, no. 12, pp. 2009–2018, Dec. 2008.

[88] B. Lammertink, R. Deckers, G. Storm, C. Moonen, and C. Bos, "Duration of ultrasound-mediated enhanced plasma membrane permeability," *Int. J. Pharm.*, vol. 482, no. 1–2, pp. 92–98, Mar. 2015.

[89] A. van Wamel, K. Kooiman, M. Harteveld, M. Emmer, F. J. ten Cate, M. Versluis, and N. de Jong, "Vibrating microbubbles poking individual cells: drug transfer into cells via sonoporation," *J. Control. Release Off. J. Control. Release Soc.*, vol. 112, no. 2, pp. 149–155, May 2006.

[90] S. Kotopoulis, A. Delalande, M. Popa, V. Mamaeva, G. Dimcevski, O. H. Gilja, M. Postema, B. T. Gjertsen, and E. McCormack, "Sonoporation-enhanced chemotherapy significantly reduces primary tumour burden in an orthotopic pancreatic cancer xenograft," *Mol. Imaging Biol. MIB Off. Publ. Acad. Mol. Imaging*, vol. 16, no. 1, pp. 53–62, Feb. 2014.

[91] O. Couture, A. Urban, A. Bretagne, L. Martinez, M. Tanter, and P. Tabeling, "In vivo targeted delivery of large payloads with an ultrasound clinical scanner," *Med. Phys.*, vol. 39, no. 8, pp. 5229–5237, Aug. 2012.

[92] K. Keyhani, H. R. Guzmán, A. Parsons, T. N. Lewis, and M. R. Prausnitz, "Intracellular drug delivery using low-frequency ultrasound: quantification of molecular uptake and cell viability," *Pharm. Res.*, vol. 18, no. 11, pp. 1514–1520, Nov. 2001.

[93] H. R. Guzmán, D. X. Nguyen, A. J. McNamara, and M. R. Prausnitz, "Equilibrium loading of cells with macromolecules by ultrasound: effects of molecular size and acoustic energy," *J. Pharm. Sci.*, vol. 91, no. 7, pp. 1693–1701, Jul. 2002.

[94] S. Song, Z. Shen, L. Chen, A. A. Brayman, and C. H. Miao, "Explorations of high-intensity therapeutic ultrasound and microbubble-mediated gene delivery in mouse liver," *Gene Ther.*, vol. 18, no. 10, pp. 1006–1014, Oct. 2011.

[95] Z. P. Shen, A. A. Brayman, L. Chen, and C. H. Miao, "Ultrasound with microbubbles enhances gene expression of plasmid DNA in the liver via intraportal delivery," *Gene Ther.*, vol. 15, no. 16, pp. 1147–1155, Aug. 2008.

[96] S. Kotopoulis, G. Dimcevski, O. Helge Gilja, D. Hoem, and M. Postema, "Treatment of human pancreatic cancer using combined ultrasound, microbubbles, and gemcitabine: A clinical case study," *Med. Phys.*, vol. 40, no. 7, p. -, 2013.

[97] Y. Zhou, K. Yang, J. Cui, J. Y. Ye, and C. X. Deng, "Controlled permeation of cell membrane by single bubble acoustic cavitation," *J. Control. Release Off. J. Control. Release Soc.*, vol. 157, no. 1, pp. 103–111, Jan. 2012.

[98] A. Yudina, M. de Smet, M. Lepetit-Coiffé, S. Langereis, L. Van Ruijssevelt, P. Smirnov, V. Bouchaud, P. Voisin, H. Grüll, and C. T. W. Moonen, "Ultrasound-mediated intracellular drug delivery using microbubbles and temperature-sensitive liposomes," *J. Control. Release Off. J. Control. Release Soc.*, vol. 155, no. 3, pp. 442–448, Nov. 2011.

[99] P. G. Sanches, R. Rossin, M. Böhmer, K. Tiemann, and H. Grüll, "Real-time imaging and kinetics measurements of focused ultrasound-induced extravasation in skeletal muscle using SPECT/CT," *J. Control. Release Off. J. Control. Release Soc.*, vol. 168, no. 3, pp. 262–270, Jun. 2013.

[100] S. Paliwal and S. Mitragotri, "Therapeutic opportunities in biological responses of ultrasound," *Ultrasonics*, vol. 48, no. 4, pp. 271–278, Aug. 2008.

[101] L. D. Johns, "Nonthermal Effects of Therapeutic Ultrasound: The Frequency Resonance Hypothesis," *J. Athl. Train.*, vol. 37, no. 3, pp. 293–299, 2002.

[102] H. Boxenbaum, "Interspecies variation in liver weight, hepatic blood flow, and antipyrine intrinsic clearance: extrapolation of data to benzodiazepines and phenytoin," *J. Pharmacokinet. Biopharm.*, vol. 8, no. 2, pp. 165–176, Apr. 1980.

2 Dynamic Contrast Enhanced Ultrasound of Slaughterhouse Porcine Livers in Machine Perfusion

The aim of this study was to enable investigations into novel imaging and surgical techniques by developing a readily-accessible, versatile liver machine perfusion system. Slaughterhouse pig livers were utilized and dynamic contrast enhanced ultrasound (DCEUS) was introduced to optimize the procurement process and provide real-time perfusion monitoring. The system comprised a single pump, oxygenator, and bubble trap, and 2 flow meters for pressure-controlled perfusion of the vessels using an off-the-shelf perfusate at room temperature. Successful livers demonstrated homogeneous perfusion in both the portal vein and hepatic artery with DCEUS, which correlated with stable oxygen uptake, bile production and hepatic resistances, and normal histology at the end of 3 hours of perfusion. DCEUS identified perfusion abnormalities invisible to the naked eye, thereby providing context to the otherwise systemic biochemical/hemodynamic measurements and focal biopsy findings. The model developed here is a simple, cost-effective approach for stable *ex-vivo* whole-organ machine perfusion.

Key words: imaging, hepatic, abattoir

Published as: M.L. Izamis, A. Efstathiades, C. Keravnou , E.L Leen and M.A. Averkiou, "Dynamic Contrast-Enhanced Ultrasound of Slaughterhouse Porcine Livers in Machine Perfusion," *Ultrasound in Med. & Biol.*, vol. 40, no. 9, pp. 2217–2230, September 2014.

2.1 Introduction

Machine perfusion (MP) functions as an artificial body with a wholly- or partially-artificial blood supply to sustain an isolated organ *ex-vivo*. Originally an experimental technique to study organ metabolism [1], [2], MP has gained a foothold in the clinic where it is currently being investigated as a donor organ preservation modality that is superior to the gold standard of static cold storage [3]–[6]. MP also has the potential to operate as a highly versatile test platform in the medical technology and pharmaceutical industries since it enables direct access to the organ for targeted diagnostic, imaging, and therapeutic investigations [7], [8]. Access to MP has generally been limited to laboratories with veterinary personnel, operating rooms, and housing facilities capable of procuring and handling large animals as a source of human-sized organs [9]–[12].

The use of slaughterhouse animals as an alternative source of organs would minimize the regulatory requirements, operational costs and ethical burden associated with live animal surgery, but very limited data are available regarding such models. In particular, the viability of the organ is frequently questioned given the obligatory warm ischemia the organs experience before being isolated from the animals. In 1993, Peter Neuhaus' group compared the isolation of hepatocytes from abattoir porcine livers with livers perfused *in-situ* [13]. Using cell isolation as a quantitative metric of a liver's viable cell content, livers from the abattoir produced cells with significantly higher rates of damage and lower yields. However, a follow-up paper in 1994 showed a marked improvement in cell yield when procured livers were exposed to 3 hours of normothermic (37°C) MP prior to cell isolation [14]. In 2001, the same group published a seminal paper which demonstrated that unless livers with 60 minutes of warm ischemic damage were treated with MP they could not be successfully transplanted (a laboratory animal model was used in this case) [15]. MP therefore has the capacity to perfuse slaughterhouse organs stably, serving as a platform for whole-organ experimentation.

To increase MP accessibility, we scaled up a recently developed sub-normothermic (20°C-30°C) rat liver MP system that was as effective at recovering ischemic damage as normothermic perfusion but simpler to operate [16]–[18]. A major limitation of this approach however, is an inability to visually inspect perfusion quality. Erythrocytes, natural but highly variable contrast agents, are unnecessary at subnormothermic conditions and are excluded from the perfusate, while the decrease in surface area to volume ratio in

comparing a 10g rat liver to a 1500g porcine liver implies less of the liver is exposed to the naked eye. To overcome this visual limitation, we introduced dynamic contrast enhanced ultrasound (DCEUS) to machine perfusion. DCEUS measurements proved to be indispensable in evaluating an organ's structural and functional integrity since they contextualized systemic perfusate and focal biopsy results. Simply by placing a transducer directly on the organ's capsule, structural variations could be identified and monitored while the extent of perfusion in each of the hepatic artery and portal vein was quantitatively visualized in real time. Here we describe in detail the methodologies of porcine liver procurement from the slaughterhouse, stable organ perfusion with asanguineous room temperature MP, and evaluation of perfusion quality with DCEUS.

2.2 Materials and methods

2.2.1 Choice of livers and abattoir

The studies were approved by the Cyprus National Bioethics Committee, the Cyprus National Veterinary Services, and the state abattoir of Kofinou, Larnaca.

Porcine livers were preferred over other species since they have greater similarities with human livers regarding physiology and anatomy (Table 2.1) [19].

	Human	**Pigs**	**Goat**	**Sheep**
Liver weight (g)	1500-1800	700-1500	600-700	400-700
Total flow rate (ml/min/g liver)	0.8	1-1.5	1-5	4-9
HA flow rate (% of total hepatic flow)	20-25	10-23	not found	1-21
Mean Arterial Pressure (mmHg)	100	60-90	95-100	97
Portal Pressure (mmHg)	5	9	not found	not found

Table 2.1: Comparison of livers from humans and commonly available farm species.

The method described here was developed with n=30 routinely-slaughtered 150-200 day-old castrated males of a variety of porcine strains. The procured livers weighed between 1200g and 1800g (adult human livers range between 1500g for females and 1800g for males) [20]. Porcine livers are reported to receive an average flow rate of 1-1.5 ml/min/g liver with approximately 10-23% of the blood flow being contributed by the hepatic artery (HA). Porcine liver mean arterial pressure is 122 cmH_2O (90mmHg) and portal pressure is less than 12 cmH_2O (9mmHg) [21], [22]. By comparison, human livers receive approximately 0.8 ml/min/g liver with 25% deriving from the HA [23]. Human liver mean arterial pressure is 136 cmH_2O (100mmHg), with an average portal pressure of 7 cmH_2O (5mmHg). Ruminants, such as goats and sheep, were not considered for this study since they have livers that are not comparable in size to human livers, with different anatomy and hemodynamics pertaining to the central, middle and left livers [24].

2.2.2 Procuring and flushing an intact liver

The process of liver procurement did not interfere significantly with the normal abattoir protocol. Briefly, animals were stunned electrically, exsanguinated, cleaned in a water bath, buffed and momentarily singed to remove bristles. The abdomen and thorax were exposed by a longitudinal dermal incision. To minimize the risk of damaging the liver during procurement, we requested that the trachea, lungs, heart, aorta, diaphragm, and esophagus in the thorax, along with the stomach, duodenum, pancreas, kidneys, and spleen in the abdomen be removed en bloc. The organs were placed into an awaiting container and the liver was inspected for disqualifying tears/cuts, particularly at the sites of the hepatic ligaments. Isolating the liver from the other organs was readily achieved with a few simple steps. The organs were first arranged ventral side down on a working surface and the lungs, heart, trachea and aorta removed to reveal the superior surface of the diaphragm. Beginning on the ventral edge, the diaphragm was reflected, away from the liver, by bisecting the coronary, left and right triangular ligaments, and the hepatic veins, thereby exposing the full length of the vena cava. The vena cava was clamped inferiorly and bisected distally exposing the posterior wall of the hilum containing the portal triad. The portal vein (PV) could be visually identified and the common hepatic artery (HA) found by palpation medial to the PV as a hard/rubbery cord. Both vessels were skeletonized with blunt dissection beginning as distal from the liver as possible, clamped to prevent air

emboli from entering the liver, and bisected. Dissection of the remainder of the hilum comprised identifying and bisecting the common bile duct (CBD), and removing the pancreas and lymph nodes from around the PV and HA, being careful to tie off major vessels and cauterize minor ones. The liver was then weighed and submerged in an iced slush solution of Lactated Ringer's solution (Multi-Pharm Co. Nicosia, Cyprus). Inverting the liver enabled removal of any air trapped in the hepatic veins. The cystic duct was ligated. The vessels were unclamped and fitted with plastic tubing connectors (OD ~1-1.5 cm for the PV and ~0.2-0.3 cm for the HA). Six to seven liters of ice-cold Lactated Ringer's flush solution spiked with 1000IU/L of heparin (LEO Pharmaceutical Products Ballerup, Denmark) were then delivered from suspended containers with 24G and 16G tubing (EW-96410-24 and SI-96410-16, Cole Parmer) that attached to the PV and HA connectors, respectively. Upon completion of flushing, the liver was disconnected from the tubing and the container sealed for transportation. Time between the start of exsanguination and the start of cold flush was $\leq$ 30 minutes. Time of static cold storage was $\leq$ 2 hours.

2.2.3 Machine perfusion design

The method used here had been optimized in a rat transplantation model to be both simple in design and effective in recovering ischemic damage [16], [17]. By operating at room temperature, stable perfusion can be maintained without using temperature regulators or oxygen carriers (usually erythrocytes, which are challenging to procure in a slaughterhouse model) (Fig. 2.1). To accommodate human-sized organs, the perfusate reservoir comprised a 7L rectangular clear plastic container measuring 23 cm W x 30 cm L x 10 cm H. The organ was suspended in the perfusate by a soft, permeable nylon membrane (B004QZ9XKI, Small Parts Inc. Logansport, IN, USA) attached to the periphery of the chamber. The perfusate was circulated (Masterflex L/S Digital Drive 600rpm, Cole Parmer) out of the organ chamber to an oxygenator (Affinity NT, Medtronic, Minneapolis, MN, USA) supplied with 95% O_2, 5% CO_2 (Tenaris, Bergamo, Italy) and then to a 500ml bubble trap (Radnoti, Monrovia, CA, USA) that also served to dampen the pulsatile flow. The perfusate exiting the bubble trap was split and passed through two flow meters (EW-32461-44 and EW-32460-40, Cole Parmer) that enabled pressure-regulated flow to each of the PV and HA respectively. The livers received average arterial flow rates

of 200-300ml/min resulting in pressures between 100-112 cmH_2O. Portal flow rates averaged 600-900ml/min resulting in pressures less than 10 cmH_2O, below the accurate detection limit of our manometer (Table 2.2). Effluent was then allowed to flow freely from the vena cava back into the reservoir, closing the circuit. By way of comparison with the rat model, the same perfusion duration of 3 hours was selected here.

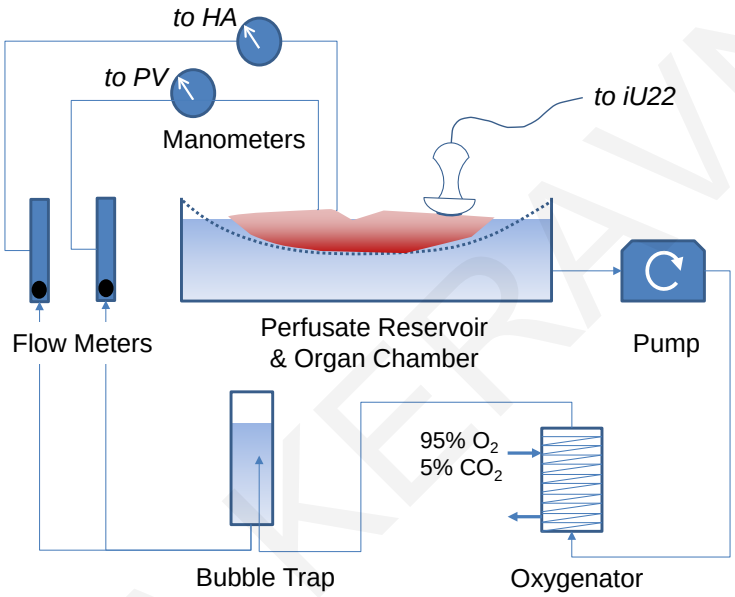

Figure 2.1: The perfusion system comprised a single closed circuit in which perfusate was pumped out of the organ chamber, through an oxygenator, and into a bubble trap prior to being split into two flow meters for each of the portal vein (PV) and hepatic artery (HA). Flow was pressure-regulated by manometers. Effluent from the organ collected in the organ chamber prior to being recirculated.

Time (hrs)	Pressure (cmH_2O)		Flow rate (ml/min/g liver)		Hepatic Resistance [cmH_2O/(ml/min/g liver)]	
	PV	HA	PV	HA	PV*	HA
0.5	<10	112±28	0.38±0.2	0.14±0.06	16±4.5	705±244
1.0	<10	111±20	0.49±0.21	0.15±0.05	14±5.3	682±273
1.5	<10	112±21	0.5±0.22	0.17±0.05	14±5.5	643±259
2.0	<10	106±23	0.49±0.22	0.17±0.05	14±6.3	599±222
2.5	<10	102±37	0.51±0.22	0.18±0.06	13±4.5	481±206
3.0	<10	112±43	0.51±0.21	0.19±0.06	13±5.2	518±273

Table 2.2: Hemodynamic measurements. *Portal resistance was calculated as an upper-bound estimate, using a portal pressure of 10 cmH_2O

2.2.4 Perfusate

Powdered Williams Medium E (10.8g/L W4125, Sigma-Aldrich Corp. St Louis, MO, USA) was reconstituted to produce 6L of perfusate. To the perfusate we added: 1000 IU/L heparin, 2 U/L insulin (Actrapid® Penfill® Novo Nordisk, Novo Alle, Denmark), and 0.4 mg/L dexamethasone (Dexamed, Medochemie Ltd, Limassol, Cyprus). We also added 2.2g/L of sodium bicarbonate (S5761, Sigma-Aldrich Corp. Medisell, Cyprus) or more as needed within the first hour to correct an initial acidosis and restore a pH of 7.3-7.4, which was subsequently measured half-hourly with a pH probe (Amarell Electronic, Kreuzwertheim, Germany) positioned in the perfusate.

2.2.5 Imaging

At the outset of perfusion, livers were evaluated for the presence of any anatomical abnormalities using B-mode imaging with an L12-5 linear array probe on a Philips iU22 ultrasound scanner (Philips Healthcare, Bothell, WA, USA). Two different DCEUS measurements were then made during the course of perfusion; a fixed probe (L9-3) evaluated perfusion through the macro- and microvasculature of a specific region of the liver, and a free probe (L12-5) provided a qualitative evaluation of the extent of perfusion (presence of contrast microbubbles) in the entire organ.

We note that despite using a closed system, recirculation of microbubbles was not an issue in our system. No secondary peaks were observed in the data and the inclusion of a transducer to destroy microbubbles prior to entering the pump had no effect on the outcomes. Upon exiting the liver, the microbubbles tended to float such that very few were taken up by the pump; of the few that were, the majority (>90%) were destroyed by the time they exited the oxygenator.

2.2.6 Monitoring perfusion through the macro- and micro-vasculature

The L9-3 probe operating at a transmit frequency of 3.1 MHz in the contrast specific mode and 6.3 MHz in the tissue mode was held in a fixed position on overlapping lobes 1 & 2 of the liver with a mechanical articulated arm (Fisso, Baitella AG, Zurich, Switzerland) (Fig.2.2). The imaging frame rate was 12 Hz. Contrast side-by-side mode was used to simultaneously display the contrast image formed with power modulation (on the

left of the screen) and the low MI tissue image (on the right). The compression (dynamic range) was set at the maximum that was available on the scanner (50 dB, which according to the manufacturer is an overestimated approximate value) to best accommodate a large range of signals and avoid saturation. The 2D gain was set at 77% such that there was no noise in the image but also not too far away from the noise floor. The MI used was 0.05 for the contrast side and 0.04 for the tissue side, with a focus at 3.5 cm. The MI was slightly lower than what is used for clinical scanning since there was no skin or other tissues between the liver and the probe. The persistence was turned off to avoid averaging of the image data between consecutive frames and to facilitate quantification. Every hour, a 0.2 ml bolus of SonoVue contrast agent (Bracco S.P.A., Milan, Italy) was injected through a rubber stop in the tubing immediately preceding each of the vessels starting with the portal vein (PV), and image loops of 40 s (480 frames) were acquired. We then administered a second bolus and captured a second loop for the HA.

2.2.7 Image quantification

To characterize the flow through the vasculature, time-intensity curves from the above loops were extracted using commercial quantification software QLAB (version 8.1; Philips Medical System, Bothell, WA, USA). This software allows for the manual selection of a region of interest (ROI), measurement of the selected ROI dimensions, and provision of linear (logarithmic compression removed) data for the time-intensity curves. ROIs were chosen around the PV, HA, parenchyma (effort was made to place the region in an area without large vessels), and hepatic veins (HV). The time-intensity curves of the ROIs were extracted from QLAB and imported into Excel.

2.2.8 Qualitative evaluation of the overall perfusion of the liver over time

After each loop was collected, another linear array probe L12-5 (at a transmit center frequency of 3.9 MHz in the contrast specific mode and 8.2 MHz in the tissue mode) was used to qualitatively evaluate the extent of perfusion of the liver by each vessel (PV and HA) since some contrast from each bolus was retained in the liver until it was destroyed. The 2D gain was set at 77%. The MI used was 0.05 for the contrast side and 0.04 for the tissue side, with a focus at 3.5 cm. The non-perfused areas and those with

patchy perfusion were indicated on a schematic of the liver and correlated with a photo of the gross appearance of the organ (Canon EOS 450D digital SLR). After collecting the images and video loops for qualitative evaluation, the MI was increased to 1 to eliminate any microbubbles left using a C5-1 curve-linear array probe which operates at lower frequencies and is thus more efficient for bubble destruction. The above procedure was repeated every hour over three hours of perfusion.

Figure 2.2: The iU22 ultrasound scanner (Philips Healthcare, Bothell, WA, USA) is positioned alongside the organ and 3 different probes are employed: (i) The L9-3 (shown here) acquires images from a fixed location over time, (ii) the L12-5 (not shown here) scans the entire organ to gauge percent perfusion over time, and (iii) the C5-1 (not shown here) is used to destroy bubbles between readings.

2.2.9 Oxygen Consumption

Oxygen uptake rate (*OUR*, ml O_2/min/100g liver) was measured as the difference between oxygen delivery (*ODR*) and exit (*OER*) rates, Eq. (2.1):

$$OUR = ODR - OER\,. \quad (2.1)$$

Dissolved oxygen in the perfusate was measured as the partial tension of oxygen (pO_2) in mmHg with an oxygen probe (Microelectrodes Inc. Bedford, NH, USA) calibrated to 21% (ambient air, 156mmHg) and 95% oxygen (oxygen tank, 722mmHg). The probe was placed in the bubble trap for influx oxygen values delivered to both the PV and HA, and in the IVC for efflux measurements. The oxygen solubility coefficient *k* (mlO_2/ 100ml blood/ mmHg) is unknown for Williams Medium E at room temperatures, therefore the product of dissolved oxygen and flow rates for measures of ODR and OER are expressed as a function of *k* [(Eqs. (2.2), (2.3)]

$$ODR = \left(k \times pO_{2\_bubble\_trap}\right) \times (\forall_{PV} + \forall_{HA}) \quad (2.2)$$

$$OER = \left(k \times pO_{2\_IVC}\right) \times (\forall_{PV} + \forall_{HA})\,. \quad (2.3)$$

2.2.10 Hepatic Resistance

Portal and arterial flow rates were recorded and resistance to flow in each vessel was estimated as the ratio of pressure to flow.

2.2.11 Bile Production

Since the cystic duct was ligated, the common bile duct was cannulated and used to collect bile in a separate container; hourly production was noted.

2.2.12 Histology

Histology was conducted on all livers using biopsies procured at the end of perfusion from the center of each lobe, stored in 10% formaldehyde, processed, and stained with hematoxylin and eosin. Images were captured using an Olympus BX51

microscope (Tokyo, Japan) and Olympus DP2-Twain compatible software (Adobe ImageReady ®, Version 8, San Jose, CA, USA).

2.3 Results

In all 30 livers examined with harmonic imaging, no anatomical abnormalities were detected. A total of 22 livers were used for model development. Cold ischemia of the liver was a necessary storage condition to transport and prepare the organ for MP. The most challenging hurdle to overcome therefore, was achieving a flush time within 30 minutes of the start of warm ischemia to minimize ischemic damage to the liver; a short warm ischemic time also improved organ flushing. Since receipt of the organ from the production line typically occurred within 20 minutes of exsanguination, some familiarity with the process was required to achieve the isolation, cannulation, and flushing the liver within the remaining 10 minutes. The second largest challenge was developing a protocol to minimize air embolisms. These occurred most frequently in the portal vasculature when the portal vein was bisected during procurement and could generally be avoided by if the entire duodenum was also procured. In our experience, the HA was never bisected, nevertheless the rigidity of the arterial walls meant the lumens were kept patent allowing blood to drain readily. Arterial embolisms were avoided by ensuring the aorta was included in the procurement since this afforded greater resistance to blood flow, and also by immediately clamping the vena cava to prevent blood drainage. Mastering these techniques ultimately produced organs that performed stably with homogeneous perfusion during MP; the results from n=8 such livers are presented here.

To ascertain that homogeneous perfusion had been achieved throughout the liver by MP, and was sustained for the duration of the experiments, the progress of a bolus of microbubbles through each of the PV and HA was recorded hourly. The bolus could be observed entering the primary branches of the PV and HA, then the secondary and tertiary branches, and finally the parenchymal space before emptying into the HVs, and being recirculated (Fig. 2.3). In the porcine liver, the HA has primary branches that form a ring around the circumference of the PV and until the microvasculature of the parenchymal space is reached, the distinct anatomical space occupied by the HA can be easily appreciated. Examined separately, the extent of hepatic perfusion by each vessel all the

way to the edges of the capsule of the liver could be observed, ensuring flow rates adequately perfused the entire liver, and that air embolisms and thrombi were absent.

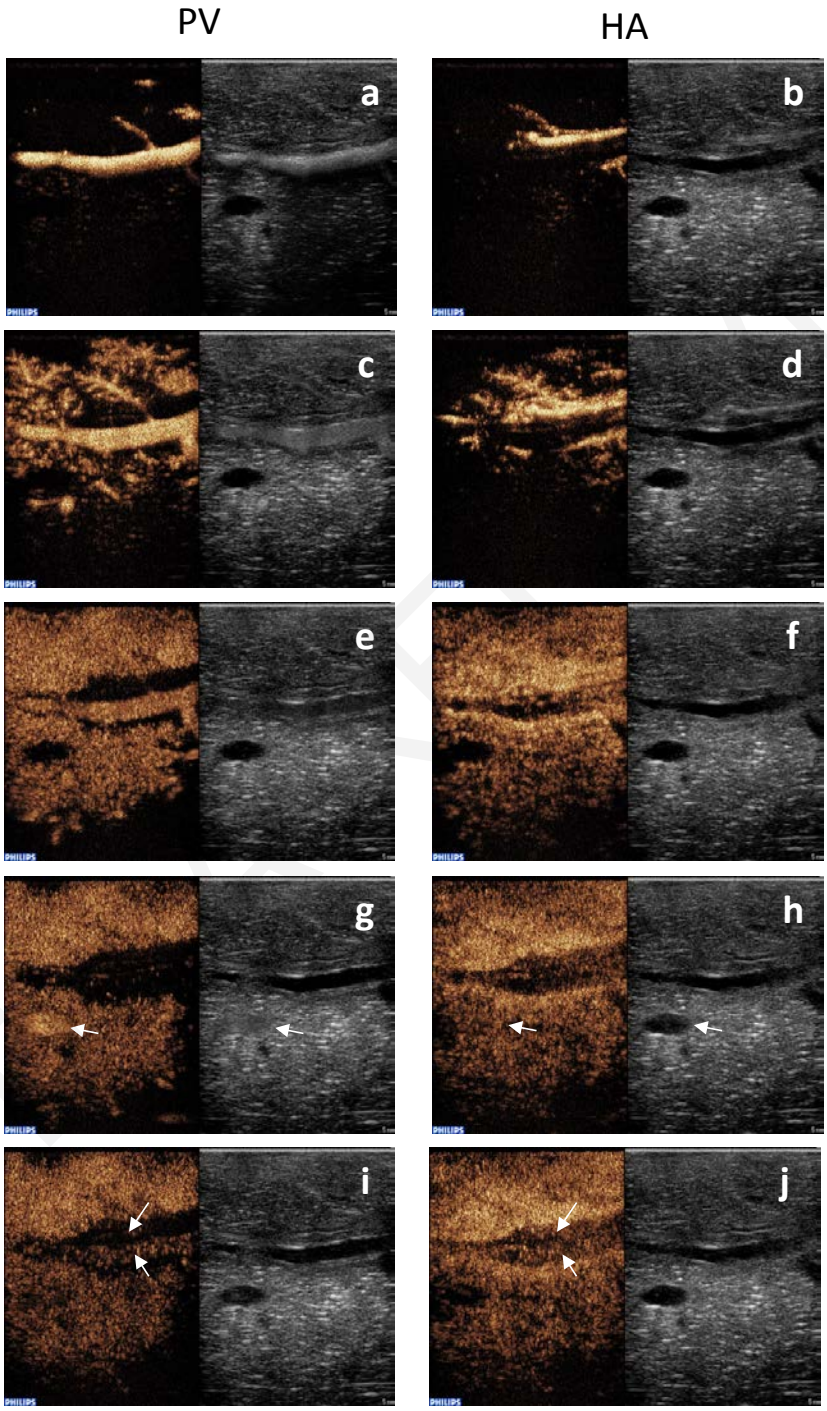

Figure 2.3: Perfusion in the vasculature of the liver can be ascertained down to the capillary scale with the introduction of contrast directly into the portal and arterial vessels. (a-b) The contrast fills the primary branches of the PV and HA. The artery surrounds the vein and the contrast enters the liver from image-right to left. (c-d) The contrast disseminates into the branches of the PV and HA prior to (e-f) entering the parenchyma. (g-h) The contrast collects into the hepatic veins (arrows) and (i-j) is recirculated into the PV and HA (arrows).

Regions of interest drawn around branches of the PV, HA, HVs and the parenchyma captured the change in contrast intensity over time as it entered and exited the region in a way that is characteristic of each of these different structures [Fig. 2.4(a, b)]. Since bolus injections of contrast were directly introduced into either the PV or HA, the microbubbles entered the vessels rapidly with an almost instantaneous rise time to peak intensity, demonstrating little dispersion of the bolus [Fig. 2.4(c, d)][25]. Later entry of the bolus into the parenchyma [Fig. 2.4(e, f)] produced lower intensity curves, as would be expected in capturing just a segment of the bolus distribution throughout the liver. Wash-out from the parenchyma tended to be very long, depicting retardation or even some sticking of microbubbles flowing through the microvasculature. The amount of "trapped," possibly larger, microbubbles in the microcirculation is probably very small; however, since the spatial resolution of the ultrasound scanner is on the order of millimeters, the "blocked" capillaries may appear larger in volume in the image than they actually are. Additionally, arterial peak intensities in the parenchyma were always lower than portal values, reflecting the smaller vascular volume occupied by the artery in any given region within the liver. The time intensity curves of the hepatic veins showed significant dispersion of the bolus as a result of the extensive variation in the sinusoidal distances between portal and arterial inflow and hepatic vein outflow [Fig. 2.4(g, h)]. Entry of the bolus into the hepatic vein also depicts the time taken to traverse the microcirculation. For stable livers, the time intensity curves generally did not differ significantly over time, and the trends between livers were similar. For simplicity, a single representative liver is therefore depicted in Figs. 2.4 and 2.5.

Frequently, flushing of the organ at the time of procurement was incapable of removing all blood clots, which could be discerned as dark spots through the liver's capsule and as areas of lower contrast intensity when scanning with the L12-5 (Fig. 2.5). Upon initiating machine perfusion, these clots were gradually washed out resulting in a homogeneous appearance of the liver. This was confirmed by DCEUS, which showed reduced contrast intensity in the presence of the thrombi that resolved over time. Perfusion in the portal and arterial vascular trees was otherwise observed to be generally homogeneous throughout the duration of perfusion.

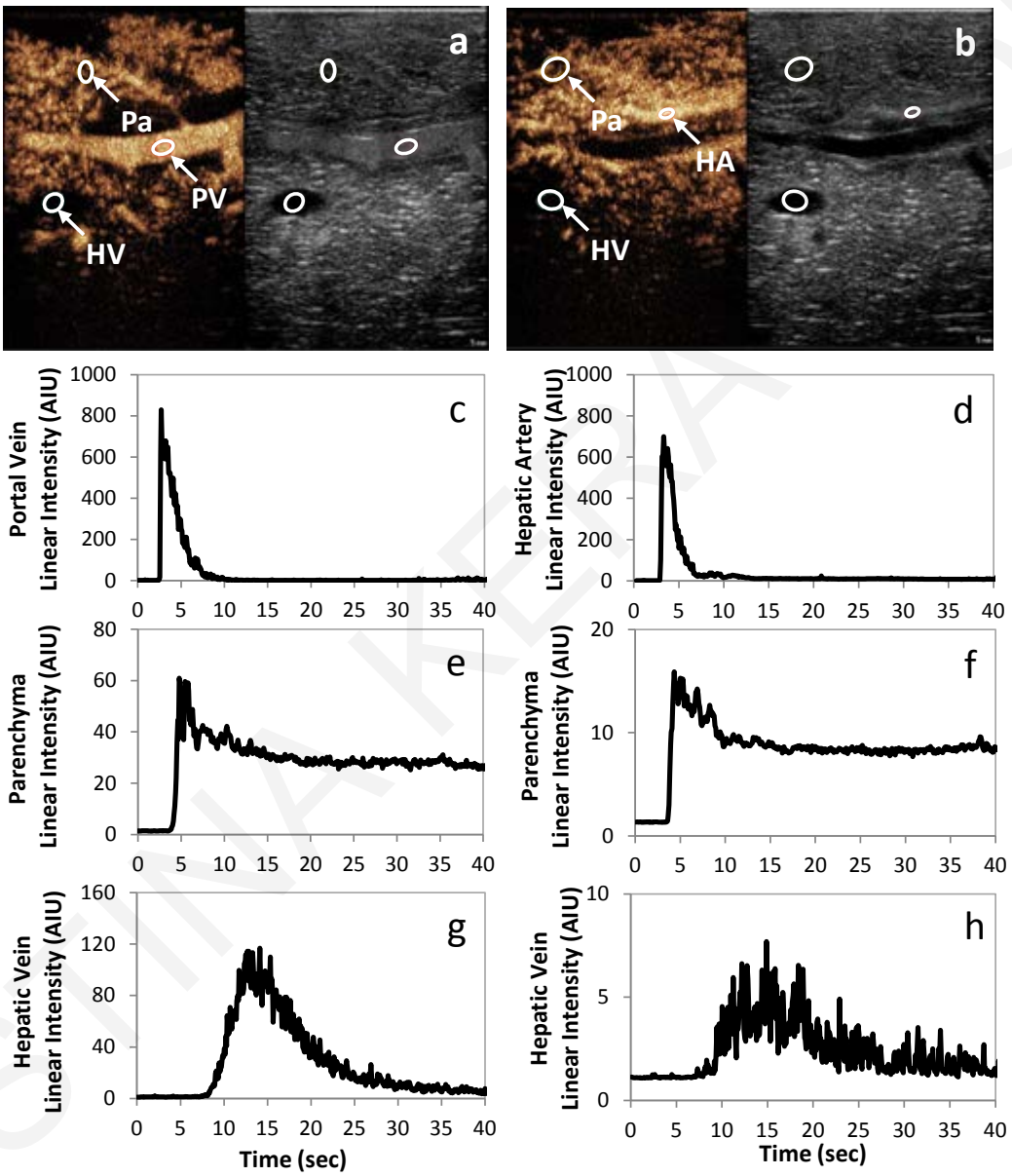

Figure 2.4: Time intensity curves quantitatively describe the progression of contrast through the liver. The curves depict characteristic differences, and changes over time, in flow between the various structures in the liver that cannot be appreciated with the naked eye. Contrast injected into the (a) portal and (b) arterial vasculature provides regions of interest around each of the (c) PV, (d) HA, (e-f) parenchyma, and (g-h) hepatic veins.

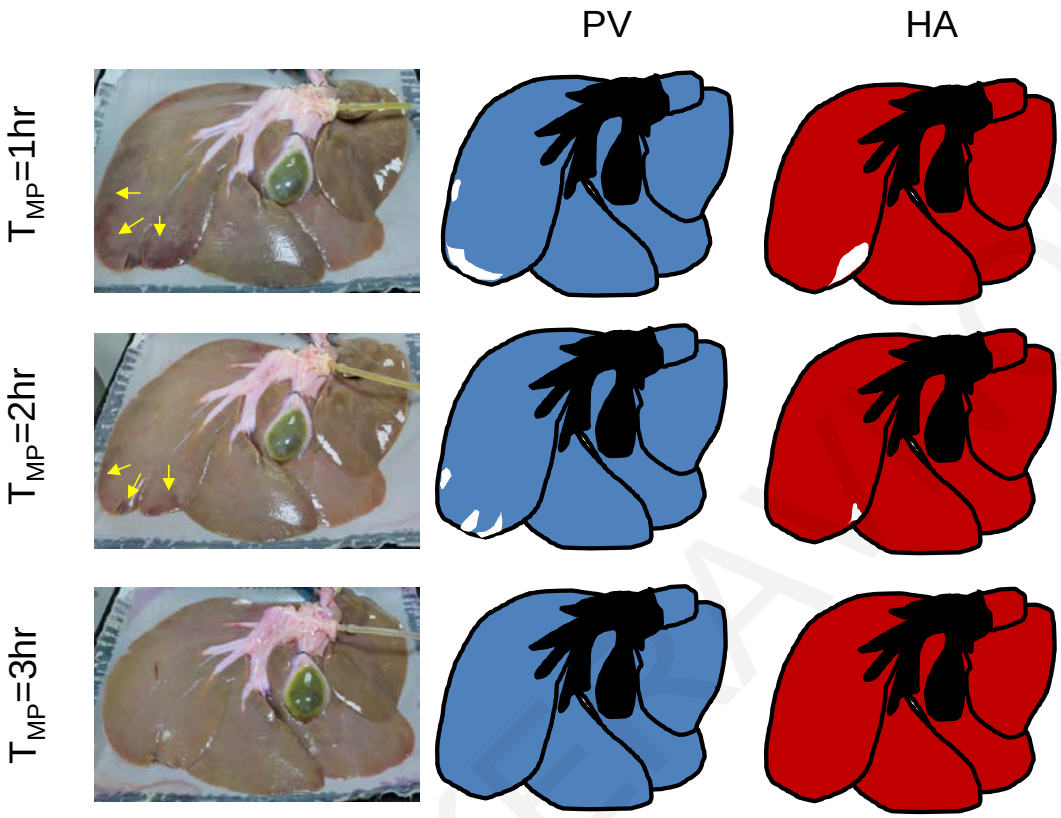

Figure 2.5: Gross morphology provides limited information regarding internal obstructions to flow; dark patches of blood suggest remnant thrombi that are gradually washed out by MP. DCEUS confirms a reduction in flow to the congested areas due to thrombi in both the PV and HA. The regions of lower contrast intensity compared to neighboring regions are restored as the thrombi are removed.

Flow rates tended to increase during perfusion in keeping portal and arterial pressures constant (Table 2.2); under these conditions, the HA contributed to 27% of the total hepatic inflow. This effectively described vasodilatation, expressed as a gradual decline in hepatic resistance to flow. As a consequence of the minor increases in flow rate to the liver over time, oxygen delivery to the liver also increased albeit a negligible amount (Table 2.3). Uptake however, stabilized within an hour of initiating perfusion at approximately 50% of the total oxygen delivered. Bile production also stabilized within the first hour, producing 4.2±3.4 ml/hr. The bile produced was thick and dark yellow initially and gradually became more fluid and lighter yellow as perfusion progressed. By the second hour, tints of pink were visible as a consequence of phenol red excretion.

Histology conducted on biopsies at the completion of liver procurement (after 30 minutes of warm ischemia) showed signs of congestion and swollen, irregular-appearing hepatocytes [Fig. 2.6(a, b)]. After 2 hours of static cold storage, the hepatocytes appeared to have regained their normal shape and size, but the sinusoids appeared edematous and

filled with neutrophils [Fig. 2.6(c, d)]. After 3 hours of perfusion, the tissue appeared significantly improved, with normal, intact architecture and clear sinusoids. Hepatocytes and endothelial cells had well-defined membranes, homogeneously eosinophilic cytoplasm, and normal-appearing nuclei with occasional evidence of meiotic cells [Fig. 2.6(e, f)]. These histological results were consistent across all livers (n=8). Minor edema was evident throughout most livers, which was consistent with an average 23%±16% weight gain post-static cold storage, and a final 25%±18% increase post-perfusion.

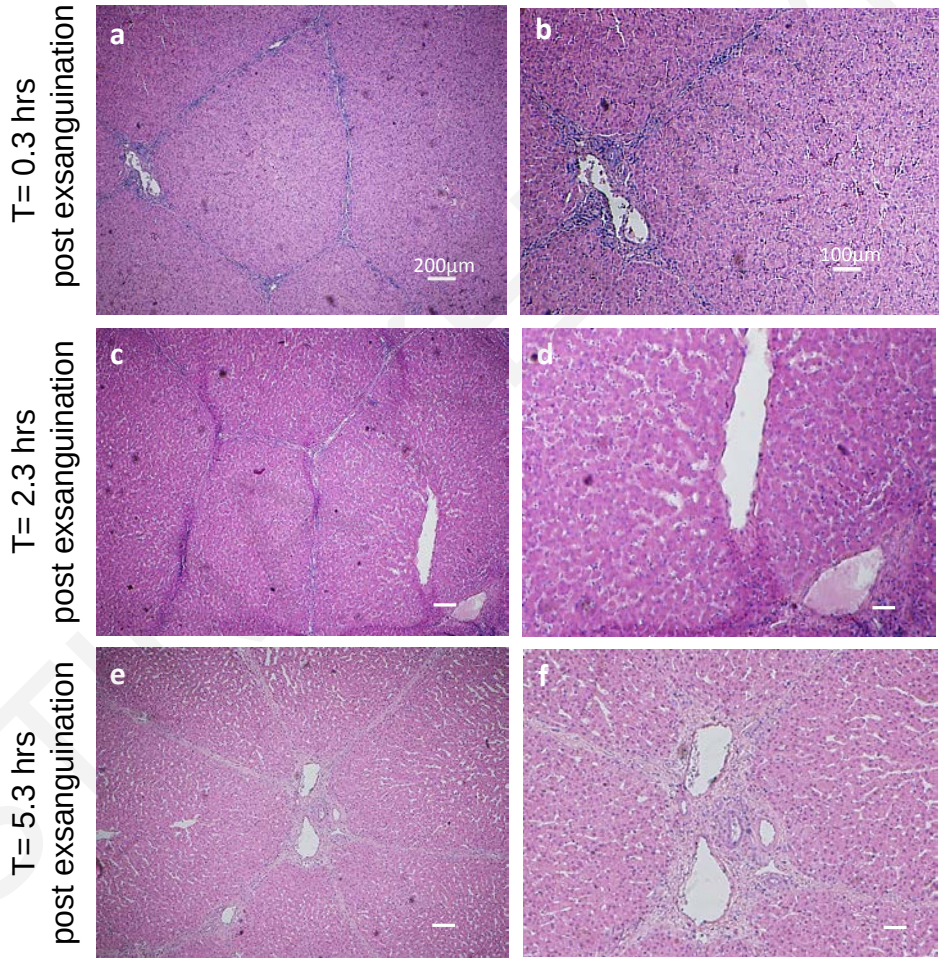

Figure 2.6: Histological evaluation of the lobes with H&E at the time of procurement (T=0.3 hours), after static cold storage (T=2.3 hours), and at the end of machine perfusion (T=5.3 hours) shows progressively improved architecture with minor, diffuse edema.

			x k (ml/min/100g liver)		
Time (hrs)	**HA influx**	**PV influx**	**Total influx**	**HV efflux**	**Uptake**
0.5	73±47	243±163	320±193	107±60	130±23
1.0	73±43	317±190	393±213	210±157	180±60
1.5	77±40	310±193	390±213	223±177	163±47
2.0	77±40	307±197	387±217	197±187	187±40
2.5	83±47	310±187	397±207	190±180	207±47
3.0	87±53	320±183	407±200	220±163	183±50

Table 2.3: Oxygen balance across the livers.

2.4 Discussion

Room temperature asanguineous perfusion of slaughterhouse porcine livers produces a stable functioning organ within the first hour of perfusion, and can be sustained for at least an additional 2 hours. The model developed here serves as a simple, cost-effective approach for *ex-vivo* whole-organ experimentation that is particularly well-suited for the optimization of surgical and imaging procedures.

2.4.1 Validity of the abattoir model

A concern in using slaughterhouse animals is the viability of the procured organs [13]. Histologically, we have seen that even by limiting warm ischemia to 30 minutes, the condition of the organ at the time of initiating cold flush appears questionable. However, within 2 hours of flushing the organ with cold storage solution, the organ appeared improved histologically, suggesting even longer transportation times may be feasible, especially with the use of superior storage solutions such as University of Wisconsin solution. Further, complete and homogeneous perfusion of the organ was achieved within an hour of initiating room temperature MP, as demonstrated by DCEUS and within 3 hours of perfusion, structural integrity appeared restored at the microscopic scale. These findings, though not able to verify organ viability, when combined with the functional parameters of sustained oxygen uptake and bile production, suggest a stable method with which to work that can likely be extended well beyond the 3 hours of perfusion

investigated here. While the simplicity of this approach will enable an increase in accessibility to *ex-vivo* whole organ experimentation, there are nevertheless, important limitations that must be considered when using abattoir livers. For instance, there is typically little control over the size, age, strain or nutritional status of the animals, and though the organs are qualified as "food grade," procurement is not conducted in a sterile fashion. Additionally, great care must be taken to avoid the introduction of air into the livers. This can be done by clamping the vessels and submerging the tissue as described since the exsanguination and organ removal process necessarily exposes the hepatic veins to air and can easily cause suction of air through the PV and HA, which significantly hinders perfusion in the organ (Fig. 2.7).

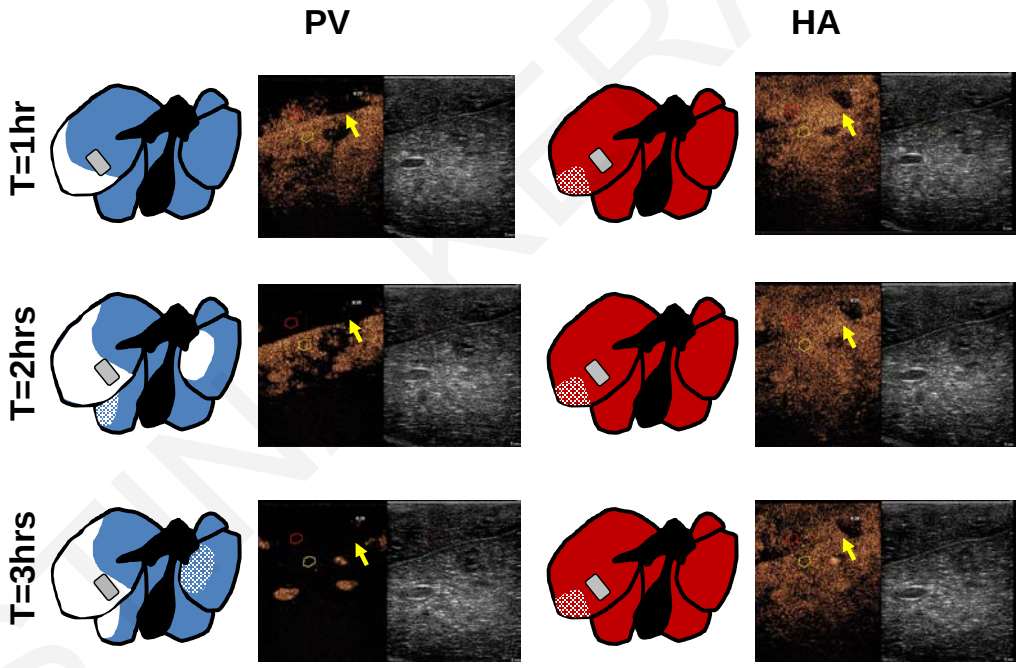

Figure 2.7: Perfusion quality declines over time in an organ with major air embolisms in Lobes 1 and 2 of the portal vein (separated at the arrow). By comparison, the hepatic artery, which has a minor infarct in Lobe 1, has otherwise stable perfusion as seen at the position of the probe (grey square) situated outside the infarct area.

2.4.2 Choice of machine perfusion design

Room temperature MP dispenses with the need for temperature regulation and oxygen carriers, resulting in a simple circuit that requires a single pump, two flow meters, an oxygenator, and a bubble trap for 6L of an off-the-shelf perfusate. In the rat model, we have shown that room temperature perfusion is capable of recovering livers with 60

minutes of warm ischemia to a transplantable state within 3 hours of perfusion [16], [17], [26]. Of the two other publications that describe room temperature machine perfusion in a pig model, only one of them investigates an ischemic model with different metrics of perfusion quality than what were used here [27], [28]. The vast majority of publications describe the use of sanguineous normothermic perfusion systems, which are more laborious to operate because of the addition of blood components to the perfusate [15], [18]. Using such a system, Grosse-Siestrup et. al. published a series of papers that demonstrated the feasibility of using abattoir-derived porcine livers for research, particularly to explore the impact of various drugs on the liver [8], [29], [30]. The group later compared the model's performance with organs procured intraoperatively from laboratory animals [31]. Livers from the abattoir were treated somewhat similarly to ours, with 15±0.6 minutes of warm ischemic time and 3 hours of static cold storage time, followed by 3.5 hours of machine perfusion. Livers procured intraoperatively experienced only 6.3±2.8 minutes of warm ischemia and 1 hour of static cold storage time, followed by 3 hours of perfusion that showed good accordance with results from other publications [32]–[35]. The abattoir livers did not function as well as the intraoperative livers. This was seen through significantly higher portal resistance, edema, and liver enzyme release. Abattoir livers also consumed oxygen at an average rate of 0.3 ml/min/100g or 16% of the consumption rate of intraoperative livers, and produced 3.1±1.1 ml/min/100g of bile, or 56% of intraoperative production rates. By way of comparison, when we assumed k=0.003 (the oxygen solubility coefficient of plasma at 37°C, an underestimate of the true value of k for Williams Medium E at room temperature) the system used here resulted in hepatic oxygen uptake rates twice that of the normothermic system. The values were 30% of intraoperative liver values, which is what is expected given the lower metabolic rates of room temperature-perfused livers [26], [36]. Bile production was 30% higher than the normothermic system and 80% of intraoperative liver values. Also, the majority of edema observed here occurred during static cold storage with perfusion contributing a negligible additional amount, while hepatic resistance gradually declined over time, enabling physiological flow rates and pressures. These findings, together with the simplicity of our system, suggest that our approach markedly improves upon existing abattoir models.

2.4.3 The role of DCEUS in machine perfusion

Dynamic contrast-enhanced ultrasound provides highly complementary qualitative and quantitative data regarding the liver's condition, conferring specificity to systemic hemodynamic and biochemical values, and context to invasive, and therefore sporadically-performed, focal biopsies. The ease with which DCEUS can be applied to MP - simply scanning the organ with a probe - while diagnosing the presence of anatomical abnormalities not visible grossly, and illustrating the quality of perfusion throughout the entire organ, make it an invaluable tool in whole organ machine perfusion.

Of significant clinical interest is the quantitative analysis of perfusion that is possible with DCEUS, which has the potential to define novel metrics of organ viability in machine perfusion. An injection of contrast produces a rapid rise in contrast intensity that becomes distorted with distance from the injection site, perfusate flow rate, and tortuosity of the vascular path as the contrast disperses [25]. Characterizing the distortion of contrast through organs is already the premise of advanced algorithms capable of highly sensitive, non-invasive, non-ionizing diagnoses of liver masses [37]. Combined with the ability to localize drug release through microbubble destruction [38], DCEUS represents a myriad of possibilities in extended isolated organ perfusion. A simple example targeted at ischemic donor livers such as those that derive from donors after cardiac death (DCD), may be the assessment of the extent of ischemia-reperfusion injury (IRI) where the "no-reflow" phenomenon negatively impacts perfusion quality and subsequently graft integrity [39]–[41]. Since the passage of a bolus of contrast agent through the liver delineates the patency of the hepatic vasculature, the nature of IRI, its prevalence throughout the organ, the points in the vascular tree at which it begins to impact perfusion quality, and the impact vasoactive drugs have on its outcome [42] may be uniquely described by DCEUS.

An important consideration in the accurate quantification of organ perfusion characteristics with DCEUS is the extent to which the contrast agent interacts with the liver, potentially biasing agent kinetics. When complete microbubble wash-out does not occur, as is seen here, time intensity curve parameters such as bolus rise time, peak intensity, and area under the curve in the microvasculature are overestimated. The persistence of the contrast agent in the microvasculature is likely a function of the choice of contrast agent. SonoVue, has a wide distribution of microbubble sizes [43], [44], the larger of which are typically filtered out by the lungs *in-vivo* prior to entering the liver;

complete wash-out of the agent from the hepatic microvasculature eventually occurs after 2 minutes [45]. The absence of a filtering mechanism in the present perfusion system implies that the liver itself is serving this function. We do not believe the microbubbles are fundamentally disrupting flow, firstly because the amount of microbubbles "stuck" in the microcirculation likely appears greater in the images than it actually is owing to the fact that the spatial resolution of ultrasound is on the order of 1 mm so single 10-20 μm diameter microbbubles would show as being much larger. Moreover, we would expect contrast intensity and vascular resistance to increase over time. In subsequent studies however, using BR38 (data not included here), which has the smaller median diameter [46], an appreciable decline in intensity occurs during wash-out, more closely resembling the *in-vivo* scenario. Subsequently, these findings support our use of the presence of microbubbles in the vasculature as a qualitative evaluation of perfusion in isolated organs during machine perfusion, while small microbubbles or the use of a filtering system are recommended for quantification studies.

DCEUS proved critical in confirming the robustness of the perfusion design, which had been previously established in a highly-controlled syngeneic laboratory animal model, and now also appears effective in wild type animals of different strains, gender, and ages. DCEUS enabled efficient scaling of the MP system from 10g rat livers to 1500g human-sized livers, particularly by identifying air and blood embolisms as the primary limiting parameters to successful perfusion. This knowledge facilitated the efficient procurement of slaughterhouse livers, reducing the time to cannulate and initiate cold flush to approximately 10 minutes, for an overall warm ischemic time no longer than 30 minutes. Clamping the PV and HA minimized further suction of air into the vessels while submerging the liver enabled removal of air in the HVs. Without DCEUS, livers with occlusions to flow could not be distinguished macroscopically from organs that were well-perfused. Since DCEUS can diagnose whether an occlusion is due to an air embolism or blood clot, in the circumstances of accidental introduction of air or stubborn clots, it can also direct appropriately targeted treatment strategies. Finally, DCEUS also enabled dynamic fine-tuning of perfusion conditions, such as minimizing flow rates without causing hypo-perfusion, which is associated with greater viable cell yields [17].

2.5 Conclusions

We have developed a simple, stable, highly versatile machine perfusion methodology for the *ex-vivo* evaluation of isolated human-sized livers. An efficient protocol enables rapid isolation of livers from slaughterhouse pigs, enabling a cost-effective approach to organ procurement. The methodology, validated with hemodynamic and biochemical parameters, histology, and, for the first time, dynamic contrast enhanced ultrasound, demonstrates organs are stable for at least 3 hours of experimentation. This model is especially useful in the study of diseases that characteristically impact perfusion quality and for interventions that depend on controllable and quantifiable perfusion, such as the study of vasoactive drugs, drug delivery, and tumor ablation.

Acknowledgements

This work was supported by the Didaktor/0311/78 Fellowship under the Framework Program for Research, Technological Development and Innovation 2009-2010; DESMI 2009-2010 is co-funded by the Republic of Cyprus and the European Regional Development Fund. We gratefully acknowledge Bracco for the SonoVue used in this study. We are also grateful to Dr. Soteria Georgiadou at the National Reference Laboratory for Animal Health in Nicosia, Cyprus for her assistance with the preparation and examination of the histology slides.

REFERENCES

[1] R. Hems, B. D. Ross, M. N. Berry, and H. A. Krebs, "Gluconeogenesis in the perfused rat liver," *Biochem. J.*, vol. 101, no. 2, pp. 284–292, Nov. 1966.

[2] H. F. Woods and H. A. Krebs, "Lactate production in the perfused rat liver," *Biochem. J.*, vol. 125, no. 1, pp. 129–139, Nov. 1971.

[3] C. Fondevila, A. J. Hessheimer, M.-H. J. Maathuis, J. Muñoz, P. Taurá, D. Calatayud, H. Leuvenink, A. Rimola, R. J. Ploeg, and J. C. García-Valdecasas, "Superior preservation of DCD livers with continuous normothermic perfusion," *Ann. Surg.*, vol. 254, no. 6, pp. 1000–1007, Dec. 2011.

[4] H. Groen, C. Moers, J. M. Smits, J. Treckmann, D. Monbaliu, A. Rahmel, A. Paul, J. Pirenne, R. J. Ploeg, and E. Buskens, "Cost-effectiveness of hypothermic machine preservation versus static cold storage in renal transplantation," *Am. J. Transplant. Off. J. Am. Soc. Transplant. Am. Soc. Transpl. Surg.*, vol. 12, no. 7, pp. 1824–1830, Jul. 2012.

[5] J. V. Guarrera, S. D. Henry, B. Samstein, R. Odeh-Ramadan, M. Kinkhabwala, M. J. Goldstein, L. E. Ratner, J. F. Renz, H. T. Lee, R. S. Brown, and J. C. Emond, "Hypothermic machine preservation in human liver transplantation: the first clinical series," *Am. J. Transplant. Off. J. Am. Soc. Transplant. Am. Soc. Transpl. Surg.*, vol. 10, no. 2, pp. 372–381, Feb. 2010.

[6] M. Krüger, N. Zinne, H. Höffler, R. Zhang, I. Kropivnitskaja, J. Schmitto, A. Ciubotaru, and A. Haverich, "Ex situ tracheobronchoplastic operations using the organ care system," *Chir. Z. Für Alle Geb. Oper. Medizen*, vol. 84, no. 3, pp. 208–213, Mar. 2013.

[7] R. Czymek, M. Gebhard, A. Lubienski, U. Roblick, H.-P. Bruch, and P. Hildebrand, "A comparison of the use of electrochemical treatment and radio frequency ablation in porcine liver," *Zentralblatt Für Chir.*, vol. 136, no. 4, pp. 379–385, Aug. 2011.

[8] C. Grosse-Siestrup, V. Unger, J. Pfeffer, Q. T. Dinh, S. Nagel, J. Springer, C. Witt, A. Wussow, and D. A. Groneberg, "Hepatotoxic effects of polidocanol in a model of autologously perfused porcine livers," *Arch. Toxicol.*, vol. 78, no. 12, pp. 697–705, Dec. 2004.

[9] C. J. Imber, S. D. St Peter, I. L. de Cenarruzabeitia, H. Lemonde, M. Rees, A. Butler, P. T. Clayton, and P. J. Friend, "Optimisation of bile production during normothermic preservation of porcine livers," *Am. J. Transplant. Off. J. Am. Soc. Transplant. Am. Soc. Transpl. Surg.*, vol. 2, no. 7, pp. 593–599, Aug. 2002.

[10] A. Schlegel, O. de Rougemont, R. Graf, P.-A. Clavien, and P. Dutkowski, "Protective mechanisms of end-ischemic cold machine perfusion in DCD liver grafts," *J. Hepatol.*, vol. 58, no. 2, pp. 278–286, Feb. 2013.

[11] A. Van der Plaats, M. H. J. Maathuis, N. A. 'T Hart, A. A. Bellekom, H. S. Hofker, E. B. van der Houwen, G. J. Verkerke, H. G. D. Leuvenink, P. Verdonck, R. J. Ploeg, and G. Rakhorst, "The Groningen hypothermic liver perfusion pump: functional evaluation of a new machine perfusion system," *Ann. Biomed. Eng.*, vol. 34, no. 12, pp. 1924–1934, Dec. 2006.

[12] H. Xu, T. Berendsen, K. Kim, A. Soto-Gutiérrez, F. Bertheium, M. L. Yarmush, and M. Hertl, "Excorporeal normothermic machine perfusion resuscitates pig DCD livers with extended warm ischemia," *J. Surg. Res.*, vol. 173, no. 2, pp. e83–88, Apr. 2012.

[13] J. Gerlach, K. Klöppel, M. R. Schön, J. Brombacher, J. M. Courtney, J. Unger, and P. Neuhaus, "Comparison of pig hepatocyte isolation using intraoperative perfusion without warm ischemia and isolation of cells from abattoir organs after warm ischemia," *Artif. Organs*, vol. 17, no. 11, pp. 950–953, Nov. 1993.

[14] M. R. Schön, G. Puhl, J. Gerlach, J. Frank, and P. Neuhaus, "Hepatocyte isolation from pig livers after warm ischaemic injury," *Transpl. Int. Off. J. Eur. Soc. Organ Transplant.*, vol. 7 Suppl 1, pp. S159–162, 1994.

[15] M. R. Schön, O. Kollmar, S. Wolf, H. Schrem, M. Matthes, N. Akkoc, N. C. Schnoy, and P. Neuhaus, "Liver transplantation after organ preservation with normothermic extracorporeal perfusion," *Ann. Surg.*, vol. 233, no. 1, pp. 114–123, Jan. 2001.

[16] T. A. Berendsen, B. G. Bruinsma, J. Lee, V. D'Andrea, Q. Liu, M.-L. Izamis, K. Uygun, and M. L. Yarmush, "A simplified subnormothermic machine perfusion system restores ischemically damaged liver grafts in a rat model of orthotopic liver transplantation," *Transplant. Res.*, vol. 1, no. 1, p. 6, 2012.

[17] M.-L. Izamis, C. Calhoun, B. E. Uygun, M. A. Guzzardi, G. Price, M. Luitje, N. Saeidi, M. L. Yarmush, and K. Uygun, "Simple machine perfusion significantly enhances hepatocyte yields of ischemic and fresh rat livers," *Cell Med.*, vol. 4, no. 3, pp. 109–123, 2013.

[18] H. Tolboom, R. Pouw, K. Uygun, Y. Tanimura, M.-L. Izamis, F. Berthiaume, and M. L. Yarmush, "A model for normothermic preservation of the rat liver," *Tissue Eng.*, vol. 13, no. 8, pp. 2143–2151, Aug. 2007.

[19] H. Boxenbaum, "Interspecies variation in liver weight, hepatic blood flow, and antipyrine intrinsic clearance: extrapolation of data to benzodiazepines and phenytoin," *J. Pharmacokinet. Biopharm.*, vol. 8, no. 2, pp. 165–176, Apr. 1980.

[20] P. S. Price, R. B. Conolly, C. F. Chaisson, E. A. Gross, J. S. Young, E. T. Mathis, and D. R. Tedder, "Modeling interindividual variation in physiological factors used in PBPK models of humans," *Crit. Rev. Toxicol.*, vol. 33, no. 5, pp. 469–503, 2003.

[21] S. M. Jakob, H. Bracht, F. Porta, B. M. Balsiger, L. Brander, R. Knuesel, H.-Q. Feng, A. Kolarova, Y. Ma, and J. Takala, "Effects of cardiac preload reduction and dobutamine on hepatosplanchnic blood flow regulation in porcine endotoxemia," *Am. J. Physiol. Gastrointest. Liver Physiol.*, vol. 303, no. 2, pp. G247–255, Jul. 2012.

[22] S. Yagi, T. Iida, T. Hori, K. Taniguchi, M. Nagahama, S. Isaji, and S. Uemoto, "Effect of portal haemodynamics on liver graft and intestinal mucosa after small-for-size liver transplantation in swine," *Eur. Surg. Res. Eur. Chir. Forsch. Rech. Chir. Eur.*, vol. 48, no. 3, pp. 163–170, 2012.

[23] R. N. Upton, "Organ weights and blood flows of sheep and pig for physiological pharmacokinetic modelling," *J. Pharmacol. Toxicol. Methods*, vol. 58, no. 3, pp. 198–205, Dec. 2008.

[24] C. P. Brizard, N. Goussef, J. C. Chachques, and A. F. Carpentier, "Model of complete separation of the hepatic veins from the systemic venous system," *Ann. Thorac. Surg.*, vol. 70, no. 6, pp. 2096–2101, Dec. 2000.

[25] M. Mischi, M. P. J. Kuenen, and H. Wijkstra, "Angiogenesis imaging by spatiotemporal analysis of ultrasound contrast agent dispersion kinetics," *IEEE Trans. Ultrason. Ferroelectr. Freq. Control*, vol. 59, no. 4, pp. 621–629, Apr. 2012.

[26] H. Tolboom, M.-L. Izamis, N. Sharma, J. M. Milwid, B. Uygun, F. Berthiaume, K. Uygun, and M. L. Yarmush, "Subnormothermic machine perfusion at both 20°C and 30°C recovers ischemic rat livers for successful transplantation," *J. Surg. Res.*, vol. 175, no. 1, pp. 149–156, Jun. 2012.

[27] R. Bu, J. Zou, L. Yin, F. Wu, S. Meng, F. Liu, X. Zhao, J. Jiao, and H. Yang, "Establishment of an isolated porcine liver machine perfusion model for high-intensity focused ultrasound studies," *Nan Fang Yi Ke Da Xue Xue Bao*, vol. 32, no. 11, pp. 1564–1567, Nov. 2012.

[28] E. Gringeri, P. Bonsignore, D. Bassi, F. E. D'Amico, C. Mescoli, M. Polacco, M. Buggio, R. Luisetto, R. Boetto, G. Noaro, A. Ferrigno, E. Boncompagni, I. Freitas, M. P. Vairetti, A. Carraro, D. Neri, and U. Cillo, "Subnormothermic machine perfusion for non-heart-beating donor liver grafts preservation in a Swine model: a new strategy to increase the donor pool?," *Transplant. Proc.*, vol. 44, no. 7, pp. 2026–2028, Sep. 2012.

[29] C. Grosse-Siestrup, S. Nagel, V. Unger, M. Meissler, J. Pfeffer, A. Fischer, and D. A. Groneberg, "The isolated perfused liver. a new model using autologous blood and porcine slaughterhouse organs," *J. Pharmacol. Toxicol. Methods*, vol. 46, no. 3, pp. 163–168, Dec. 2001.

[30] C. Grosse-Siestrup, J. Pfeffer, V. Unger, S. Nagel, C. Witt, A. Fischer, and D. A. Groneberg, "Isolated hemoperfused slaughterhouse livers as a valid model to study hepatotoxicity," *Toxicol. Pathol.*, vol. 30, no. 6, pp. 749–754, Dec. 2002.

[31] S. Nagel, O. Hegemann, D. A. Groneberg, and C. Grosse-Siestrup, "An improved model of isolated hemoperfused porcine livers using pneumatically driven pulsating blood pumps," *Toxicol. Pathol.*, vol. 33, no. 4, pp. 434–440, 2005.

[32] M. Adham, S. Peyrol, M. Chevallier, C. Ducerf, M. Vernet, C. Barakat, E. De La Roche, A. Taibi, T. Bizollon, D. Rigal, M. Pouyet, and J. Baulieux, "The isolated perfused porcine liver: assessment of viability during and after six hours of perfusion," *Transpl. Int. Off. J. Eur. Soc. Organ Transplant.*, vol. 10, no. 4, pp. 299–311, 1997.

[33] J. Brockmann, S. Reddy, C. Coussios, D. Pigott, D. Guirriero, D. Hughes, A. Morovat, D. Roy, L. Winter, and P. J. Friend, "Normothermic perfusion: a new paradigm for organ preservation," *Ann. Surg.*, vol. 250, no. 1, pp. 1–6, Jul. 2009.

[34] A. J. Butler, M. A. Rees, D. G. D. Wight, N. D. Casey, G. Alexander, D. J. G. White, and P. J. Friend, "Successful extracorporeal porcine liver perfusion for 72 hr," *Transplantation*, vol. 73, no. 8, pp. 1212–1218, Apr. 2002.

[35] S. D. St Peter, C. J. Imber, I. Lopez, D. Hughes, and P. J. Friend, "Extended preservation of non-heart-beating donor livers with normothermic machine perfusion," *Br. J. Surg.*, vol. 89, no. 5, pp. 609–616, May 2002.

[36] S. Fujita, I. Hamamoto, K. Nakamura, K. Tanaka, and K. Ozawa, "Isolated perfusion of rat livers: effect of temperature on O2 consumption, enzyme release, energy store, and morphology," *Nihon Geka Hokan Arch. Für Jpn. Chir.*, vol. 62, no. 2, pp. 58–70, Mar. 1993.

[37] S. R. Wilson and P. N. Burns, “An algorithm for the diagnosis of focal liver masses using microbubble contrast-enhanced pulse-inversion sonography,” *AJR Am. J. Roentgenol.*, vol. 186, no. 5, pp. 1401–1412, May 2006.

[38] J.-M. Escoffre, C. Mannaris, B. Geers, A. Novell, I. Lentacker, M. Averkiou, and A. Bouakaz, “Doxorubicin liposome-loaded microbubbles for contrast imaging and ultrasound-triggered drug delivery,” *IEEE Trans. Ultrason. Ferroelectr. Freq. Control*, vol. 60, no. 1, pp. 78–87, Jan. 2013.

[39] M. Abu-Amara, S. Y. Yang, N. Tapuria, B. Fuller, B. Davidson, and A. Seifalian, “Liver ischemia/reperfusion injury: processes in inflammatory networks--a review,” *Liver Transplant. Off. Publ. Am. Assoc. Study Liver Dis. Int. Liver Transplant. Soc.*, vol. 16, no. 9, pp. 1016–1032, Sep. 2010.

[40] H. Jaeschke, “Mechanisms of reperfusion injury after warm ischemia of the liver,” *J. Hepatobiliary. Pancreat. Surg.*, vol. 5, no. 4, pp. 402–408, 1998.

[41] E. E. Montalvo-Jave, T. Escalante-Tattersfield, J. A. Ortega-Salgado, E. Piña, and D. A. Geller, “Factors in the pathophysiology of the liver ischemia-reperfusion injury,” *J. Surg. Res.*, vol. 147, no. 1, pp. 153–159, Jun. 2008.

[42] E. Leen, M. Averkiou, M. Arditi, P. Burns, D. Bokor, T. Gauthier, Y. Kono, and O. Lucidarme, “Dynamic contrast enhanced ultrasound assessment of the vascular effects of novel therapeutics in early stage trials,” *Eur. Radiol.*, vol. 22, no. 7, pp. 1442–1450, Jul. 2012.

[43] M. Schneider, A. Broillet, I. Tardy, S. Pochon, P. Bussat, T. Bettinger, A. Helbert, M. Costa, and F. Tranquart, “Use of intravital microscopy to study the microvascular behavior of microbubble-based ultrasound contrast agents,” *Microcirc. N. Y. N 1994*, vol. 19, no. 3, pp. 245–259, Apr. 2012.

[44] M. Schneider, “Characteristics of SonoVue,” *Echocardiogr. Mt. Kisco N*, vol. 16, no. 7, Pt 2, pp. 743–746, Oct. 1999.

[45] M. Averkiou, M. Lampaskis, K. Kyriakopoulou, D. Skarlos, G. Klouvas, C. Strouthos, and E. Leen, “Quantification of tumor microvascularity with respiratory gated contrast enhanced ultrasound for monitoring therapy,” *Ultrasound Med. Biol.*, vol. 36, no. 1, pp. 68–77, Jan. 2010.

[46] M. Schneider, B. Anantharam, M. Arditi, D. Bokor, A. Broillet, P. Bussat, X. Fouillet, P. Frinking, I. Tardy, J. Terrettaz, R. Senior, and F. Tranquart, “BR38, a new ultrasound blood pool agent,” *Invest. Radiol.*, vol. 46, no. 8, pp. 486–494, Aug. 2011.

3 A method for estimating the acoustic pressure in tissues using low amplitude measurements in water

The aim of this study was to evaluate a simple, reliable, and reproducible method for its accuracy in estimating the acoustic pressure delivered in tissue exposed to ultrasound. Such a method would be useful for therapeutic applications of ultrasound with microbubbles e.g. sonoporation. The method is based (a) on low amplitude water measurements, that are easily collected and they do not suffer from nonlinear propagation effects, and (b) the attenuation coefficient of tissue of interest. The range of validity of the extrapolation method for different attenuation and pressure values was evaluated with a nonlinear propagation theoretical model. Depending on the specific tissue attenuation, the method produces good estimates for pressures in excess of 10 MPa. *Ex-vivo* machine perfused pig liver tissue was used to validate the method for source pressures up to 3.5 MPa. The method can be used to estimate the delivered pressure *in-vivo* in diagnostic and therapeutic applications of ultrasound.

Keywords: liver attenuation, porcine liver, nonlinear distortion, drug delivery, *in-situ* pressure, exposimetry, derating

Published as: C. P. Keravnou, M. L. Izamis, and M. A. Averkiou, "Method for Estimating the Acoustic Pressure in Tissues Using Low-Amplitude Measurements in Water," *Ultrasound Med. Biol.*, August 2015.

3.1 Introduction

Novel therapeutic methods such as sonoporation, sonothrombolysis and other recent gene and drug delivery techniques make use of the combined effects of ultrasound and microbubbles [1]–[5]. Therapeutic ultrasound is also utilized in high intensity applications which cause irreversible tissue changes such as thermal ablation and mechanical tissue fragmentation (histotripsy) [6], [7]. The accurate knowledge of the acoustic pressure in the region exposed to ultrasound (*in-situ* acoustic pressure) is therefore essential for the applications mentioned above.

As ultrasound pressure employed for both diagnostic and therapeutic purposes varies a lot (up to 3 orders of magnitude) according to the specific application, nonlinear propagation effects are often encountered that cause errors to the linear pressure derating method. In addition to nonlinear propagation, the attenuation of ultrasound in biological tissues plays an important role in the calculation of the delivered pressure *in-situ*. Measurements in water are strongly affected by nonlinear propagation, thus various published methods propose to account nonlinearity in the pressure derating process, or measure the acoustic field in dissipative media.

Schafer [8] suggested the use of a wideband derating factor that would apply the deration of each frequency component of the measured ultrasound pulse. More recently, Bessanova et al. [9] proposed a method of scaling the source amplitudes used to generate pulses in tissue and in water so that the propagated pulses yield the same acoustic pressure at the geometric focus of the source in both media. The derating method was proposed for therapeutic applications of high intensity focused ultrasound and it was validated with both simulations and experimental measurements, with good agreement between the derated method results and numerical simulations in tissues. However this method has very good results only at the cases where the pressure amplitude at the focus is much higher than the rest of the propagation path (G=20-50). Other methods propose the use of plastic disk attenuators in the acoustic path [10], [11], or the substitution of water with attenuative fluid to create a tissue mimicking environment to perform measurements [12]. Nevertheless, the use of attenuative fluids such as castor oil or water-glycerin mixtures to create a tissue mimicking environment for measurements introduces errors and discrepancies such as variations in properties of the fluids between different laboratories and different attenuation frequency dependence than tissue.

Currently, the *in-situ* pressure delivered from diagnostic ultrasound scanners and thus the mechanical index (MI), are estimated using measurements in water that are derated for the traveled distance according to a known tissue attenuation value at the center frequency of the propagated pulse. However, for the estimation of the *in-situ* pressure, World Federation of Ultrasound in Medicine and Biology, recommended also the use of low-amplitude hydrophone measurements, linearly scaled based on the source pressure and the attenuation of tissue [13]. Such a method, avoids experimental errors associated with hydrophone measurements of sound fields at high output levels and simplifies the theoretical and computational aspects of the derating problem [14].

Previously published works have dealt with linear derating methods issues. Bacon [15] established a nonlinear propagation model to predict acoustic levels in tissue. In that work, linear extrapolation of low amplitude measurements in water was used to calculate the input data for the simulations and to validate the nonlinear propagation model. The author compared nonlinear theory results and linear extrapolation pressure values with measurements after propagation through a tissue-mimicking gel phantom. He concluded that linear extrapolation from measurements made in water is inadequate for predicting *in-situ* exposure to ultrasound as it might have errors up to 80%. However, the author evaluated the method only under the assumption of the specific properties of the tissue-mimicking gel phantom rather than using real tissue. Christopher and Carstensen [14] used a nonlinear propagation model that takes into account the effects of diffraction, attenuation, nonlinearity and planar (fluid) boundary transmission of axially symmetric acoustic beams to evaluate the nature of the effects that occur under realistic exposure conditions encountered in diagnostic procedures. Simulations based on water, liver and fat tissue properties were compared to linear theory to point out the necessity of counting for nonlinear propagation when estimating the in-situ pressure. In the review of Duck [16], detailed description is given to finite-amplitude wave effects associated with nonlinear propagation, distortion and harmonic component generation which are associated with ultrasound beams used in therapeutic applications.

If the measurements are performed in a non-dissipative media such as water, the attenuation values utilized in the derating process are very important. Liver attenuation, which is used in our work, has been extensively studied in the past using animal liver samples [17], [18], post mortem specimens of human liver [18], [19] and *in-vivo* measurements [20], [21]. The liver attenuation reported at studies above varies between

0.3dB/cm/MHz (3.45 Np/m) and 1.2 dB/cm/MHz (14 Np/m) for healthy livers (human and animals), and even more for diseased liver cases (cirrhotic livers and liver with malignancies). As there are great deviations in the published values, the accurate knowledge of tissue attenuation in individuals could obviously offer improvements in the estimation of the pressure *in-situ*. However there are difficulties in collecting measurements from each patient. To this end, measurements of attenuation in a well-functioning machine-perfused liver environment could improve the *in-situ* pressure estimation.

In this work, a method for estimating the acoustic pressure delivered in tissue based on extrapolation of low amplitude water measurements with linear theory was evaluated for its accuracy. The aim of this study was to test and establish a simple, reliable, and reproducible tool with known limitations and errors that can be used to quickly predict the delivered pressure in an area exposed to ultrasound. The acoustic field was measured in water only under low amplitude conditions, thus linear scaling of the source amplitudes was adequate to estimate higher source pressures. The method was validated by comparing the extrapolated values with actual measurements of the acoustic pressure after propagation through samples taken from *ex-vivo* machine-perfused porcine livers. The knowledge of the attenuation coefficient of the tissue was necessary for the extrapolation method. Thus, to assess the exact acoustic properties of the experimental samples used to validate the linear extrapolation method, porcine liver attenuation was measured in the range of 2 – 8 MHz. The range of validity of the extrapolation method for different pressures and attenuation values was also investigated with a nonlinear propagation theoretical model.

3.2 Materials and methods

3.2.1 Theory

Linear propagation of ultrasound in an absorptive medium

Linear propagation of ultrasound in an absorptive medium is described with Eq. (3.1)

$$p(x,y,z) = \frac{p_{02}}{p_{01}} p_1(x,y,z) e^{-\alpha z}, \qquad (3.1)$$

where p_1 (x,y,z) is the spatial distribution of the linear lossless field produced by a transducer assuming plane wave propagation in the z direction. α is the attenuation coefficient measured in nepers/m and p_{01} and p_{02} are the source pressures at two amplitudes (voltages in the case of measurements). Specifically, p_{01} is the source pressure resulting in the pressure field $p_1(x,y,z)$ and p_{02} is the source pressure resulting in the pressure field $p(x,y,z)$.

The frequency dependence of attenuation, $\alpha(f)$ is different in various media depending on their material properties. For tissues, attenuation is related to frequency with a power law,

$$\alpha(f) = \alpha_0 f^{\eta}, \qquad (3.2)$$

where α_0 is the attenuation coefficient at 1 MHz, f is measured in MHz, and the exponent η is usually between 1 and 2 [22], [23], depending on the composition and biochemical environment of tissue [24]. The complete spatial distribution of the sound field of a transducer with source pressure p_{02} in tissue may be estimated by knowing the spatial distribution of the linear lossless field at a low source pressure p_{01}.

Nonlinear propagation of ultrasound in an absorptive medium

Nonlinear propagation and dissipation are competing phenomena. Nonlinearity causes distortion to the wave by generating harmonics, while the thermoviscous absorption reduces the harmonics resulting from nonlinear effects. To calculate the combined effects of absorption and nonlinearity in sound beams, the KZK equation [25], [26] was used. Details regarding the numerical solution of the KZK equation can be found elsewhere [27], [28]. Briefly, Eq. (3.3) is a non-dimensional form of the KZK equation,

$$\frac{\partial P}{\partial \sigma} = \frac{1}{4G}\int_{-\infty}^{\tau}\left(\frac{\partial^2 P}{\partial \rho^2} + \frac{1}{\rho}\frac{\partial P}{\partial \rho}\right)d\tau' + A\frac{\partial^2 P}{\partial \tau^2} + \mathrm{N}\frac{\partial P^2}{\partial \tau}, \qquad (3.3)$$

where p_0 is the source pressure and $P = p/p_0$; d is the focal length and $\sigma = z/d$; r is the transverse direction, a the source radius and $\rho = r/a$; and t is the time, c_0 the speed of sound and $\tau = \omega_0(t - z/c_0)$. The first term in the right hand side of Eq. (3) accounts for diffraction, the second term for thermoviscous absorption, and the third for nonlinear propagation. A and N are dimensionless parameters that account for absorption and nonlinearity

respectively, where $A = \alpha d$ and $N = d / \bar{z}$ ($\bar{z}$ is the distance where a shock first forms in a waveform under plane wave propagation conditions for a given source amplitude) [27].

A single-element circular source with 25.4 mm diameter, 101.6 mm focal length (*d*), and frequency of 2 MHz was assumed in the simulations (focusing gain *G*=6.65). The values used for attenuation were α = 4, 8, 16 and 32 Np/m, while the dimensionless nonlinearity parameter was $0<N<1.6$, linearly depending on the source pressure, p_0. The aim of these simulations was to investigate the effect of attenuation (*A*) and nonlinearity (*N*) on the accuracy of the linear extrapolation method. The attenuation values used here cover a range of different tissue types while the nonlinearity coefficient represents source pressures up to 3 MPa. A single-element circular transducer with low focusing gain (similar to that of diagnostic ultrasound transducers) was chosen for this study because of its simplicity and ease to model. The results from the nonlinear simulation were compared with the linear theory approach [Eq.(3.1)] to evaluate the range of validity of the proposed method.

3.2.2 Experimental Setup

Equipment

A C5-1 curved array of an iU22 diagnostic ultrasound scanner (Phillips Medical Systems, Bothell, WA, USA) was used to transmit ultrasound pulses. The Color Power Angio (CPA) imaging mode was selected, which uses pulses with center frequency of *f*=2 MHz and 8 cycles duration [Fig. 3.2(a, b)]. The scan plane focus was placed at 50 mm. Through a research interface only the central line of the sector scan was fired. A 0.4 mm membrane hydrophone (Precision Acoustics Ltd, Dorchester, UK) was used to record the acoustic pressure. A modified Ultra-Pro II Needle Guidance System (CIVCO Medical Solutions, Kalona, IA, USA) was used to hold C5-1 probe [see Fig. 3.1(b)]. A motorized micro-positioning system (Newport, Irvine, CA, USA) was used to align the transducer and the hydrophone and to move the hydrophone to the desired location. A rotation stage and two goniometers (Newport, Irvine, CA, USA) were also used in the alignment procedure allowing rotation over *x*, *y* and *z* axes [see Fig. 3.1(c)]. In order to align the probe with the micro-positioner axes the location of the maximum pressure for two axial points, one before the focus and one after, was noted and the angle in each axis was

calculated. Then, the goniometers were used to correct for the calculated angle in each axis. The liver sample was placed in a 35ø x 70 mm cylindrical acrylic container. The sides of the container had acoustically transparent windows made from a 0.01 mm mylar film. The transducer, hydrophone, and cylindrical sample container were all submerged in a tank filled with deionized water [Fig. 3.1(a)]. The measurements were transferred to a Tektronix DPO 7054 digital oscilloscope (Tektronix, Inc., Beaverton, OR, USA) and captured using LabVIEW (National Instruments, Austin, Texas, USA) computer software.

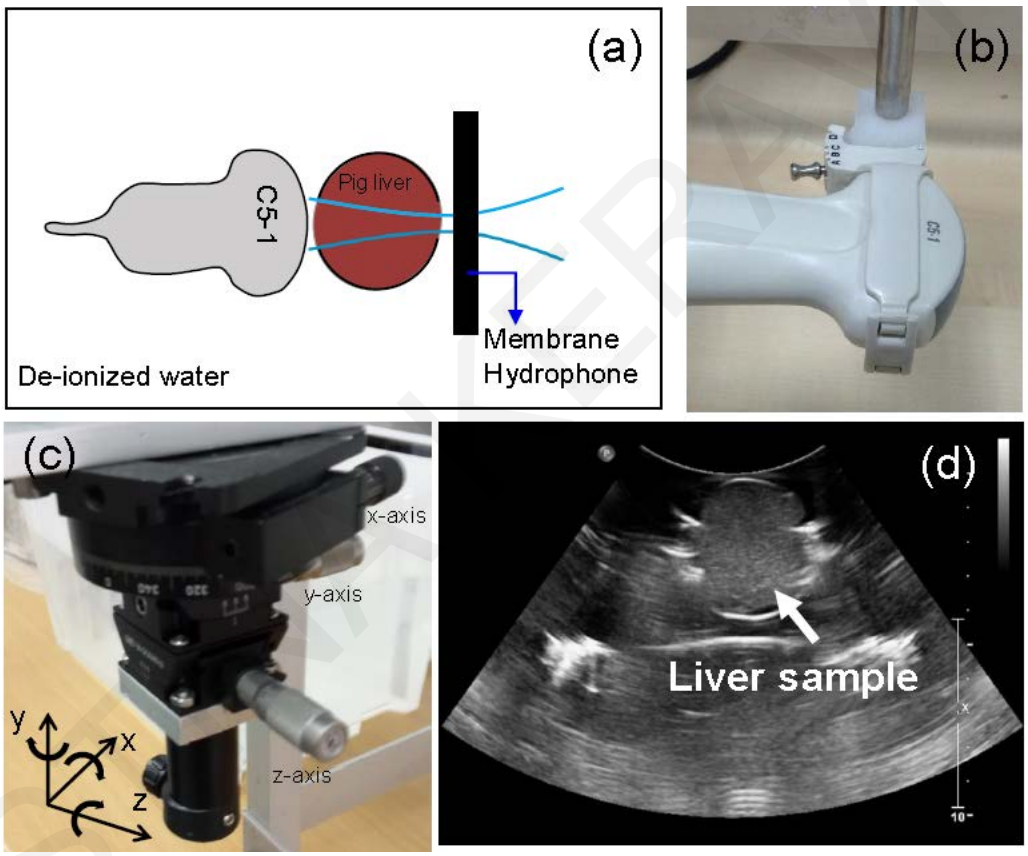

Figure 3.1: (a) Schematic representation of the setup used for attenuation measurements. (b) Close-up of the transducer holding device. (c) The rotation stage and the two goniometers used for alignment. The system allows rotation over x, y and z axes. (d) B-mode ultrasound image of the pig liver sample in the enclosure.

Sample preparation

Liver tissue samples were collected from a normally functioning *ex-vivo* machine-perfused porcine liver. The method employed for porcine liver perfusion has been described in detail elsewhere [29]. Briefly, healthy porcine livers were procured from the local slaughterhouse. Livers were flushed with 8L of ice cold Lactated Ringers (Multi-

Pharm Co. Nicosia, Cyprus) through both the portal vein (PV) and hepatic artery (HA). The organs were stored on ice and transported to the laboratory where they were connected to the machine perfusion system. The perfusion was monitored via Dynamic Contrast-Enhanced Ultrasound (DCEUS) imaging. After 3 hours of perfusion, a sample was dissected from the organ and placed in the cylindrical container described above. Vessels were filled with the perfusate and clamped to avoid having any air entering the vasculature. The placement of the liver sample in the sample container was performed underwater to further avoid possible air embolisms. B-mode imaging of the liver sample in the enclosure [Fig. 3.1(d)] was also performed with the C5-1 curved array to secure that no air was present. The temperature of the liver sample during measurements was maintained at 25°C. Three different porcine livers were used for attenuation measurements (one measurement was performed in each sample).

3.2.3 Acoustic pressure and attenuation measurements

Measurement of the linear ultrasound probe field

The linear acoustic field (MI=0.07, where $MI = \frac{p_-}{\sqrt{f}}$, and p_- is the peak negative pressure) produced by the C5-1 curved array (CPA mode, central line, f=2 MHz, 8 cycles) was measured. The alignment procedure described above was used here as well. The measurements were taken in deionized water using a step of 3 mm in the axial direction and 1 mm in the transverse direction to create a two dimensional beam profile. The measured low amplitude 2D beam profile may then be used to calculate a higher pressure field by taking into consideration the measured attenuation and the proposed method based on linear theory in Eq. (3.1).

Measurement of liver attenuation

A single, high amplitude pulse (MI=1.3) was transmitted in water and in liver tissue [Fig. 3.2(c)] to ensure nonlinear propagation and harmonic generation. The different harmonic components generated in water and in liver tissue [Fig. 3.2(d)] were compared to extract an attenuation value per frequency,

$$\alpha_l(f) = \alpha_w(f) + \frac{\Delta S(f)}{8.686 z}, \qquad (3.4)$$

where $\Delta S(f)$ is the spectral difference in dB for every harmonic component between water and tissue. Our approach assumes that the differences between the two media coefficient of nonlinearity (*B/A*) are small and their effect on the measurements may be neglected. The porcine liver coefficient of nonlinearity (*B/A*) is given by Hamilton and Blackstock [30], as 6.7 with uncertainty ±1.5 measured by the finite amplitude method, while the water *B/A* value is about 5.2. To test the validity of our assumption, nonlinear propagation in these two media was modeled with a nonlinear theoretical model (KZK equation) for the two *B/A* values (*B/A* =5.2, 6.5) while the absorption coefficient was kept the same. Only small differences in higher harmonic levels were observed (3^{rd} and 4^{th} harmonics) and they were less than 4 dB. Thus, we have concluded that the assumption of a negligible influence of the different nonlinearity values was valid. The spectral analysis of the pulses and the attenuation calculations were performed using MATLAB (The MathWorks, Inc., Natick, MA, USA) computer software.

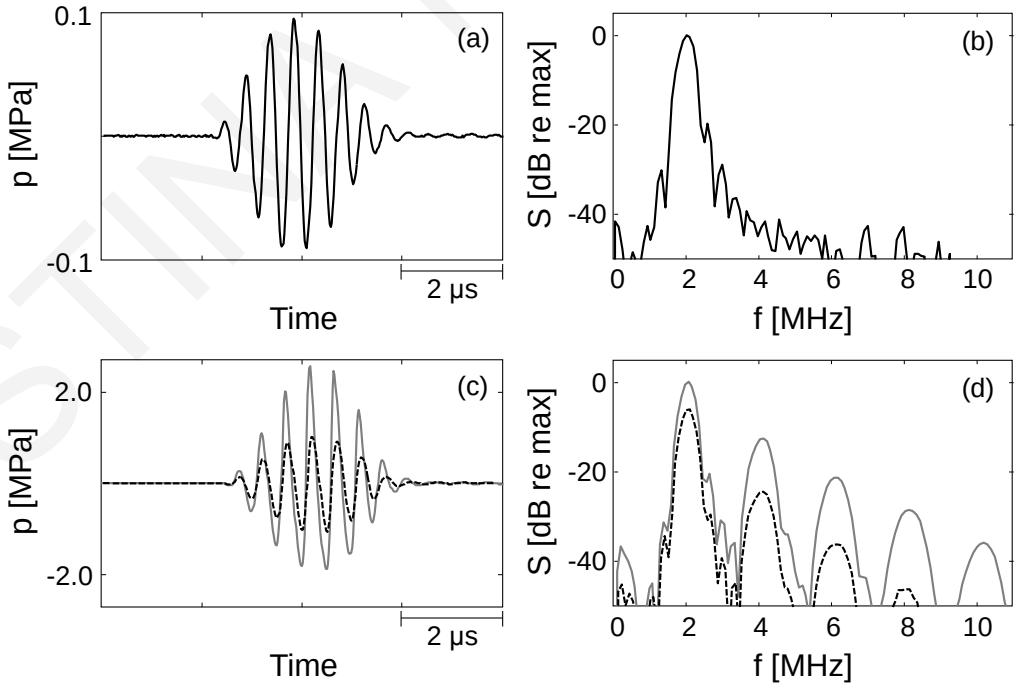

Figure 3.2: (a, b) Time waveform and frequency spectrum of a low amplitude pulse measured in water. (c, d) Time waveforms and frequency spectra of a high amplitude pulse after propagation through water (solid line) and pig liver (dashed line).

Measurement of acoustic pressure in liver tissue

The validity of the linear theory [Eq. (3.1)] for focal pressures up to 1.8 MPa was examined by comparing the extrapolated values with actual measurements of the acoustic pressure after propagation through samples taken from *ex-vivo* machine-perfused porcine livers on axis at 50 mm [$p1(0, 0, 50)$]. After propagation through the liver sample [Fig 3.1(a)], each pulse was received by the membrane hydrophone, transferred to the digital oscilloscope and transferred to a computer with LabVIEW (National Instruments, Austin, Texas, USA) computer software.

3.3 Results

The comparison between the estimated pressure using the linear theory (dashed line) and the KZK equation (solid line) for different nonlinearity coefficients, $0 \leq N \leq 1.6$, and for 4 different cases of attenuation (α = 4, 8, 16 and 32 Np/m) is shown in Fig. 3.3. The first column show the peak positive p_+ and the peak negative pressure p_- as a function of source pressure while the second column shows the pressure ratio p_+/p_-. As demonstrated in these plots, increasing p_0 causes more waveform distortion due to nonlinear propagation and p_+/p_- becomes greater than 1 at a different rate according to the attenuation coefficient.

When the attenuation is low, (α = 4 Np/m, [Fig. 3.3(a, b)]), there are more differences between the linear extrapolation method and the KZK equation. Specifically, the pressure estimation from the two methods agree within 20% only up to p_0<0.5 MPa at which source pressure p_+/p_- <1.5. At higher source pressures, due to the increased influence of nonlinear propagation on the pulses, the difference between the two methods is larger. As attenuation increases (α = 8 Np/m, [Fig. 3.3(c, d)]), dissipation effects start to be comparable with the nonlinear effects and an agreement within 20% between the two pressure estimations is observed up to p_0 = 1.5 MPa ($p_+/p_- \leq 1.5$). Here we note that the two methods result in almost identical value for p_+ up to p_0 = 3 MPa. At even higher attenuation values (α = 16 Np/m and α = 32 Np/m, [Fig. 3.3 (e, f), (g, h)]), the ratio p_+/p_- is below 1.5 for the whole range of p_0 and the differences are less than 17% for both p_+ and p_-.

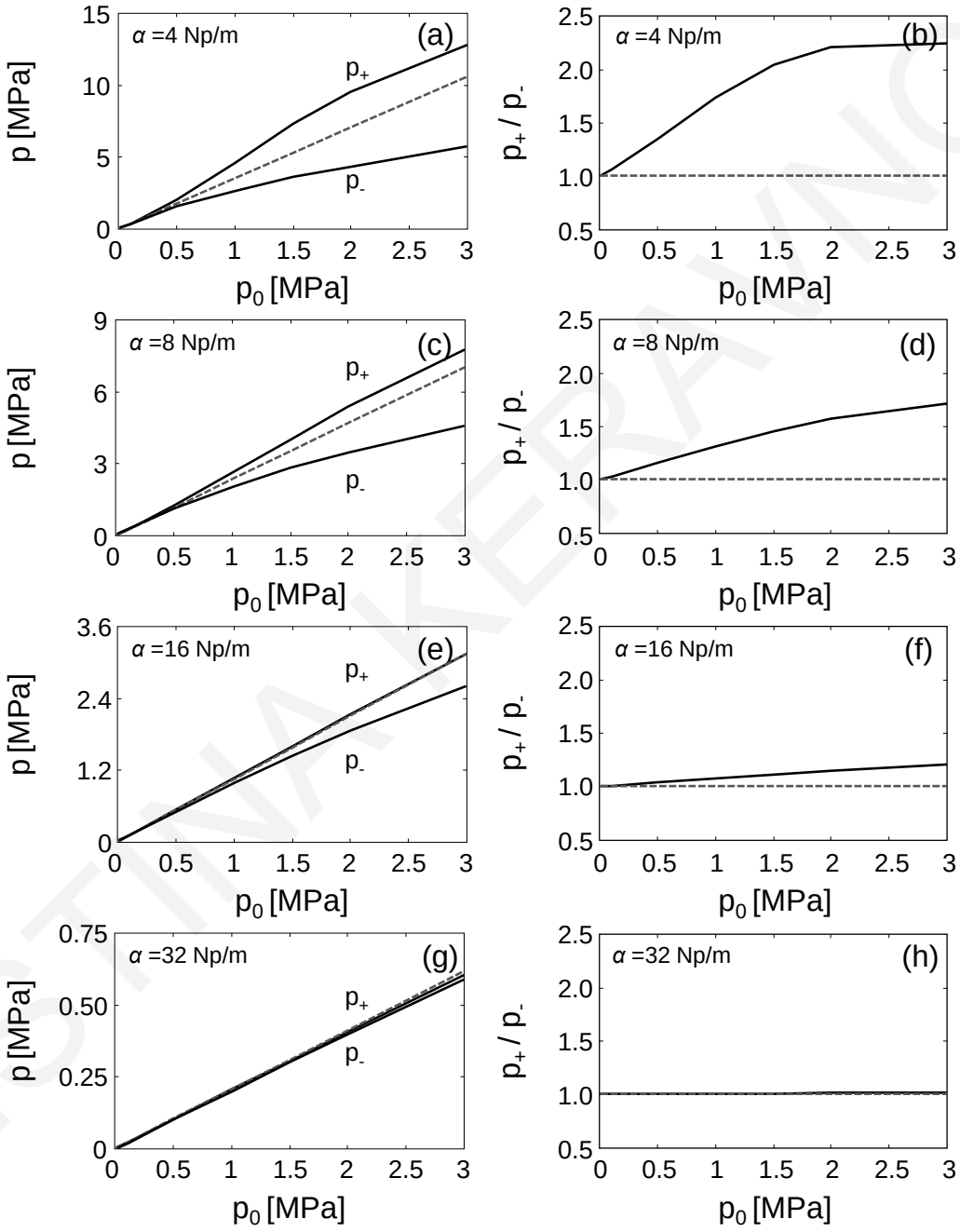

Figure 3.3: Comparison of pressure extrapolated values (dashed lines) and KZK simulations (solid lines) for different source amplitudes and different attenuation coefficients. (a, b) α = 4 Np/m, (c, d) α = 8 Np/m, (e, f) α = 16 Np/m, (g, h) α = 32 Np/m.

Figure 3.4(a, b) presents the low amplitude (MI=0.07), two dimensional beam profiles of the selected CPA imaging setting of the C5-1 probe. In Fig. 3.4(a) the spatial distribution of the sound field of the scan (azimuthal) plane is shown, while Fig. 3.4(b) shows the elevation plane. The spatial distribution of the acoustic pressure [$p_1(x, y, z)$] was measured in the range -10<x<10, -10<y<10 mm in the transverse direction and 15<z<120 mm in the axial direction.

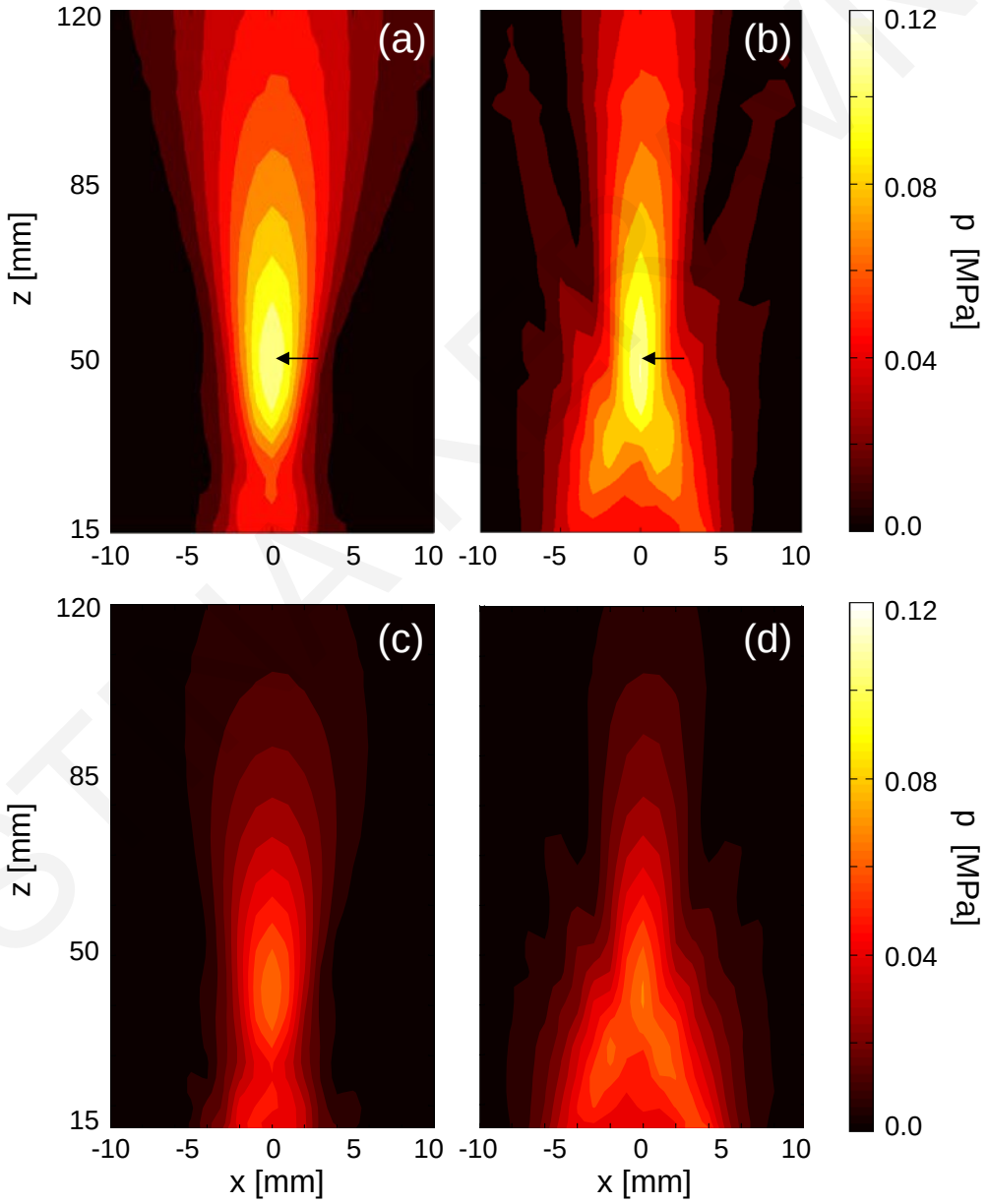

Figure 3.4: Measurements of low amplitude beam profiles in water of a Color Power Angio (CPA) imaging setting of C5-1 probe (*f*=2 MHz, 8 cycles, MI=0.07); (a) scan plane and (b) elevation plane of focus = 50 mm. The arrows indicate the point in the acoustic field where the linear extrapolation method was performed. Bottom row: Deration of the measured low amplitude beam profiles (a, b) using liver tissue attenuation.

The attenuation in both Np/m and dB/cm as a function of frequency for porcine liver tissue in the frequency range 2 to 8 MHz is shown in Fig. 3.5. The average of three measurements is shown in circles ('○'), while the fit using Eq. (2) is shown in dashed line. The error bars show the standard error of the mean. An attenuation coefficient (α_0) of 9.05 Np/m at 1 MHz and an exponent (η) of 0.73 was calculated from the fit of attenuation measurements. The goodness of the fit was $R^2 = 0.99$. Attenuation at 2 MHz was found to be 15 Np/m and this value has been used in the linear extrapolation method throughout this study (the CPA imaging setting chosen for measurements uses pulses with center frequency 2 MHz).

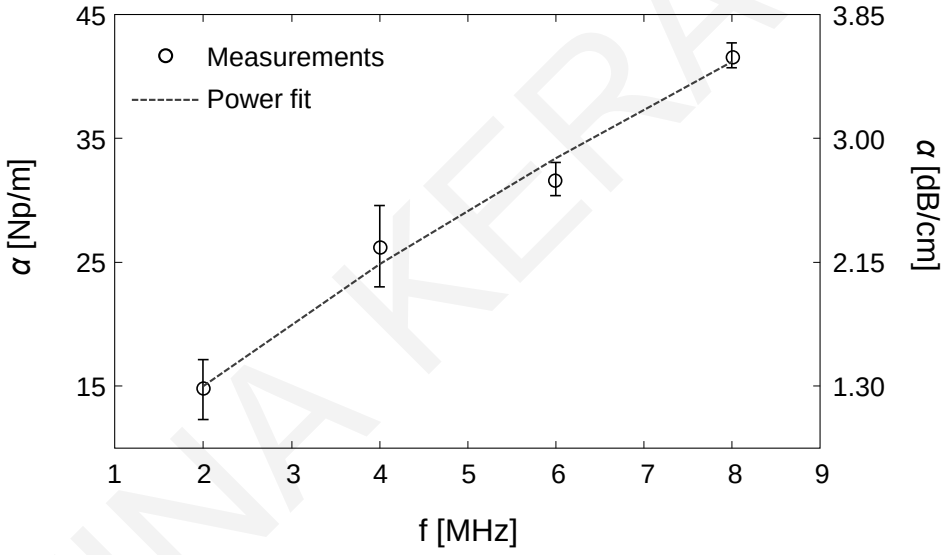

Figure 3.5: The attenuation (Np/m on the left, dB/cm on the right) as a function of frequency (MHz). The average of the three measurements is shown in circles (○), while the fit is shown in dashed line.

Figure 3.6 shows the estimated pressure (with the linear extrapolation method) at the focus (50 mm for this case) as a dashed line. The low amplitude water measurement of Fig. 3.4 was used (as indicated by the arrows) and scaled according to Eq. (3.1). We note that for the estimated pressure with Eq. (1) $p_+=p_-$ since the method is based on linear acoustics. The measured pressure (p_+ and p_-) for $0.05<p_0<3.5$ MPa after propagation in porcine liver is shown as a solid line. The source pressure range corresponds to MI values on the scanner of 0.07 to 2.8 (which assume 0.3 dB/cm/MHz attenuation). Figure 3.6(a) shows p_+ and p_-, while Fig. 3.6(b) presents the ratio p_+/p_- as a function of source pressure. It is observed that the measured value of p_+ has <25% deviation from the linear

extrapolation method throughout the range of source pressures used, while the measured value of p_- deviates more from the linear extrapolation calculation than p_+. At higher source pressures for this specific tissue (2 – 3.5 MPa) there are discrepancies >25% between the measured p_- and the estimated values due to the level of nonlinear propagation as demonstrated by the increase in the p_+/p_- ratio [asymmetric nonlinear distortion, Fig. 3.6(b)]. However the value $(p_+-p_-)/2$ (not shown in the plot) is much closer to the linear estimation since p_+ is slightly underestimated and p_- overestimated.

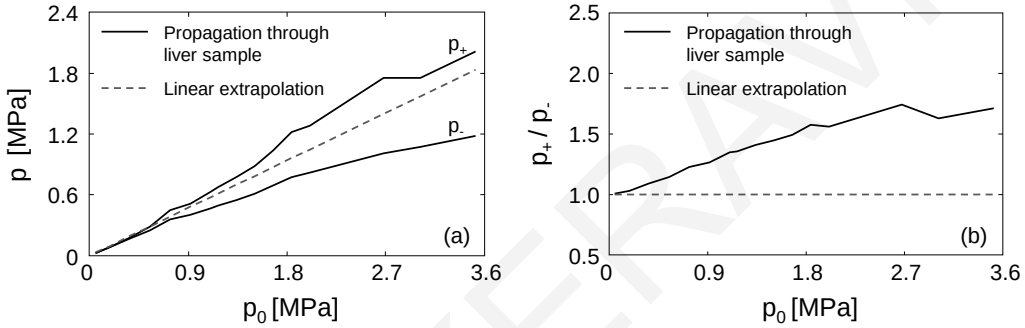

Figure 3.6: Comparison of extrapolated (dashed line) and measured (solid line) pressures after propagation through porcine liver tissue for different source amplitudes. (a) Peak positive (p+) and peak negative pressure (p-) and (b) the ratio p+/p- as a function of source pressures (p0).

The range of validity of the linear extrapolation method is shown in Fig. 3.7, where the percent deviation of linear theory from simulations and measurements is plotted as a function of the Gol'dberg number (Γ). The Gol'dberg number is the ratio of *N/A* (nonlinearity over absorption). Figure 3.7 (a-c) shows the difference between the KZK simulations and the linear method, while Fig. 3.7(d-f) shows the differences between our measurements and the linear method. The errors of the linear extrapolation method for the peak positive pressure, Fig. 3.7(a, d), are <25% through the range of Γ values considered. For peak negative pressure [Fig. 3.7(b, e)] which plays an important role in microbubble response, it is observed that the linear method is accurate (with ≤20% deviations from actual pressure values) up to Γ=1 where absorption and nonlinearity effects are comparable. When Γ>1, the deviations increase and reach about 50% for Γ=4. The maximum error of the linear extrapolation method for the average pressure $[(p_+-p_-)/2]$ is about 15% even up to Γ=4 which we consider as good overall agreement.

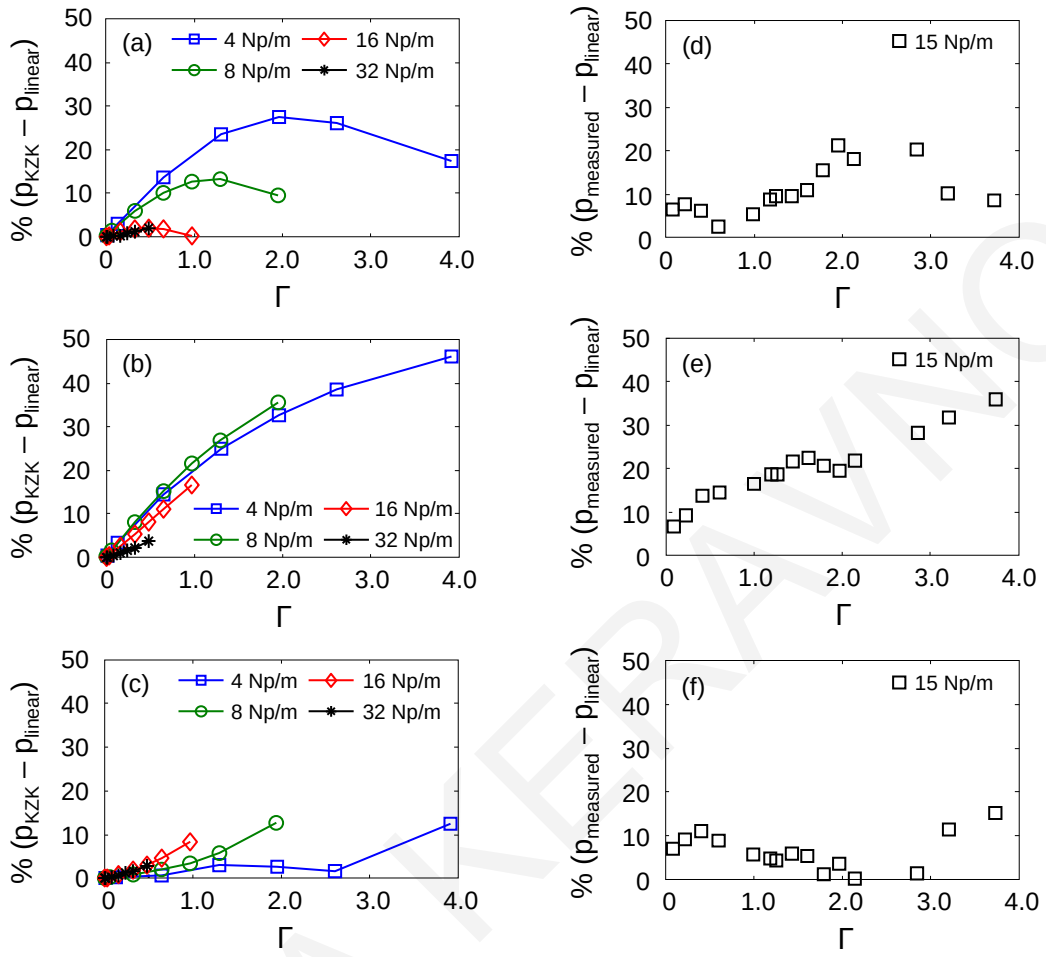

Figure 3.7: Percentage deviation of linear theory from KZK simulations (top row) and measurements through *ex-vivo* pig liver tissue (bottom row) as a function of Gol'dberg number. (a, d) peak positive pressure, (b, e) peak negative pressure and (c, f) ($p_+ - p_-$)/2.

3.4 Discussion

A method for estimating the *in-situ* acoustic pressure in tissues based on low amplitude measurements in water and knowledge of the attenuation at the frequency of interest has been presented. The method was validated for source pressures up to 3.5 MPa produced by a C5-1 probe with the Philips-iU22 scanner. For reference, at the maximum source pressure of 3.5 MPa the scanner MI reading was 2.8 (with 0.3 dB/cm/MHz assumed attenuation). Special research software allowed for reaching MI's greater than the FDA limit in order to evaluate the validity of our method at amplitudes higher than diagnostic. Detailed two dimensional beam profiles of the C5-1 curved array were measured in water at low amplitude. What's important with this work is the fact that the complete field of the probe can now be easily converted to the estimated resulting acoustic pressure in tissue

using the extrapolation method presented here [Fig. 3.4(c, d)]. Overall, the comparison of the estimated acoustic pressures with actual measurements in machine-perfused liver tissue showed only small differences up to source pressures of 3.5MPa [for $(p_+ - p_-)/2$ values, where errors were less than 15%].

An interesting test case for the linear extrapolation method is the estimation of the MI at various source pressures and while assuming a tissue attenuation of 0.3 dB/cm/MHz (the value assumed by diagnostic ultrasound systems). Figure 3.8 shows the MI as a function of source pressure for the C5-1 curved array of the iU22 for a CPA setting. The dashed line is the linear extrapolation method from low amplitude water measurements and α=0.3 dB/cm/MHz. The solid line is the MI reading on the iU22 as a function of source pressure (transmitted voltage is converted to pressure). A good agreement is observed between the extrapolation method and the actual MI reading. Overall, the MI reading on the iU22 is slightly higher. One possible source for the differences is the fact that the ultrasound system does not indicate the axial distance of the maximum MI whereas in our calculations we have always used the location of the maximum pressure at low amplitude in water. Additionally, the ultrasound manufacturers measure the MI in water at all amplitudes (low and high) and errors are introduced in those measurements due to nonlinear propagation and pulse distortion. Thus both approaches (manufacturer measurement and the linear scaling method) despite their agreement in Fig. 3.8 have possible errors. The correct MI value is what can be calculated from Fig. 3.6 which is the actual measurement of the peak negative pressure after propagation in liver tissue [shown in Fig. 3.8 as solid line with square markers ('□')].

Another interesting observation in Fig. 3.8 is that the source pressures for the CPA imaging setting used are slightly lower than the delivered acoustic focal pressures. This suggests that the increase in pressure due to focusing is countered by the tissue attenuation, thus resulting in a relatively "uniform" pressure field. This result is also confirmed in Fig. 3.4(c, d), where two-dimensional beam profiles are estimated based on linear extrapolation and liver tissue attenuation. It is observed that the near field pressure values (15 mm from the source) and the focal area pressure values are similar. It is interesting to note that for the transducer and medium properties considered here, microbubbles used for either diagnosis or therapy would experience roughly the same acoustic pressure irrespective of their image depth.

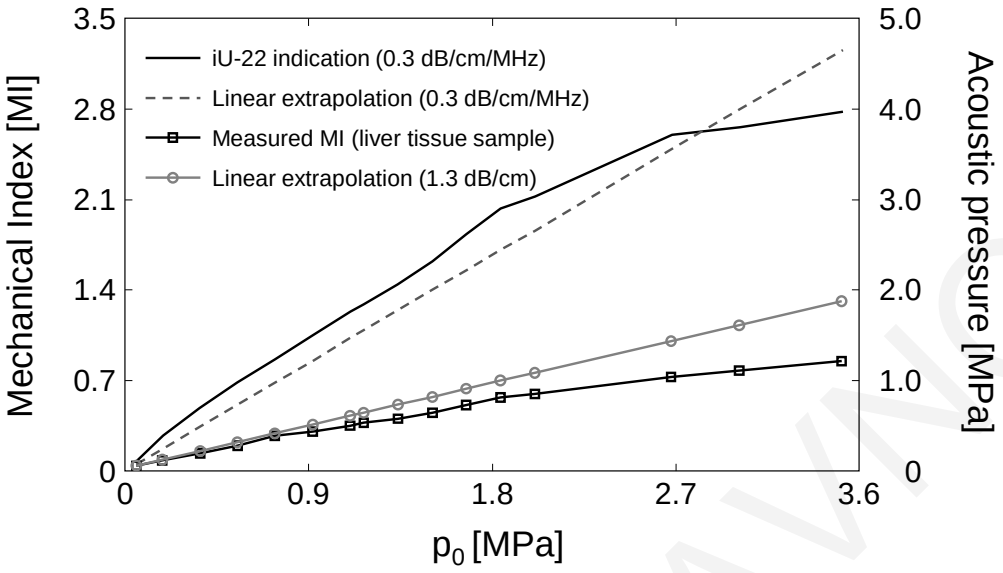

Figure 3.8: Comparison of MI values calculated from extrapolated pressures (dashed line) with iU-22 MI indications (solid line). For the calculated MI an attenuation coefficient of 0.3 dB/cm/MHz was used. The line with square markers (□) presents the MI based on the measured peak negative pressure after propagation through liver tissue, while the line with circles (○) shows the estimated MI based on linear extrapolation method and liver tissue attenuation.

In this study, pig liver tissue was selected to evaluate the range of validity of the linear extrapolation method for predicting is-situ acoustic pressure. Since the nonlinearity and attenuation values vary between different tissues, the range of validity of the linear extrapolation method is also expected to vary. A nonlinear propagation theoretical model (KZK equation), was used to test the range of validity of the linear extrapolation method for tissues with different attenuation and nonlinearity values. As the source pressure amplitude increases, the ratio of the peak positive to the peak negative pressure becomes greater than 1 at a different rate depending on the attenuation coefficient. The theoretical simulations (Fig. 3.3) also revealed that p_- is affected more at higher amplitudes in comparison to p_+.

As the transducer's geometry and characteristics are very important for the produced beam profiles, the KZK equation was also used to investigate the effect of focusing gain on the accuracy of the linear extrapolation method. Figure 3.9 shows the comparison of pressure extrapolated values (dashed lines) and KZK simulations (solid lines) as a function of source pressure amplitude for α=16 Np/m and 3 different focusing gains: (a) G=6.65, (b) G=13 and (c) G=26. It is observed that deviations from linearity increase with increasing focusing gain [Fig. 3.9(b, c)]. Nevertheless, for tissue types with

higher attenuation (such as liver) the linear extrapolation method can estimate *in-situ* pressures in excess of 6 MPa with <20% errors when higher gain sources are utilized in ultrasound applications [G=26, Fig. 3.9(c)].

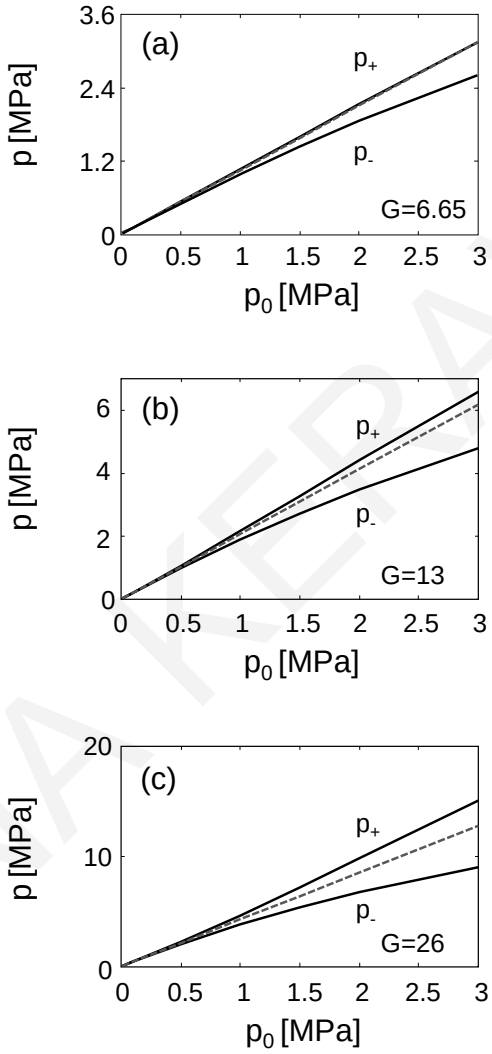

Figure 3.9: Comparison of pressure extrapolated values (dashed lines) and KZK simulations (solid lines) as a function of source pressure amplitude, for α=16 Np/m and 3 different focusing gains: (a) G=6.65, (b) G=13 and (c) G=26.

The main required input for the extrapolation method is the attenuation coefficient of the tissue of interest. Porcine liver attenuation was measured and the specific power law for the attenuation–frequency relationship was derived. Here is the first time that samples taken from a re-perfused organ are being used to measure attenuation. This is of great

importance since the samples used are harvested from a viable and normal functioning organ instead of excised tissue samples that were used in the past.

In the present work, the attenuation at 1 MHz, α_0 was found to be 9.05 Np/m and the exponent η in the power law was calculated from the data to be 0.73. Zderic et al. [31] in *in-vivo* porcine liver measurements calculated an exponent of 0.84 which is similar with ours. Comparing porcine liver attenuation values with *in-vivo* human liver measured values, the latter appear to be slightly higher. The range for exponent η for human liver attenuation is 1 – 1.14 and the coefficient α_0 varies between 5 and 7 Np/m [32]–[35]. However, our measured porcine liver attenuation values $\alpha(f)$, are within the range of attenuation values reported previously in literature for human liver from the authors above. We note here that the differences between attenuation measurements in humans are quite large and the measurements are also affected by various types of tissue (fatty, cirrhotic etc.) [20]. For more accurate estimation of in-situ pressure knowledge of the specific tissue attenuation is of course necessary.

The knowledge of the acoustic pressure and intensity is very important in a variety of therapeutic ultrasound applications. In ablative ultrasound techniques such as HIFU and histotripsy, knowledge of the acoustic field helps with treatment planning by accurate identification of the ablation zone. In ultrasound-mediated drug delivery, the physical interaction of ultrasound and microbubbles has the potential to facilitate localized drug enhancement by altering cell membrane permeability and thus allowing for the uptake of macromolecules [36]. It is suggested that depending on the acoustic pressure, the cell membrane permeability change may either be reversible or irreversible, thus accurate knowledge of the delivered pressure is again very essential.

3.5 Conclusions

A method for estimating the delivered acoustic pressure in tissue was validated for a large range of pressures. The proposed method is quick and easy since it is based on low amplitude measurements in water and the attenuation value of the tissue of interest. From measurements and simulations based on the KZK equation it was shown that the proposed method can predict in-situ pressure for a large range of nonlinearity and attenuation values. As the attenuation value increases it counters the nonlinear distortion effects and the proposed method becomes more accurate even at very high acoustic pressures. The

proposed method can estimate the in-situ peak negative pressure with errors ≤20% for Γ values up to 1, and the peak positive pressures with errors ≤20% for Γ values up to 4.

Acknowledgements

This work was co-funded by the European Regional Development Fund and the Republic of Cyprus through the Research Promotion Foundation (Project: DIDAKTOR/0311/78).

REFERENCES

[1] R. Deckers and C. T. W. Moonen, "Ultrasound triggered, image guided, local drug delivery," *J. Control. Release Off. J. Control. Release Soc.*, vol. 148, no. 1, pp. 25–33, Nov. 2010.

[2] S. Kotopoulis, G. Dimcevski, O. Helge Gilja, D. Hoem, and M. Postema, "Treatment of human pancreatic cancer using combined ultrasound, microbubbles, and gemcitabine: A clinical case study," *Med. Phys.*, vol. 40, no. 7, p. -, 2013.

[3] K. H. Martin and P. A. Dayton, "Current status and prospects for microbubbles in ultrasound theranostics," *Wiley Interdiscip. Rev. Nanomed. Nanobiotechnol.*, vol. 5, no. 4, pp. 329–345, Aug. 2013.

[4] C. A. Molina, M. Ribo, M. Rubiera, J. Montaner, E. Santamarina, R. Delgado-Mederos, J. F. Arenillas, R. Huertas, F. Purroy, P. Delgado, and J. Alvarez-Sabín, "Microbubble administration accelerates clot lysis during continuous 2-MHz ultrasound monitoring in stroke patients treated with intravenous tissue plasminogen activator," *Stroke J. Cereb. Circ.*, vol. 37, no. 2, pp. 425–429, Feb. 2006.

[5] A. A. Rahim, S. L. Taylor, N. L. Bush, G. R. ter Haar, J. C. Bamber, and C. D. Porter, "Spatial and acoustic pressure dependence of microbubble-mediated gene delivery targeted using focused ultrasound," *J. Gene Med.*, vol. 8, no. 11, pp. 1347–1357, Nov. 2006.

[6] M. Z. Mahmoud, M. Alkhorayef, K. S. Alzimami, M. S. Aljuhani, and A. Sulieman, "High-Intensity Focused Ultrasound (HIFU) in Uterine Fibroid Treatment: Review Study," *Pol. J. Radiol. Pol. Med. Soc. Radiol.*, vol. 79, pp. 384–390, 2014.

[7] E. Vlaisavljevich, A. Maxwell, M. Warnez, E. Johnsen, C. A. Cain, and Z. Xu, "Histotripsy-induced cavitation cloud initiation thresholds in tissues of different mechanical properties," *IEEE Trans. Ultrason. Ferroelectr. Freq. Control*, vol. 61, no. 2, pp. 341–352, Feb. 2014.

[8] M. E. Schafer, "Alternative approaches to in-situ intensity estimation [medical diagnostic ultrasound]," presented at the Ultrasonics Symposium, 1990. Proceedings., IEEE 1990, 1990, pp. 1381–1384 vol.3.

[9] O. V. Bessonova, V. A. Khokhlova, M. S. Canney, M. R. Bailey, and L. A. Crum, "A derating method for therapeutic applications of high intensity focused ultrasound.," *Acoust. Phys.*, vol. 56, no. 3, pp. 354–363, Jan. 2010.

[10] R. C. Preston, A. Shaw, and B. Zeqiri, "Prediction of in situ exposure to ultrasound: a proposed standard experimental method," *Ultrasound Med. Biol.*, vol. 17, no. 4, pp. 333–339, 1991.

[11] R. C. Preston, A. Shaw, and B. Zeqiri, "Prediction of in situ exposure to ultrasound: an acoustical attenuation method," *Ultrasound Med. Biol.*, vol. 17, no. 4, pp. 317–332, 1991.

[12] T. L. Szabo, F. Clougherty, and C. Grossman, "Effects on nonlinearity on the estimation of in situ values of acoustic output parameters," *J. Ultrasound Med. Off. J. Am. Inst. Ultrasound Med.*, vol. 18, no. 1, pp. 33–41, Jan. 1999.

[13] WFUMB, "WFUMB Symposium on Safety and Standardisation in Medical Ultrasound. Issues and Recommendations Regarding Thermal Mechanisms for

Biological Effects of Ultrasound. Hornbaek, Denmark, 30 August-1 September 1991," *Ultrasound Med. Biol.*, vol. 18, no. 9, pp. 731–810, 1992.

[14] T. Christopher and E. L. Carstensen, "Finite amplitude distortion and its relationship to linear derating formulae for diagnostic ultrasound systems," *Ultrasound Med. Biol.*, vol. 22, no. 8, pp. 1103–1116, 1996.

[15] D. R. Bacon, "Prediction of in situ exposure to ultrasound: an improved method," *Ultrasound Med. Biol.*, vol. 15, no. 4, pp. 355–361, 1989.

[16] F. A. Duck, "Nonlinear acoustics in diagnostic ultrasound," *Ultrasound Med. Biol.*, vol. 28, no. 1, pp. 1–18, Jan. 2002.

[17] J. C. Bamber, M. J. Fry, C. R. Hill, and F. Dunn, "Ultrasonic attenuation and backscattering by mammalian organs as a function of time after excision," *Ultrasound Med. Biol.*, vol. 3, no. 1, pp. 15–20, 1977.

[18] S. A. Goss, R. L. Johnston, and F. Dunn, "Comprehensive compilation of empirical ultrasonic properties of mammalian tissues," *J. Acoust. Soc. Am.*, vol. 64, no. 2, pp. 423–457, Aug. 1978.

[19] R. C. Chivers and C. R. Hill, "Ultrasonic attenuation in human tissue," *Ultrasound Med. Biol.*, vol. 2, no. 1, pp. 25–29, Oct. 1975.

[20] N. F. Maklad, J. Ophir, and V. Balsara, "Attenuation of ultrasound in normal liver and diffuse liver disease in vivo," *Ultrason. Imaging*, vol. 6, no. 2, pp. 117–125, Apr. 1984.

[21] K. J. Parker, M. S. Asztely, R. M. Lerner, E. A. Schenk, and R. C. Waag, "In-vivo measurements of ultrasound attenuation in normal or diseased liver," *Ultrasound Med. Biol.*, vol. 14, no. 2, pp. 127–136, 1988.

[22] F. A. Duck, "Acoustic properties of tissue at ultrasonic frequencies," in *Physical properties of tissue : a comprehensive reference book*, London; San Diego: Academic Press, 1990.

[23] J. Ophir and P. Jaeger, "Spectral shifts of ultrasonic propagation through media with nonlinear dispersive attenuation," *Ultrason. Imaging*, vol. 4, no. 3, pp. 282–289, Jul. 1982.

[24] F. Dunn, P. D. Edmonds, and W. Fry, "Absorption and Dispersion of Ultrasound in Biological Media," in *Biological engineering.*, H. P. Schwan, Ed. New York: McGraw-Hill, 1969.

[25] R. V. Khokhlov and E. A. Zabolotskaya, "Quasi-plane waves in the non- linear acoustics of confined beams," *Sov Phys Acoust*, vol. 15, pp. 35–40, 1969.

[26] V. P. Kuznetsov, "Equation of nonlinear acoustics," *Sov Phys Acoust*, vol. 16, pp. 467–470, 1970.

[27] M. A. Averkiou and M. F. Hamilton, "Nonlinear distortion of short pulses radiated by plane and focused circular pistons.," *J. Acoust. Soc. Am.*, vol. 102, no. 5, pp. 2539–48, 1997.

[28] Y.-S. Lee and M. F. Hamilton, "Time-domain modeling of pulsed finite-amplitude sound beams," *J. Acoust. Soc. Am.*, vol. 97, no. 2, pp. 906–917, 1995.

[29] M.-L. Izamis, A. Efstathiades, C. Keravnou, E. L. Leen, and M. A. Averkiou, "Dynamic contrast-enhanced ultrasound of slaughterhouse porcine livers in machine perfusion," *Ultrasound Med. Biol.*, vol. 40, no. 9, pp. 2217–2230, Sep. 2014.

[30] M. F. Hamilton and D. T. Blackstock, *Nonlinear acoustics*. San Diego, CA: Academic Press, 1998.

[31] V. Zderic, A. Keshavarzi, M. A. Andrew, S. Vaezy, and R. W. Martin, "Attenuation of porcine tissues in vivo after high-intensity ultrasound treatment," *Ultrasound Med. Biol.*, vol. 30, no. 1, pp. 61–66, Jan. 2004.

[32] Y. Fujii, N. Taniguchi, K. Itoh, K. Shigeta, Y. Wang, J.-W. Tsao, K. Kumasaki, and T. Itoh, "A new method for attenuation coefficient measurement in the liver: comparison with the spectral shift central frequency method," *J. Ultrasound Med. Off. J. Am. Inst. Ultrasound Med.*, vol. 21, no. 7, pp. 783–788, Jul. 2002.

[33] B. S. Garra, T. H. Shawker, M. Nassi, and M. A. Russell, "Ultrasound attenuation measurements of the liver in vivo using a commercial sector scanner," *Ultrason. Imaging*, vol. 6, no. 4, pp. 396–407, Oct. 1984.

[34] T. Lin, J. Ophir, and G. Potter, "Frequency-dependent ultrasonic differentiation of normal and diffusely diseased liver," *J. Acoust. Soc. Am.*, vol. 82, no. 4, pp. 1131–1138, Oct. 1987.

[35] K. J. Parker, "Attenuation measurement uncertainties caused by speckle statistics," *J. Acoust. Soc. Am.*, vol. 80, no. 3, pp. 727–734, Sep. 1986.

[36] I. Lentacker, I. De Cock, R. Deckers, S. C. De Smedt, and C. T. W. Moonen, "Understanding ultrasound induced sonoporation: definitions and underlying mechanisms," *Adv. Drug Deliv. Rev.*, Nov. 2013.

4 Accurate measurement of microbubble response to ultrasound with a diagnostic ultrasound scanner

Ultrasound and microbubbles are often used to enhance drug delivery and the suggested mechanisms are extravasation and sonoporation. Drug delivery schemes with ultrasound and microbubbles at both low and high acoustic amplitudes have been suggested. A diagnostic ultrasound scanner may play a double role as both an imaging and a therapy device. It was not possible to accurately measure microbubble response with an ultrasound scanner for a large range of acoustic pressures and microbubble concentrations up to now, mainly due to signal saturation issues. A method for continuously adjusting the receive gain of a scanner and limiting signal saturation was developed in order to accurately measure backscattered echoes from microbubbles for Mechanical Index (MI) up to 2.1. The intensity of backscattered echoes from microbubbles increased quarticly with MI without reaching any limit. The signal intensity from microbubbles was found to be linear with concentration at both low and high MIs. However, at very high concentrations acoustic shadowing occurs which limits the delivered acoustic pressure in deeper areas. The contrast to tissue ratio was also measured and found to stay constant with MI. These results can be used to better guide drug delivery approaches and to also develop imaging techniques for therapy procedures.

Published as: C.P. Keravnou, C. Mannaris, and M. Averkiou, “Accurate measurement of microbubble response to ultrasound with a diagnostic ultrasound scanner,” *IEEE Trans. Ultrason. Ferroelectr. Freq. Control*, vol. 62, no. 1, pp. 176–184, January 2015.

4.1 Introduction

Ultrasound contrast agents (UCAs) are micron-sized gas filled bubbles stabilized with a lipid or polymeric shell. Delivered intravenously, UCAs are considered a true blood-pool agent as they are small enough to pass through the alveolar–capillary barrier of the lungs and large enough to stay within the circulation. The high echogenicity of microbubbles compared to that of red blood cells is used to enhance image contrast in diagnostic ultrasound. Today, dynamic contrast enhanced ultrasound (DCEUS) is used in the clinic to image and quantify the perfusion of organs by depicting the macro- and microcirculation [1]–[4]. UCAs have been used in various clinical applications including cardiology [5], oncology [6], [7], and molecular imaging [8]. Recently interest has shifted towards the use of UCAs in therapeutic applications such as gene and DNA transfection [9], [10], thrombolysis [11], tissue ablation [12] and targeted drug delivery [13]–[16].

A key characteristic of microbubble behavior is that when interrogated with ultrasound pulses they undergo nonlinear oscillations and produce nonlinear scattering. The backscattered ultrasound contains harmonics, sub-harmonics and ultra-harmonics which are being utilized in nonlinear imaging methods like pulse inversion [17], [18] and power modulation [19], [20] which detect signals from harmonic frequencies and cancel out the linear tissue response. As a result, contrast-specific images are formed where only areas perfused with UCAs appear bright whereas everything else appears black. Since the image intensity of a given region is proportional to the amount of UCAs present [21], quantification of the perfusion is possible.

At high acoustic pressures [Mechanical Index (MI) > 0.5], violent destruction of the microbubbles occurs with even the possibility of inertial cavitation [22]–[24] and the formation of high velocity micro-jets [25]. These physical phenomena have been linked to an increased therapeutic effect due to enhanced extravasation and alteration of the cell membrane permeability, a process referred to as sonoporation [26]–[29].

Diagnostic ultrasound together with UCAs may be used to induce sonoporation. Several preclinical reports on gene and drug delivery [30]–[32], sonothrombolysis [33], and blood brain barrier opening [34] with the use of diagnostic ultrasound and microbubbles have been published. A clinical pilot study for the treatment of pancreatic cancer combining a commercial ultrasound scanner with UCAs has also been reported [35].

Ultrasound scanners have been used in the past as a research tool to investigate bubble dynamics. Lampaskis et al. [21] investigated the relationship between image intensity and microbubbles concentration for SonoVue (Bracco, S.P.A., Milan, Italy) at low MI. They demonstrated a linear relationship between linearized image intensity and contrast agent concentration. Sboros et al. [36] reported on the backscatter of UCA suspensions as a function of concentration and pressure using Definity (DuPont Pharmaceutical, Waltham, MA) and Quantison (Quadrant Healthcare, Nottingham, UK) contrast agents and MIs <1. Hung et al. [37] quantified the destruction effects of different MIs (up to MI=1) *in-vivo* using SonoVue microbubbles.

When microbubble properties are investigated using a diagnostic ultrasound scanner, signal saturation can be a problem for quantification of time-intensity curves (TICs) [21], [37]–[39]. The dynamic range of the backscattered signals varies dramatically depending on the bubble concentration and the MI used. Typically, to image the small signals from the microcirculation, high receive gains are used and this results in signal saturation in areas of larger vessels with higher bubble concentrations. If low receive gains are used, then the small signals from the microcirculation are not detected. This problem becomes even worse at higher MI's which are typically used for therapeutic applications. If not taken into consideration, signal saturation may lead to erroneous results and false conclusions [38], [40].

In this work, a diagnostic ultrasound scanner was used to study the backscatter echoes of BR14 microbubbles (Bracco S.P.A., Milan, Italy) [41] as a function of pressure and concentration in a tissue flow phantom. The question of microbubble response with increasing acoustic amplitude is addressed. Signal saturation with increasing pressure and bubble concentration, often encountered with commercial scanners, was carefully avoided by continuously adjusting the scanner's 2D analog gain. The acoustic pressure was varied from 0.06 MPa up to 2.6 MPa peak negative pressure (above FDA diagnostic limit) while various concentrations, were considered. The intensity-concentration relationship was investigated at both low and high pressures. The contrast to tissue ratio (CTR) as a function of MI and now without the effect of signal saturation was calculated for a range of concentrations and it was found to be constant for the MI range considered. Knowledge of accurate bubble response to ultrasound is critical in therapeutic applications such as sonoporation.

4.2 Materials and methods

4.2.1 Experimental setup

Imaging of the microbubbles and measurements of their response to ultrasound were carried out using the flow phantom setup shown in Fig. 4.1. A freshly prepared microbubble solution was placed in a glass beaker and was continuously mixed with a magnetic stirrer. A peristaltic pump (Model 7524-45, Masterflex; Cole-Palmer, Vernon Hills, IL, USA) was used to draw the solution into an 8-mm wall-less tube of a tissue mimicking flow phantom (Model 523A; ATS Laboratories Inc., Bridgeport, CT, USA) with a flow rate of 200 ml/min. An iU-22 diagnostic ultrasound scanner (Philips Medical Systems, Bothell, WA) was used to interrogate and image the microbubbles.

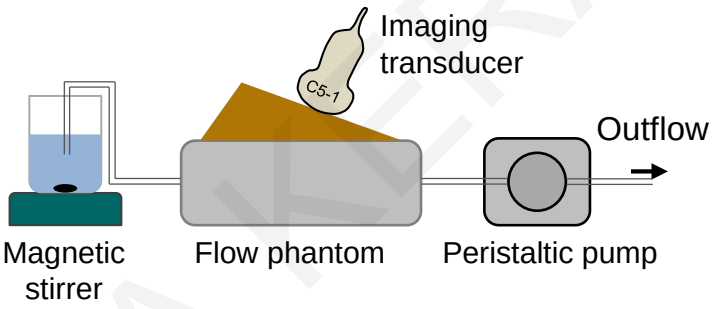

Figure 4.1: Schematic representation of the flow phantom setup.

4.2.2 Microbubbles

BR14 microbubbles were used throughout this work. The microbubbles were prepared according to the manufacturer's specifications. A total of 4 microbubble solutions were prepared with concentrations 0.01‰, 0.05‰, 0.1‰, 0.3‰. The concentrations are given in milliliters of contrast agent per liter of deionized water (e.g. 0.01‰ = 0.01 ml UCA / liter of DI water) and they cover a very wide range of concentrations often used in clinical cases. It is possible though with these microbubble concentrations to encounter the nonlinear propagation artifact [42], [43], and acoustic shadowing [44].

The total experiment time was held below one hour following vial reconstitution in order to limit microbubble deterioration to an absolute minimum. Vial-to-vial reproducibility was addressed by repeating the experiments 3 times using different vials and the results are presented as mean ± standard error of the mean.

4.2.3 Ultrasound scanner settings and imaging

Microbubble interrogation and imaging was performed with a C5-1 probe (curve-linear array) of the Phillips iU-22 diagnostic ultrasound scanner. The penetration setting in harmonic mode (HPEN) was used where a 3.5 cycle hamming windowed pulse with center frequency of 1.5 MHz was transmitted (largest duration at lowest frequency available on B-mode on the C5-1 probe). A single pulse scheme (we avoided pulse inversion) was chosen to eliminate any effects due to motion or destruction of the microbubbles between multiple pulses. The receive center frequency was 3 MHz. The MI was varied from 0.05 to 2.1 (see Table 4.1) which corresponds to peak negative pressures of 0.06 MPa to 2.6 MPa. Research software on the iU22 allowed us to increase the MI beyond the maximum FDA limit of 1.9. The frame rate was set at 1.0 Hz, to ensure that the tube in the image plane was refreshed with new bubbles in every frame.

4.2.4 Image quantification and gain adjustment procedure

Video loops of 8 images (taken over 8 s) were captured for each MI. The quantification software QLAB (Philips Medical Systems, Bothell, WA) was used to measure backscattered signal intensity by placing a region of interest (ROI) at the top of the phantom tube (to avoid acoustic shadowing if present) and calculating the average backscatter intensity from that region. In order to check for the possibility of acoustic shadowing, a ROI at the bottom of the phantom tube was also placed and the analysis was repeated.

To avoid signal saturation in quantification, the compression (dynamic range) was set to the maximum value and a specific 2D gain setting for each MI was carefully selected making sure that the image of the microbubbles was not very close to the maximum value of the color map. In order to accurately select the 2D gain and avoid saturation the following procedure was followed. Three values for 2D gain that differed by 6 dB were selected and the image intensity of a fixed ROI placed in the flow phantom tube in the presence of microbubbles was noted. If the image intensity of each ROI did not differ by 6 dB (due to signal saturation) the high gain was dropped and another 2D gain value 6 dB less than the previous lowest value was selected. If the image intensity of the ROI differed by 6 dB for all 2D gain settings then the middle value was selected as the reference gain for that MI. For example, 3 images were collected at 64, 70 and 76 dB gain and if the ROI

intensity differed by 6 dB between them, then 70 dB was the selected gain. A list of the 2D gain settings chosen for each MI is shown in Table 4.1.

During the analysis of the data an inverse adjustment to a chosen reference 2D gain value was made so that the results from different gains could be plotted together. If for example, at MI=0.1 the 2D gain was adjusted from a reference 80 dB to 70 dB to avoid signal saturation, then during the analysis of the results, the measured intensity data was increased by 10 dB in order to match the reference value of 80 dB. Similarly, MI=0.3 was increased by 26 dB, MI 0.5 by 32dB and so on (see Table 4.1).

MI	**Gain [dB] (C≤0. 1‰)**	**Gain [dB] (C>0. 1‰)**
<0.05	80	77
0.1	70	67
0.3	54	51
0.5	48	45
0.6	44	41
0.8	41	38
1.0	38	35
1.3	34	31
1.6	33	30
2.1	31	28

Table 4.1: Optimal 2D gain per MI to avoid signal saturation for concentrations C≤0.1‰ and for C>0.1‰.

The gain adjustment method is further explained and demonstrated in Figs. 4.2 and 4.3. In Fig. 4.2(a-c) images of the flow phantom in the absence of microbubbles at MIs 0.6, 1.0 and 2.1 with a fixed 2D gain of 44 dB are shown. Images at MIs 0.8, 1.3, and 1.6 also captured but not shown here. A region of interest is chosen in the tissue and its average intensity (AIU: arbitrary intensity units) is measured as a function of MI as shown by the solid line with cross-hair markers in Fig. 4.3. The same procedure is followed at a higher 2D gain (56 dB) and the images acquired are shown in Fig. 4.2(d-e). The corresponding measured intensity-MI relation is shown in Fig. 4.3(solid line with square markers). When

each intensity point on the 44 dB curve is given an additional 12 dB, the line labeled as "Gain 56 corrected" (dashed line with circle markers) in Fig. 4.3 is obtained. Good agreement between the measured and corrected 56 dB 2D gain values is obtained. The measured intensities can be adjusted to any reference value as long as there is no signal saturation. For the work presented here, the maximum 2D gain (80 dB) was chosen as the reference point.

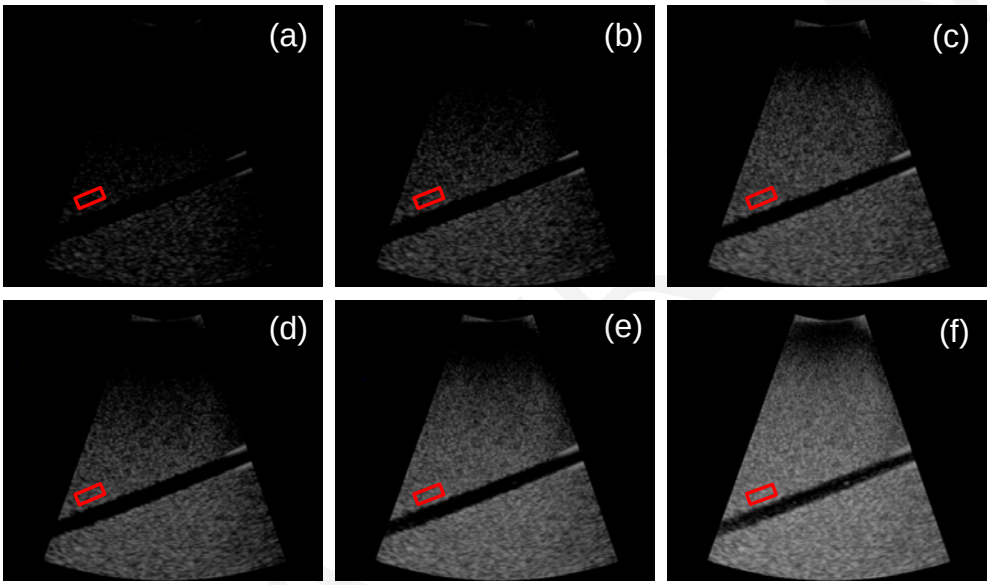

Figure 4.2: Flow phantom images without UCAs. (a-c) 2D Gain set at 44 dB for MI=0.6, 1.0 and 2.1 respectively. (d-f) 2D Gain set at 56 dB for MI=0.6, 1.0 and 2.1 respectively.

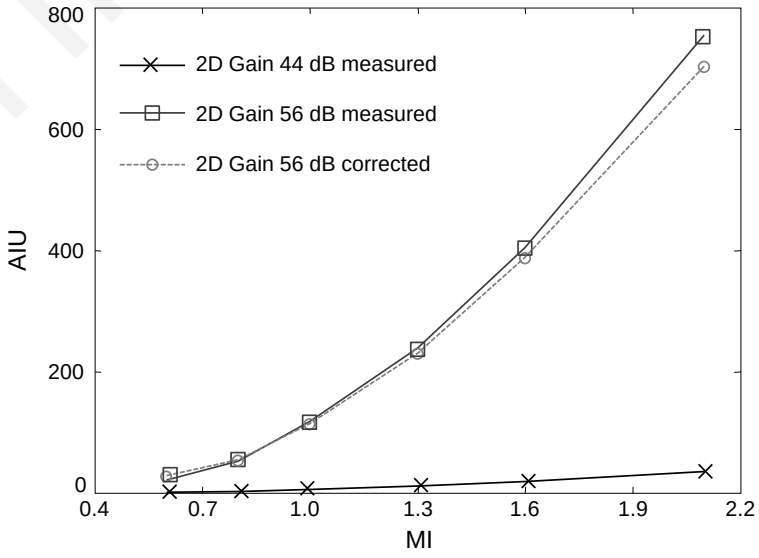

Figure 4.3: Backscatter tissue signal intensity (AIU: arbitrary intensity units) as a function of MI measured at two different 2D Gains (56 and 44 dB) and intensity collected at 44 dB and adjusted to 56 dB.

4.3 Results

In Fig. 4.4 images of the phantom vessel filled with microbubbles are shown for multiple gain settings. In Fig. 4.4(a-c) images of microbubbles acquired with MIs 0.1, 1.0 and 2.1 respectively are shown. The concentration was 0.1‰ and the 2D gain was held fixed at the default value of 70 dB. While the image in Fig. 4.4(a) offers a clean signal with a high CTR, the bubble backscatter signal in (b) and (c) is saturated (very close to being all white) and the CTR is significantly reduced (the vessel is not easily separated from the tissue). Images of the same microbubble solution under the same pressures are shown in Fig. 4.4(d-f) with the 2D gain adjusted accordingly. For MI 0.1 the gain was kept at 70 dB, but was reduced to 38 dB for MI 1.0 and 31 dB for MI 2.1 thus limiting saturation and increasing the CTR.

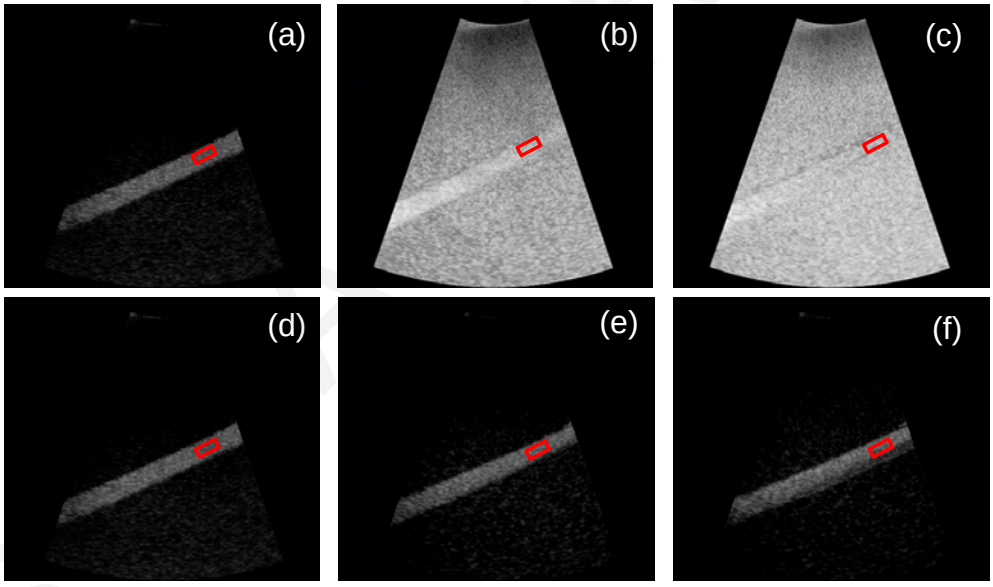

Figure 4.4: Flow phantom images at MI (a) 0.1, (b) 1.0, and (c) 2.1 at constant 2D Gain (70 dB). The images in (d), (e), and (f) are taken at their optimal gain (70, 38, and 31 dB respectively) to avoid saturation. The microbubble concentration is 0.1‰.

A comparison of the microbubble backscatter intensity as a function of MI with and without the gain adjustment method is made in Fig. 4.5. The measured intensity with the 2D gain fixed at 80 dB is shown with the solid line, while the dashed line presents the results after the gain adjustment method was applied. A logarithmic scale was used in this plot in order to better accommodate the large dynamic range of the intensities obtained. With a fixed 2D gain of 80 dB, signal saturation begins as early as MI 0.3 and the signal

becomes completely saturated at MI>0.5 where further increase in pressure does not result in any increase in backscatter intensity. When the proposed 2D gain adjustment method is applied however, saturation is eliminated and the true microbubble response to increasing amplitude can be obtained.

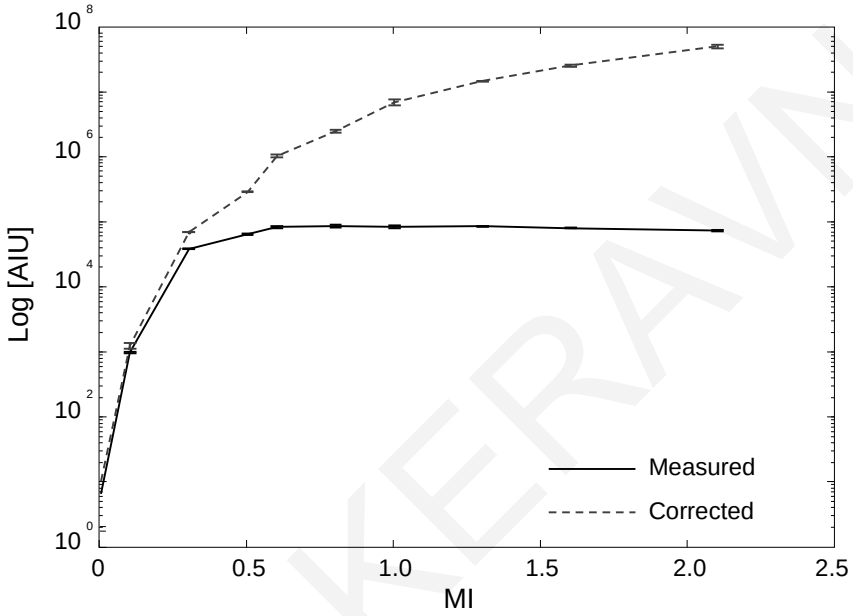

Figure 4.5: Contrast microbubble intensity as a function of MI. Measurements with 2D Gain fixed at 80 dB (solid line) compared to corrected values using the 2D Gain adjustment method (dashed line) for microbubble concentration of 0.1‰.

Figure 4.6(a) shows the backscattered intensity as a function of MI for microbubble concentrations 0.1‰, 0.05‰, and 0.01‰. The intensity values shown are with reference to 80 dB. Figure 4.6(b) displays the backscattered intensity in log-log scale as a function of MI for the same microbubble concentrations as Fig. 4.6(a). Since we were measuring second harmonic amplitude of the backscattered intensity, a fourth order polynomial equation was fit to the data and a quartic increase (fourth order) of backscattered signal intensity with MI is observed.

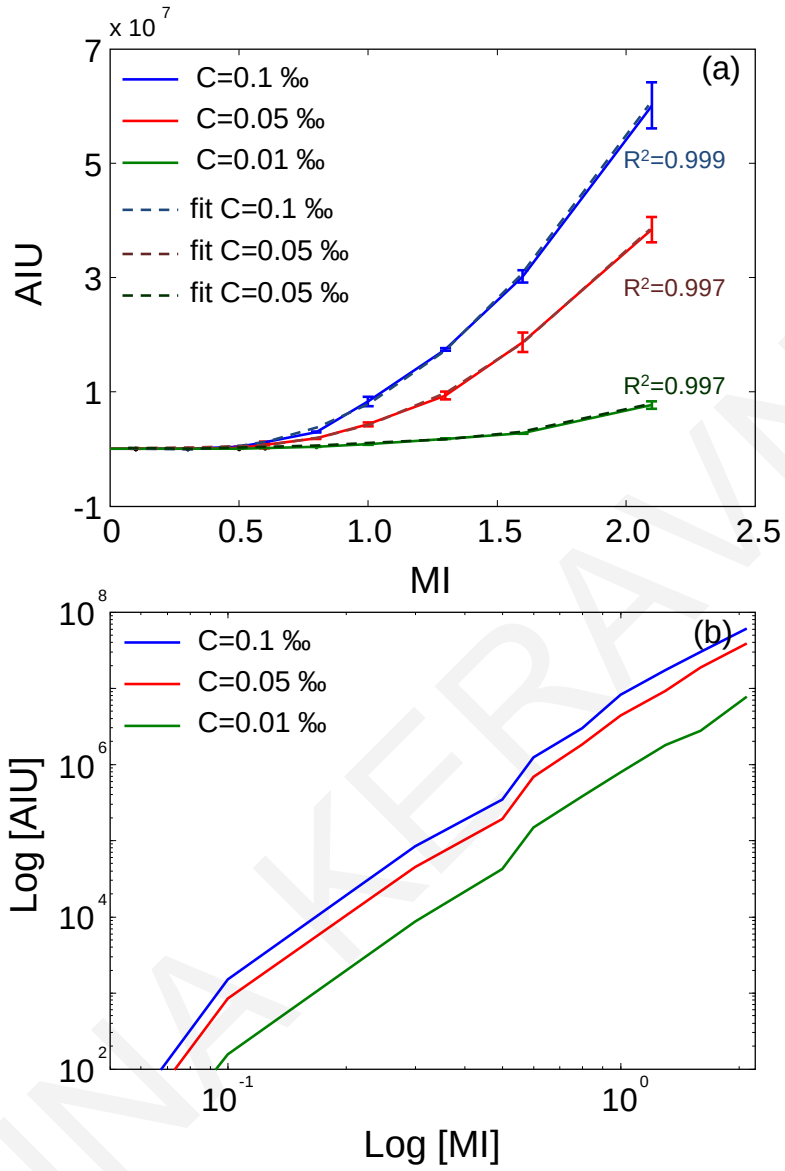

Figure 4.6: (a) Bubble backscattered signal intensity as a function of MI for 3 different concentrations. A fourth order polynomial equation was fit to the data with R^2 >0.99 for all cases. A quartic increase of intensity with acoustic pressure increase is being observed. (b) Bubble backscattered intensity plotted in log-log scale as a function of MI for the same microbubble concentrations as (a). Slope was found to be ≈3.6 for all lines. All values are adjusted to a reference 2D Gain of 80 dB.

The backscattered intensity as a function of concentration for three different MIs (0.1, 1.0 and 2.1) is shown in Fig. 4.7. At MI=0.1, an almost linear relationship is observed, confirming previously published results [21]. There is some deviation from linearity at higher concentrations (not shown here). As the pressure increases however [Fig. 4.7(b, c)], the deviation from linearity occurs at a lower concentrations.

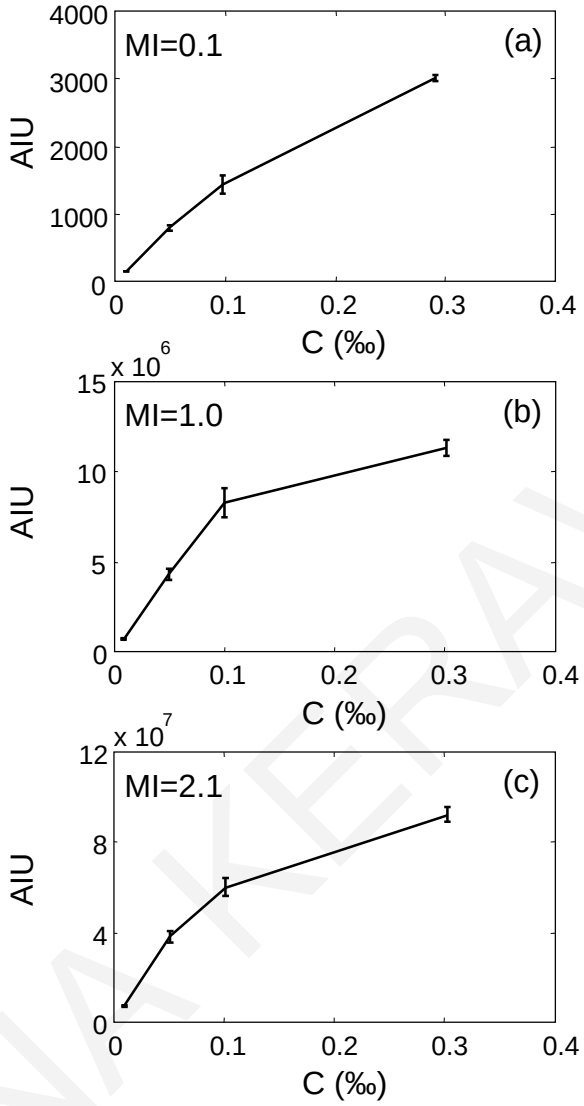

Figure 4.7: Intensity as a function of microbubble concentration for 3 different MIs. (a) MI=0.1, (b) MI=1.0 and (c) MI=2.1, adjusted to a reference 2D Gain of 80 dB.

To be able to demonstrate the effect of acoustic shadowing, the analysis of the signal from the vessel was repeated by placing two ROIs one at the top and one at the bottom of the tube as seen in Fig. 4.8(a-d). The backscattered intensity in logarithmic scale as a function of MI for the two ROIs is shown in Fig. 4.8(e-h) for microbubble concentrations 0.01‰, 0.05‰, 0.1‰, and 0.3‰ respectively. The solid lines represent the top ROIs and the dashed lines the bottom ROIs. At low MIs we observe that the signal intensities from the two regions are very similar. As the pressure increases the backscatter intensity from the top region becomes significantly greater than the backscatter intensity from the bottom region. This difference is greater as the concentration increases and it is

observed at a lower MI. At concentration 0.3‰, the deviation is observed as low as MI 0.15 while for concentration 0.01‰ there is no difference and two lines coincide though the entire MI range.

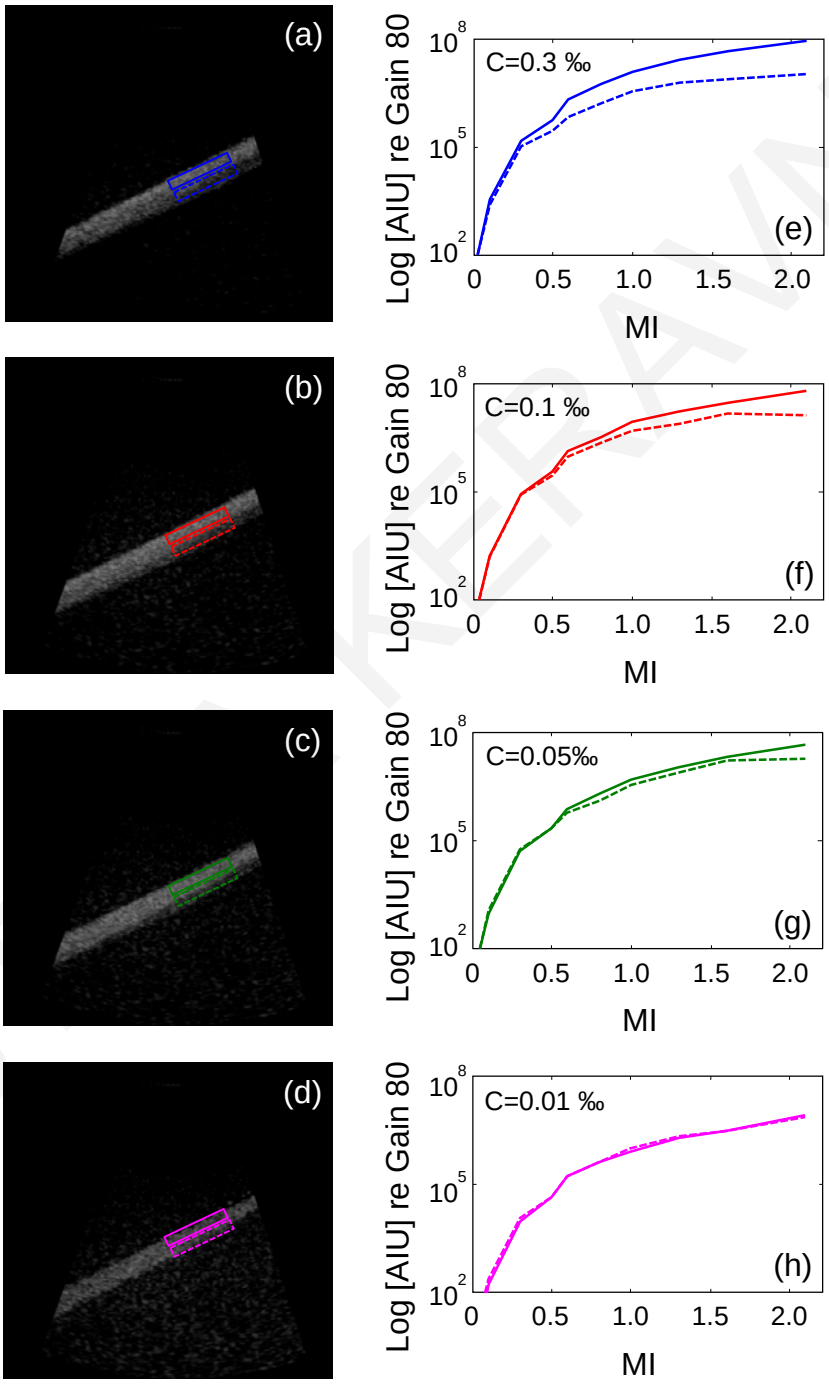

Figure 4.8: Images taken at MI=2.1 of the flow tube (a-d) and bubble backscattered signal intensity in logarithmic scale as a function of mechanical index (e-h) from 2 ROIs; one at the top and one at the bottom of the flow tube. All intensity plots are adjusted to a reference 2D Gain of 80 dB.

A comparison between tissue nonlinear echoes resulting from nonlinear propagation and microbubble backscattered nonlinear signal as a function of MI is shown in Fig. 4.9. The ROIs which were used to extract the signal for this plot (one in tissue and one in the phantom vessel) were placed at the same image depth. The dashed line shows the tissue and the solid line the microbubble signal intensity. Both the tissue and bubble signals increase with the same rate with MI. The CTR, which is the difference between the bubble and tissue signals (in dB), is shown in dashed line. Surprisingly, constant (a small increase of only 3 dB) CTRs are observed with increasing MI. The same trend for CTR was also observed for all microbubble concentrations used in this work.

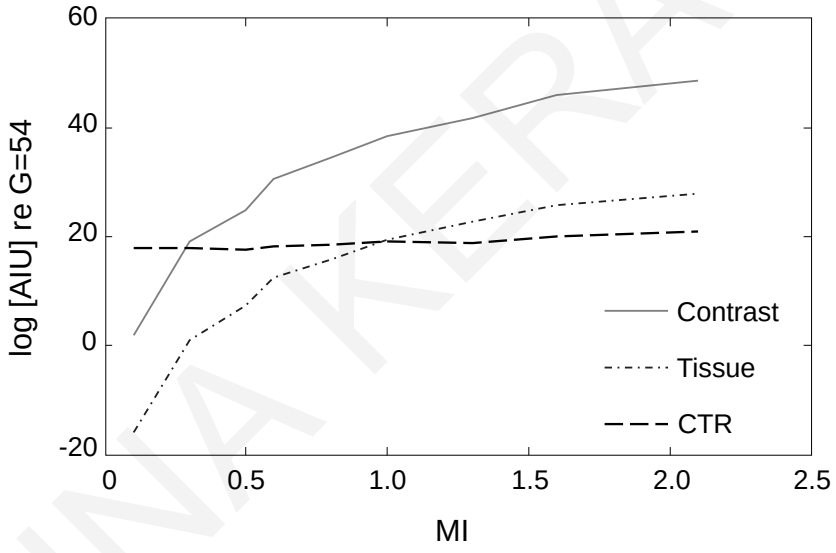

Figure 4.9: Tissue (dotted line) and contrast microbubbles (solid line) backscattered signal intensity at the second harmonic as a function of MI. The reference 2D Gain is 54 dB and the concentration 0.05‰. Contrast to tissue ratio (CTR), calculated as the difference in dB between microbubbles and tissue intensity is shown in dashed line.

4.4 Discussion

In this work, a diagnostic ultrasound scanner was used to accurately measure microbubble backscattering produced with large range of MIs (0.05-2.1). Despite the fact that this is a relatively simple task, it has not been addressed in the past and one of the main obstacles was signal saturation often present in diagnostic ultrasound scanners. The question of how the microbubbles behave as the MI is increased (even above the FDA imaging limit) was addressed. It was observed that up to acoustic pressures of 2.6 MPa, the intensity backscattered signals from microbubbles increased quarticly in agreement

with previously published results [45]. Specifically, in the work of Shi and Forsberg [45], the measured (with a single element transducer setup) second harmonic of the backscattered signal as a function of acoustic pressure plotted in a log-log scale could be fitted to curves with slopes of 1.8-1.9 and our results of Fig.4.6(b) show a slope of 3.6 (for intensity). Those results were in good agreement with theoretical predictions [46], [47] showing that the second harmonic bubble response amplitude is proportional to the square of the acoustic amplitude. Sboros et al. [48] reported a linear increase in backscattered intensity with increasing acoustic pressure.

A key factor in being able to accurately record backscattered signals at very high pressures was the 2D gain adjustment procedure. Knowledge of bubble response to a range of acoustic pressures is important when studying therapeutic applications of microbubbles and ultrasound such as sonoporation, sonothrombolysis, and gene transfection. Being able to image microbubbles in response to high excitation amplitudes might be beneficial when considering the various sonoporation hypothesis relying on phenomena such as microjet formation and cell membrane disruption [49]. Additionally, with a variety of drug loaded microbubbles in development, accurate measurements of backscattered echoes will be important in both evaluating and differentiating them. Another important utility of imaging in therapeutic applications is the control of the destruction process and its balance with microbubble supply (e.g., estimating the specific rate for continuous infusion).

Figure 4.7(a) shows a linear dependence of backscattered intensity as a function of bubble concentration at low MI which is in agreement with previously published results [21]. However at higher MIs [MI=1 in Fig. 4.7(b) and MI=2.1 in Fig. 4.7(c)] there is a deviation from linearity in the intensity–concentration relationship. Since signal saturation was limited with the method of continuously adjusting the analog gain and accounting for it in the quantification software, the only other possible cause of deviation from linearity in the intensity–concentration relationship is acoustic shadowing. It was confirmed from the results of Fig. 4.8 that acoustic shadowing was indeed present, as the signal from the top ROI increased quarticly with MI while the signal from the bottom ROI plateaued at a certain value. As expected, acoustic shadowing increased with concentration and so did the difference in backscattered intensity between the top and bottom ROI [Fig. 4.8 (e)-(h)]. Additionally, according to the results of Fig. 4.8, shadowing also increases with increasing MI. It was observed that the differences between the top and bottom ROI for a given

concentration were increased with MI. This result is in agreement with previously published results [50], [51] that show a linear increase of attenuation as pressure increases.

Nonlinear propagation in tissue takes place as the transmitted pressure increases [52], [53]. The tissue harmonics are mixed with the microbubble harmonics at the higher MIs. The careful and accurate measurement of CTR has revealed that there is not an optimal MI at which microbubbles may be imaged, contrary to previous perception [15]. The low MI is chosen today in order to avoid bubble destruction, but microbubbles may be imaged equally well at larger MIs with triggered imaging. Real-time low MI imaging has become the method of choice for clinical ultrasound contrast imaging, due to its ease of use (real time scanning) and specificity (displays only bubble signals while eliminating tissue). However, low MI imaging is often penetration (and signal) limited, for example in liver cirrhosis patients. High MI triggered imaging on the other hand, is very specific due to the fact that it displays the bubble destruction signal and is less penetration limited due to the higher MI's utilized. However it is also harder to use due to the need to image only intermittently (microbubbles are destroyed within a few frames in an imaging plane and then we must wait for microbubble replenishment of that plane). According to the results in Fig. 4.9, the general trend is that CTR is constant and very slightly (only 3 dB in the whole MI range) increasing with MI even at higher than diagnostic imaging MIs. For example, in drug delivery applications at MIs that cause bubble destruction, good triggered images (in order to allow for microbubble replenishment in the imaging plane) with nonlinear techniques (e.g. harmonic imaging) may be formed by simply thresholding the tissue signals due to nonlinear propagation. Based on these results, the only benefit of using a low MI is for enabling real-time imaging but it does not offer any increased CTR compared to using high MI.

An interesting outcome of our results is that both tissue and microbubble nonlinear signals continue to increase at the same rate in the range of MIs considered. The tissue nonlinear signal from Fig. 4.9 is compared with a theoretical prediction (performed at each MI), based on the KZK equation [54], [55] in Fig. 4.10. The nonlinear propagation in a tissue-like medium of a sound beam from a circular focused source was simulated. The excellent agreement of the measurement with theoretical predictions suggests once more that our method of adjusting the 2D gain to avoid signal saturation enables the true representation of the tissue response.

Nonlinear propagation can affect microbubble excitation pulses since at high pressures the propagated pulse gets distorted and also contains harmonic components in addition to the fundamental frequency. A change of the excitation pulse to include harmonic components has an impact on the microbubble response and has been briefly addressed before [56], [57], but it must be revisited again now when large amplitude pulses are used in therapeutic applications of ultrasound and microbubbles.

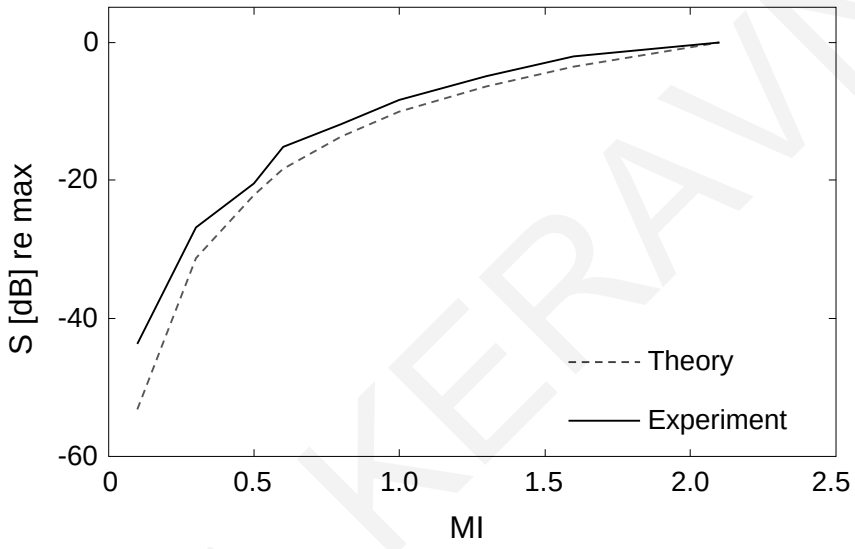

Figure 4.10: Theoretical prediction (dashed line) and measurements (solid line) of second harmonic echoes from tissue as a function of increasing amplitude.

4.5 Conclusions

A method for accurately and continuously adjusting the receive gain of ultrasound scanners and accounting for it in the quantification software in order to effectively limit signal saturation was developed. A quartic (fourth power) relationship of backscattered intensity with acoustic excitation pressures for up to MI=2.1 for BR14 was measured in a flow phantom. Contrast microbubbles produced higher responses with higher pressures without reaching any plateau. The intensity of the microbubbles echoes increased with concentration both at low MI, as previously measured, but also at high MIs. The contrast to tissue ratio was measured and found to slightly increase with MI (~3 dB) for all the range of MIs considered, thus allowing for imaging approaches in therapeutic procedures that use MIs above the bubble destruction threshold.

REFERENCES

[1] D. Cosgrove and N. Lassau, “Imaging of perfusion using ultrasound,” *Eur. J. Nucl. Med. Mol. Imaging*, vol. 37 Suppl 1, pp. S65–85, Aug. 2010.

[2] V. Sboros and M.-X. Tang, “The assessment of microvascular flow and tissue perfusion using ultrasound imaging,” *Proc. Inst. Mech. Eng. [H]*, vol. 224, no. 2, pp. 273–290, 2010.

[3] S. R. Wilson and P. N. Burns, “Microbubble-enhanced US in body imaging: what role?,” *Radiology*, vol. 257, no. 1, pp. 24–39, Oct. 2010.

[4] M. Averkiou, M. Lampaskis, K. Kyriakopoulou, D. Skarlos, G. Klouvas, C. Strouthos, and E. Leen, “Quantification of tumor microvascularity with respiratory gated contrast enhanced ultrasound for monitoring therapy,” *Ultrasound Med. Biol.*, vol. 36, no. 1, pp. 68–77, Jan. 2010.

[5] K. Wei, A. R. Jayaweera, S. Firoozan, A. Linka, D. M. Skyba, and S. Kaul, “Quantification of myocardial blood flow with ultrasound-induced destruction of microbubbles administered as a constant venous infusion,” *Circulation*, vol. 97, no. 5, pp. 473–483, Feb. 1998.

[6] S. R. Wilson and P. N. Burns, “Liver mass evaluation with ultrasound: the impact of microbubble contrast agents and pulse inversion imaging,” *Semin. Liver Dis.*, vol. 21, no. 2, pp. 147–159, May 2001.

[7] E. Leen, J. A. Goldberg, W. J. Angerson, and C. S. McArdle, “Potential role of doppler perfusion index in selection of patients with colorectal cancer for adjuvant chemotherapy,” *Lancet*, vol. 355, no. 9197, pp. 34–37, Jan. 2000.

[8] J. R. Lindner, “Microbubbles in medical imaging: current applications and future directions,” *Nat. Rev. Drug Discov.*, vol. 3, no. 6, pp. 527–532, Jun. 2004.

[9] S. Mehier-Humbert, F. Yan, P. Frinking, M. Schneider, R. H. Guy, and T. Bettinger, “Ultrasound-mediated gene delivery: influence of contrast agent on transfection,” *Bioconjug. Chem.*, vol. 18, no. 3, pp. 652–662, Jun. 2007.

[10] A. A. Rahim, S. L. Taylor, N. L. Bush, G. R. ter Haar, J. C. Bamber, and C. D. Porter, “Spatial and acoustic pressure dependence of microbubble-mediated gene delivery targeted using focused ultrasound,” *J. Gene Med.*, vol. 8, no. 11, pp. 1347–1357, Nov. 2006.

[11] C. A. Molina, M. Ribo, M. Rubiera, J. Montaner, E. Santamarina, R. Delgado-Mederos, J. F. Arenillas, R. Huertas, F. Purroy, P. Delgado, and J. Alvarez-Sabín, “Microbubble administration accelerates clot lysis during continuous 2-MHz ultrasound monitoring in stroke patients treated with intravenous tissue plasminogen activator,” *Stroke J. Cereb. Circ.*, vol. 37, no. 2, pp. 425–429, Feb. 2006.

[12] M. R. Böhmer, A. L. Klibanov, K. Tiemann, C. S. Hall, H. Gruell, and O. C. Steinbach, “Ultrasound triggered image-guided drug delivery,” *Eur. J. Radiol.*, vol. 70, no. 2, pp. 242–253, May 2009.

[13] D. B. Ellegala, H. Leong-Poi, J. E. Carpenter, A. L. Klibanov, S. Kaul, M. E. Shaffrey, J. Sklenar, and J. R. Lindner, “Imaging tumor angiogenesis with contrast ultrasound and microbubbles targeted to alpha(v)beta3,” *Circulation*, vol. 108, no. 3, pp. 336–341, Jul. 2003.

[14] G. E. R. Weller, M. K. K. Wong, R. A. Modzelewski, E. Lu, A. L. Klibanov, W. R. Wagner, and F. S. Villanueva, "Ultrasonic imaging of tumor angiogenesis using contrast microbubbles targeted via the tumor-binding peptide arginine-arginine-leucine," *Cancer Res.*, vol. 65, no. 2, pp. 533–539, Jan. 2005.

[15] J.-M. Escoffre, C. Mannaris, B. Geers, A. Novell, I. Lentacker, M. Averkiou, and A. Bouakaz, "Doxorubicin liposome-loaded microbubbles for contrast imaging and ultrasound-triggered drug delivery," *IEEE Trans. Ultrason. Ferroelectr. Freq. Control*, vol. 60, no. 1, pp. 78–87, Jan. 2013.

[16] C. Mannaris and M. A. Averkiou, "Investigation of microbubble response to long pulses used in ultrasound-enhanced drug delivery," *Ultrasound Med. Biol.*, vol. 38, no. 4, pp. 681–691, Apr. 2012.

[17] M. A. Averkiou, M. Bruce, S. Jensen, P. G. Rafter, G. A. Brock-Fisher, and J. Powers, "Pulsing schemes for the detection of nonlinear echoes from contrast microbubbles," presented at the 9th European Symposium on Ultrasound Contrast Imaging, Rotterdam, The Netherlands, 2004.

[18] D. H. Simpson, C. T. Chin, and P. N. Burns, "Pulse inversion Doppler: a new method for detecting nonlinear echoes from microbubble contrast agents," *IEEE Trans. Ultrason. Ferroelectr. Freq. Control*, vol. 46, no. 2, pp. 372–382, 1999.

[19] M. Averkiou, J. Powers, D. Skyba, M. Bruce, and S. Jensen, "Ultrasound contrast imaging research," *Ultrasound Q.*, vol. 19, no. 1, pp. 27–37, Mar. 2003.

[20] G. A. Brock-Fisher, M. K. D. Poland, and P. G. Rafter, "Means for increasing sensitivity in non-linear ultrasound imaging systems," US5577505 A, 26-Nov-1996.

[21] M. Lampaskis and M. Averkiou, "Investigation of the relationship of nonlinear backscattered ultrasound intensity with microbubble concentration at low MI," *Ultrasound Med. Biol.*, vol. 36, no. 2, pp. 306–312, Feb. 2010.

[22] R. E. Appel, "Possibility of microcavitation from diagnostic ultrasound," *IEEE Trans. Ultrason. Ferroelectr. Freq. Control*, vol. 33, no. 2, pp. 139–142, 1986.

[23] C. K. Holland and R. E. Apfel, "Thresholds for transient cavitation produced by pulsed ultrasound in a controlled nuclei environment," *J. Acoust. Soc. Am.*, vol. 88, no. 5, pp. 2059–2069, Nov. 1990.

[24] W. T. Shi, F. Forsberg, A. Tornes, J. Ostensen, and B. B. Goldberg, "Destruction of contrast microbubbles and the association with inertial cavitation," *Ultrasound Med. Biol.*, vol. 26, no. 6, pp. 1009–1019, Jul. 2000.

[25] P. Marmottant and S. Hilgenfeldt, "Controlled vesicle deformation and lysis by single oscillating bubbles," *Nature*, vol. 423, no. 6936, pp. 153–156, May 2003.

[26] M. R. Böhmer, C. H. T. Chlon, B. I. Raju, C. T. Chin, T. Shevchenko, and A. L. Klibanov, "Focused ultrasound and microbubbles for enhanced extravasation," *J. Control. Release Off. J. Control. Release Soc.*, vol. 148, no. 1, pp. 18–24, Nov. 2010.

[27] K. Kooiman, M. Emmer, M. Foppen-Harteveld, A. van Wamel, and N. de Jong, "Increasing the endothelial layer permeability through ultrasound-activated microbubbles," *IEEE Trans. Biomed. Eng.*, vol. 57, no. 1, pp. 29–32, Jan. 2010.

[28] A. Yudina, M. Lepetit-Coiffé, and C. T. W. Moonen, "Evaluation of the temporal window for drug delivery following ultrasound-mediated membrane permeability

enhancement," *Mol. Imaging Biol. MIB Off. Publ. Acad. Mol. Imaging*, vol. 13, no. 2, pp. 239–249, Apr. 2011.

[29] K. Ferrara, R. Pollard, and M. Borden, "Ultrasound microbubble contrast agents: fundamentals and application to gene and drug delivery," *Annu. Rev. Biomed. Eng.*, vol. 9, pp. 415–447, 2007.

[30] S. Chen, R. V. Shohet, R. Bekeredjian, P. Frenkel, and P. A. Grayburn, "Optimization of ultrasound parameters for cardiac gene delivery of adenoviral or plasmid deoxyribonucleic acid by ultrasound-targeted microbubble destruction," *J. Am. Coll. Cardiol.*, vol. 42, no. 2, pp. 301–308, Jul. 2003.

[31] R. Bekeredjian, S. Chen, P. A. Grayburn, and R. V. Shohet, "Augmentation of cardiac protein delivery using ultrasound targeted microbubble destruction," *Ultrasound Med. Biol.*, vol. 31, no. 5, pp. 687–691, May 2005.

[32] H. Fujii, Z. Sun, S.-H. Li, J. Wu, S. Fazel, R. D. Weisel, H. Rakowski, J. Lindner, and R.-K. Li, "Ultrasound-targeted gene delivery induces angiogenesis after a myocardial infarction in mice," *JACC Cardiovasc. Imaging*, vol. 2, no. 7, pp. 869–879, Jul. 2009.

[33] F. Xie, J. Lof, T. Matsunaga, R. Zutshi, and T. R. Porter, "Diagnostic ultrasound combined with glycoprotein IIb/IIIa-targeted microbubbles improves microvascular recovery after acute coronary thrombotic occlusions," *Circulation*, vol. 119, no. 10, pp. 1378–1385, Mar. 2009.

[34] K. F. Bing, G. P. Howles, Y. Qi, M. L. Palmeri, and K. R. Nightingale, "Blood-brain barrier (BBB) disruption using a diagnostic ultrasound scanner and Definity in Mice," *Ultrasound Med. Biol.*, vol. 35, no. 8, pp. 1298–1308, Aug. 2009.

[35] S. Kotopoulis, G. Dimcevski, O. H. Gilja, D. Hoem, and M. Postema, "Treatment of human pancreatic cancer using combined ultrasound, microbubbles, and gemcitabine: a clinical case study," *Med. Phys.*, vol. 40, no. 7, p. 072902, Jul. 2013.

[36] V. Sboros, K. V. Ramnarine, C. M. Moran, S. D. Pye, and W. N. McDicken, "Understanding the limitations of ultrasonic backscatter measurements from microbubble populations," *Phys. Med. Biol.*, vol. 47, no. 23, pp. 4287–4299, Dec. 2002.

[37] S.-H. Hung, C.-K. Yeh, T.-H. Tsai, T. Chen, and R.-C. Chen, "A simple method for quantifying ultrasound-triggered microbubble destruction," *Ultrasound Med. Biol.*, vol. 37, no. 6, pp. 949–957, Jun. 2011.

[38] T. P. Gauthier, M. A. Averkiou, and E. L. S. Leen, "Perfusion quantification using dynamic contrast-enhanced ultrasound: the impact of dynamic range and gain on time-intensity curves," *Ultrasonics*, vol. 51, no. 1, pp. 102–106, Jan. 2011.

[39] T. Schlosser, C. Pohl, S. Kuntz-Hehner, H. Omran, H. Becher, and K. Tiemann, "Echoscintigraphy: a new imaging modality for the reduction of color blooming and acoustic shadowing in contrast sonography," *Ultrasound Med. Biol.*, vol. 29, no. 7, pp. 985–991, Jul. 2003.

[40] N. de Jong, "Mechanical index," *Eur. J. Echocardiogr. J. Work. Group Echocardiogr. Eur. Soc. Cardiol.*, vol. 3, no. 1, pp. 73–74, Mar. 2002.

[41] M. Schneider, A. Broillet, P. Bussat, N. Giessinger, J. Puginier, R. Ventrone, and F. Yan, "Gray-scale liver enhancement in VX2 tumor-bearing rabbits using BR14, a

new ultrasonographic contrast agent," *Invest. Radiol.*, vol. 32, no. 7, pp. 410–417, Jul. 1997.

[42] M.-X. Tang and R. J. Eckersley, "Nonlinear propagation of ultrasound through microbubble contrast agents and implications for imaging," *IEEE Trans. Ultrason. Ferroelectr. Freq. Control*, vol. 53, no. 12, pp. 2406–2415, Dec. 2006.

[43] A. Thapar, J. Shalhoub, M. Averkiou, C. Mannaris, A. H. Davies, and E. L. S. Leen, "Dose-dependent artifact in the far wall of the carotid artery at dynamic contrast-enhanced US," *Radiology*, vol. 262, no. 2, pp. 672–679, Feb. 2012.

[44] M.-X. Tang, H. Mulvana, T. Gauthier, A. K. P. Lim, D. O. Cosgrove, R. J. Eckersley, and E. Stride, "Quantitative contrast-enhanced ultrasound imaging: a review of sources of variability," *Interface Focus*, vol. 1, no. 4, pp. 520–539, Aug. 2011.

[45] W. T. Shi and F. Forsberg, "Ultrasonic characterization of the nonlinear properties of contrast microbubbles," *Ultrasound Med. Biol.*, vol. 26, no. 1, pp. 93–104, Jan. 2000.

[46] C. C. Church, "The effects of an elastic solid surface layer on the radial pulsations of gas bubbles," *J. Acoust. Soc. Am.*, vol. 97, no. 3, pp. 1510–1521, 1995.

[47] N. de Jong, R. Cornet, and C. T. Lancée, "Higher harmonics of vibrating gas-filled microspheres. Part one: simulations," *Ultrasonics*, vol. 32, no. 6, pp. 447–453, Nov. 1994.

[48] V. Sboros, C. A. MacDonald, S. D. Pye, C. M. Moran, J. Gomatam, and W. N. McDicken, "The dependence of ultrasound contrast agents backscatter on acoustic pressure: theory versus experiment," *Ultrasonics*, vol. 40, no. 1–8, pp. 579–583, May 2002.

[49] I. Lentacker, I. De Cock, R. Deckers, S. C. De Smedt, and C. T. W. Moonen, "Understanding ultrasound induced sonoporation: definitions and underlying mechanisms," *Adv. Drug Deliv. Rev.*, Nov. 2013.

[50] M.-X. Tang, R. J. Eckersley, and J. A. Noble, "Pressure-dependent attenuation with microbubbles at low mechanical index," *Ultrasound Med. Biol.*, vol. 31, no. 3, pp. 377–384, Mar. 2005.

[51] Q. Chen, J. Zagzebski, T. Wilson, and T. Stiles, "Pressure-dependent attenuation in ultrasound contrast agents," *Ultrasound Med. Biol.*, vol. 28, no. 8, pp. 1041–1051, Aug. 2002.

[52] M. A. Averkiou, "Tissue harmonic ultrasonic imaging," *Comptes Rendus Acad. Sci. - Ser. IV Phys. Astrophys.*, vol. 2, no. 8, pp. 1139–1151, 2001.

[53] B. Ward, A. C. Baker, and V. F. Humphrey, "Nonlinear propagation applied to the improvement of resolution in diagnostic medical ultrasound," *J. Acoust. Soc. Am.*, vol. 101, no. 1, pp. 143–154, Jan. 1997.

[54] Y.-S. Lee and M. F. Hamilton, "Time-domain modeling of pulsed finite-amplitude sound beams," *J. Acoust. Soc. Am.*, vol. 97, no. 2, pp. 906–917, 1995.

[55] M. A. Averkiou and M. F. Hamilton, "Nonlinear distortion of short pulses radiated by plane and focused circular pistons.," *J. Acoust. Soc. Am.*, vol. 102, no. 5, pp. 2539–48, 1997.

[56] E. J. Ayme and E. L. Carstensen, “Cavitation induced by asymmetric distorted pulses of ultrasound: theoretical predictions,” *IEEE Trans. Ultrason. Ferroelectr. Freq. Control*, vol. 36, no. 1, pp. 32–40, 1989.

[57] E. J. Aymé and E. L. Carstensen, “Occurrence of transient cavitation in pulsed sawtooth ultrasonic fields,” *J. Acoust. Soc. Am.*, vol. 84, no. 5, pp. 1598–1605, Nov. 1988.

5 Evaluation of perfusion quantification methods with ultrasound contrast agents in a machine-perfused pig liver

Objective: To evaluate dynamic contrast enhanced ultrasound (DCEUS) as a tool for measuring blood flow in the macro- and micro-circulation of an *ex-vivo* machine-perfused pig liver. Confirm the ability of DCUES to accurately detect induced flow rate changes so that it could be then used as a clinical tool for monitoring flow changes in liver tumors.

Materials and Methods: Three fully functioning, machine-perfused pig livers were used in the present study. Flow changes were induced by the pump of the machine perfusion system and they naturally propagated to the liver macro- and micro-vasculature. The induced flow changes were of clinical relevance (150-400 ml/min for the hepatic artery and 400-1400 ml/min for the portal vein) and similar to those taking place during tumor growth or during therapeutic procedures targeting tumor angiogenesis. From DCEUS image loops after bolus injections in either the hepatic artery or the portal vein, time-intensity curves were formed and the Local Density Random Walk indicator dilution model was fitted on the data. From the fitted model various quantification parameters [rise time (*RT*), mean transit time (*MTT*), area under the curve (*AUC*) and peak intensity (*PI*)] were extracted in order to evaluate whether the induced flow changes were reflected in these parameters. The quantification parameters are related to flow with known indicator dilution relationships.

Results: A linear relationship between the image intensity and the microbubble concentration was confirmed first (R^2=0.8-0.93 for PV injections and R^2=0.72-0.93 for HA injections), while time parameters (*RT*, *MTT*) were found to be independent of

concentration. This result enables the use of indicator dilution methods for measuring flow in the liver vasculature. The induced flow changes which propagated from the larger vessels to the parenchyma and the hepatic vein tree were successfully reflected in the quantification parameters extracted from the indicator dilution model. Specifically, *RT*, *MTT* and area *AUC* correlated with flow rate changes (curve fits with $0.81<R^2<0.93$ for HA and PV main vessels, $R^2=0.91$ for HV, and $R^2=0.66$ for parenchyma) while the *PI* stayed constant. The above results are in agreement with the indicator dilution relationships.

Conclusion: *Ex-vivo* machine perfused pig liver is an excellent test-bed for DCEUS quantification approaches for measuring flow changes in the macro- and micro-circulation and it allows for the study of the hepatic vascular networks. Since the measured intensity-bubble concentration relationship was found to be linear, indicator dilution methods maybe used to measure relative flow changes. Bubble concentration does not affect time quantification parameters and thus variations in the amount of injected microbubbles in the clinic will not affect the quantification results. DCEUS quantification parameters (*RT*, *MTT*, and *AUC*) can measure relative flow changes of about 20% and above in the liver vasculature. DCEUS quantification is a promising tool for real-time monitoring of therapeutic applications which target the vascular network of tumors.

Keywords: DCEUS quantification, *ex-vivo* pig liver, machine perfusion, liver flow rate, therapy monitoring.

A shorter version of the present chapter has been submitted for review to *Ultraschall* by: C.P. Keravnou, M.L. Izamis, E. Leen and M.A. Averkiou

5.1 Introduction

Ultrasound contrast agents (UCAs) are a true blood-pool agent since their size (1-10 μm) allows them to pass through the alveolar–capillary barrier of the lungs but maintains them in the vasculature. Thus, the use of UCAs combined with a variety of available nonlinear imaging techniques enables real-time visualization of blood flow in the macro- and micro-circulation [1]–[3]. Today, dynamic contrast-enhanced ultrasound (DCEUS) is clinically utilized in cardiology [4], [5] and oncology [6], [7] as it has minimal adverse effects, it is safe and low cost, and available at bedside [1]–[3]. The use of DCEUS for diagnosis has offered improvements in the detection and characterization of tumors and opened the way for the evaluation of tumor angiogenesis [8].

Beyond qualitative assessment and diagnosis in oncology, recently DCEUS has gained a foothold in the clinic as an important disease staging and therapy monitoring tool by offering quantitative evaluation of tissue, organ, and tumor perfusion [8]–[11]. Time-intensity curves (TICs) obtained by placing a region of interest (ROI) on a contrast image, display the mean pixel intensity of the ROI as a function of time. Depending on the protocol of contrast agent administration (bolus or constant infusion [8], [9]), different mathematical models [12], [13] derived from the indicator dilution theory [14] can be fitted to TICs to limit the noise and isolate the primary pass of microbubbles [13]. In addition, curve-fitting allows an analytical determination of important DCEUS quantification parameters such as the rise time (*RT*), the mean transit time (*MTT*), peak intensity (*PI*) and the area under the TIC curve (*AUC*). The underlying hypothesis is that these quantification parameters are sensitive to changes in blood flow caused by both tumor growth and novel anti-angiogenic therapies [9]–[11]. Since anti-angiogenic therapies target the new vessels that are formed during tumor angiogenesis [15], tumor local blood supply is expected to change during the course of therapy.

A relatively simple way to study DCEUS quantification is in-vitro using flow tissue phantoms, typically constructed from tubing of various sizes to facilitate flow [16]–[20]. Lampaskis and Averkiou [21] used a diagnostic ultrasound scanner and a flow phantom to investigate the relationship between image intensity and microbubbles concentration (SonoVue) at low Mechanical Index (MI). They proved a linear relationship between linearized image intensity and contrast agent concentration (up to 1‰). A plateau observed at greater concentrations (>2‰) may be attributed to signal saturation and acoustic

shadowing. Gauthier et al. [22] used a kidney dialysis cartridge as a microvascular flow phantom to evaluate the impact of ultrasound scanner settings and contrast bolus volume on TICs in terms of accuracy and reproducibility. In-vitro experiments have however limited physiological relevance since they represent a single passage of contrast through simple tubing, ignoring the dispersion of microbubbles through branching vessels, variable flow resistance, and variable flow states.

Clinical trials have also been performed in order to assess DCEUS quantification ability to predict patient response to drugs targeting angiogenesis. The extracted quantification parameters were correlated with the response evaluation criteria in solid tumors (RECIST method) [23] and overall survival (OS), both currently used in clinics as the approved metrics for therapy evaluation [8], [9], [24]–[27]. However, in addition to the difficulty in measuring flow in the tumors due to their complex vasculature, many problems exist: low reproducibility, conflicting views as to which quantification parameters best correlate with flow changes, and variations in machine settings between sessions. Due to the above limitations DCEUS quantification has not reached yet wide clinical utility and acceptance.

Recently, Izamis et al. [28] developed and evaluated a sub-normothermic human-sized machine perfusion system suitable to preserve slaughterhouse pig livers. They showed using biochemical and hemodynamic measurements and DCEUS imaging that the developed model is a simple, cost-effective approach for at least 3 hours of stable, *ex-vivo* whole organ preservation. To overcome the limitations of DCEUS quantification listed above, avoid costly and complex *in-vivo* animal experiments, and ethical issues in clinical trials we propose the use of the machine perfused pig liver model as perfusion quantification development and validation test bed.

In the present work, slaughterhouse pig livers were sustained for up to 4 hours connected to a machine perfusion system allowing the investigation of bolus kinetics of contrast microbubbles in a highly controlled environment which closely resembles *in-vivo* conditions. The effect of bubble concentration on the bolus kinetics parameters was examined first. The underlying assumption of using the indicator dilution models in DCEUS quantification is the proportionality of image intensity with concentration, as established in the past but only *in-vitro* [21]. This relationship was confirmed in a normal functioning human-sized liver and while correcting for signal saturation [29]. Then,

various flow changes with clinical/physiological relevance were induced in the machine perfused liver and were measured in the liver vasculature with DCEUS quantification. The quantification parameters (*RT*, *MTT*, *PI*, *AUC*) extracted from curve fitting of the local density random walk (LDRW) model based on indicator dilution theory were evaluated for their ability to detect the induced flow changes in the liver vasculature. The accuracy and resolution as well as the limitations of DCEUS flow quantification of machine perfused livers were investigated in an effort to decide whether this technique may be used clinically for real-time monitoring of therapeutic applications which target the vascular network of tumors.

5.2 Materials and methods

5.2.1 Indicator dilution theory

The wash-in and washout of contrast microbubbles in a ROI may be modeled by the indicator dilution theory [14]. According to the Stewart-Hamilton relationships [30], [31], if the amount of indicator m in a bolus injection is known and the indicator concentration as a function of time $c(t)$ is measured in a ROI, the volumetric blood flow (Q) and the blood volume (V) can be calculated in terms of *AUC* and *MTT*:

$$Q = m \cdot (AUC)^{-1} \qquad (5.1)$$

$$V = Q \cdot MTT \ , \qquad (5.2)$$

where,

$$AUC = \int_0^\infty c(t)\,dt \qquad (5.3)$$

$$MTT = \frac{\int_0^\infty tc(t)\,dt}{\int_0^\infty c(t)\,dt}. \qquad (5.4)$$

Microbubble concentration cannot be measured directly, thus the backscattered intensity $I(t)$ is measured instead. Since intensity is linearly proportional to the concentration [21], [29], Eqs. (5.1) & (5.2) can be used to calculate Q and V from *AUC* and *MTT*. Here we also note that the rise time (*RT*), is linearly related with *MTT* (see Eq. (10) in the work of Strouthos et al. [13]) and hence flow rate.

5.2.2 Ex-vivo liver machine perfusion model

The studies were approved by the Cyprus National Bioethics Committee and the Cyprus National Veterinary Services. Three healthy porcine livers were procured from a local abattoir. Details on liver procurement can be found elsewhere [28]. Briefly, immediately after animal death, livers were isolated from the rest of the thoracic and abdominal organs and flushed with 8L of Lactated Ringers (6L room temperature and 2L ice cold) through the portal vein (PV) and hepatic artery (HA). The organs were then stored on ice and transported to the laboratory (time of static cold storage was $\leq$ 1 hour), where they were connected to the machine perfusion system [Fig. 5.1(a)] and sustained for up to 4 hours.

The perfusion system comprised a 6L perfusate reservoir (Powdered Williams Medium E (10.8g/L W4125, Sigma-Aldrich Corp. St Louis, MO, USA) with addition of 2.2g/L of sodium bicarbonate (S5761, Sigma-Aldrich Corp. Medisell, Cyprus), 1000 IU/L heparin, 2 U/L insulin (Actrapid® Penfill® Novo Nordisk, Novo Alle, Denmark), and 0.4 mg/L dexamethasone (Dexamed, Medochemie Ltd, Limassol, Cyprus), in which the organ was suspended. A pump (Masterflex L/S Digital Drive 600rpm, Cole Parmer) circulated the perfusate through an oxygenator (Affinity NT, Medtronic, Minneapolis, MN, USA) supplied with 95% O_2, 5% CO_2 (Tenaris, Bergamo, Italy) before being split and passed through two flow meters (EW-32461-44 and EW-32460-40, Cole Parmer) that enable pressure-regulated flow to each of the PV and HA respectively. Effluent was then allowed to flow freely from the liver's vena cava back into the reservoir, closing the circuit. Flow rate was typically set to 800 ml/min for the PV and 400 ml/min for the HA. The selected flow rates ensured that PV pressure was $\leq$10 cmH_2O and HA pressure was between 60 and 100 cmH_2O. Hepatic stability was ascertained with half-hour interval measurements of bile production, oxygen consumption, and sustained vascular perfusion. The perfusion was monitored via DCEUS imaging (Fig. 5.2). The circuit provided individual syringe port access to each of the hepatic vessels so that contrast could be administered to either the PV or HA. Typical images of a bolus injection administered to PV (in this case) are shown in Fig. 5.2. As soon as the contrast microbubbles enter the imaged area, the primary branches of the PV are filled first [Fig. 5.2(a)]. Contrast microbubbles then enter venules and the smallest capillaries and fill the parenchyma (Pa) [Fig. 5.2(b, c)]. During wash-out, microbubbles drain in the hepatic vein (HV), as indicated by the white arrows in Fig. 5.2(d).

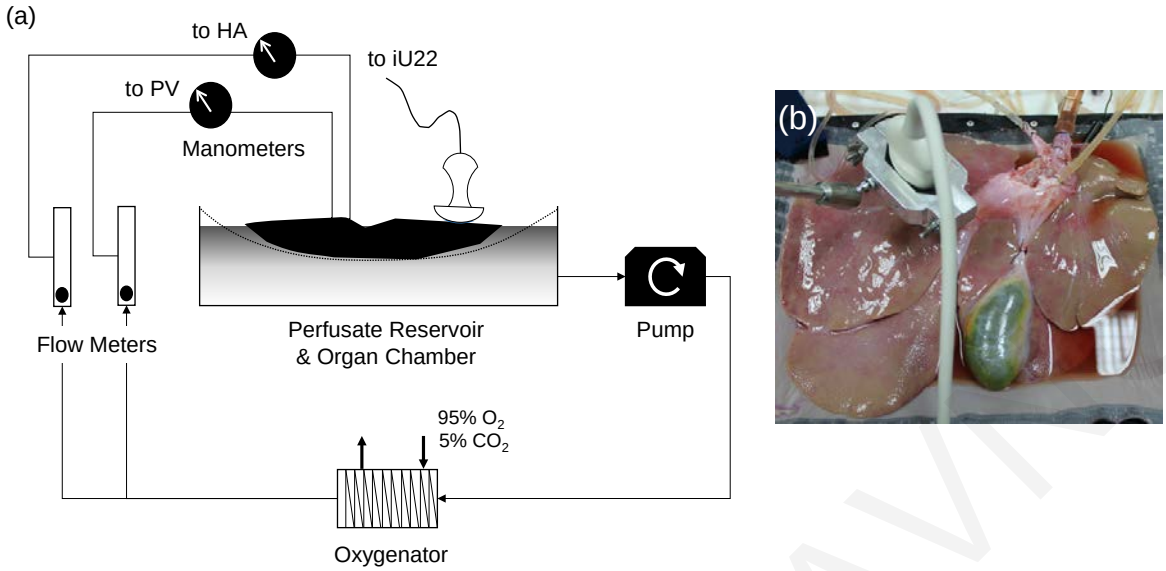

Figure 5.1: (a) The *ex-vivo* machine perfusion system consists of an organ chamber in which the liver is suspended, a single pump and oxygenator, and two flow meters/regulators connected to the hepatic artery and portal vein. (b) Picture of the pig liver connected to the machine perfusion system and the L9-3 imaging probe fixed on a specific location.

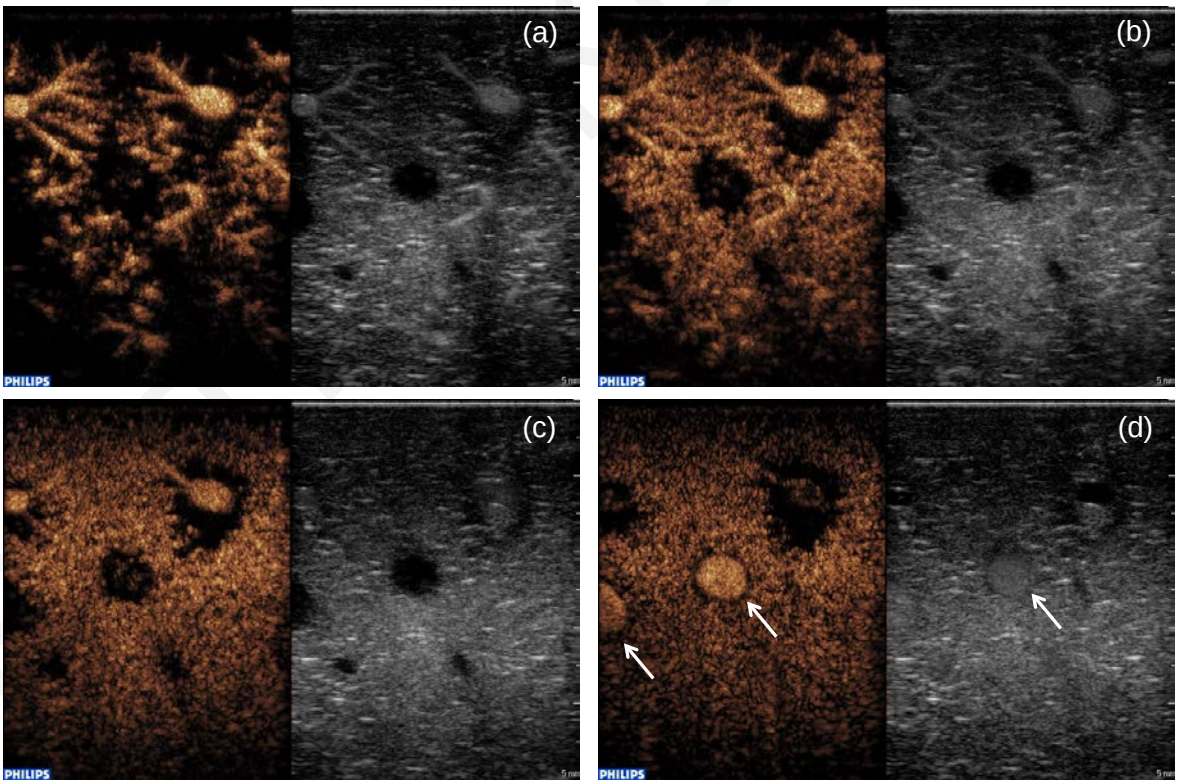

Figure 5.2: Images of microbubbles in the liver vasculature in a dual imaging mode where the left is the contrast image and the right is the tissue image. Flow in the vasculature of the liver can be depicted with administration of a contrast agent bolus directly into the portal vein (PV) or the hepatic artery (HA). A PV injection is used in this example. (a) First the primary branches are filled. (b, c) Contrast microbubbles enter the smallest capillaries and fill the parenchyma. (d) The contrast microbubbles appear in the hepatic vein (white arrows).

5.2.3 Imaging

An L12-5 and L9-3 linear array probes of an iU22 diagnostic ultrasound scanner (Phillips Medical Systems, Bothell, WA, USA) were used to image the livers. As soon as the livers were connected to the machine perfusion system, they were evaluated for the presence of any anatomical abnormalities and air using the L12-5 linear array and B-mode imaging. The L12-5 probe was also used after contrast bolus injection in a "contrast side–by–side" setting to scan the whole liver to ensure uniform perfusion as time was progressing.

The L9-3 probe was held fixed in a position using a mechanical arm (Fisso, Baitella AG, Zurich, Switzerland) [Fig. 5.1(b)] to monitor the perfusion of that specific region and record contrast image loops (Fig. 5.2). The L9-3 probe was set in a "contrast side–by–side" setting with the following parameters: power modulation, frequency=3.1 MHz, MI=0.05, focus of 3.5 cm, frame rate=12 Hz. The persistence was turned off to avoid averaging of the image data between consecutive frames necessary for quantification. The compression was set at the maximum that was available on the scanner (50 dB) to best accommodate a large range of signals and avoid saturation. The 2D gain was continuously adjusted and recorded when intensity-concentration relationship was under investigation, to avoid signal saturation which would result in inaccuracies in the quantification parameters [29]. To select the fixed location of the probe, a preliminary bolus of contrast first to the PV and then to the HA was administrated and the liver was scanned. The image plane was chosen such that it contained a cross-sectional view of each input vessel (PV and HA), a branch of the HV, and well-perfused parenchyma [Fig. 5.3(a-c)].

5.2.4 Experiment design/procedure

Two specific tasks were studied in each of the 3 livers:

1. The effect of bubble concentration on quantification parameters (*RT*, *MTT*, *AUC*, *PI*) under constant flow (Table 5.1).

2. The effect of flow changes in the HA and PV on bolus quantification parameters measured on the macro-circulation, the micro-circulation in the parenchyma, and the HV vascular tree.

In task (2), 3 different flow changes were considered as outlined in Table 5.2. Flow changes A allowed for changes in both the HA and the PV while the overall total flow remained constant. In flow changes B the PV was held constant while the HA was varied and thus the overall total flow was varied. Similarly in flow changes C the HA was held constant while the PV was varied and thus the overall total flow was varied. The measurements of the tasks above were repeated on 3 different livers on different days.

For the study of the effect of bolus concentration on DCEUS quantification parameters, a total of 8 microbubble solutions were prepared with concentrations shown in Table 5.1. The concentrations are given in milliliters of contrast agent per liter of deionized water (e.g. 0.004‰ = 0.004 ml UCA / liter of deionized water) and they cover a very wide range of physiologically and clinically relevant concentrations. The measurement acquisition time was kept below 1 hour to avoid bubble deterioration. The bolus volume was 1 ml and it was injected through a rubber stop in either the PV and the HA. One minute video loops were collected for every injection. Between injections, a C5-1 curve linear array probe (Phillips Medical Systems, Bothell, WA, USA) operating at low frequency (<2 MHz), high MI (>1.0) was used to destroy any remaining microbubbles in the system.

In order to study the ability of DCEUS quantification to detect flow changes in the macro- and micro-circulation, flow changes either at the PV, the HA or both were induced via the flow regulators. These flow changes (Table 5.2) are clinically relevant and mimic in a simplified and controlled manner flow changes that might be caused during the course of progression or regression of tumor angiogenesis. A waiting time of 2 minutes between flow rate changes was allowed for the flow to reach its new equilibrium in the liver vasculature. Bolus injections of 1 ml and contrast concentration of c=0.1‰ were used. One minute loops were collected for every bolus injection. A new vial of contrast agent was used for the whole set of flow variation measurements and the total acquisition time was kept below 1 hour.

Contrast Agent Concentration (‰)
0.1665
0.0908
0.0196
0.0099
0.0040
0.0020
0.0010
0.0005

Table 5.1: Contrast agent concentrations used in the plots of Figs. 5.4 and 5.5.

Flow Changes A (ml/min)			Flow Changes B (ml/min)			Flow Changes C (ml/min)		
PV	**HA**	**Total flow**	**PV**	**HA**	**Total flow**	**PV**	**HA**	**Total flow**
800	400	1200	1000	400	1400	1400	200	1600
850	350	1200	1000	350	1350	1200	200	1400
900	300	1200	1000	300	1300	1000	200	1200
950	250	1200	1000	250	1250	800	200	1000
1000	200	1200	1000	200	1200	600	200	800
1050	150	1200	1000	150	1150	400	200	600

Table 5.2: List of flow variations induced in the perfusion system. Three different cases were studied. Flow Changes A: the total flow rate was kept constant while both the PV and the HA flow rate were changing to maintain the total flow rate at 1200 ml/min. Flow Changes B: PV flow rate was kept constant while the HA flow rate was changing. Flow Changes C: HA flow rate was kept constant while the PV flow rate was changing.

5.2.5 Contrast agent

Custom made microbubbles (Department of Pharmaceutics, University of Ghent, Ghent, Belgium), very similar to Definity clinical ultrasound contrast agents were used throughout this work. The composition of the microbubbles was DPPC/DSPE-PEG in 95:5 molar ratio. The microbubbles contained Perfluorobutane gas (PFB, C_4F_{10}), and were stabilized with a PEGylated lipid shell. The average size of the microbubbles was 2.5 μm and the concentration of the microbubbles was 3- 8 $x10^8$ microbubbles/mL. These custom microbubbles were selected to avoid incomplete washout in the parenchyma which was previously observed when other microbubbles were used in machine perfused livers [28], and it is believed to be specific for pig livers only.

5.2.6 Image quantification and curve fitting

QLAB software (Philips Medical Systems, Bothell, WA) was used to form TICs from the DICOM files by placing a ROI on the image. Three ROIs were placed on each DICOM image [Fig. 5.3(a-c)]: one around the input vessel (PV or HA depending on the bolus injection site), one around the HV and one in a well perfused area in the parenchyma.

TICs of both input vessels (PV or HA), the output vessel (HV) and the parenchyma (Pa) were extracted from QLAB [Fig. 5.3(d), solid lines)] and were fitted to an LDRW model using purpose created MATLAB (The MathWorks, Inc., Natick, MA, USA) code [Fig. 5.3(d), dashed lines)]. DCEUS quantification parameters, *RT*, *MTT*, *AUC* and *PI*, were measured from the fitted model. The DCEUS quantification parameters were also measured after fitting the TICs to a Log-normal model in order to compare which of the two models is the most appropriate for machine perfusion liver use.

5.2.7 Statistics

The experiments were repeated in a total of 3 livers and results are shown as the mean ± standard deviation. In order to be able to combine parameters from different livers, which also meant different ROIs and different vasculature, the extracted quantification parameters were normalized with respect to the maximum value of each parameter in every liver.

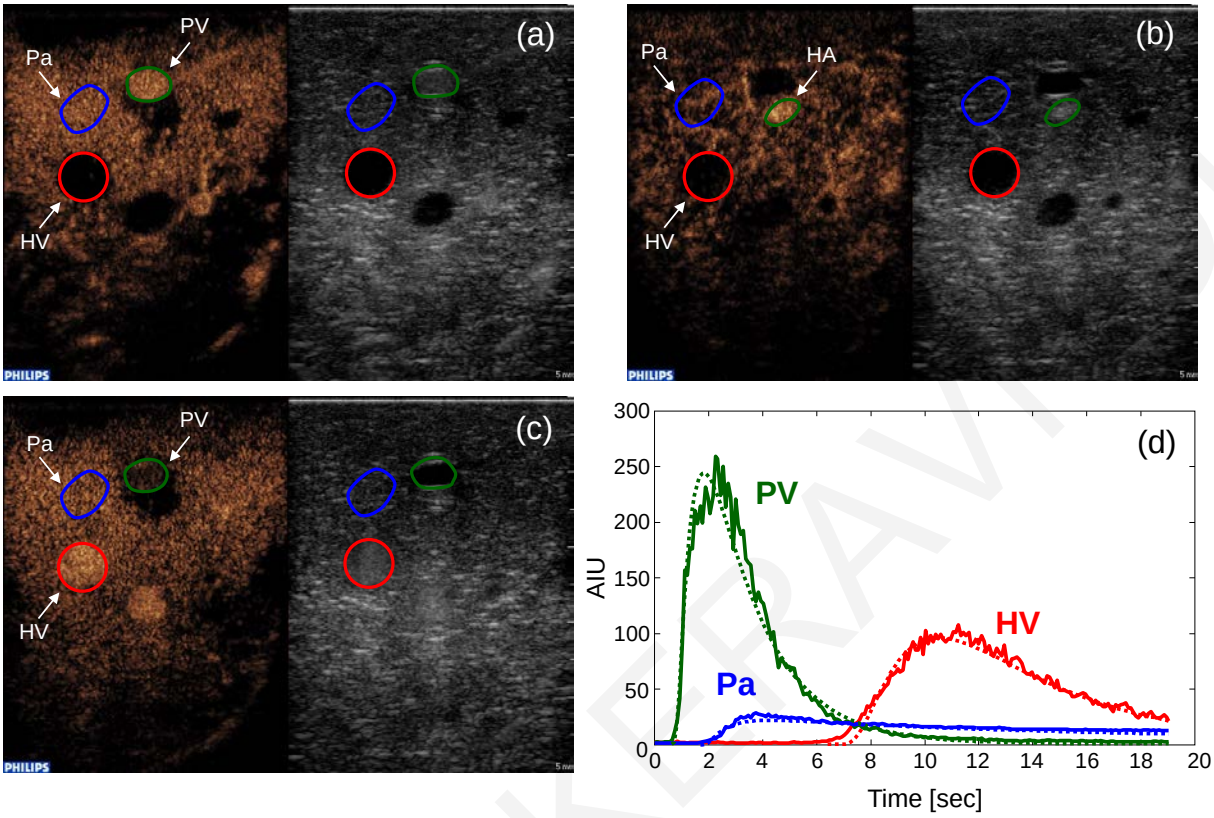

Figure 5.3: (a-c) Images of the liver after bolus injection in the PV (a),(c), and the HA(b). (a) and (c) are from the same image loop but at different times. Three ROIs were placed on each image: one around the input vessels [the portal vein (PV) or the hepatic artery (HA)], one around the output vessel [hepatic vein (HV)] and one in an area of well perfused parenchyma (Pa). (d) Typical time-intensity curves (TICs) for portal vein, hepatic vein and parenchyma. The formed TICs are shown in solid lines and the LDRW model fit is shown in dashed lines.

5.3 Results

After fitting both the LDRW and the Log-Normal models to the extracted TICs, the LDRW model had significantly higher coefficient of determination (R^2). Thus, only the DCEUS quantification parameters calculated analytically from the fitted LDRW model are shown here.

The effect of bubble concentration on quantification parameters under constant flow are shown in Figs. 5.4, 5.5 for injections at the PV and HA, respectively. In both figures, the top row shows *RT* and the bottom row shows *PI* as a function of the concentration in a semi-log scale. Logarithmic scale was chosen for the horizontal axis to better accommodate the large range of concentrations used (Table 5.1). Here, only 6 out of 8 concentrations are displayed since the higher concentrations were affected by increased

acoustic shadowing [29]. It is observed that *RT* remains constant with increasing concentration both in macro- (larger vessels of the PV, HA and HV) and micro-circulation (Pa) [Fig. 5.4(a-c) and Fig. 5.5(a-c)]. This result was expected as flow rate was kept constant during these measurements [see Eq. (5.2)]. However, it is observed that *PI* is increasing linearly with increasing concentration [Fig. 5.4(d-f) and Fig. 5.5(d-f)], which is both expected and in agreement with previously published results [21], [29]. A straight line ($y=a$ for *RT* and $y=ax$ for *PI*, where a is a constant) was fitted in the data to make it easier for the reader to appreciate the linear relationship between the parameters in a semi-log scale. We note that in both figures (5.4 and 5.5) the quality of fit is excellent with $0.72<R^2<0.96$. The deviations of *PI* from the linear fit are attributed to the increased acoustic shadowing (higher attenuation at higher microbubbles concentrations) [29].

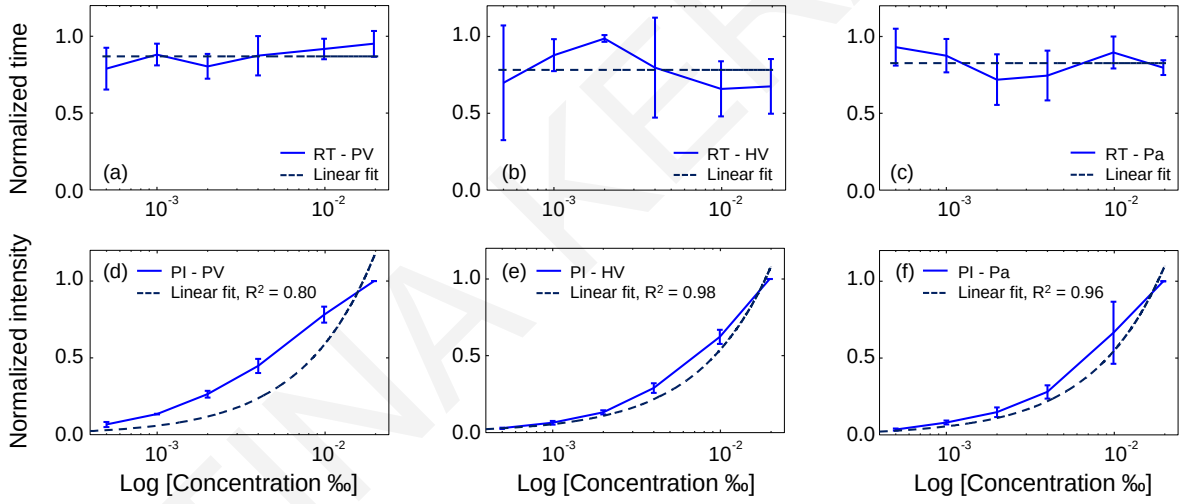

Figure 5.4: (a-c) Normalized rise time (top row) and normalized peak intensity (bottom row) as a function bubble concentration in semi-log scale after a PV bolus injection. (a),(d) ROI on a PV main vessel, (b), (e) ROI on an HV main vessel, (c), (f) ROI on the parenchyma. A straight line (*y=constant* for *RT* and *y=αx* for *PI)* was fitted in the data and it is shown in dashed lines.

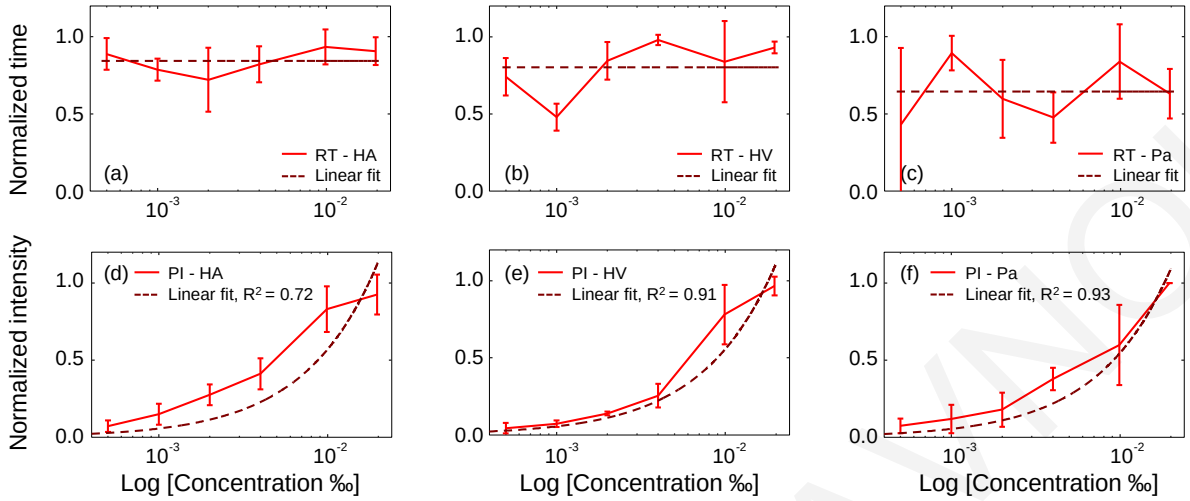

Figure 5.5: (a-c) Normalized rise time (top row) and normalized peak intensity (bottom row) as a function bubble concentration in semi-log scale after an HA bolus injection. (a), (d) ROI on an HA main vessel, (b), (e) ROI on an HV main vessel, (c), (f) ROI on the parenchyma. A straight line (*y=constant* for *RT* and *y=αx* for *PI*) was fitted in the data and it is shown in dashed lines.

Figure 5.6 shows the normalized *RT* as a function of flow rate for the case where the total flow rate of the machine perfusion system was kept constant at 1200 ml/min (Table 5.2, Flow Changes A). The top row presents *RT* for HA bolus injections, while the bottom row shows *RT* for PV bolus injections. It is observed that the normalized *RT* decreases when flow rate increases in both large vessels, the HA [Fig. 5.6(a)] and the PV [Fig. 5.6(d)]. However, the *RT* change in HA is more pronounced than in the PV. This difference is because the induced flow rate change in the HA was greater (from 150 to 400 ml/min, 2.7 times) than in the PV (from 800 to 1050 ml/min, 1.3 times). The measurements in Fig. 5.6 (a) and (d) are fitted with curve $1/Q$ and shown as a dashed line, with R^2=0.93 and R^2=0.90, respectively. In the HV [Fig. 5.6(b, e)] it is observed that *RT* does not follow a specific trend with increasing flow rate in both arterial and venous injections. This result is attributed to the fact that the HV reflects the summation of PV and HA flows, which is kept constant at 1200 ml/min in this case. In the parenchyma after injection in the HA [Fig. 5.6(c)], despite the induced 2.7x HA flow rate change, still the *RT* stays constant. Since the microcirculation is the place where the HA and PV flows converge, the overall flow change is zero for this case. The same applies for the *RT* of the parenchyma after PV injection [Fig. 5.6 (f)] and it does not change with increasing flow rate.

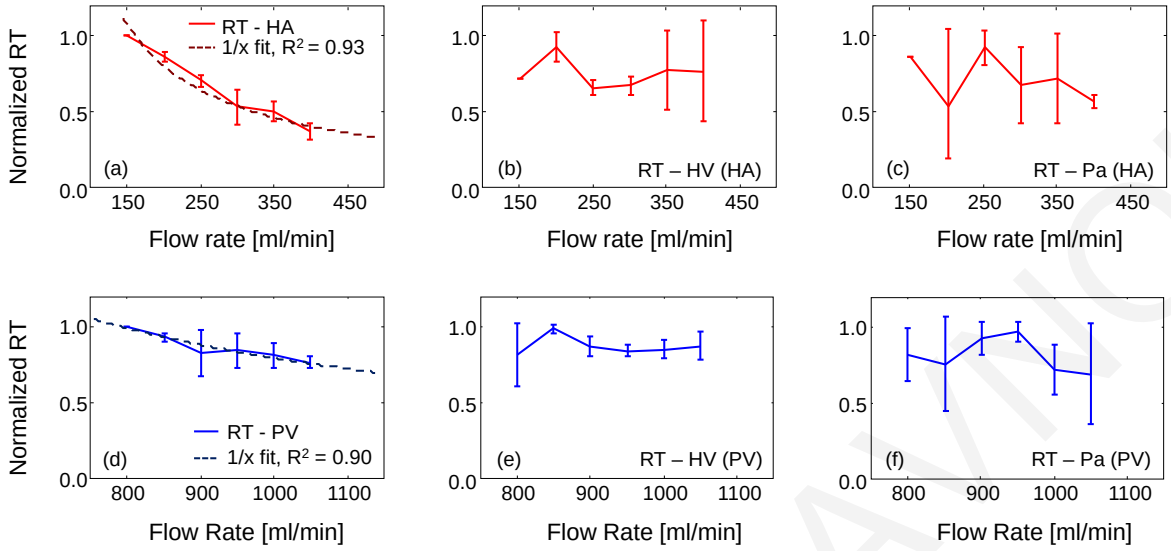

Figure 5.6: Flow Changes A. Normalized rise time (*RT*) as a function of flow rate. Top row: bolus injections in the hepatic artery; bottom row: bolus injections in the portal vein. The total flow rate was kept constant at 1200 ml/min while both the portal vein and the hepatic artery flow rate were changing. A 1/*x* curve ($y=\alpha x^{-1}$) was fitted in the data and it is shown in dashed lines.

The case where flow rate changes were induced only in the HA tree while the flow rate of the PV vasculature was maintained constant, (Table 5.2, Flow Changes B), is shown in Fig. 5.7(a-c). It is observed that the induced flow rate changes are easily measured in the input vessel as *RT* decreases with increasing flow rate [Fig. 5.7(a)]. With a dashed line, 1/*Q* curve fit is shown with R^2=0.93. However flow rate changes cannot be detected in the HV vessel, Fig. 5.7(b), or the microcirculation in the parenchyma, Fig. 5.7(c), as no clear trends or significant changes of *RT* with increasing flow rate are observed. Figures 5.7(d-f) show *RT* for the case where flow rate changes were induced in the PV while the HA flow rate was kept constant (Table 5.2, Flow Changes C). It is observed that *RT* decreases with increasing flow and the induced flow rate changes are reflected in the *RT* of both in the input [Fig. 5.7(d)] and the outflow vessel [Fig. 5.7(e)] and also can be detected in the micro-vasculature [Fig. 5.7(f)]. With dashed lines, 1/*Q* curve fits are shown in Figs. 5.7(d)-(f). As mentioned earlier the outflow vessel (HV) reflects the summation of PV and HA flows. Taking into account that approximately 75% of the total flow is supplied by the PV, the outflow is only minimally affected by the changes in the arterial vascular tree when PV flow is kept constant [Fig. 5.7(b)]. Thus, the changes

induced in the HA (Table 5.2, Flow Changes B) cannot be measured from the quantification parameters extracted from the TICs.

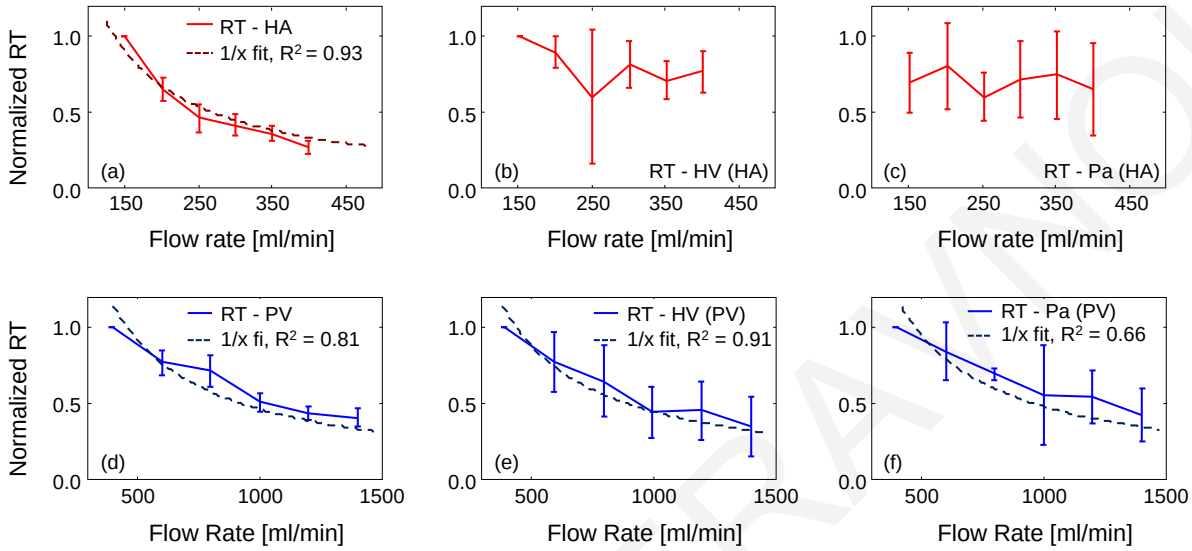

Figure 5.7: Normalized rise time (*RT*) as a function of flow rate. Top row: bolus injections in the hepatic artery. Portal vein flow was kept constant at 1000 ml/min while the hepatic artery flow was changing between 150 - 400 ml/min (Table 5.2, Flow Changes B). Bottom row: bolus injections in the portal vein. Hepatic artery flow was kept constant at 200 ml/min while portal venous flow was changing between 400 - 1400 ml/min (Table 5.2, Flow Changes C). A 1/*x* curve ($y=\alpha x^{-1}$) was fitted in the data and it is shown in dashed lines.

Figure 5.8 shows *AUC* as a function of flow rate for the cases of Flow Changes B [Fig. 5.8 (a-c)] and Flow Changes C [Fig. 5.8 (d-f)], (Table 5.2). In these figures *AUC* calculated after fitting of TIC image loops of a single liver are shown. The trends in Fig. 5.8 are similar with those of Fig. 5.7, where *RT* is measured for the same flow changes. Specifically, in Fig. 5.8(a-c) where flow rate changes were induced only in the HA, the flow changes could be easily detected only in the input vessel [Fig. 5.8(a)]. *AUC* decreases with increasing flow rate as expected according to Eq. (5.2). In Fig. 5.8(d-f) where flow rate changes were induced only in the PV, it is observed that *AUC* decreases with increasing flow both in the input [Fig. 5.8(d)] and the outflow vessel [Fig. 5.8(e)], as well as the parenchyma [Fig. 5.8(f)]. With dashed lines, 1/*Q* curve fits are also shown.

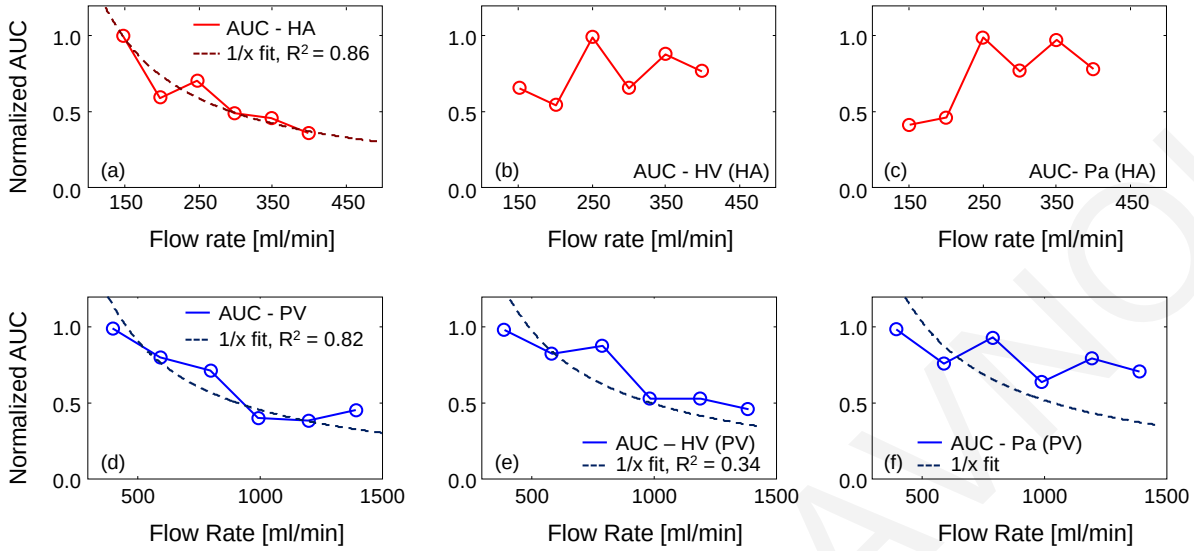

Figure 5.8: Normalized area under the curve (*AUC*) as a function of flow rate. Top row: bolus injections in the hepatic artery. Portal vein flow was kept constant at 1000 ml/min while the hepatic artery flow was changing between 150 - 400 ml/min (Table 5.2, Flow Changes B). Bottom row: bolus injections in the portal vein. Hepatic artery flow was kept constant at 200 ml/min while portal venous flow was changing between 400 - 1400 ml/min (Table 5.2, Flow Changes C). A 1/*x* curve ($y=\alpha x^{-1}$) was fitted in the data and it is shown in dashed lines.

The average time parameters (*RT* and *MTT*) of each of the 3 different livers and for a total of 9 measurements per liver (8 measurements from Table 5.1 plus one from Table 5.2 Flow Changes A) before normalization, and when HA flow rate was 400 ml/min and PV flow rate was 800 ml/min are shown in Table 5.3. For these flow rates, *RT* in the input vessels (PV and HA) was significantly smaller than *RT* for the HV and the Pa and thus suggesting that the flow rate was lower there, as expected. The small *RT* of the input vessels are due to the fact that the injected bolus did not travel a very long path before arriving in the ROI and thus did not have the chance to spread in space. However, the passage to the parenchyma and eventually to the HV introduced a considerable spreading of the bolus and thus the *RT* and *MTT* were considerably larger. From this table we also observe that these parameters vary between the 3 livers for 2 reasons: (a) due to differences between the selected ROIS, and (b) due to physiological differences between the livers. The values of *MTT* for liver 3 are somewhat large, possibly due to some larger microbubble "sticking" in the microcirculation due to the absence of lungs.

Liver 1	RT (sec)	MTT (sec)	Liver 2	RT (sec)	MTT (sec)
HA	0.68±0.11	2.00±0.83	**HA**	0.89±0.07	1.61±0.30
PV	0.62±0.05	1.32±0.24	**PV**	1.01±0.1	1.84±0.27
HV (HA)	9.35±3.85	13.52±3.88	**HV (HA)**	3.63±0.92	11.69±2.52
HV (PV)	8.33±1.89	13.55±3.04	**HV (PV)**	5.77±2.29	12.89±1.65
Pa (HA)	2.48±1.45	21.62±7.09	**Pa (HA)**	2.51±0.76	47.21±26.05
Pa (PV)	2.37±0.66	26.72±8.72	**Pa (PV)**	1.69±0.25	44.72±24.77

Liver 3	RT (sec)	MTT (sec)
HA	0.84±0.20	2.03±0.75
PV	1.12±0.14	2.11±0.44
HV (HA)	3.13±0.64	6.15±1.69
HV (PV)	3.66±0.38	6.94±0.64
Pa (HA)	1.53±0.76	89.00±31.42
Pa (PV)	2.39±0.54	85.18±55.19

Table 5.3: Average rise time (*RT*) and mean transit time (*MTT*) when physiological flow rates were used during machine perfusion. Hepatic artery flow rate was 400 ml/min and portal vein flow rate was 800 ml/min.

Finally, Fig. 5.9(a) and (b) show *PI* as a function of flow rate for the cases of Flow Changes B (Table 5.2) and Flow Changes C (Table 5.2), respectively. It is observed that *PI* is relatively constant with flow rate changes for both the input vessels [HA, Fig. 5.9(a) and PV Fig. 5.9(b)]. *PI* is expected to change when the vascular density changes which of course for the healthy livers studied here did not change. It is also noted that *PI* is more prone to signal saturation and acoustic shadowing errors and differences in machine settings from session to session.

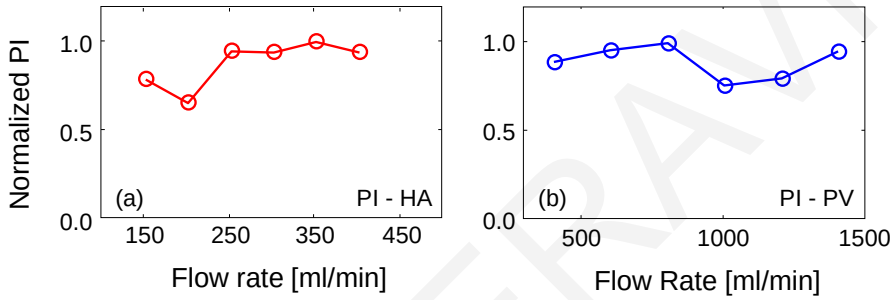

Figure 5.9: Normalized peak intensity (*PI*) as a function of flow rate. (a) Bolus injection in the hepatic artery. Portal vein flow was kept constant at 1000 ml/min while the hepatic artery flow was changing between 150 - 400 ml/min (Table 5.2, Flow Changes B). (b) Bolus injection in the portal vein. Hepatic artery flow was kept constant at 200 ml/min while portal venous flow was changing between 400 - 1400 ml/min (Table 5.2, Flow Changes C).

5.4 Discussion

DCEUS has the potential to measure relative flow changes in the microcirculation and this opens the possibility to use it as an imaging biomarker of tumor response to therapy. Despite its existence for over 10 years and a number of published works, there are still some basic questions and issues. Some of those are the relationship of the bolus dynamics quantification parameters with flow, its accuracy and resolution, reproducibility, and its limitations. When applying DCEUS for therapy monitoring of metastatic liver disease, the above issues are further amplified and outcomes from such studies are even harder to interpret due to the dual supply nature of the liver (HA and PV). In trying to investigate DCEUS as an imaging biomarker and address some of the issues above, machine perfusion of pig liver presents itself as the ideal test bed as it is almost identical to the clinical *in-vivo* case. One small drawback is the fact that there are no tumor models for such a system, but in-depth understanding of the DCEUS ability to measure the flow in the microcirculation in a normal functioning liver is of great importance.

One problem we have encountered is that certain microbubbles may be sticking in the pig liver microvasculature [28] and those must be avoided when trying to quantify flow in the microcirculation. In addition to the experimental microbubbles that we used, Sonovue (Bracco S.P.A., Milan, Italy) [32] was also used (results not shown here) and very similar trends were observed with the exception that some sticking to the microcirculation was observed. The microbubbles currently in clinical use do not have any similar "sticking" issues reported in humans. In machine perfusion models like ours, the absence of lungs to filter larger microbubbles also presents a small problem as larger microbubbles that would normally be removed by the lungs are now circulating in the liver. However, according to the principles of indicator dilution, the size of the indicator (microbubbles in our case) is not directly affecting the flow measurements.

The intensity-bubble concentration relationship under low MI conditions and with a nonlinear pulsing scheme was studied for first time in a machine perfused liver which is very close to the *in-vivo* case. A linear relationship was confirmed for up to a certain concentration at which point acoustic shadowing begins. All errors from signal saturation in the ultrasound scanner were removed by the previously published method [29] of continuous gain adjustment in both the scanner and the quantification software. A linear relationship between image intensity and bubble concentration is the underlying assumption for being able to use quantification methods based on indicator dilution. *RT* and *MTT* are not affected by bubble concentration changes. This is an important result for clinical studies as measurements of flow rates *in-vivo* from *RT* and *MTT* will not be affected by variation in the concentrations between injections. Our results demonstrated that effort must be placed in carefully controlling the bubble concentration and avoiding any related artifacts for reliable and accurate quantification of flow.

We have induced a variety of flow changes by virtue of adjusting the pump controlling the flow in both the HA and the PV of the perfused livers and tried to measure the induced changes in the larger vessels of those vascular trees, the HV, and the liver parenchyma. One advantage of the *ex-vivo* machine perfusion model is that injections to either the HA or the PV are administered and thus those specific vascular networks are studied independently. From our results, we can conclude that with DCEUS quantification we can measure induced flow changes in all three family of vessels: input (HA or PV), output (HV) and parenchyma.

In the first set of flow changes (Table 5.2, Flow Changes A) where the overall flow rate was held constant while the HA and the PV were changing proportionally, the change on the specific input vessel (HA or PV) was clearly reflected in terms of *RT* changes. Similar trends were observed with the *MTT* (not shown here) which according to Eq. (5.2) is proportional to the flow rate. We remind the reader that *RT* is also linearly related with the *MTT*. However, flow changes in either the HA and the PV while the overall flow (HA+PV) was held constant should not amount to any flow changes in the HV or the parenchyma which is in agreement with our measurements [Fig. 5.6 (b)-(c), (e)-(f)]. Perhaps it is more obvious why the HV where both HA and PV vascular networks drain should not change since the overall flow was kept constant. For the parenchyma, the same observation is made because it is where both networks combine right before continuing onto to the HV network. We also note here that this flow changes scenario is perhaps the closest to what happens *in-vivo* with liver tumors. It is suggested from our findings that the tumoral flow changes will best be recorded in the larger arterial vessels and not the parenchyma.

When the total liver flow was allowed to change by changing either the HA flow while keeping the PV constant and vice versa (Table 5.2, Flow Changes B and C), we were able to easily measure these changes in the input vessels (HA or PV) [Fig. 5.7(a), (d)]. In the outflow vessel (HV) and the parenchyma only when the PV flow rate was changed we could detect changes in the *RT* [Fig. 5.7(e), (f)]. By considering the overall percent changes in each case we can deduce some information about the flow resolution of our method. When the HA was changing (Table 5.2, Flow Changes B), the overall flow change was 4% to 18% (50/1200 to 250/1400). It is observed that DCEUS quantification may not detect changes in this range in the parenchyma and this may be the lower bound. When the PV was changing (Table 5.2, Flow Changes C), the overall flow change was 25% to 63% (200/800 to 1000/1600). In this range of flow changes DCEUS quantification can detect those changes down to the microvascular level (parenchyma). From these two sets of measurements, we can deduce that DCEUS can effectively measure flow changes when they are about 20% and above.

Both *RT* and *AUC* are inversely proportional to the flow rate according to Eqs. (5.2) and (5.3) and that was confirmed with our results (Figs. 5.7-5.8). In the literature, some confusion exists as to which parameter to use and different investigators suggested using either time (*RT* and *MTT*) or *AUC* for extracting flow information. Their choice was

often based on the ability of the ultrasound scanner to accurately measure them or on the statistical correlation of those parameters with other established markers in their experiments. Specifically, single-center studies in patients with metastatic renal carcinoma [33], hepatocellular carcinoma [34] and gastrointestinal stromal tumor [35], showed that *AUC* was consistently correlated with RECIST criteria [33]. A multi-center study performed in patients with different types of solid tumors [26] enhanced previous results and showed that *AUC* had the most significant association among other quantification parameters with overall survival. In another clinical trial, a correlation of *RT* with early tumor response to therapy in patients undergoing a combination of antiangiogenic and cytotoxic treatment for colorectal metastasis in the liver was demonstrated [10]. Williams et al. [27] suggested DCEUS with both bolus injection and infusion protocols for predicting response of renal cell carcinoma. They reported that they detected tumor fractional blood volume changes from the quantification parameters but with poor reproducibility. Our work here shows that *RT*, *MTT* and *AUC* are all related to flow. However measurements performed in clinics may suffer from different sources of error [36]. Generally, intensity parameters (*AUC* and *PI*) are more error prone due to signal saturation, nonlinear propagation artifact [37], [38] acoustic shadowing and bubble destruction.

In the present work, we have used both the HA and the PV vascular trees of machine perfused healthy pig livers to test the ability of DCEUS to measure flow changes. However, when studying tumors where the majority of the blood supply is arterial with almost no PV supply, according to our findings DCEUS quantification would be able to measure those HA microvascular changes when they are more than about 20%. It is also noted that during chemotherapy often dramatic changes in both the size and the microvascular flow of tumors are taking place, it becomes even more challenging to accurately measure those changes with 2D ultrasound due to the inhomogeneous nature of the tumor vasculature. However, our work here shows that it is possible to use DCEUS quantification to monitor those changes and once 3D ultrasound technology (imaging and quantification) is clinically available quantification will easily be adapted.

One area where DCEUS quantification can play a very important role is monitoring ultrasound-mediated drug delivery approaches like sonoporation [39]. The safety, bedside availability, and relatively low cost of ultrasound, combined with the ability to measure flow in the microcirculation make DCEUS quantification a valuable tool for real-time

monitoring of therapeutic applications which target the vascular network of tumors. Finally, machine perfusion of human-sized livers combined with DCEUS quantification may play a pivotal role in the study of tumor ablative techniques such as radio frequency and microwave ablation, cryoablation, and irreversible electroporation where not only the lesion formation may be closely monitored but also the changes in the microcirculation in an area around the ablation zone (penumbra).

In tumor perfusion monitoring where vascular changes are happening either as a result of tumor growth or as a response to chemotherapy, the arterial input to the tumor is changing and thus making it more difficult to accurately apply the techniques described. To this effect, also changes due to the cardiac output of the patient as a result of the possible cardiotoxicity of chemotherapy are added, which also further influence the arterial input function. Thus, we have refrained from trying to estimate absolute blood flow rates and instead noted relative changes. In addition, estimation of *PI* relating to the vascular volume and vascular density, in combination with time parameters related to flow, would be important in those cases despite the fact that amplitude parameters (*PI* and *AUC*) are more prone to signal saturation and acoustic shadowing errors.

5.5 Conclusions

Ex-vivo machine perfused pig liver is an excellent test-bed for DCEUS quantification approaches for measuring flow in the macro- and micro-vasculature. It allows for careful control of flow rate changes and the study of the HA and PV vascular networks. The intensity-bubble concentration relationship was found to be linear, which is the underlying assumption for using indicator dilution to measure flow. Rise time and mean transit time are not affected by bubble concentration changes. Induced flow changes in the livers were detected in the larger vessel of either the HA or PV, depending where the injection was administered, and also in the HV and the parenchyma. DCEUS quantification can detect relative flow changes of about 20% and more everywhere in the liver vasculature, i.e., in the larger vessels (arteries and portal veins), the parenchyma and the HV vessels.

Acknowledgements

This work was co-funded by the European Regional Development Fund and the Republic of Cyprus through the Research Promotion Foundation (Project: DIDAKTOR/0311/78). Ine de Cock from University of Ghent is gratefully acknowledged for microbubble preparation used in this work. We are also grateful to Kypros Stylianou for his invaluable technical assistance.

REFERENCES

[1] D. Cosgrove and N. Lassau, "Imaging of perfusion using ultrasound," *Eur. J. Nucl. Med. Mol. Imaging*, vol. 37 Suppl 1, pp. S65–85, Aug. 2010.

[2] S. R. Wilson and P. N. Burns, "Microbubble-enhanced US in body imaging: what role?," *Radiology*, vol. 257, no. 1, pp. 24–39, Oct. 2010.

[3] V. Sboros and M.-X. Tang, "The assessment of microvascular flow and tissue perfusion using ultrasound imaging," *Proc. Inst. Mech. Eng. [H]*, vol. 224, no. 2, pp. 273–290, 2010.

[4] K. Wei, A. R. Jayaweera, S. Firoozan, A. Linka, D. M. Skyba, and S. Kaul, "Quantification of myocardial blood flow with ultrasound-induced destruction of microbubbles administered as a constant venous infusion," *Circulation*, vol. 97, no. 5, pp. 473–483, Feb. 1998.

[5] T. R. Porter and F. Xie, "Myocardial perfusion imaging with contrast ultrasound," *JACC Cardiovasc. Imaging*, vol. 3, no. 2, pp. 176–187, Feb. 2010.

[6] S. R. Wilson and P. N. Burns, "Liver mass evaluation with ultrasound: the impact of microbubble contrast agents and pulse inversion imaging," *Semin. Liver Dis.*, vol. 21, no. 2, pp. 147–159, May 2001.

[7] P. Ricci, V. Cantisani, L. Ballesio, E. Pagliara, E. Sallusti, F. M. Drudi, F. Trippa, F. Calascibetta, S. M. Erturk, M. Modesti, and R. Passariello, "Benign and malignant breast lesions: efficacy of real time contrast-enhanced ultrasound vs. magnetic resonance imaging," *Ultraschall Med. Stuttg. Ger. 1980*, vol. 28, no. 1, pp. 57–62, Feb. 2007.

[8] C. F. Dietrich, M. A. Averkiou, J.-M. Correas, N. Lassau, E. Leen, and F. Piscaglia, "An EFSUMB introduction into Dynamic Contrast-Enhanced Ultrasound (DCE-US) for quantification of tumour perfusion," *Ultraschall Med. Stuttg. Ger. 1980*, vol. 33, no. 4, pp. 344–351, Aug. 2012.

[9] E. Leen, M. Averkiou, M. Arditi, P. Burns, D. Bokor, T. Gauthier, Y. Kono, and O. Lucidarme, "Dynamic contrast enhanced ultrasound assessment of the vascular effects of novel therapeutics in early stage trials," *Eur. Radiol.*, vol. 22, no. 7, pp. 1442–1450, Jul. 2012.

[10] M. Averkiou, M. Lampaskis, K. Kyriakopoulou, D. Skarlos, G. Klouvas, C. Strouthos, and E. Leen, "Quantification of tumor microvascularity with respiratory gated contrast enhanced ultrasound for monitoring therapy," *Ultrasound Med. Biol.*, vol. 36, no. 1, pp. 68–77, Jan. 2010.

[11] N. Lassau, L. Chami, B. Benatsou, P. Peronneau, and A. Roche, "Dynamic contrast-enhanced ultrasonography (DCE-US) with quantification of tumor perfusion: a new diagnostic tool to evaluate the early effects of antiangiogenic treatment," *Eur. Radiol.*, vol. 17 Suppl 6, pp. F89–98, Dec. 2007.

[12] M. Arditi, P. J. A. Frinking, X. Zhou, and N. G. Rognin, "A new formalism for the quantification of tissue perfusion by the destruction-replenishment method in contrast ultrasound imaging," *IEEE Trans. Ultrason. Ferroelectr. Freq. Control*, vol. 53, no. 6, pp. 1118–1129, Jun. 2006.

[13] C. Strouthos, M. Lampaskis, V. Sboros, A. McNeilly, and M. Averkiou, "Indicator dilution models for the quantification of microvascular blood flow with bolus administration of ultrasound contrast agents," *IEEE Trans. Ultrason. Ferroelectr. Freq. Control*, vol. 57, no. 6, pp. 1296–1310, Jun. 2010.

[14] K. Zierler, "Indicator dilution methods for measuring blood flow, volume, and other properties of biological systems: a brief history and memoir," *Ann. Biomed. Eng.*, vol. 28, no. 8, pp. 836–848, Aug. 2000.

[15] Y. Kubota, "Tumor angiogenesis and anti-angiogenic therapy," *Keio J. Med.*, vol. 61, no. 2, pp. 47–56, 2012.

[16] L. Claassen, G. Seidel, and C. Algermissen, "Quantification of flow rates using harmonic grey-scale imaging and an ultrasound contrast agent: an in vitro and in vivo study," *Ultrasound Med. Biol.*, vol. 27, no. 1, pp. 83–88, Jan. 2001.

[17] X. Chen, K. Q. Schwarz, D. Phillips, S. D. Steinmetz, and R. Schlief, "A mathematical model for the assessment of hemodynamic parameters using quantitative contrast echocardiography," *IEEE Trans. Biomed. Eng.*, vol. 45, no. 6, pp. 754–765, Jun. 1998.

[18] J. M. Hudson, R. Karshafian, and P. N. Burns, "Quantification of flow using ultrasound and microbubbles: a disruption replenishment model based on physical principles," *Ultrasound Med. Biol.*, vol. 35, no. 12, pp. 2007–2020, Dec. 2009.

[19] P.-C. Li and M.-J. Yang, "Transfer function analysis of ultrasonic time-intensity measurements," *Ultrasound Med. Biol.*, vol. 29, no. 10, pp. 1493–1500, Oct. 2003.

[20] P.-C. Li, C.-K. Yeh, and S.-W. Wang, "Time-intensity-based volumetric flow measurements: an in vitro study," *Ultrasound Med. Biol.*, vol. 28, no. 3, pp. 349–358, Mar. 2002.

[21] M. Lampaskis and M. Averkiou, "Investigation of the relationship of nonlinear backscattered ultrasound intensity with microbubble concentration at low MI," *Ultrasound Med. Biol.*, vol. 36, no. 2, pp. 306–312, Feb. 2010.

[22] T. P. Gauthier, M. Chebil, P. Peronneau, and N. Lassau, "In vitro evaluation of the impact of ultrasound scanner settings and contrast bolus volume on time-intensity curves," *Ultrasonics*, vol. 52, no. 1, pp. 12–19, Jan. 2012.

[23] E. A. Eisenhauer, P. Therasse, J. Bogaerts, L. H. Schwartz, D. Sargent, R. Ford, J. Dancey, S. Arbuck, S. Gwyther, M. Mooney, L. Rubinstein, L. Shankar, L. Dodd, R. Kaplan, D. Lacombe, and J. Verweij, "New response evaluation criteria in solid tumours: revised RECIST guideline (version 1.1)," *Eur. J. Cancer Oxf. Engl. 1990*, vol. 45, no. 2, pp. 228–247, Jan. 2009.

[24] N. Lassau, M. Lamuraglia, L. Chami, J. Leclère, S. Bonvalot, P. Terrier, A. Roche, and A. Le Cesne, "Gastrointestinal Stromal Tumors Treated with Imatinib: Monitoring Response with Contrast-Enhanced Sonography," *Am. J. Roentgenol.*, vol. 187, no. 5, pp. 1267–1273, Nov. 2006.

[25] V. Lazar, N. Lassau, G. Meurice, Y. Loriot, C. Peña, C. Massard, C. Robert, T. Robert, M.-A. Le Berre, T. de Baere, P. Dessen, J.-C. Soria, and J.-P. Armand, "Sorafenib plus dacarbazine in solid tumors: a phase I study with dynamic contrast-enhanced ultrasonography and genomic analysis of sequential tumor biopsy samples," *Invest. New Drugs*, vol. 32, no. 2, pp. 312–322, Apr. 2014.

[26] N. Lassau, J. Bonastre, M. Kind, V. Vilgrain, J. Lacroix, M. Cuinet, S. Taieb, R. Aziza, A. Sarran, C. Labbe-Devilliers, B. Gallix, O. Lucidarme, Y. Ptak, L. Rocher, L.-M. Caquot, S. Chagnon, D. Marion, A. Luciani, S. Feutray, J. Uzan-Augui, B. Coiffier, B. Benastou, and S. Koscielny, "Validation of dynamic contrast-enhanced ultrasound in predicting outcomes of antiangiogenic therapy for solid tumors: the French multicenter support for innovative and expensive techniques study," *Invest. Radiol.*, vol. 49, no. 12, pp. 794–800, Dec. 2014.

[27] R. Williams, J. M. Hudson, B. A. Lloyd, A. R. Sureshkumar, G. Lueck, L. Milot, M. Atri, G. A. Bjarnason, and P. N. Burns, "Dynamic microbubble contrast-enhanced US to measure tumor response to targeted therapy: a proposed clinical protocol with results from renal cell carcinoma patients receiving antiangiogenic therapy," *Radiology*, vol. 260, no. 2, pp. 581–590, Aug. 2011.

[28] M.-L. Izamis, A. Efstathiades, C. Keravnou, E. L. Leen, and M. A. Averkiou, "Dynamic contrast-enhanced ultrasound of slaughterhouse porcine livers in machine perfusion," *Ultrasound Med. Biol.*, vol. 40, no. 9, pp. 2217–2230, Sep. 2014.

[29] C. Keravnou, C. Mannaris, and M. Averkiou, "Accurate measurement of microbubble response to ultrasound with a diagnostic ultrasound scanner," *IEEE Trans. Ultrason. Ferroelectr. Freq. Control*, vol. 62, no. 1, pp. 176–184, Jan. 2015.

[30] W. F. Hamilton, J. W. Moore, J. M. Kinsman, and R. G. Spurling, "Simultaneous determination of the pulmonary and systemic circulation times in man and of a figure related to the cardiac output," *Am. J. Physiol. -- Leg. Content*, vol. 84, no. 2, pp. 338–344, Mar. 1928.

[31] G. N. Stewart, "Researches on the Circulation Time in Organs and on the Influences which affect it: Parts I.-III," *J. Physiol.*, vol. 15, no. 1–2, pp. 1–89, Jul. 1893.

[32] M. Schneider, "Characteristics of SonoVue™," *Echocardiography*, vol. 16, pp. 743–746, 1999.

[33] N. Lassau, S. Koscielny, L. Albiges, L. Chami, B. Benatsou, M. Chebil, A. Roche, and B. J. Escudier, "Metastatic renal cell carcinoma treated with sunitinib: early evaluation of treatment response using dynamic contrast-enhanced ultrasonography," *Clin. Cancer Res. Off. J. Am. Assoc. Cancer Res.*, vol. 16, no. 4, pp. 1216–1225, Feb. 2010.

[34] N. Lassau, S. Koscielny, L. Chami, M. Chebil, B. Benatsou, A. Roche, M. Ducreux, D. Malka, and V. Boige, "Advanced hepatocellular carcinoma: early evaluation of response to bevacizumab therapy at dynamic contrast-enhanced US with quantification--preliminary results," *Radiology*, vol. 258, no. 1, pp. 291–300, Jan. 2011.

[35] N. Lassau, L. Chami, S. Koscielny, M. Chebil, C. Massard, B. Benatsou, S. Bidault, A. Cioffi, J.-Y. Blay, and A. Le Cesne, "Quantitative functional imaging by dynamic contrast enhanced ultrasonography (DCE-US) in GIST patients treated with masatinib," *Invest. New Drugs*, vol. 30, no. 2, pp. 765–771, Apr. 2012.

[36] M.-X. Tang, H. Mulvana, T. Gauthier, A. K. P. Lim, D. O. Cosgrove, R. J. Eckersley, and E. Stride, "Quantitative contrast-enhanced ultrasound imaging: a review of sources of variability," *Interface Focus*, vol. 1, no. 4, pp. 520–539, Aug. 2011.

[37] G. L. ten Kate, G. G. J. Renaud, Z. Akkus, S. C. H. van den Oord, F. J. ten Cate, V. Shamdasani, R. R. Entrekin, E. J. G. Sijbrands, N. de Jong, J. G. Bosch, A. F. L.

Schinkel, and A. F. W. van der Steen, “Far-wall pseudoenhancement during contrast-enhanced ultrasound of the carotid arteries: clinical description and in vitro reproduction,” *Ultrasound Med. Biol.*, vol. 38, no. 4, pp. 593–600, Apr. 2012.

[38] A. Thapar, J. Shalhoub, M. Averkiou, C. Mannaris, A. H. Davies, and E. L. S. Leen, “Dose-dependent artifact in the far wall of the carotid artery at dynamic contrast-enhanced US,” *Radiology*, vol. 262, no. 2, pp. 672–679, Feb. 2012.

[39] I. Lentacker, I. De Cock, R. Deckers, S. C. De Smedt, and C. T. W. Moonen, “Understanding ultrasound induced sonoporation: definitions and underlying mechanisms,” *Adv. Drug Deliv. Rev.*, Nov. 2013.

6 Extravasation and vascular perfusion changes induced by ultrasound and microbubbles in a machine-perfused pig liver model

Drug delivery and uptake may be improved with the application of ultrasound and microbubbles and some of the possible mechanisms suggested are sonoporation and extravasation. *Ex-vivo* machine perfusion of human-sized organs is a new technique that provides an ideal environment for preclinical investigations with high physiological relevance not available in *in-vitro* experiments. In this work, *ex-vivo* machine-perfused pig livers combined with an image-guided therapy system were used to investigate extravasation and the induced microvascular changes. The interaction of ultrasound driven microbubbles with the capillaries were qualitatively and quantitatively assessed and the acoustic parameters that are capable of causing extravasation and detectable perfusion changes in the treated area were derived. Areas that were exposed to acoustic pressure above 3 MPa showed a detectable perfusion change. Complete mechanical damage was present at much larger acoustic pressures (~10 MPa). Shorter acoustic pulses (20 cycles) produced less perfusion changes than longer pulses (1000 cycles) under the same acoustic amplitude exposure.

Keywords: sonoporation, extravasation, machine perfusion, machine-perfused pig liver, drug delivery

---

In preparation for submission to *Physics in Medicine and Biology* by: C.P. Keravnou, I. de Cock, M.L. Izamis and M.A. Averkiou

6.1 Introduction

Currently, microbubbles are considered to be an integral part of ultrasound-mediated drug delivery applications since they can facilitate local release of therapeutics at the diseased site while also increase local uptake. Several published studies have reported that the physical interaction of ultrasound and microbubbles has the potential to enhance drug delivery by altering cell membrane permeability, a process referred to as sonoporation, allowing for the uptake of normally impermeable molecules into the cells [1], [2].

One of the main mechanisms of sonoporation is acoustic cavitation. When acoustic pressures above the cavitation threshold of a medium are used, the rarefactional portion of the propagated ultrasound wave may initiate cavitation activity (if cavitation nuclei are present). Alternatively, ultrasound will also induce cavitation by the pulsation of pre-existing gas bodies (such as microbubbles). Stable oscillations of microbubbles are observed under low acoustic pressure exposure (MI< 0.2). In contrast, when microbubbles are exposed to higher acoustic pressure, inertial cavitation takes place, leading to violent collapse of the oscillating bubbles. It is stated in literature that various effects which occur during stable and inertial cavitation (such as microstreaming, microjets and shock wave formation) contribute towards cell membrane disruption and mediate drug uptake either by direct pore formation (a process called sonoporation) or by enhancing endocytosis [1], [3].

Sonoporation has been extensively studied both *in-vitro* (using multiple types of cell cultures) [4]–[6] and *in-vivo* (mainly in small animal models) [7], [8]. It was reported that compounds <1kDa [9], macromolecules [10] and genes [11], [12] have successfully been delivered into the cells. Recently a small pilot clinical study on treating pancreatic cancer utilizing the combined effects of ultrasound, microbubbles and gemcitabine has also been published [13].

However, the translation of the acoustic parameters studied *in-vitro* to clinical application is still a great challenge. This is because at *in-vitro* studies, tumor cells are directly exposed to the ultrasound field and microbubbles, while in *in-vivo* applications of ultrasound-enhanced drug delivery, the interactions between microbubbles and cells are much more complex. After intravenously injected, microbubbles and drugs are present in the systemic circulation for a period of time. Thus, the first step towards ultrasound-mediated drug delivery is to alter the permeability of endothelial cells of the vessel wall.

With increased endothelial permeability, drugs that would otherwise remain confined within the vasculature are allowed to extravasate into the interstitial space and reach the targeted cells (e.g. tumor cells). The need of investigating basic drug delivery mechanisms in an environment that closely resembles the *in-vivo* conditions is therefore essential prior to clinical studies.

Machine perfusion (MP) is a method of sustaining an isolated organ alive outside the body (*ex-vivo*) by supplying it with oxygen and nutrients. Recently, Izamis et al. (2014) developed and evaluated a sub-normothermic human-sized machine perfusion system suitable to preserve slaughterhouse pig livers. They showed using biochemical and hemodynamic measurements and dynamic contrast-enhanced ultrasound (DCEUS) that the developed model is a simple, cost-effective approach for at least 3 hours of stable, *ex-vivo* whole organ preservation. Since MP enables several hours of controlled and stable experimentation with the organ of interest, while maintains high physiological relevance lacking from *in-vitr*o experiments, it is an ideal environment for preclinical diagnostic, imaging and therapeutic investigations.

The objective of this work was to identify the ultrasound parameters that are capable of causing detectable perfusion changes and extravasation in the area exposed to ultrasound in a test platform that closely resembles *in-vivo* conditions. Thus, the interactions of ultrasound-driven microbubbles with the capillaries were investigated in a functioning *ex-vivo* machine perfused pig liver model. An experimental setup was developed that allowed real-time monitoring of the therapy procedure and imaging of the cavitation activity. The effect of acoustic pressure, number of cycles, and microbubble presence on the induced bioeffects in tissue was evaluated with qualitative and quantitative DCEUS and histology. Microvascular flow changes were measured and used as a metric of the degree of extravasation.

6.2 Materials and methods

6.2.1 Ex-vivo machine perfusion of porcine livers

The studies were approved by the Cyprus National Bioethics Committee and the Cyprus National Veterinary Services. Healthy porcine livers were procured from a local abattoir. Details on liver procurement can be found elsewhere [14]. Briefly, immediately

after the animal death, the livers were isolated from the rest of the thoracic and abdominal organs at the slaughterhouse and they were flushed with 8L of Lactated Ringers (6L room temperature and 2L ice cold) through the portal vein (PV) and the hepatic artery (HA).

The organs were then stored on ice and transported to the laboratory (time of static cold storage was ≤ 1 hour), where they were connected to the machine perfusion system [Fig. 6.1(a)] and sustained for up to 6 hours. The perfusion system comprised a 6L perfusate reservoir (Powdered Williams Medium E (10.8g/L W4125, Sigma-Aldrich Corp. St Louis, MO, USA) with addition of 2.2g/L of sodium bicarbonate (S5761, Sigma-Aldrich Corp. Medisell, Cyprus), 1000 IU/L heparin, 2 U/L insulin (Actrapid® Penfill® Novo Nordisk, Novo Alle, Denmark), and 0.4 mg/L dexamethasone (Dexamed, Medochemie Ltd, Limassol, Cyprus), in which the organ was suspended. A pump (Masterflex L/S Digital Drive 600rpm, Cole Parmer) circulated the perfusate through an oxygenator (Affinity NT, Medtronic, Minneapolis, MN, USA) supplied with 95% O_2, 5% CO_2 (Tenaris, Bergamo, Italy) before being split and passed through two flow meters (EW-32461-44 and EW-32460-40, Cole Parmer) that enable pressure-regulated flow to each of the PV and HA, respectively. Effluent was then allowed to flow freely from the liver's vena cava back into the reservoir, closing the circuit. Flow rate was set to 800 ml/min for the PV and 400 ml/min for the HA. The selected flow rates ensured that PV pressure was ≤10 cmH_2O and HA pressure was between 60 and 100 cmH_2O. Hepatic stability was ascertained with one-hour interval measurements of bile production, oxygen consumption, and sustained vascular perfusion as described in [14]. The perfusion was monitored via DCEUS imaging [Fig. 6.1(b, c)]. The circuit provided individual syringe port access to each of the hepatic vessels so that ultrasound contrast agents could be administered to either the PV or HA.

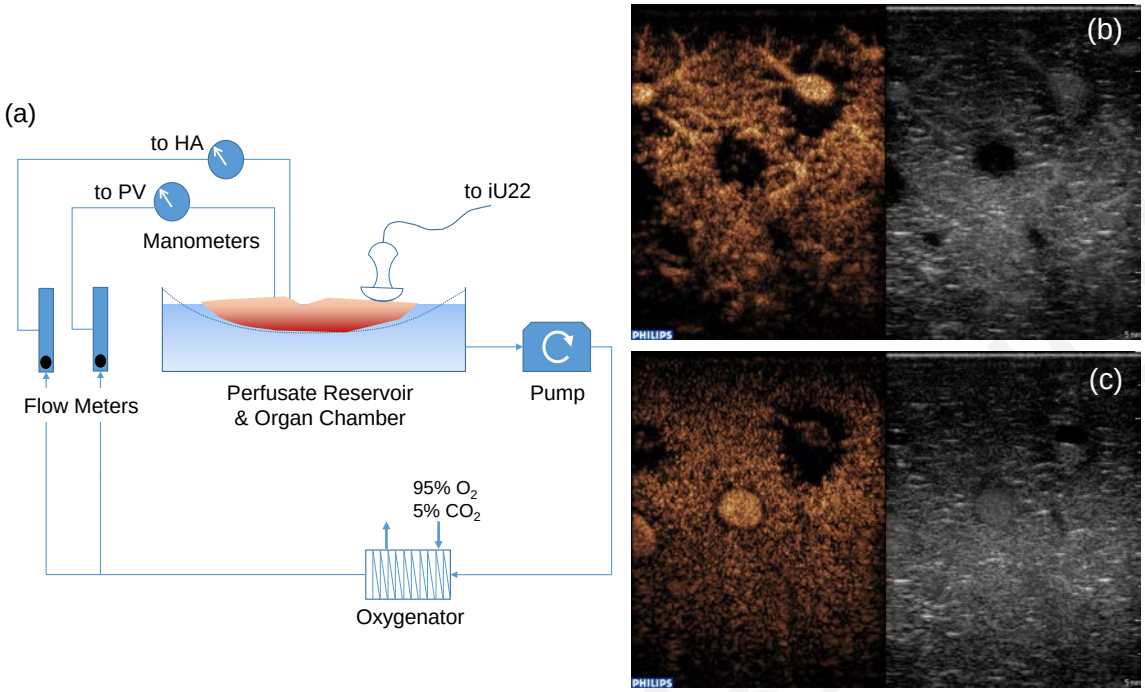

Figure 6.1: (a) The machine perfusion system consists of an organ chamber in which the liver is suspended, a single pump and oxygenator, and two flow meters/regulators connected to the hepatic artery (HA) and the portal vein (PV). Dynamic contrast-enhanced ultrasound images taken at 10 sec (b) and at 20 sec (c) after a PV bolus injection.

6.2.2 Experimental setup

The complete experimental setup is shown in Fig 6.2(a). Briefly, the experimental setup consisted of two diagnostic ultrasound scanners, the *ex-vivo* machine perfusion system and a focused, single element circular transducer. The focused, single element circular transducer (diameter *diam.*=60 mm, focal distance d = 75 mm, frequency f = 1 MHz) was used to treat a specific target area of the machine-perfused pig liver [Fig 6.2(b)]. In front of the transducer, a 50mm x 100ø mm custom made acrylic cylinder filled with de-ionized water was placed, to ensure that the focus of the transducer (area of treatment) would be roughly in the middle of the chosen liver lobe (approximate size of a liver lobe 50 mm) [Fig. 6.3(a)]. The bottom side of the cylinder had an acoustically transparent window made of a 0.01 mm mylar membrane. The therapy transducer was held fixed with it's focus placed in a well-perfused liver area using a mechanical articulated arm (Fisso, Baitella AG, Zurich, Switzerland). To monitor the perfusion of the treated area and record contrast loops, a C5-1 curved array probe of a Philips iU22 diagnostic ultrasound scanner (Phillips Medical Systems, Bothell, WA, USA) was placed under the perfusate container using a mechanical arm as shown in Fig 6.2(c). The alignment of the therapy transducer

with the C5-1 image probe was achieved using a micro-positioning system (Newport, Irvine, CA). The therapy transducer spatial extend was accurately overlaid in the ultrasound images of the C5-1 probe by a novel technique where the Radio Frequency (RF) noise of the power amplifier was transmitted through the therapy transducer and detected by the diagnostic ultrasound probe as shown in Fig. 6.2(d). The perfusion of an area located at a different lobe [Fig 6.2(b, c)] was also monitored using an L9-3 linear probe of a second iU22 diagnostic ultrasound scanner to be used as control (untreated site).

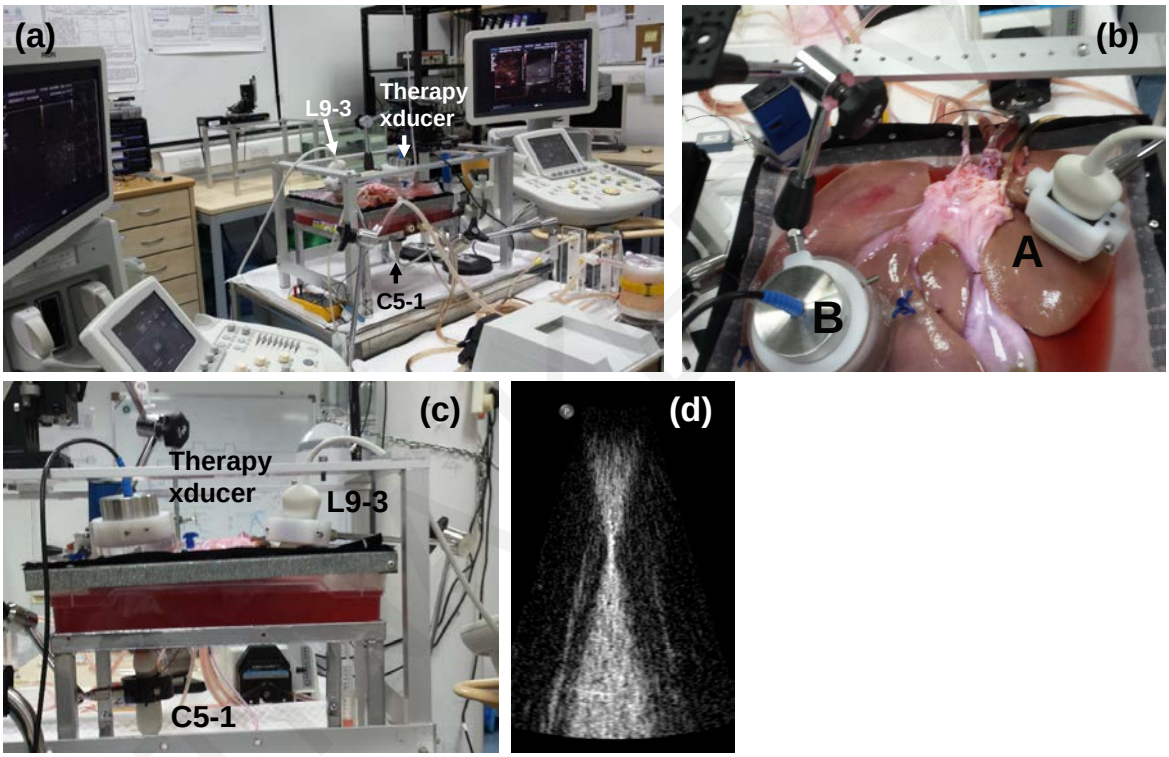

Figure 6.2: (a) Experimental setup of the *ex-vivo* machine perfused pig liver combined 2 ultrasound scanners and a therapy transducer. (b) Close-up of the control area (A) and the treated area (B) located at two different lobes of the liver. (c) The perfusion of the treated area was monitored with a C5-1 imaging probe and the perfusion of the control area was monitored with an L9-3 imaging probe. (d) Therapy transducer RF interference signal picked by the imaging probe.

6.2.3 Ultrasound transducer characterization

The linear acoustic field of the single element circular transducer which was used to treat the livers was measured using a 0.4 mm membrane hydrophone (Precision acoustics Ltd., Dorchester, UK). A motorized micro-positing system (Newport, Irvine, CA) was used to align the transducer and the hydrophone and to move the hydrophone to the desired location.

The measurements were taken in deionized water using a step of 2.5 mm in the axial direction and 0.5 mm in the transverse direction to create a two dimensional beam profile. The measured low amplitude 2D beam profile was then used to calculate a higher pressure field up to 10 MPa, [Fig. 6.3(b)] – by taking into consideration liver attenuation ($\bar{\alpha}$ = 9.05 Np/m at 1 MHz) and linear extrapolation [15].

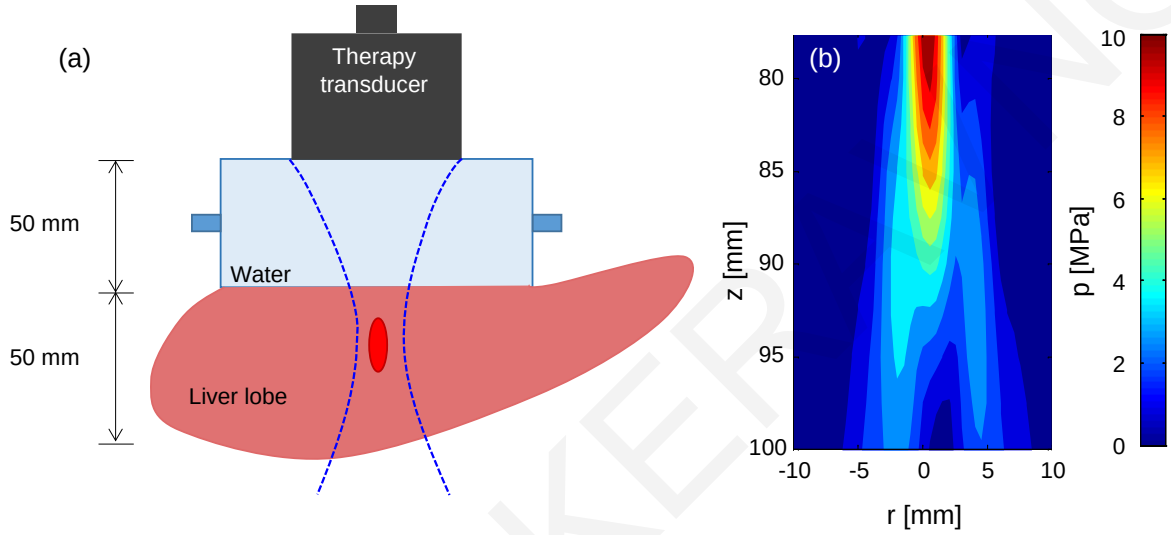

Figure 6.3: (a) Schematic representation of the experimental setup. The sound beam first goes through a water column before reaching the therapy site in the liver. (b) Estimated beam profile of the therapy transducer in liver tissue, calculated from low amplitude water measurements and liver tissue attenuation.

6.2.4 Therapy protocol

In order to investigate the interaction of ultrasound driven microbubbles with the capillaries and study the effect of ultrasound parameters relevant for extravasation, 15 liver experiments were divided in 5 groups (n=3 in each group). The ultrasound frequency was 1 MHz and the duty cycle (DC) was <8% in all liver groups to avoid heating during ultrasound exposure. More details on the acoustic parameters used in the 5 liver groups are given below:

a. The first liver group was exposed to the highest acoustic pressure and number of cycles (10 MPa, 1000 cycles), while microbubbles were sequentially administrated in the PV and HA during treatment.
b. The second liver group was also exposed to the highest acoustic pressure and number of cycles (10 MPa, 1000 cycles) however microbubbles were not

administrated during treatment, to be able to compare with case (a) and investigate the effect of microbubble absence or presence in vascular disruption.

c. The third liver group was exposed to the highest acoustic pressure (10 MPa) and short pulses (20 cycles) in the absence of microbubble administration during treatment. This group may be compared with group (b) in order to investigate the effect of number of cycles in the absence of microbubbles in vascular disruption.
d. The forth liver group was exposed to 6 MPa while 1000 cycles were used during treatment. In this liver group microbubbles were sequentially administrated in the PV and HA during treatment. This group is similar to group (a) except the pressure now is lower.
e. The fifth liver group was exposed to 3 MPa while 1000 cycles were used during treatment. In this liver group microbubbles were sequentially administrated in the PV and HA during treatment. Groups (a), (d), and (e) only differ in acoustic pressure. Acoustic pressure in groups (d) and (e) was decreased to investigate the threshold of vascular disruption and mechanical ablation of tissue.

Tone bursts were generated using a Tektronix AFG 3102 Function Generator (Tektronix, Inc., Beaverton, OR) amplified by a 150A100B RF Amplifier (Amplifier Research, Souderton, PA) and transmitted via the focused transducer. The transmission protocol was 5 seconds on and 5 seconds off for 15 minutes. After 15 minutes of treatment the transducer was moved 4 mm and the protocol was repeated for total treatment time of 1 hour.

6.2.5 Microbubbles preparation

Custom made microbubbles (Department of Pharmaceutics, University of Ghent, Ghent, Belgium), very similar to Definity clinical ultrasound contrast agents were used throughout this work. The composition of the microbubbles was DPPC/DSPE-PEG in 95:5 molar ratio. Microbubbles were made of Perfluorobutane gas (PFB, C_4F_{10}), while at the shell a PEGylated lipid was added to enhance stability. The average size of the microbubbles was 2.5 μm and the concentration of the microbubbles was $3\text{-}8x10^8$ microbubbles/mL. Microbubbles were diluted to a concentration of 0.04‰ (0.04 ml to 1 litter of de-ionized water) prior to bolus injections.

6.2.6 Imaging protocol and microbubbles administration

Contrast side-by-side mode was selected in both ultrasound probes (C5-1 and L9-3) to monitor macro- and micro- vascular flow (contrast image left side), and liver's anatomical features (tissue image right side). The imaging frame rate was 9 and 12 Hz for C5-1 and L9-3 respectively. The compression (dynamic range) was set at the maximum that was available on the scanner (50 dB) and persistence was turned off to avoid temporal averaging between consecutive frames and to facilitate quantification. Imaging depth and MI were 10 cm and 0.06 for C5-1, and 5 cm and 0.06 for L9-3.

Prior to US treatment and every 15 minutes (for a total of 1 hour), a 2 ml bolus of microbubbles was injected in the syringe port connected to the PV. Image loops of 60 seconds were captured using both imaging probes (C5-1 and L9-3) and the procedure was repeated for the HA. At the end of the 1 hour treatment and before collecting image loops to quantify the effects of the ultrasound treatment, a fresh vial of microbubbles was opened and used for the bolus injections to the PV and the HA. The reason for the fresh vial was to make sure that any vascular changes were due to the treatment and not due to bubble deterioration due to the length of the treatment.

6.2.7 Quantification and data analysis

QLAB software (Philips Medical Systems, Bothell, WA) was used to form time-intensity curves (TICs) from the DICOM files by placing a region of interest (ROI) on the image. The ROI was placed on each image in a well perfused parenchyma area avoiding large vessels [Fig. 6.4(a, b)]. The ROI at the liver treated site was placed near the focus of the therapy transducer.

Time-intensity curves were extracted [Fig. 6.4(c, d)] from QLAB and fitted to an LDRW model [16] using purpose created MATLAB (The MathWorks, Inc., Natick, MA, USA) code. Quantification parameters [17] such as rise time (RT), mean transit time (MTT), area under the curve (AUC) and peak intensity (PI) were recorded after the fit and plotted as a function of treatment time. In order to be able to compare parameters between different livers and different ROIs, the extracted quantification parameters were normalized with respect to the maximum value of each parameter per studied liver.

Analysis was also performed using a Log-normal model [16] (not shown here) but the LDRW model had significantly higher coefficient of determination (R^2).

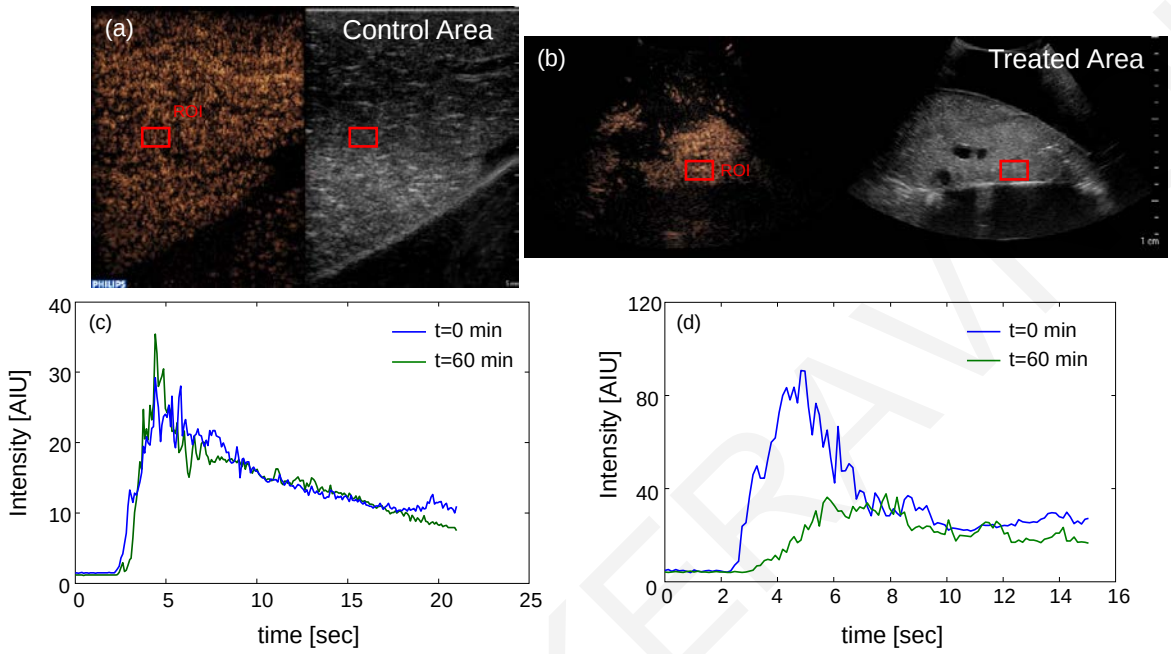

Figure 6.4: Dynamic contrast-enhanced ultrasound quantification was used to detect microvascular perfusion changes after ultrasound treatment. An example of time-intensity curves formed from regions of interest taken at the control (a) and the treated area (b) is shown in (c) and (d) respectively. Regions of interest at the control area were placed so that large vessels were avoided.

6.2.8 Histology

Histology was conducted on all livers using biopsies procured at the end of perfusion. For each liver, one biopsy was collected from the center of a lobe that was not treated with ultrasound (control) and one from the treated lobe after examining the gross morphology of the treated area. All samples were stored in 4% formaldehyde, processed and stained with hematoxylin and eosin (H&E). Images were captured using an Olympus BX51 microscope (Tokyo, Japan) and Olympus DP2-Twain compatible software (ImageReady, Version 8, Adobe, San Jose, CA, USA).

6.3 Results

Figure 6.5 shows B-mode images of cavitation activity taking place during the therapeutic procedure. These images were obtained from group (a) of the therapy protocol (p=10 MPa, 1000 cycles, plus microbubbles). It is observed that cavitation activity begins almost immediately after the therapeutic transducer is turned on [Fig. 6.5(a)], while the phenomenon continues and enhances with time [Fig. 6.5(b, c)]. As a side note, the observation of the cavitation activity confirms that the imaging and therapy planes coincide.

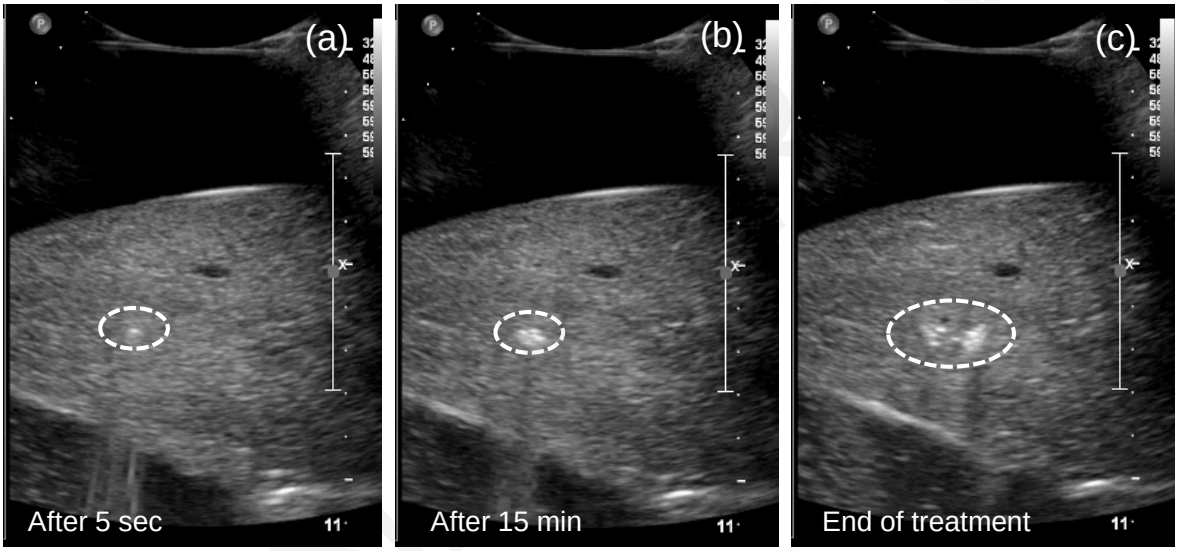

Figure 6.5: Imaging of the cavitation activity in tissue during ultrasound exposure. (a) 5 sec after ultrasound exposure, (b) after 15 minutes of treatment, (c) at the end of the treatment (1 hour). These images were obtained when 10 MPa and 1000 cycles were applied to the treated site while microbubbles were also injected.

Visual evaluation of the imaged treated site and overall gross morphology inspection was performed at the end of the therapeutic procedure. Examples of gross morphology of the liver tissue at the end of the experiments for different liver groups are shown in Fig. 6.6. It is observed that the size and extent of the created lesion highly correlates with the applied acoustic pressure. In addition, great correlation between B-mode images and gross morphology was observed in all cases, suggesting that ultrasound imaging is an accurate way to monitor such therapeutic approaches.

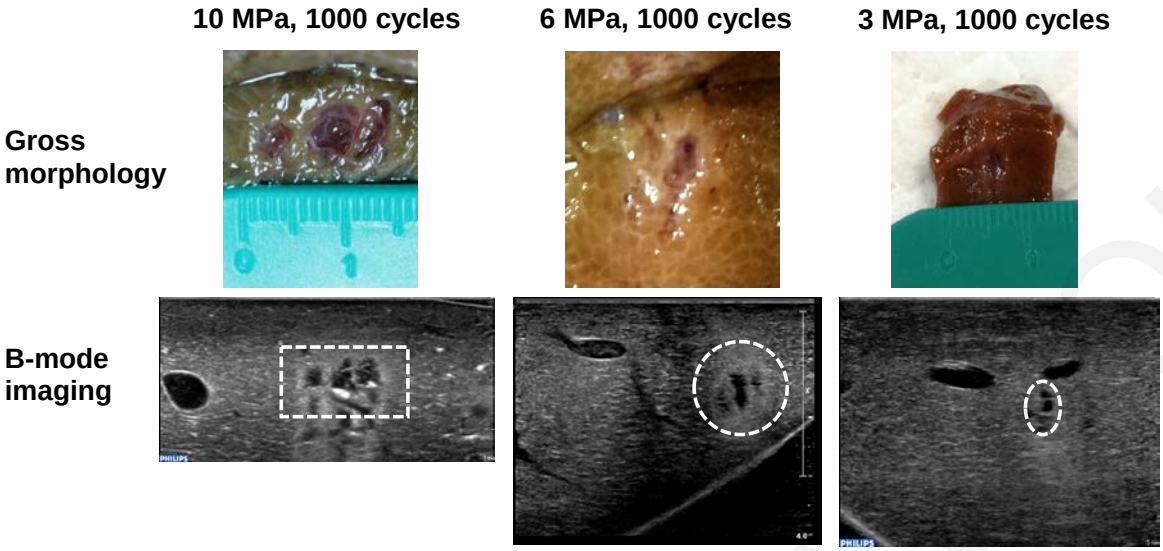

Figure 6.6: Observations (gross morphology and B-mode images) after 1 hour of ultrasound treatment for different acoustic pressure amplitudes. Good correlation between gross morphology and B-mode imaging was obtained and lesion size depends on the applied acoustic pressure.

Qualitative evaluation of the perfusion of the treated area as a function of time was performed with DCEUS. Figure 6.7 shows contrast and tissue images (side-by-side) of perfusion after a PV injection (on the left) and HA (on the right) at the beginning of the treatment, at 15 minutes, and at the end of the treatment (p=10 MPa, plus microbubbles, 1000 cycles). It is observed that lesion formation at tissue exposed to the focal area of the transducer appears within minutes of ultrasound application, while the lesion spreads to a larger area by the end of the treatment. Lesion formation highly correlates with cavitation activity shown in Fig. 6.5. Perfusion changes at the portal venous vascular tree were [white arrow in Fig. 6.7(e)] were limited in extend. In contrast, almost complete mechanical damage of the arterial vascular tree was observed [Fig. 6.7(f)].

Quantitative evaluation was also performed using DCEUS image loops and indicator dilution approach in order to measure flow changes in the treated area most probably induced by the extravasation. Since the arterial vascular tree suffered severe perfusion changes after ultrasound exposure, prober curve fitting with the formed TICs was not possible. However, the normalized intensity with respect to the intensity before ultrasound was applied was measured and it is shown in Fig. 6.8. The intensity is reduced by more than 60% at the treated site in group (a) of the therapy protocol (p=10 MPa, plus microbubbles, 1000 cycles).

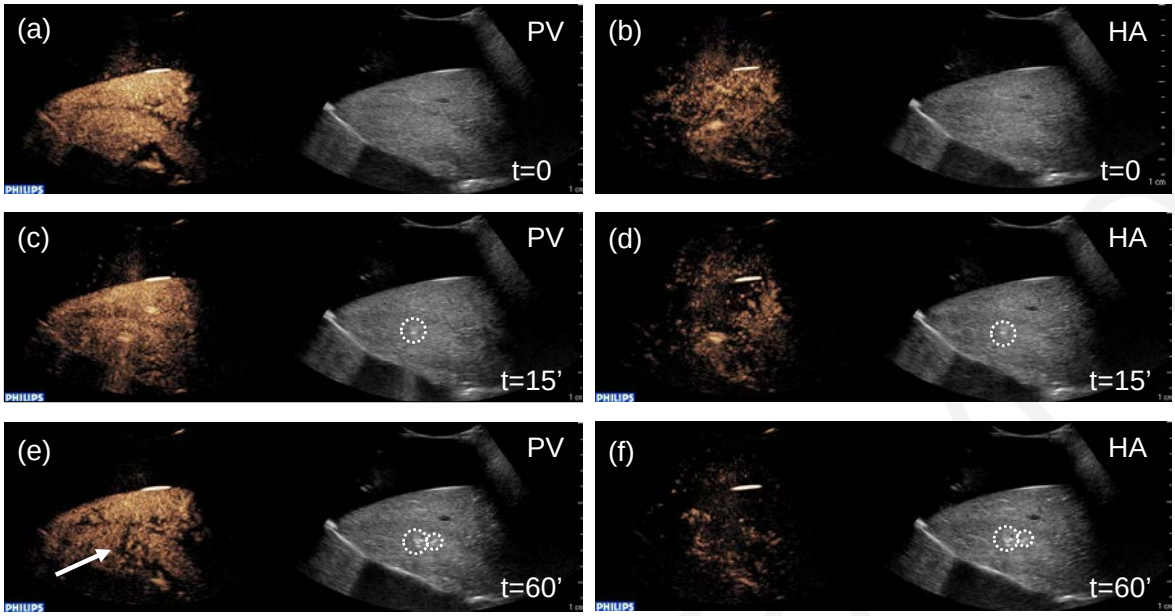

Figure 6.7: Qualitative evaluation of liver perfusion as therapy time progresses. Images obtained after portal vein (PV) bolus injections are shown on the left [(a), (c), (e)] and images obtained after hepatic artery (HA) bolus injections are shown on the right [(b), (d), (f)] . 10 MPa and 1000 cycles were applied to the treated site with the addition of microbubbles during ultrasound exposure. More pronounced changes are observed on the arterial vasculature.

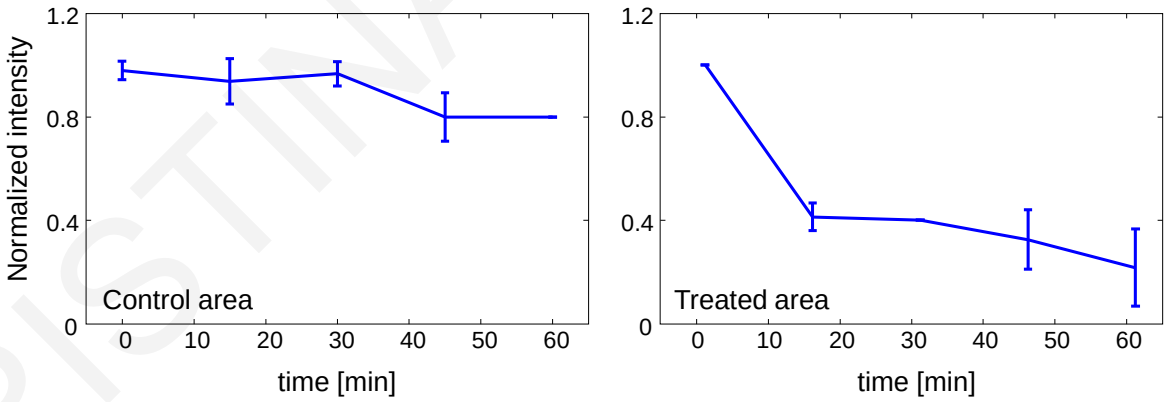

Figure 6.8: Intensity as a function of treatment time for the control area (left) and the treated area (right) for hepatic artery perfusion. The treated site was exposed to 10 MPa and 1000 cycles. Here, microbubbles were also injected during ultrasound exposure.

Time-intensity curves after portal vein injections were formed and the LDRW model was fitted on the data. Figure 6.9 shows the average rise time (normalized with respect to the maximum value obtained in each liver) for the various liver groups of the therapy protocol as a function of therapy time. Time-intensity curves for the control area are shown in the left column and for the treated area in the right. The effect of the acoustic pressure is observed in Fig. 6.9(a, b), the pulse duration (20 vs 1000 cycles) in Fig. 6.9(c, d) and the presence or absence of microbubbles during therapy in Fig. 6.9(e, f). No significant changes in microvascular perfusion (in terms of rise time) of the control area were observed for the different groups studied here [Fig. 6.9(a, c, e)].

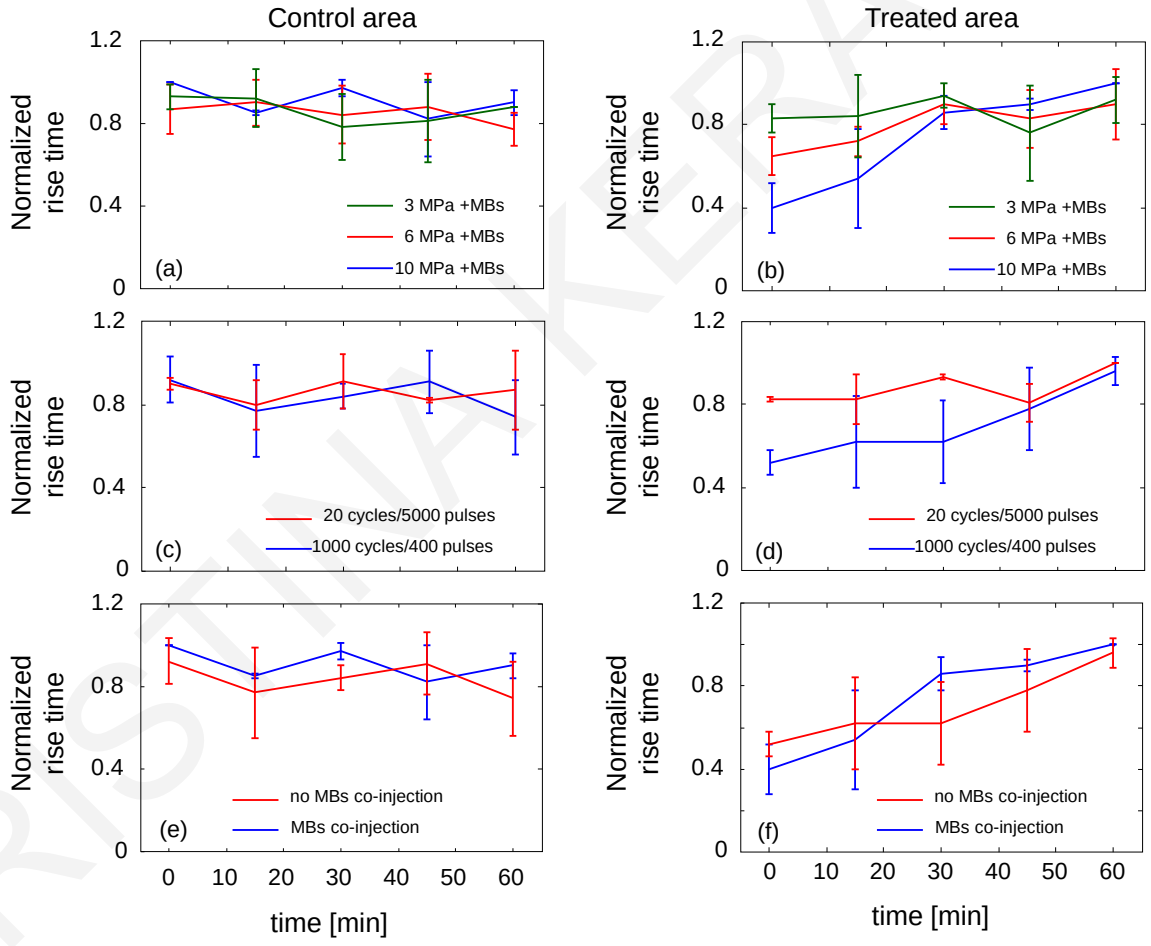

Figure 6.9: Normalized rise time (RT) extracted from LDRW indicator dilution model as a function of treatment time for the control (left) and the treated area (right). Portal vein bolus injections were quantified here. Different liver groups are compared; (a, b) the effect of pressure amplitude when 1000 cycles were applied in the presence of microbubbles, (c, d) the effect of pulse length when 10 MPa were applied in the absence of microbubbles and (e, f) the effect of microbubble presence when 10 MPa and 1000 cycles were applied.

The effect of the acoustic pressure on perfusion changes during ultrasound exposure is shown in Fig. 6.9(b). It is observed that RT increases over time at a different rate for each treatment group (10 MPa, 6 MPa, and 3 MPa). Rise time increase is clearly seen when higher acoustic pressures are used (10 MPa and 6 MPa). Since RT increase is related to flow decrease, the results presented here suggest that micro-vascular flow on the treated area is significantly reduced by the end of the treatment when pressures $\geq$ 6 MPa are utilized. Pulse length effect on flow changes during ultrasound exposure (for the same acoustic pressure, 10 MPa no MBs) is shown in Fig. 6.9(d). Rise time change (thus flow change) was not detected when short pulses (20 cycles) were utilized in the therapy protocol. In contrast, when long pulses were used (1000 cycles) RT increased with therapy time, suggesting that microvascular flow changes were occurring. Finally, the effect of microbubble use during treatment is shown in Fig. 6.9(f). It is observed that there are no significant differences in RT among the two groups (MB presence or absence). Both groups show comparable RT increase as therapy progresses when tissue is exposed to acoustic pressure p=10 MPa.

Leakage of the perfusate in the interstitial space was detected at the end of the treatment after microbubble injection and imaging of the area, using an L12-5 probe which has higher resolution. This observation is an indication of extravasation. As shown in Fig. 6.10, contrast microbubbles were pooling in the treated area while the parenchyma in the surrounding tissue appeared to wash-out. Pooling of microbubbles around the treated area was noticed in all liver groups when long pulses (1000 cycles) were used during treatment.

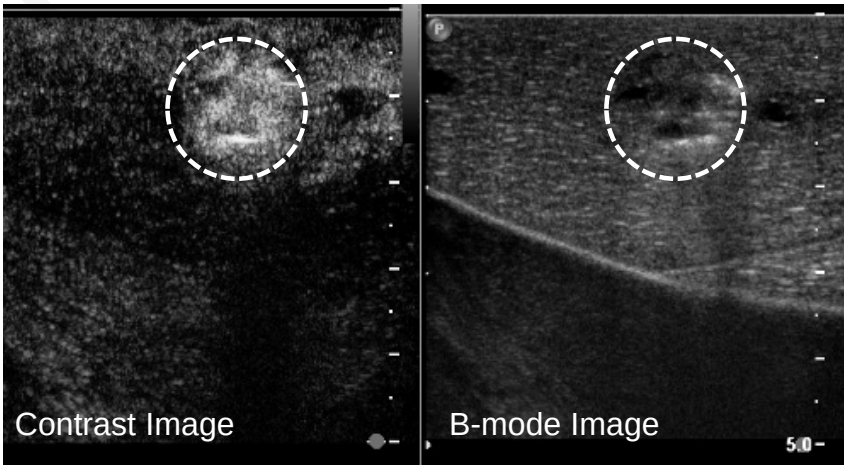

Figure 6.10: Indication of extravasation as a result of vascular alterations after ultrasound exposure. These images were obtained when 6 MPa and 1000 cycles were applied to the treated site. Microbubbles were also injected during ultrasound exposure.

Figure 6.11, shows comparison between histological results of the control and the treated area in the presence or absence of microbubbles when exposed to acoustic pressure of 10 MPa and 1000 cycles. The architecture of the liver tissue samples is shown in Fig. 6.11 (top row), while the morphology of the cells are shown in Fig. 6.11(bottom row). It is observed that there are not significant architectural differences among the compared liver tissue samples [Fig. 6.11 (top row)] concluding that tissue damage is highly controlled in the focal zone of the transducer and taking into account that these samples are from different machine perfused livers. However, more cell damage is observed in the case where liver tissue was exposed to 10 MPa combined with microbubbles [Fig. 6.11 (e)].

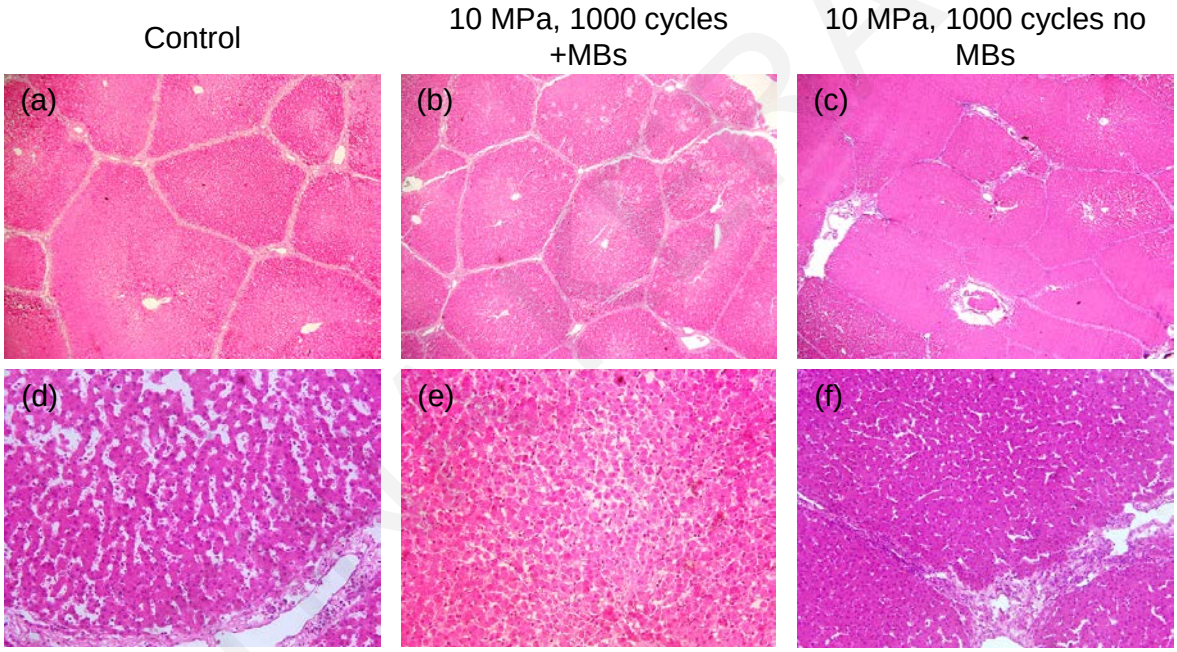

Figure 6.11: Comparison of histological results (H&E staining) between the control (a, d) and the treated areas exposed to acoustic pressure of 10 MPa and 1000 cycles in the presence (b, e) or absence (c, f) of contrast microbubbles. The top row shows the architecture of the liver tissue samples (4x magnification) while the bottom row shows the morphology of the cells (20x magnification).

6.4 Discussion

The interaction of ultrasound-driven resonant microbubbles with the microvasculature was investigated in a functioning *ex-vivo* pig liver model. The size of the microbubbles that were used in the experiments was 2.5μm, and thus they were very close to resonance when exposed to 1 MHz frequency. In addition, the proposed microbubbles did not interact with the environment of the pig liver and a satisfactory wash-out was observed in the parenchyma, despite the luck of lungs or filtering, thus making possible perfusion quantification. The proposed machine-perfused slaughterhouse liver model offers an experimental environment which highly resembles *in-vivo* conditions while it is easily accessible and minimizes the regulatory requirements, operational costs and ethical burden associated with live animal surgery. As the perfused livers are fully functioning and maintain intact their micro-vasculature, microbubbles interacted with endothelium cells of the vessel walls in order to extravasate into the interstitial space before reaching the hepatocytes. This is a significant difference compared to the environment of *in-vitro* cell culture experiments where tumor cells are directly exposed to ultrasound and the sonoporation process forces drugs to enter cells immediately after membrane disruption.

In the present work, we have not used any drugs in order to observe and quantify any increased drug uptake. However, this work is still important as it focused (a) on establishing an experimental setup which resembles *in-vivo* conditions, (b) on studying the acoustic parameters which can then be utilized in drug delivery applications, and (c) developing the microbubble handling, dosage, administration, and activation method. The alignment of the therapy transducer with the imaging probe (with the RF artifact that shows in the imaging plane once the therapy and imaging planes overlap) allowed accurate control and close monitoring of the procedure, and also helped locating the relatively small treated area (the focal beam width was 1-2 mm) at the end of the treatment.

Both qualitative observations and quantitative methods were used to evaluate the effect of different ultrasound parameters necessary to induce extravasation. It was shown that acoustic pressures >3 MPa combined with microbubbles are capable of inducing mechanical changes to the vasculature and the surrounding tissue. The extent of the vascular damage and thus extravasation was highly dependent on the applied acoustic pressure and the pulse length. It was shown that long pulses (~1000 cycles) were necessary in order to induce detectable perfusion changes at the pressures considered here, while

shorter acoustic pulses (20 cycles) could not induce detectable perfusion changes in the area exposed to ultrasound.

Dynamic contrast-enhanced ultrasound quantification, previously used to measure microvascular flow in therapy monitoring of tumors [18], is also an excellent tool for detecting ultrasound induced microvascular alterations during extravasation. Although the proposed *ex-vivo* liver model maintains high physiological relevance compared to *in-vitro* experiments, the lack of the immune system is a difference that must be taken into consideration in future investigations. In a living organism, the processes of extravasation and sonoporation would normally induce increased local microvascular flow at first as a response to the induced inflammation in the area. With higher acoustic pressures and inertial cavitation mechanical tissue and vascular damages are induced which would then present as a decrease in the local microvascular flow. In our experiments with an *ex-vivo* organ (outside a living body) only the mechanical "damages" and the reduction in microvascular flow was detected.

The hepatic artery vasculature suffered severe changes (damage) in an extended area when livers were exposed to higher acoustic pressures (6 MPa and 10 MPa). In contrast, the portal venous vasculature suffered a much milder damage which was strictly confined in a small region around the focal area. The different extent of vascular changes of PV and HA under the same ultrasound exposure conditions might be attributed to the different morphology of veins and arteries. Three distinct layers are found in vessel walls structure: intima, media and adventitia which are mainly composed of elastin, collagen and smooth muscle. The proportions of these three components differ among arteries and veins. Thus, the mechanical properties of arteries and veins and their resistance to mechanical stress are different and this may be an explanation in the observed differences in the damage patterns. In addition, often the arterial tumor vasculature contains leaky vessels due to the increased endothelial spaces, arterial-venous shunts and generally more abnormal structure, which would be more prone to the mechanical changes by the ultrasound-induced microbubble oscillations. We would expect that the tumor HA vasculature would possibly experience even more changes than those observed in normal HA vasculature with the present therapy protocol.

The quantification results of Fig. 6.9(e, f) suggest that the presence of microbubbles would not make any significant difference in vascular disruption and consequently

perfusion during ultrasound therapeutic applications when the pressures are high (~10 MPa). However, the microbubble effect on extravasation was studied only when 10 MPa and long pulses were used, thus ultrasound cavitation in tissue due to pre-existing cavitation nuclei or possible air emboli was present even when microbubbles were not injected.

6.5 Conclusions

Ultrasound-mediated extravasation was investigated in an *ex-vivo* machine perfused pig liver model which closely resembles *in-vivo* conditions. The application of MHz-ultrasound in the presence of microbubbles is capable of inducing extravasation and perfusion changes detectable by diagnostic ultrasound at lower acoustic pressures (~3 MPa), and complete devascularization at high acoustic pressures (~10 MPa). Shorter acoustic pulses (20 cycles) produced less perfusion changes than longer pulses (1000 cycles) under the same acoustic amplitude exposure. DCEUS quantification methods were used to monitor and accurately measure microvascular changes induced by the extravasation process. Histology indicated that vascular and tissue disruption was highly focused in the area exposed to ultrasound. The findings of the present work imply that a variable level of controlled extravasation is possible which in turn may have positive implications on drug delivery of macromolecules.

Acknowledgements

Dr. Soteria Georgiadou at the National Reference Laboratory for Animal Health in Nicosia, Cyprus, and Dr. Christiana Polydorou from University of Cyprus are acknowledged for their assistance with the preparation and examination of the histology slides. Charis Rousou and Elena Pieri, MSc students in the Biomedical Ultrasound Laboratory of University of Cyprus are acknowledged for their help during experiments. We are also grateful to Kypros Stylianou for his invaluable technical assistance.

REFERENCES

[1] I. Lentacker, I. De Cock, R. Deckers, S. C. De Smedt, and C. T. W. Moonen, "Understanding ultrasound induced sonoporation: definitions and underlying mechanisms," *Adv. Drug Deliv. Rev.*, Nov. 2013.

[2] M. R. Böhmer, A. L. Klibanov, K. Tiemann, C. S. Hall, H. Gruell, and O. C. Steinbach, "Ultrasound triggered image-guided drug delivery," *Eur. J. Radiol.*, vol. 70, no. 2, pp. 242–253, May 2009.

[3] B. D. M. Meijering, L. J. M. Juffermans, A. van Wamel, R. H. Henning, I. S. Zuhorn, M. Emmer, A. M. G. Versteilen, W. J. Paulus, W. H. van Gilst, K. Kooiman, N. de Jong, R. J. P. Musters, L. E. Deelman, and O. Kamp, "Ultrasound and microbubble-targeted delivery of macromolecules is regulated by induction of endocytosis and pore formation," *Circ. Res.*, vol. 104, no. 5, pp. 679–687, Mar. 2009.

[4] M. M. Forbes, R. L. Steinberg, and W. D. O'Brien, "Examination of inertial cavitation of Optison in producing sonoporation of chinese hamster ovary cells," *Ultrasound Med. Biol.*, vol. 34, no. 12, pp. 2009–2018, Dec. 2008.

[5] B. Lammertink, R. Deckers, G. Storm, C. Moonen, and C. Bos, "Duration of ultrasound-mediated enhanced plasma membrane permeability," *Int. J. Pharm.*, vol. 482, no. 1–2, pp. 92–98, Mar. 2015.

[6] A. van Wamel, K. Kooiman, M. Harteveld, M. Emmer, F. J. ten Cate, M. Versluis, and N. de Jong, "Vibrating microbubbles poking individual cells: drug transfer into cells via sonoporation," *J. Control. Release Off. J. Control. Release Soc.*, vol. 112, no. 2, pp. 149–155, May 2006.

[7] S. Kotopoulis, A. Delalande, M. Popa, V. Mamaeva, G. Dimcevski, O. H. Gilja, M. Postema, B. T. Gjertsen, and E. McCormack, "Sonoporation-enhanced chemotherapy significantly reduces primary tumour burden in an orthotopic pancreatic cancer xenograft," *Mol. Imaging Biol. MIB Off. Publ. Acad. Mol. Imaging*, vol. 16, no. 1, pp. 53–62, Feb. 2014.

[8] O. Couture, A. Urban, A. Bretagne, L. Martinez, M. Tanter, and P. Tabeling, "In vivo targeted delivery of large payloads with an ultrasound clinical scanner," *Med. Phys.*, vol. 39, no. 8, pp. 5229–5237, Aug. 2012.

[9] K. Keyhani, H. R. Guzmán, A. Parsons, T. N. Lewis, and M. R. Prausnitz, "Intracellular drug delivery using low-frequency ultrasound: quantification of molecular uptake and cell viability," *Pharm. Res.*, vol. 18, no. 11, pp. 1514–1520, Nov. 2001.

[10] H. R. Guzmán, D. X. Nguyen, A. J. McNamara, and M. R. Prausnitz, "Equilibrium loading of cells with macromolecules by ultrasound: effects of molecular size and acoustic energy," *J. Pharm. Sci.*, vol. 91, no. 7, pp. 1693–1701, Jul. 2002.

[11] Z. P. Shen, A. A. Brayman, L. Chen, and C. H. Miao, "Ultrasound with microbubbles enhances gene expression of plasmid DNA in the liver via intraportal delivery," *Gene Ther.*, vol. 15, no. 16, pp. 1147–1155, Aug. 2008.

[12] S. Song, Z. Shen, L. Chen, A. A. Brayman, and C. H. Miao, "Explorations of high-intensity therapeutic ultrasound and microbubble-mediated gene delivery in mouse liver," *Gene Ther.*, vol. 18, no. 10, pp. 1006–1014, Oct. 2011.

[13] S. Kotopoulis, G. Dimcevski, O. Helge Gilja, D. Hoem, and M. Postema, “Treatment of human pancreatic cancer using combined ultrasound, microbubbles, and gemcitabine: A clinical case study,” *Med. Phys.*, vol. 40, no. 7, p. -, 2013.

[14] M.-L. Izamis, A. Efstathiades, C. Keravnou, E. L. Leen, and M. A. Averkiou, “Dynamic contrast-enhanced ultrasound of slaughterhouse porcine livers in machine perfusion,” *Ultrasound Med. Biol.*, vol. 40, no. 9, pp. 2217–2230, Sep. 2014.

[15] C. P. Keravnou, M.-L. Izamis, and M. A. Averkiou, “A method for estimating the acoustic pressure in tissues using low amplitude measurements in water,” *Ultrasound Med. Biol.*, In press.

[16] C. Strouthos, M. Lampaskis, V. Sboros, A. McNeilly, and M. Averkiou, “Indicator dilution models for the quantification of microvascular blood flow with bolus administration of ultrasound contrast agents,” *IEEE Trans. Ultrason. Ferroelectr. Freq. Control*, vol. 57, no. 6, pp. 1296–1310, Jun. 2010.

[17] C. F. Dietrich, M. A. Averkiou, J.-M. Correas, N. Lassau, E. Leen, and F. Piscaglia, “An EFSUMB introduction into Dynamic Contrast-Enhanced Ultrasound (DCE-US) for quantification of tumour perfusion,” *Ultraschall Med. Stuttg. Ger. 1980*, vol. 33, no. 4, pp. 344–351, Aug. 2012.

[18] E. Leen, M. Averkiou, M. Arditi, P. Burns, D. Bokor, T. Gauthier, Y. Kono, and O. Lucidarme, “Dynamic contrast enhanced ultrasound assessment of the vascular effects of novel therapeutics in early stage trials,” *Eur. Radiol.*, vol. 22, no. 7, pp. 1442–1450, Jul. 2012.

7 Summary and future directions

"The voyage of discovery is not in seeking new landscapes but in having new eyes."

Marcel Proust [1]

7.1 Summary

Cancer is considered to be one of the leading causes of death in Europe and the Unites States. Thus, the need for improved healthcare where the treatments will take into account individual patient needs emerges, especially in the fields of oncology and cardiology. The therapeutic prospective of ultrasound combined with microbubbles and drugs has gained increased attention in research and clinics as the advantages of such localized treatments are associated with increased medication efficacy and improved life quality of the patients [2]. This thesis aimed to contribute in the field of ultrasound-mediated drug delivery by developing new tools and methods that will advance research from *in-vitro* experiments and small animal models to a full scale clinically relevant environment.

Chapter 2 described the development of a machine perfusion system and the methodology for *ex-vivo* preservation and evaluation of isolated human-sized livers. The *ex-vivo* machine perfusion system for human-sized liver preservation was used throughout this thesis as the test platform for investigations associated with ultrasound therapeutic approaches. Pig livers were preferred over livers from other species as they are more similar to human livers with respect to physiology and anatomy [3]. The functionality and viability of slaughterhouse pig livers sustained in machine perfusion was evaluated with hemodynamic and biochemical measurements and histological findings. In addition, dynamic contrast-enhanced ultrasound (DCEUS) was specifically optimized to become a valuable tool in the assessment of the condition of machine-perfused organs.

The introduction of DCEUS is an invaluable tool in whole-organ machine perfusion preservation as it offers both qualitative and quantitative control of livers condition in a non-invasive and easy manner. Gross morphology examination could not detect the presence of anatomic abnormalities and illustrate the perfusion throughout the entire organ, which is now possible with DCEUS. Dynamic contrast-enhanced ultrasound has the potential to define novel metrics of organ viability while sustained in machine perfusion, evaluate the perfusion quality in either the portal venous, the arterial vascular

tree or both and recognize obstacles in physiological flow such as thrombi or air embolisms.

It was shown that porcine livers preserved in the developed machine perfusion system are viable and well-functioning organs which are stable for at least 3 hours of experimentation. The developed model can be used as a versatile test platform for the study of diseases that characteristically affect perfusion quality and for interventions that depend on controllable and quantifiable perfusion, such as the study of vasoactive drugs, drug delivery and tumor ablation.

According to Apfel [4], three golden rules are necessary to be considered when studying cavitation related phenomena; "*know thy sound field*", "*know thy liquid*" and "*know when something happens*". Thus, prior to any investigations related to ultrasound therapeutic applications in this thesis, Chapter 3 focused on the estimation of the *in-situ* acoustic field when tissue is exposed to ultrasound. A simple, reliable, and reproducible method based on low amplitude measurements in water and knowledge of the attenuation of the tissue of interest was evaluated for its accuracy in estimating the acoustic pressure delivered in the exposed area. Such a method has small experimental errors when compared with hydrophone measurements of sound fields at high output levels and simplifies the theoretical and computational aspects of the acoustic pressure derating problem.

Both simulations and experiments were contacted for validation of the linear extrapolation method. A well-established nonlinear model, the KZK equation [5], was used in simulations and a wide parameter space (attenuation and nonlinearity values) was considered to cover a range of different tissue types and source pressure amplitudes. In experiments, pressure values measured after propagation through *ex-vivo* machine-perfused liver tissue samples were compared to the estimated pressure values calculated using linear extrapolation. From measurements and simulations it was shown that the proposed method can predict *in-situ* pressure for a large range of nonlinearity and attenuation values. As the attenuation value increases it counters the nonlinear distortion effects and the proposed method becomes more accurate even at very high acoustic pressures. The proposed method can estimate the *in-situ* peak negative pressure with errors ≤20% for Γ values up to 1, and the peak positive pressures with errors ≤20% for Γ values up to 4.

The main required input for the extrapolation method studied in Chapter 3 is the attenuation coefficient of the tissue of interest. Thus, to assess the exact acoustic properties of the experimental samples used to validate the linear extrapolation method, pig liver attenuation was measured in the range of 2 – 8 MHz and the attenuation–frequency relationship was derived. It is the first time that samples taken from a re-perfused organ are being used to measure liver tissue attenuation. This is of great importance since the samples used were harvested from a viable and normal functioning organ instead of excised tissue samples that were used in the past.

Microbubbles combined with ultrasound may be one of the most promising theranostic tools [2]. Thus, in Chapter 4 of this thesis a diagnostic ultrasound scanner was considered as both an imaging and therapy device and was used to measure microbubble response to increasing acoustic amplitude. A wide range of acoustic pressure was considered (0.06 – 2.6 MPa) that might be utilized in ultrasound therapeutic applications. At the same time, the problem of signal saturation observed when ultrasound scanners are used to record backscattering from microbubbles was addressed and a correction method was provided.

Without the effect of signal saturation, it was observed that up to acoustic pressures of 2.6 MPa, the intensity of backscattered signals from microbubbles increased quarticly in agreement with the relevant theory and previously published results [6]. Additionally, signal saturation reduction enabled for the first time accurate measurements of CTR, which was found to be constant with MI contrary to previous perception [7]. These results suggest that microbubbles may be imaged equally well even above bubble destruction threshold which is very important for imaging approaches in therapeutic procedures that use high MIs. For example, in drug delivery applications at MIs that cause bubble destruction, good triggered images (in order to allow for microbubble replenishment in the imaging plane) with nonlinear techniques (e.g. harmonic imaging) may be formed by simply thresholding the tissue signals due to nonlinear propagation. Bubble response measurements in a wide range of MIs may also advance investigations of therapeutic applications that combine microbubbles and ultrasound such as sonoporation, sonothrombolysis, and gene transfection. The potential of imaging microbubbles in response to high excitation amplitudes might be beneficial when considering the various sonoporation and extravasations hypothesis relying on phenomena such as micro-jet formation and cell membrane disruption [8].

The correction of signal saturation is also very important for the DCEUS quantification methods that were developed and described in Chapter 5 of this thesis. Errors in the calculated quantification parameters related to signal intensity were carefully avoided with our new approach.

In Chapter 5, contrast-enhanced ultrasound quantification approaches were studied in order to develop an accurate technique of micro-flow measurements. DCEUS quantification based on indicator dilution theory has been proposed to be used for monitoring the outcomes of therapies targeting tumor angiogenesis under the hypothesis that bolus quantification parameters are sensitive to flow changes caused by antiangiogenic treatments received by the patients. Clinical studies are found in the literature that support the hypothesis above [9]–[12], however preclinical investigations that quantify the possibilities and limitations of the method are scarce. Thus, in this thesis, DCEUS quantification methods were evaluated in the functioning *ex-vivo* pig liver model to find the range of accuracy and strength and weaknesses in measuring flow in the microcirculation in a highly controlled environment which closely resembles *in-vivo* conditions.

Two tasks were studied for the first time in a machine-perfused liver; (1) the effect of bubble concentration on quantification parameters under constant flow rate and (2) the effect of flow rate changes on the extracted quantification parameters using constant contrast concentration. One advantage of the *ex-vivo* machine perfusion model is that injections can be administered to either the hepatic artery (HA) or the portal vein (PV) and consequently those specific vascular networks can be studied independently. An important aspect of this work was that during data collection the gain correction method (avoiding signal saturation) developed in Chapter 4 was used to avoid errors associated with the calculation of the quantification parameters after curve fitting of the time-intensity curves.

The intensity-concentration relationship was found to be linear in agreement with theoretical predictions and previously published *in-vitro* results [13], [14]. This is important as the linear relationship between image intensity and bubble concentration is the underlying assumption for being able to use quantification methods based on indicator dilution theory. In contrast, time quantification parameters were not affected by bubble concentration changes, which is also important for clinical studies and suggest that small

variations in the amount of contrast agents being administered are not affecting the accuracy of flow measurement.

This study also showed that DCEUS quantification is capable of measuring flow changes in both macro- and micro-circulation for a bolus injection [15], [16] as the rise time (RT), the mean transit time (MTT) and the area under the curve (AUC) were all found to be inversely proportional to flow rate (as predicted by the Stewart-Hamilton relationships). When flow changes were induced in the HA, they were detected only in the large branches of the input vessel and they could not be measured in the outflow vessel (hepatic vein, HV) nor the parenchyma. This is attributed to the fact that HA is only the 25% of the liver blood supply thus the flow changes that reached outflow (which is the summation of PV and HA flows) and the parenchyma [where both (PV+HA) networks combine right before continuing onto to the HV network] were small. However, when flow changes were induced in the PV vasculature, which is typically the 75% of the liver blood supply, they were easily detected also in the micro-vasculature (parenchyma) and the outflow (HV). Nevertheless this will not be an issue when trying to monitor tumor response to therapy as tumor blood supply is mostly arterial.

DCEUS can be a valuable tool in predicting patient response to drugs targeting angiogenesis. However in the present thesis it was also proposed as a metric for evaluation of ultrasound therapeutic applications, such as sonoporation. Ultrasound-mediated drug delivery aims in advancing therapeutics deposition on the diseased site after alterations of the tumor vasculature (extravasation or cell membrane disruption) due to microbubble-induced bioeffects. Thus, DCEUS quantification can be used to measure flow changes caused by microbubble interactions with the vessels.

Chapter 6 focused on the study of the interactions of ultrasound-driven microbubbles with the microvasculature of a functioning *ex-vivo* pig liver under image guidance. Specifically, the objective was to identify the ultrasound parameters that are capable of causing detectable perfusion changes and extravasation in the area exposed to ultrasound in a test platform that highly resembles *in-vivo* conditions. The effect of acoustic pressure, number of cycles, and microbubble presence on vessel poration and extravasation were evaluated using gross morphology by lesion size examination and histology. In addition, micro-vascular flow changes caused during therapeutic ultrasound exposure were detected using DCEUS quantification based on indicator dilution

approaches. The developed experimental setup allowed real time monitoring of the therapy procedure and imaging of the cavitation activity.

DCEUS quantification was able to detect flow changes induced due to extravasation. The magnitude of flow changes was dependent on acoustic pressure and pulse length. It was shown that the application of MHz-ultrasound in the presence of resonant microbubbles was capable of inducing extravasation and perfusion changes detectable by diagnostic ultrasound at lower acoustic pressures (~3 MPa); complete devascularization was observed at high acoustic pressures (~10 MPa). Shorter acoustic pulses (20 cycles) produced less perfusion changes than longer pulses (1000 cycles) under the same acoustic amplitude exposure.

Histology showed that the applied acoustic field caused highly localized damage in the liver even when applying the higher acoustic pressure (10 MPa). Liver tissue samples did not show significant differences between the control and the treated area.

Last, it was observed that HA vasculature suffered severe damage in an extended area when livers were exposed to high acoustic pressures (6 MPa and 10 MPa). In contrast, PV vasculature suffered a much milder damage which was strictly confined in a smaller area around the focus of the therapy source. The different extent of vascular damage of PV and HA under the same ultrasound exposure conditions might be attributed to the different morphology of veins and arteries. It is further believed that the tumoral HA network would be even more prone to extravasation and perfusion changes by ultrasound driver microbubbles.

7.2 List of Original Contributions

This thesis offered the following contributions in the field of ultrasound-mediated image-guided drug delivery approaches:

- Developed a fully functioning, human-sized organ (*ex-vivo* machine-perfused pig liver) as a versatile test platform for DCEUS quantification and ultrasound-mediated drug delivery investigations. This environment offers several hours of controlled experimentation while maintains highly relevance to *in-vivo* conditions in respect to physiology and anatomy.

- Established the use of DCEUS for monitoring and evaluating perfusion quality in *ex-vivo* machine perfusion whole organ preservation. Gross morphology inspection could not detect the presence of anatomic abnormalities and illustrate the perfusion throughout the entire organ, which is now possible with DCEUS.

- Evaluated the limitations and accuracy of a simple method based on low amplitude measurements in water and knowledge of the attenuation of the tissue of interest in estimating the acoustic pressure delivered in the area exposed to ultrasound (*in-situ*) using both simulations and measurements. The knowledge of the *in-situ* acoustic field is important for cavitation-related phenomena found in ultrasound-mediated drug delivery. A variety of different tissue types and acoustic pressures were considered.

- Performed measurements of attenuation in tissue samples harvested from *ex-vivo* machine-perfused livers. As attenuation differs according to organs or tissue state, these measurements highly resemble attenuation values of physiological functioning *in-vivo* organs and are important for pressure derating methods in diagnostic and therapeutic applications.

- Developed a method that eliminates signal saturation in diagnostic ultrasound scanners for microbubbles-related investigations. This allowed accurate measurements of contrast to tissue ratio with increasing MI, which was not done in the past. Signal saturation removal also further improved DCEUS quantification.

- Proved that the tissue nonlinearity dependence with acoustic pressure is very similar to that of microbubbles (contrary to the current understanding) and thus the contrast to tissue ratio is constant across all acoustic pressures. This finding enabled the development of equally effective imaging approaches in high MIs therapeutic applications as low non-destructive MIs.

- Studied for the first time the intensity-concentration relationship in a functioning machine-perfused pig liver without the effect of signal saturation. This finding is important as the linear relationship between image intensity and bubble concentration is the underlying assumption for being able to use quantification methods based on indicator dilution theory.

- Studied the strengths and weaknesses of flow measurements using DCEUS quantification based on indicator dilution theory in a machine-perfused pig liver. It was proved that DCEUS quantification is capable of measuring flow changes both in the macro- and micro- circulation using parameters such as RT, MTT and AUC according to Stewart-Hamilton relationships for a bolus injection. This finding can establish DCEUS quantification as a valuable tool for monitoring therapies that target tumor vascularity.

- Investigated the interactions of ultrasound-driven resonant microbubbles with the microvasculature of a machine-perfused pig liver for different acoustic pressures, pulse length and microbubble presence or absence. The developed experimental setup allowed real time imaging of the cavitation activity during therapy.

- Showed that extravasation and perfusion changes correlate with the acoustic pressure. Shorter acoustic pulses (20 cycles) produced less perfusion changes than longer pulses (1000 cycles) under the same acoustic amplitude exposure.

- Showed that the arterial vasculature is more sensitive to acoustic pressure exposure than the portal venous vasculature which can be an important finding in ultrasound-mediated drug delivery as tumors blood supply is mostly arterial.

7.3 Conclusion

Marcel Proust in his novel "La Prisonnière" wrote that "*The voyage of discovery is not in seeking new landscapes but in having new eyes.*" The studies in this thesis were performed in a new, clinically relevant environment and the developed tools and methods can advance ultrasound-mediated image-guided drug delivery which is a promising approach in the fight against cancer. Research is an endless voyage with unlimited potentials. Here, a stepping stone has been set; plethora of future ultrasound therapeutic investigations can be performed in the proposed machine-perfused liver that will further advance the state of the art in ultrasound-mediated drug delivery and help its establishment in the clinics.

7.4 Future directions

We envision further development of the proposed experimental setup, accompanied by the administration of drugs in this clinically relevant test platform (*ex-vivo* machine-perfused liver). Measurements of drug uptake facilitated by ultrasound and microbubbles in an environment that mimics *in-vivo* conditions would be invaluable for the better understanding of the mechanisms of ultrasound-mediated drug delivery.

Another interesting future direction is that human organs (or part of organs) surgically removed from patients with cancer might be preserved in a similar machine perfusion system. Thus, ultrasound-mediated drug delivery can be studied in a real tumor model prior to clinical trials.

REFERENCES

[1] M. Proust, *La Prisonnière*. Paris: Nouvelle revue francaise, 1923.

[2] K. H. Martin and P. A. Dayton, "Current status and prospects for microbubbles in ultrasound theranostics," *Wiley Interdiscip. Rev. Nanomed. Nanobiotechnol.*, vol. 5, no. 4, pp. 329–345, Aug. 2013.

[3] H. Boxenbaum, "Interspecies variation in liver weight, hepatic blood flow, and antipyrine intrinsic clearance: extrapolation of data to benzodiazepines and phenytoin," *J. Pharmacokinet. Biopharm.*, vol. 8, no. 2, pp. 165–176, Apr. 1980.

[4] L. A. Crum, Advanced Study Institute on Sonochemistry and Sonoluminescence, and NATO Advanced Study Institute on Sonochemistry and Sonoluminescence, *Sonochemistry and sonoluminescence : [proceedings of the NATO Advanced Study Institute on Sonochemistry and Sonoluminescence, Leavenworth, Washington, USA, 18 - 29 August 1997]*. Dordrecht: Kluwer, 1999.

[5] M. A. Averkiou and M. F. Hamilton, "Nonlinear distortion of short pulses radiated by plane and focused circular pistons.," *J. Acoust. Soc. Am.*, vol. 102, no. 5, pp. 2539–48, 1997.

[6] W. T. Shi and F. Forsberg, "Ultrasonic characterization of the nonlinear properties of contrast microbubbles," *Ultrasound Med. Biol.*, vol. 26, no. 1, pp. 93–104, Jan. 2000.

[7] J.-M. Escoffre, C. Mannaris, B. Geers, A. Novell, I. Lentacker, M. Averkiou, and A. Bouakaz, "Doxorubicin liposome-loaded microbubbles for contrast imaging and ultrasound-triggered drug delivery," *IEEE Trans. Ultrason. Ferroelectr. Freq. Control*, vol. 60, no. 1, pp. 78–87, Jan. 2013.

[8] I. Lentacker, I. De Cock, R. Deckers, S. C. De Smedt, and C. T. W. Moonen, "Understanding ultrasound induced sonoporation: definitions and underlying mechanisms," *Adv. Drug Deliv. Rev.*, Nov. 2013.

[9] N. Lassau, L. Chami, B. Benatsou, P. Peronneau, and A. Roche, "Dynamic contrast-enhanced ultrasonography (DCE-US) with quantification of tumor perfusion: a new diagnostic tool to evaluate the early effects of antiangiogenic treatment," *Eur. Radiol.*, vol. 17 Suppl 6, pp. F89–98, Dec. 2007.

[10] N. Lassau, M. Lamuraglia, L. Chami, J. Leclère, S. Bonvalot, P. Terrier, A. Roche, and A. Le Cesne, "Gastrointestinal Stromal Tumors Treated with Imatinib: Monitoring Response with Contrast-Enhanced Sonography," *Am. J. Roentgenol.*, vol. 187, no. 5, pp. 1267–1273, Nov. 2006.

[11] M. Averkiou, M. Lampaskis, K. Kyriakopoulou, D. Skarlos, G. Klouvas, C. Strouthos, and E. Leen, "Quantification of tumor microvascularity with respiratory gated contrast enhanced ultrasound for monitoring therapy," *Ultrasound Med. Biol.*, vol. 36, no. 1, pp. 68–77, Jan. 2010.

[12] E. Leen, M. Averkiou, M. Arditi, P. Burns, D. Bokor, T. Gauthier, Y. Kono, and O. Lucidarme, "Dynamic contrast enhanced ultrasound assessment of the vascular effects of novel therapeutics in early stage trials," *Eur. Radiol.*, vol. 22, no. 7, pp. 1442–1450, Jul. 2012.

[13] C. Keravnou, C. Mannaris, and M. Averkiou, “Accurate measurement of microbubble response to ultrasound with a diagnostic ultrasound scanner,” *IEEE Trans. Ultrason. Ferroelectr. Freq. Control*, vol. 62, no. 1, pp. 176–184, Jan. 2015.

[14] M. Lampaskis and M. Averkiou, “Investigation of the relationship of nonlinear backscattered ultrasound intensity with microbubble concentration at low MI,” *Ultrasound Med. Biol.*, vol. 36, no. 2, pp. 306–312, Feb. 2010.

[15] G. N. Stewart, “Researches on the Circulation Time in Organs and on the Influences which affect it: Parts I.-III,” *J. Physiol.*, vol. 15, no. 1–2, pp. 1–89, Jul. 1893.

[16] W. F. Hamilton, J. W. Moore, J. M. Kinsman, and R. G. Spurling, “Simultaneous determination of the pulmonary and systemic circulation times in man and of a figure related to the cardiac output,” *Am. J. Physiol. -- Leg. Content*, vol. 84, no. 2, pp. 338–344, Mar. 1928.

List of publications

Journal articles

1. M.-L. Izamis, A. Efstathiades, **C. Keravnou**, S. Georgiadou, P. N. Martins, and M. Averkiou, "Effects of air embolism size and location on porcine hepatic microcirculation in machine perfusion," *Liver Transplant. Off. Publ. Am. Assoc. Study Liver Dis. Int. Liver Transplant. Soc.*, vol. 20, no. 5, pp. 601–611, May 2014.

2. **C. Keravnou**, M. Averkiou, "Harmonic generation with a dual frequency pulse," *J. Acoust. Soc. Am.*, vol. 135, no. 5, pp. 2545–2552, May 2014.

3. M.L. Izamis, A. Efstathiades, **C. Keravnou** , E.L Leen, M. A. Averkiou, "Dynamic Contrast Enhanced Ultrasound of Slaughterhouse Porcine Livers in Machine Perfusion," *Ultrasound in Med. & Biol.*, vol. 40, no. 9, pp. 2217–2230, September 2014.

4. **C. Keravnou**, C. Mannaris, and M. Averkiou, "Accurate measurement of microbubble response to ultrasound with a diagnostic ultrasound scanner," *IEEE Trans. Ultrason. Ferroelectr. Freq. Control*, vol. 62, no. 1, pp. 176–184, January 2015.

5. **C. Keravnou**, M.L. Izamis, and M. Averkiou, "A method for estimating the acoustic pressure in tissues using low amplitude measurements in water", *Ultrasound in Med. & Biol*, August 2015.

6. **C. Keravnou**, M.L. Izamis, E. Leen and M. Averkiou, "Evaluation of perfusion quantification methods with ultrasound contrast agents in a machine-perfused pig liver," Submitted to *Ultraschall*, August 2015.

7. **C. Keravnou**, I. De Cock, M.L Izamis and M. Averkiou, "Extravasation and vascular perfusion changes induced by ultrasound and microbubbles in a machine-perfused pig liver model," In preparation for submission to *Physics in Medicine and Biology*.

Abstracts and Conference proceedings

1. **C. Keravnou**, C. Mannaris, M. A. Averkiou, "Dual frequency excitation for broadband nonlinear imaging," *17th European Symposium on Ultrasound Contrast Imaging, Rotterdam*, The Netherlands, Jan. 2012.

2. M.L. Izamis, A. Efstathiades, **C. Keravnou**, M. Averkiou, "Quantitative Evaluation of ex vivo Livers in Machine Perfusion with Dynamic Contrast-Enhanced Ultrasound,"

18th European Symposium on Ultrasound Contrast Imaging, pg. 68 -71, Rotterdam, The Netherlands, Jan. 2013.

3. **C. Keravnou**, M. Averkiou, "Harmonic generation with a dual frequency pulse," *IEEE joined UFFC, EFTF and PMF symposium*, Prague, Czech Republic, Jul. 2013.

4. M.L. Izamis, **C. Keravnou**, D. Christofides, M. Averkiou, "Quantification of liver perfusion is a sensitive approach to non-invasive evaluation of donor liver viability," *AASLD*, Washington D.C, USA, November 2013

5. **C. Keravnou**, M.L. Izamis, M. Averkiou, "A method for calculating acoustic pressure in the liver using linear measurements in water," *19th European Symposium on Ultrasound Contrast Imaging*, pg. 119-123, Rotterdam, The Netherlands, Jan. 2014. (Best Poster Award in the category: New Directions I)

6. M.L. Izamis, **C. Keravnou**, D. Christofides, E. Leen, M. Averkiou, "Basic bolus kinetics explored in an ex vivo liver machine perfusion model," *19th European Symposium on Ultrasound Contrast Imaging*, pg. 90-93, Rotterdam, The Netherlands, Jan. 2014.

7. **C. Keravnou**, C. Mannaris, M.L Izamis, M. Averkiou, "Image-Guided Sonoporation in an Ex-Vivo Machine Perfused Porcine Liver," *4th International Symposium of Current and Future Applications of Focused Ultrasound*, North Bethesda, Maryland, USA, Oct. 2014. (Young Investigator Award)

8. M. Averkiou, **C. Keravnou**, M.L Izamis, "Image-Guided Sonoporation in an Ex-Vivo Machine Perfused Porcine Liver," *15th International Symposium of Therapeutic Ultrasound*, Utrecht, The Netherlands, April 2015

9. **C. Keravnou**, C. Rousou, M.L Izamis, M. Averkiou, "Evaluation of perfusion quantification methods for measuring therapy outcomes with DCEUS in a machine-perfused pig liver model," *15th International Symposium of Therapeutic Ultrasound*, Utrecht, The Netherlands, April 2015